UNIVERSITY OF LEEDS

Consequences of decellularisation on the biomechanical and biological properties of a porcine tendon at a whole-tendon and sub-tendon scale

Beatriz Jacqueline Solis Cordova

Submitted in accordance with the requirements for
the degree of Doctor of Philosophy

The University of Leeds
Institute of Medical and Biological Engineering
School of Mechanical Engineering

September 2023

Abstract

Anterior cruciate ligament (ACL) ruptures occur in 1 – 10 in 1000 people annually, increasingly affecting younger populations. Around 400 thousand ACL reconstructions (ACLR) are performed annually, relying on autografts and allografts, both with disadvantages including donor site morbidity, limited availability and structural degradation causing a reduction in the graft's mechanical properties. An alternative solution could be to use decellularised porcine superflexor tendon (pSFT) as a biocompatible graft. Decellularisation removes the cellular components from the tissue, providing a non-immunogenic, highly conserved extracellular matrix scaffold. However, the effect of the decellularisation process on the structure and biomechanics of pSFT have not been fully elucidated.

The aim of this study was to investigate the biological and biomechanical consequences of the decellularisation process on pSFT using a hierarchical approach, analysing at different levels of scale to prove its suitability to act as a graft for ACLR. It was found that alternative solutions to phosphate buffered saline used during end-stage washes of the decellularisation process reduced pSFT swelling while effectively removing cellular components. It was apparent that the decellularisation process affected the interfascicular matrix of pSFT, contributing to the changes seen in collagen crimp and mechanical properties of whole tendon, while also observed in the topography at the sub-tendon scale. The complete mechanical profile of decellularised pSFT was obtained for the first time, showing the tensile and compressive properties were mostly comparable to native pSFT, with no significant loss of collagenous or non-collagenous components. Fascicle structures showed a mostly unaltered arrangement of fibre and fibril structures, with an apparent loss of endotendineum post-decellularisation.

Although there is a need for further studies to investigate the biocompatibility, nanomechanics, proteomics and recellularisation of pSFT, particularly at the sub-tendon scale, this study demonstrated decellularised superflexor tendon is a viable biological graft for ACLR.

Intellectual Property

The candidate confirms that the work submitted is her own and that appropriate credit has been given where reference has been made to the work of others.

Acknowledgements

I would like to thank my wonderful, joyful and incredibly helpful supervisory team. Without the guidance, support, patience and motivation of Dr Anthony Herbert, Prof Claire Brockett, Dr Jen Edwards and Dr Hazel Fermor, none of this project would have been possible. I am deeply grateful for the massive part you played in this research, but particularly for always believing in me and going above and beyond during difficult times. I am honoured to have worked alongside such a brilliant group of people, both in and outside an academic setting. You are truly special, and helped achieve what sometimes seemed unattainable dreams.

I am very grateful to colleagues in iMBE laboratories, both in Biological Sciences and Mechanical Engineering. I would especially like to express massive thanks to Mrs Nicola Conway, who provided me with much needed knowledge, but more importantly, a beautiful friendship and support whenever I needed it. I would also like to thank Mr Andrew Stockdale and Dr Lekshmi Kailas, for all their advice and lovely chats. I would also like to show appreciation to all postgraduate researchers who provided a helping hand in ridding of tissue waste, or simply offered a warm conversation.

I want to express thankfulness to the Mexican National Council for Science and Technology (CONACyT) for financially supporting this endeavour.

I would like to express the sincerest gratitude to my two best friends who shared most of the PhD journey, Dr Sahirah Islam and Emily Absalom. It is truly amazing how wise you both are, and I will forever be in debt to you for allowing me to be a part of your lovely lives. Sahirah, I do not know what I would have done without you in Biological Sciences. You pushed me to be the best version of myself on a daily basis, inspiring me with your strength. Emily, you never ceased to believe in me, no matter how many mistakes I made. You allowed me to be your family in a country foreign to me. You are the reason I didn't give up on my dreams. I have never known a friend like you.

I would like to thank my best friend, my dearest Dr Juan Martinez Ojeda. Without you, I wouldn't have made it this far. Your intelligence never ceases to amaze me, you're truly an inspiration. Thank you for always being there and for helping me understand my failures do not define who I am. I am forever thankful to Ryan Absalom for letting me into his home and family with open arms, for showing me kindness and patience expecting nothing in return. I would not have reached the finish line without you. I would also like to thank my friends back home, Dylan Garcia, David Coiffier and Daniela Yeo. No matter the distance, you always offered me true friendship and support. Thank you for believing I could accomplish this!

Finally, I would like to show the greatest appreciation to my parents, Dr Jose Solis-Romero and Beatriz Cordova. I aspire to be half as exceptional as you both one day. Thank you for your endless support. The videocalls keeping me updated on family news, the texts asking if I'd eaten, the words of encouragement to finish this thesis! I hope I have made you proud and continue to do so throughout life. I would also like to thank my extended family who constantly show me love and support, sustaining me through this long journey away from home.

This thesis is dedicated to my uncle
Salvador Ortiz and my aunt Maria Luisa
Cordova, who were taken from us too soon.
Thank you for your unconditional and
transcendental love.

Contents

List of Figures

List of Tables

Abbreviations

2D	Two-dimensional
3D	Three-dimensional
ACL	Anterior cruciate ligament
ACLR	Anterior cruciate ligament replacement
AFM	Atomic Force Microscopy/Microscope
alpha-Gal	Galactose-alpha-1, 3-galactose
ANOVA	Analysis of variance
ChABC	Chondroitinase ABC
CI	Confidence intervals
DAPI	4',6-diamidino-2-phenylindole
DC	Decellularised
DMB	1,9-dimethylmethylene blue
ECM	Extracellular matrix
EDTA	Ethylenediaminetetraacetic acid
GAG	Glycosaminoglycan
H&E	Haematoxylin and eosin
HCl	Hydrochloric acid
IFM	Interfascicular matrix
ISO	International organisation for standardisation
NaOH	Sodium hydroxide
NBF	Neutral buffered formalin
OA	Osteoarthritis
PAA	Peracetic acid

PBS	Phosphate buffered saline
PG	Proteoglycan
pSFT	Porcine superflexor tendon
SDS	Sodium dodecyl sulfate
UTS	Ultimate tensile strength

Outputs

Conference presentations

Centre for Doctoral Training in Tissue Engineering and Regenerative Medicine Symposium, University of Leeds, UK (2019) Poster presentation

Jacqueline Solis, Jennifer H. Edwards, Hazel L. Fermor, Claire Brockett and Anthony Herbert, Consequences of decellularisation on the biomechanical and biological properties of a porcine tendon at a sub-tendon scale

Cross Centres for Doctoral Training Symposium, University of Leeds, UK (2019) Poster presentation

Jacqueline Solis, Jennifer H. Edwards, Hazel L. Fermor, Claire Brockett and Anthony Herbert, Consequences of decellularisation on the biomechanical and biological properties of a porcine tendon at a sub-tendon scale

EPSRC and MRC Centres for Doctoral Training in Tissue Engineering and Regenerative Medicine Joint Conference, Manchester University, UK (2019) Oral presentation

Jacqueline Solis, Jennifer H. Edwards, Hazel L. Fermor, Claire Brockett and Anthony Herbert, Consequences of decellularisation on the biomechanical and biological properties of a porcine tendon at a sub-tendon scale

Future Leaders Joint Centres for Doctoral Training and UK Society for Biomaterials Virtual Conference, online, UK (2020) Flash poster presentation

Jacqueline Solis and Anthony Herbert, The influence of swelling during decellularisation and its impact on the biomechanics of porcine tendon

Annual Meeting of the White Rose Biomaterials and Tissue Engineering Group, online, UK (2020) Flash oral presentation and poster presentation

Jacqueline Solis, Jennifer H. Edwards, Hazel L. Fermor, Claire Brockett and Anthony Herbert, Modification of decellularisation methods to assess the effects of swelling on the mechanical properties of porcine tendon

Future Leaders in Regenerative Medicine Joint Centres for Doctoral Training and UK Society for Biomaterials Virtual Conference, online, UK (2021) Flash poster presentation

Jacqueline Solis, Jennifer H. Edwards, Hazel L. Fermor, Claire Brockett and Anthony Herbert, Modification of decellularisation methods to assess the effects of swelling on the mechanical properties of porcine tendon

Tissue Engineering and Regenerative Medicine International Society 6th World Congress, Netherlands, online, UK (2021) Poster presentation

Jacqueline Solis, Jennifer H. Edwards, Hazel L. Fermor, Claire Brockett and Anthony Herbert, Modification of decellularisation methods to assess the effects of swelling on the mechanical properties of porcine tendon

British Orthopaedic Society Annual Meeting, online, UK (2021) Oral presentation

Jacqueline Solis, Jennifer H. Edwards, Hazel L. Fermor, Claire Brockett and Anthony Herbert, Modification of decellularisation methods to assess the effects of swelling on the mechanical properties and composition of porcine tendon

Tissue and Cell Engineering Society and Joint EPSRC Centres for Doctoral Training Conference, University of Birmingham, UK (2022) Oral presentation

Jacqueline Solis, Jennifer H. Edwards, Hazel L. Fermor, Philip L. Riches, Claire Brockett and Anthony Herbert, Characterisation of native and decellularised porcine tendon under tension and compression: a closer look at glycosaminoglycan contribution to tendon mechanics

International Combined Orthopaedic Research Societies World Orthopaedic Congress: oral poster presentation, University of Edinburgh, UK (2022) Oral presentation and poster presentation

Jacqueline Solis, Jennifer H. Edwards, Hazel L. Fermor, Philip L. Riches, Claire Brockett and Anthony Herbert, Characterisation of native and decellularised porcine tendon under tension and compression: a closer look at glycosaminoglycan contribution to tendon mechanics

9th International Ankle Symposium, Japan, online (2022) Oral presentation

Jacqueline Solis, Jennifer H. Edwards, Hazel L. Fermor, Philip L. Riches, Claire Brockett and Anthony Herbert, Decellularised porcine tendon as a potential graft for ankle ligament reconstruction: a biomechanical characterisation under tension and compression assessing the contribution of glycosaminoglycans to tendon mechanics

Publications

Solis-Cordova J, Edwards JH, Fermor HL, Riches P, Brockett CL, Herbert A. Characterisation of native and decellularised porcine tendon under tension and compression: A closer look at glycosaminoglycan contribution to tendon mechanics. J Mech Behav Biomed Mater. 2023 Mar;139:105671. doi: 10.1016/j.jmbbm.2023.105671. Epub 2023 Jan 11. PMID: 36682172.

Chapter 1

Introduction

1.1 Tendons and ligaments

1.1.1 Structure and function

The main structures that stabilise and facilitate joint movement are ligaments and tendons [1]. These are bands of dense fibrous connective tissue, bearing similarities in both composition and architecture [2]. Tendons/ligaments are characteristically white and glossy, while dense and firm (Figure 1.1) [3]. The structure of ligaments and tendons varies in shape, according to attachment sites, location and loads the tissue is subject to [4].

Figure 1.1: Porcine deep digital flexor tendon,
with a white and glossy surface along the length of the tendon.

Tendons connect muscle to bone, transmitting forces from one structure to the other, enabling movement [1]. Every muscle has a proximal and distal tendon, joined at the as myotendinous junction [5]. Similarly, the union point between tendon and bone is an osteotendinous junction. These are complex specialised regions that facilitate the function of tendons, i.e. force transmission [6].

Ligaments connect bone to bone, acting as static restraints, helping maintain stability while preventing excessive motion [1, 7]. These insert into bone in a structurally organised manner through a transitional zone called insertion or enthesis [8]. The enthesis is a crucial structure given as it enable forces to be transmitted and dissipated, facilitating loading and movement [9]. Entheses can be fibrous or fibrocartilaginous, varying according to ligament location in the body[10].

Tendons and ligaments are passive structures, not exercising movement directly, yet contributing to normal joint motion [11]. Both respond to extrinsic factors, including exercise, immobilisation and mechanical loading [12]. Examples of their attachments sites are presented in Figure 1.2.

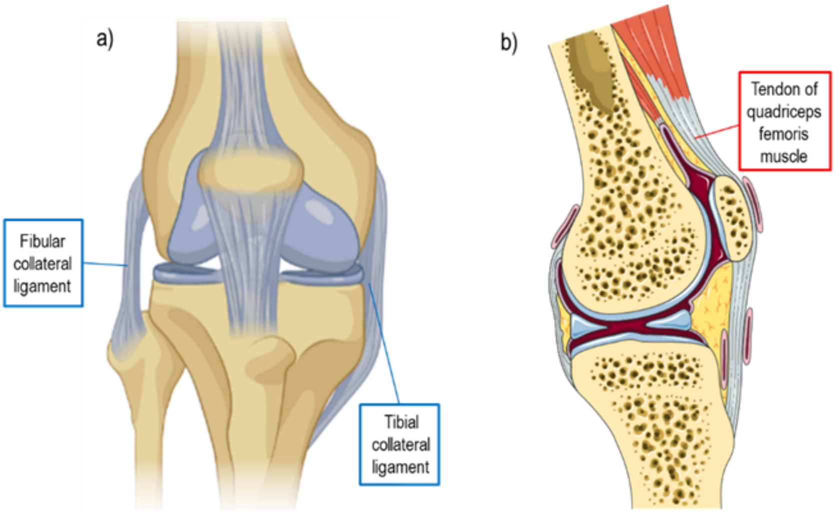

Figure 1.2: Tendon and ligament attachments in the knee, where the frontal view (a) shows two ligaments attaching bone to bone in blue, and the parasagittal section (b) shows a tendon attaching muscle to bone in red. Created with BioRender.com.

Tendons and ligaments are characterised by their hierarchical organisation, which contributes to the tissue's high tensile strength [13]. At the smallest level of scale, the predominant component of tendon/ligament is collagen, a triple helical protein [14]. Five collagen units bound by intermolecular crosslinks form microfibrils [15]. These bundle forming fibrils, with diameters ranging from 20 to 500 nanometres [16]. Fibrils are enveloped by interfibrillar matrix [17], composed mainly of small proteoglycans, glycoproteins such as collagen oligomeric matrix protein and tenascin-C, and tenomodulin.

A bundle of fibrils form collagen fibres, and numerous fibres bound together form fascicles, the basic functional unit of tendon/ligament [18]. Fascicles have variable diameters, ranging from 150 to 500 micrometres [19]. These hierarchical units are mostly aligned longitudinally, parallel to the tissue's native loading or mechanical axis [20]. A schematic representation of tendon structure at different levels of scale is shown in Figure 1.3.

Fascicles are enveloped by a connective tissue compartment or mesh known as interfascicular matrix [21]. In tendons, this is also referred to as endotenon [22]. The interfascicular matrix is comprised of elastic fibres, lubricin, decorin, versican and glycosaminoglycans (GAGs) [23]. The interfascicular matrix connects with the peripheral region of tendons and ligaments, called epitenon/epiligament [24]. This peripheral sheath is frequently unnoticeable, meshed with the core structure of the tissue [25]. Epitenons/epiligaments are contiguous with the paratenon, another layer of loose connective and fatty tissue [26, 27].

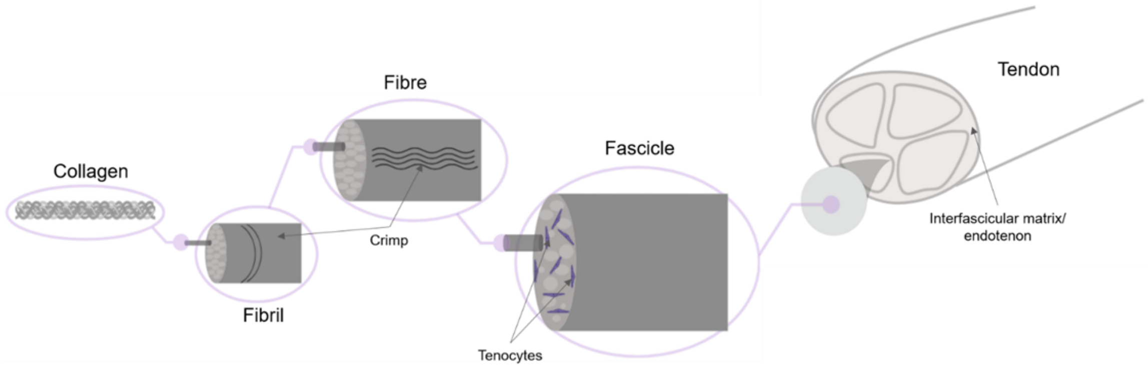

Figure 1.3: Schematic representation of the hierarchical structure of tendons,

created with BioRender.com.

The structure of ligaments and tendons varies according to their location, but can also change along the length of a single structure [4]. This can be attributed to different regions of a single tendon/ligament requiring specific material properties to ensure the tissue's function is carried out. The collagenous extracellular (ECM) primarily provides tensile strength, while the non-collagenous components facilitate viscous behaviour [27].

Two of the most notable and important variations in the composition of a single tendon/ligament structure lie in the entheses regions. The tendon/ligament to bone interface consists of a complex transitional tissue, where four zones can be distinguished longitudinally [28]. These include tendon/ligament proper, unmineralised fibrocartilage, mineralised fibrocartilage and bone [29]. The tendon/ligament zone is pure dense fibrous connective tissue where tenocytes/ligamentocytes are found, along with collagen type I and III. The unmineralised fibrocartilaginous zone contains fibrochondrocytes and increased proteoglycans. It is here where the characteristic waviness of collagen fibres dissipates. The mineralised fibrocartilaginous zone also contains fibrochondrocytes and collagen changes to type II. Finally the bone contains osteocytes, osteoclasts and osteoblasts and collagen type I. Alternatively, some ligaments, such as the medial collateral ligament have an indirect insertion connecting to bone through Sharpey's fibres [30].

The myotendinous junction is a specialised region where collagen fibrils from the tendon undergo a finger-like process interdigitating with muscle fibre membrane at the extremes of muscle fibres [30]. The composition is similar to tendon ECM with a combination of collagen and non-collagenous components.

Both types of enthesis constitute a challenge in tendon/ligament repair, mainly due to the difficulty in replicating the complex transition between tissues, and inability to maintain a native-like transition from tendon to bone and muscle and ligament to bone. This leads to an impaired function of the entheses, which is of considerable interest within tendon/ligament repair research at present.

1.1.2 Composition

1.1.2.1 Cells

The main type of cells present in tendons and ligaments are fibroblasts, also referred to as tenocytes in tendons and ligamentous fibroblasts or ligamentocytes in ligaments [6]. These are sparsely distributed throughout the structure of both tissues, being hypocellular tissues [31]. Other cell populations in tendons and ligaments, found in much lower quantities compared to the predominant tenocytes/ligamentocytes are mentioned in Table 1.1.

Table 1.1: Cells in tendon and ligaments [31]

Site	Cells	Comments
Throughout structure	Fibroblasts	Specialised fibroblasts called tenocytes/ ligamentocytes
Entheses, where subject to compression	Fibrocartilaginous cells	-
Throughout structure	Fat cells, mast cells, Schwann cells	Scarce
Paratenon	Synovial cells	Line the inner surface of the paratenon
Variable	Neutrophils, macrophages, lymphocytes	Present during wound healing

The synthesis and maintenance of tendon/ligament ECM is carried out by tenocytes/ligamentocytes [32]. The decrease in cell density is analogue to ECM synthesis, commencing with frequent production of its components, particularly during development, slowly declining with age [19, 33]. Tenocytes/ligamentocytes in mature tendons and ligaments become quiescent [18], showing low proliferation rates.

1.1.2.2 Vasculature

Vascularisation is significant during development of ligaments and tendons, with characteristic high cellular density and metabolic activity [34, 35]. With tissue maturity, vasculature decreases significantly, accompanied by a slower rate in cell renewal and matrix turnover [36]. Hypovascularity is characteristic of both tissues, constituting one of the main reasons their healing process after an injury is limited [36, 37]. The native repair processes that follow injury lead to the development of a biologically, morphologically and mechanically inferior neo-tissue [38].

Vasculature of tendons and ligaments originates from three main sites [35]: the musculotendinous junction, the osseotendinous junction and surrounding connective tissue. Vessels are distributed along the length of the tissue, predominantly surrounding the collagen fibre bundles in the epitenon/epiligament.

In mature tendons/ligaments, nutrition occurs through synovial fluid diffusion [34]. This provides the maintenance of the tissue, by delivering nutrients that allow cells to synthesise its ECM [34]. However, due to the limited vasculature, as well as low tenocyte-ligamentocyte density and quiescence, tendon and ligaments have a significantly limited healing capability.

In fact, the collagen matrix of healthy tendon/ligament does not undergo neo-synthesis after puberty. A study utilising the $[C^{14}]$ bomb pulse method showed that tendon core is developed during the first $13 - 17$ years of an individual's life and not restored during adulthood [39]. Therefore, when tendons and ligaments undergo injuries and ruptures, the most common route to restoring function and stability relies on surgical intervention, requiring exogenous material to provide the structure and mechanics of the damaged tissue.

1.1.2.3 The extracellular matrix

The ECM is a complex mixture of molecules that facilitate unique functional, biological, biochemical and biomechanical properties [40]. Tendons and ligaments are viscoelastic structures, flexible enough to allow relative motion, while also providing stiffness to maintain joint conformity [41]. This can be attributed to their total mass composition, being two-thirds fluid and one-third solid components [42]. These solids include primarily collagen, with lesser amounts of proteoglycans, elastin, actin, laminin and integrins [43, 44]. A summary of the structural composition of tendon/ligament mass is presented in Table 1.2.

Table 1.2: Structural composition of tendons and ligaments, adapted from [1]

Component	Tendon	Ligament
Cellular material	20%	20%
Water	60-80%	60-80%
Collagen	>80%	70-80%
Type I	˜99%	90%
Type III	˜5%	10%
Ground substance*	<30%	20-30%

*Proteoglycans, structural glycoproteins, and other small molecules.

There are some compositional differences between tendons and ligaments [45]. The latter contains more collagen III [46], and have a higher GAG content [47]. Molecular arrangement in tendon and ligament matrices differs, with a highly organised collagen fibril content aligned longitudinally in the loading axis of tendons, while ligaments have a more heterogenous orientation of collagenous components [47]. This relates to their specific native function, as each element plays a role in facilitating motion. In tendons, when transmitting forces from muscle to bone, the high tension they resist is mainly uniaxial, requiring little elongation [48]. Ligaments, while preventing excessive motion, also withstand tension, which may occur in different directions according to the location in the body and range of motion [49]. Ligaments thus stretch and recoil more compared to tendons, accounting for the difference in matrix composition.

Collagen

Collagen is the most widely distributed protein in the human body [50]. Different collagen types relate to their role in carrying out tissue-specific functions, while being essential for withstanding physiological loading [51].

Collagen is a triple helical protein. Every polypeptide is constituted by three repeating amino acids, commonly glycine, proline and hydroxyproline [43]. The helical domain is flanked by regions where crosslinking occurs [52].

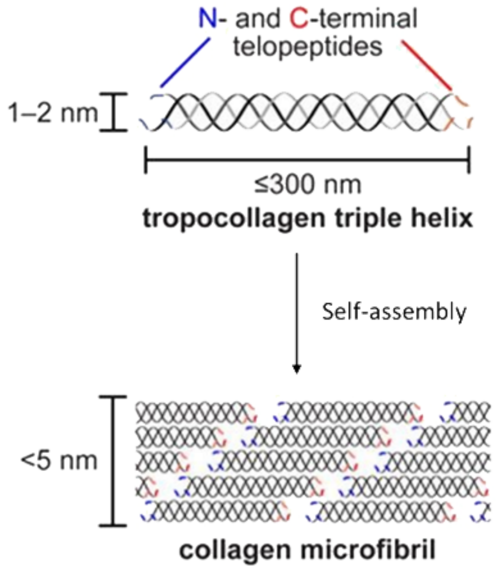

Figure 1.4: Collagen molecule structure
of a fibril forming collagen, adapted from [52].

The mechanical properties of collagen depend on covalent crosslinking [53]. This process provides stability to recently formed or assembling fibrils. Crosslinking can occur intra- and intermolecularly, between the same type of collagen molecule or different types [54]. Crosslinks are essential for maintaining a stable ECM structure.

The crosslinks in immature tendon/ligament create intermediary reducible divalent bonds [53, 55]. These reducible crosslinks allow remodelling and rearrangements in the fibrillar structure prior to permanent crosslinking [56]. Reducible crosslinks are transformed into non-reducible bonds in mature tissue, providing stability to the molecule [57]. Collagen content and density, including number, types and location of inter- and intramolecular bonds contribute to the tissue's tensile strength [58].

The main type of collagen in tendons and ligaments is type I. There second most abundant is collagen type III, and there exist smaller amounts of other collagen types [59]. The two most relevant collagen types are briefly described in Table 1.3.

Table 1.3: Collagen type I and III as the main component of tendon/ligament ECM

[60–64]

Collagen	Location	Description
I	Skin, teeth, bone, tendon, ligament, vascular ligature, sclera, cornea, blood vessels.	Around 90% of the collagen in the human body is type I, with its ubiquitous presence in most connective tissue. It is a heterotrimeric helix, with two identical alpha chains and a third different chain. Found in composite with collagen type III or V. It is a fibril forming collagen which provides structural integrity to tissue, by playing a role in biomechanical properties such as tensile stiffness, load bearing and tensile strength.
III	Reticular fibres, skin, muscle, blood vessels	Widely distributed in tissues rich in collagen type I. It is a homotrimer of three alpha chains. During wound healing, it acts an attachment scaffold for tenocytes/ligamentocytes. It also acts as ligand for diverse proteins, involved in healing processes, cell proliferation, adhesion and migration.

Collagen arrangement in tendons/ligaments is characteristically undulating, similar to planar sinusoidal waves [65]. This is known as collagen crimp, which plays a key role in the biomechanical behaviour of the tissue [66]. When tendon/ligament is subjected to loading, collagen crimp can act as a shock-absorber and contributes to the tissue's capability of elastic recoil [67]. Crimp morphology can therefore be described differently between tendons and ligaments, with a direct impact on their mechanical properties, thus contributing to performing different functions [67]. Crimp is specific to tissue location and function, impacting its mechanical properties; for example, fibres with a small crimp angle have been shown to fail before fibres with a larger crimp angle [68].

Proteoglycans

Proteoglycans are composed of a central core glycosylated protein with O-linked side chains of long, unbranched sulfated polysaccharides called GAGs [69]. The diversity of core protein species and unique patterns of glycosylation [70] give rise to two broad groups of proteoglycans, with families of diverse structures [19, 71–73]. These are briefly described in Table 1.4. The physical characteristics and biological functions of proteoglycans can be attributed to the physicochemical nature of the GAG component added to the structure of the core protein [74].

Table 1.4: Classification of proteoglycans and their role in tendon/ligament [75]

Group	Proteoglycan	Description	Comments
Large	Aggrecan Versican	Associated with many highly sulphated GAG side chains. These allow water binding, playing a role in resistance to compressive forces.	Aggrecan content is higher in regions of the tissue subject to compression.
Small	Decorin Biglycan Fibromodulin Lumican Mimican	Characterised by leucine-rich repeats. In close proximity to collagen fibrils, playing a role in collagen fibril diameters and interfibrillar spacing.	Decorin is the main proteoglycan in tendons and ligaments, associated with dermatan sulphate. Biglycan plays a role in growth factor and cytokine sequestering.

Proteoglycans are key in matrix assembly and organisation, shown to play a role in collagen fibrillogenesis [76]. Large aggregating proteoglycans facilitate spatial arrangements between collagen fibres, while providing lubrication, reducing friction and enabling sliding between fibres [77]. Proteoglycans also play a significant role in maintaining the integrity of the ECM in tendons and ligaments when subjected to high loads, helping reduce the risk of injury [78]. Mechanical loading influences proteoglycan expression. For example, tension induces decorin synthesis, while compression leads to aggrecan synthesis [73]. This phenomenon relates to varying concentration of different proteoglycans throughout a single tendon/ligament structure, according to differently loaded regions.

The highly anionic nature of the GAGs associated with proteoglycan cores provides the ability to attract water molecules and other cations, binding them in great quantities [79]. This eventually forms a hydrated gel, which is key in maintaining resistance and stability in tendon/ligament ECM [74, 80]. GAGs have also been reported to contribute significantly in the viscoelastic behaviour of these connective tissues [80].

Decorin is the most abundant proteoglycan in tendinous and ligamentous tissue, commonly associated with the GAG dermatan sulphate [77]. A smaller amount of biglycan, versican and aggrecan may also be present. These associate with chondroitin, dermatan and keratan sulphate. A brief description of relevant GAGs is provided in Table 1.5.

Table 1.5: Glycosaminoglycans commonly found in tendon/ligament [74, 75, 80, 81]

Glycosaminglycan	Function
Chondroitin sulfate	Essential for the organisation of the ECM. It helps resist compressive forces. It is key in the aggregation of protein ligands to proteoglycans.
Dermatan sulfate	Plays a key role in collagen fibril assembly and diameter. It plays a role in the viscoelastic behaviour of tendon/ligament, facilitating the tissue's elasticity.
Keratan sulfate	Involved in cellular identification of protein ligands and cellular motility.

Glycoproteins

Glycoproteins are constituted by a glycan protein, covalently bound to carbohydrates [82]. The carbohydrate regions play a role in the component's function, involved in viscosity, water binding, protein folding, biological recognition and matrix stabilisation [82]. Glycoproteins make up a small part of tendon/ligament matrices, yet they contribute to its stability [17]. Their mechanical role relates to their liaison between cells and matrix components and between matrix components. They also influence cell behaviour, improving motility, encouraging proliferation and differentiation [83]. A brief description of relevant glycoproteins is provided in Table 1.6.

Table 1.6: Glycoproteins commonly found in tendon/ligament.

Glycoprotein	Function	Reference
Cartilage oligo matrix protein (COMP)	Pentameric glycoprotein involved in the assembly of the ECM of the tissues as it has the capability of binding to collagen. In addition, it is related to collagen assembly and organisation, acting as a catalyst in fibrillogenesis.	[84–87]
Tenascin-C	Macromolecule, classified as a matricellular protein, which controls interactions with matrix molecules, cells and fibronectin. It can be described as anti-adhesive. It is present regions of the connective tissue subject to compressive loads and responds to variating mechanical stress.	[88–92]
Lubricin	Facilitates the movement of collagen bundles, enabling sliding of the hierarchical structure of tendons and ligaments with minimal friction, thus functioning as lubricant. It is also involved in regulating cell growth and anti-adhesion.	[93, 94]

Elastic fibres

Elastic fibres have an elastin core, surrounded by fibrillin 1 and 2, along with microfibril associated glycoproteins [95, 96] (Figure 1.5). This component constitutes circa 2% of tendon/ligament dry weight [83]. Elastic fibres confer extensibility and resilience, so when the tissue is subjected to repetitive deformation, it may return to its native conformation [97, 98]. Elastin is an important component in tendon/ligament matrices, allowing the tissue to resist tensile loading without suffering permanent deformation [98, 99]. This through a stretching and recoil mechanism of the collagen crimp [92]. It is also involved in cell-matrix interactions [100, 101].

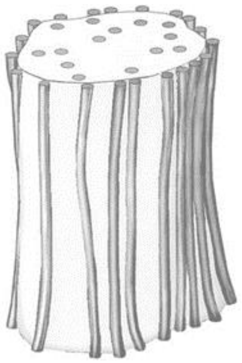

Figure 1.5: Schematic representation of an elastic fibre,
an extracellular matrix molecule formed by an elastin core (white) surrounded by fibrillin-rich microfibrils (grey tubular structures), adapted from [83].

1.1.3 Tendon/ligament injuries

Approximately 50% of musculoskeletal disorders (MSD) are tendon and ligament injuries [102, 103]. MSDs cost the global economy circa 213 billion dollars in 2011 [104]. These injuries have negative effects on patient's quality of life relating to their occupational, recreational and health performance, further burdening the economy.

Tendon injuries include rupture and tendinopathy, while ligament injuries involve partial or complete rupture of the tissue. The Achilles tendon and anterior cruciate ligament are the most commonly injured, respectively [33, 102].

Tendinopathy describes a non-rupture damage to tendon which intensifies with mechanical loading Maffulli [105], accounting for 30% of MSD [106]. It can present three broad stages, commencing with reactive tendinopathy. This occurs after acute compressive or tensile loading which initiates a proliferative cell and matrix response, such as a fall or excessive physical activity. If enough time between loads passes, the changes to the tendon can be naturally reversed. The second stage is tendon disrepair in the form of fibrillar disruption. Finally, degenerative tendinopathy involves diverse alterations to tendon matrix and tenocytes. During this stage, the likelihood of natural recovery is low [107].

Due to the poor healing capabilities of tendon and ligament, the research continues for improving tendon/ligament repair. However, it is important to note the differences between both tissues, as this proves useful in constructing more suitable solutions to both tendon and ligament injuries. A summary of differences between tendons and ligaments is provided in Table 1.7.

Table 1.7: Key differences between tendons and ligaments, [28, 59, 73, 108].

	Structure	Composition	Function
Tendon	Matrix arrangement is organised and parallel to axis of loading. Two categories: positional and energy-storing tendon. The latter are more prone to injury. Positional tendons are stiffer, with increased fibril and fibre diameters compared to energy-storing tendons. Spring-like helical component in fascicles of energy-storing tendons with smaller fibril and fibre diameters and more cross-links than positional tendons.	Cells include interfascicular and intrafascicular tenocytes, according to location and immature tenoblasts. Elastin accounts for 1 – 10% dry weight and PGs for up to 5%. Collagen types I and III are most abundant, and in lesser amounts type V, VI, XI, XII, XIV. Collagen content is similar for both tendon types, with a slight increase in collagen type III in energy-storing tendons. Energy-storing tendons contain higher glycosaminoglycan and water content, resulting in a softer matrix than positional tendons.	Positional tendons transfer the forces in muscle to bone. Energy-storing tendons store and release elastic stress energy, improving efficiency of motion.
Ligament	Matrix arrangement is random and fibres are not always aligned parallel to loading axis.	Cells include ligamentocytes with a random distribution within a single ligament, and a rounder morphology compared to tenocytes. Collagen type I and III are most abundant, with a higher proportion of type III compared to tendon. Lesser amounts of collagen type V and XII. Higher proteoglycan and elastin content than in tendon.	Resist excessive loads, prevent instability, control joint motion. Key proprioceptive role due to innervation.

1.2 The anterior cruciate ligament

The anterior cruciate ligament (ACL) is the most important stabiliser of the knee, accounting for 85% of whole joint stability [109].

1.2.1 Structure and function

The ACL extends from the anterior intercondyloid fossa of the tibia to the posterior part of the medial surface of the lateral condyle of the femur. It crosses anteriorly to the posterior cruciate ligament [110]. The ligament ranges from 25 – 30 mm in length, 4 – 10 mm in width and circa 10 mm in breadth [111]. The ACL consists of two bundles: anteromedial and posterolateral, which operate in synergy as one functional structure [112, 113]. The change in the position of the ACL during normal flexion and extension motion contributes to the varying cross sectional areas along the ligament and its non-isometric nature.

A description of the ECM of the ACL is provided in Table 1.8. Cellular content consists of a small population of ligamentocytes, as described in section 1.1.2.1. The collagenous components within ACL matrix consist of two coexisting types: one is large and inhomogeneous while the other is smaller and more homogenous, each accounting for about half of total collagen content. [97, 114]. Their distribution remains unclear.

Table 1.8: Composition of the ACL ECM, adapted from [60, 114, 115]

Component	Description
Collagen	Mainly composed of type I collagen in composite with a smaller amount of type III. Collagen type III is primarily located near the entheses. Collagen type I is orientated parallel to the ligament's loading axis, providing tensile stiffness. Collagenous components contribute to the ligament's biomechanical properties such as load bearing and torsional stiffness.
Glycosaminoglycans	Part of the ground substance. GAGs, associated with proteoglycans, help bind the vast proportion of water of which the ACL is composed, thus providing lubrication. GAGs contribute to the viscoelastic behaviour of the ACL. They also play a role in controlling the metabolic activity of the tissue, binding cells to the matrix and facilitating nutrient diffusion.
Elastic components	Elastic components mainly refer to elastic fibres, described previously. Elasticity facilitates smooth motion, resilience and recoil. Elastic components play a role in regulating cell functions and behaviour.

Vascularisation of the ACL is supplied by the middle genicular artery [116]. Small vessels infiltrate the ligament, aligned parallel to ACL matrix collagen bundles. Blood vessels from the synovial sheath also penetrate the ligament, joining endoligamentous vessels [117]. Nonetheless, vasculature is inhomogenous and scarce, particularly in entheses, which are largely avascular, accounting for ACL limited healing capabilities [4, 118].

The hierarchical organisation of the ACL is summarised in Figure 1.6 [119].

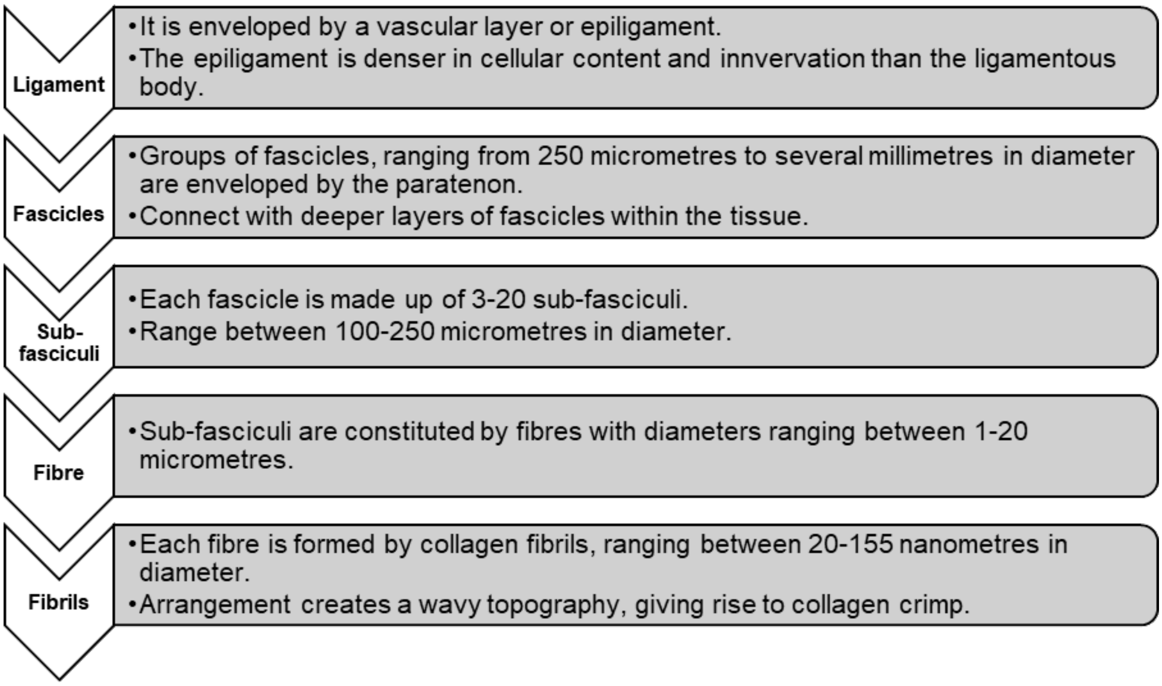

Ligament
- It is enveloped by a vascular layer or epiligament.
- The epiligament is denser in cellular content and innvervation than the ligamentous body.

Fascicles
- Groups of fascicles, ranging from 250 micrometres to several millimetres in diameter are enveloped by the paratenon.
- Connect with deeper layers of fascicles within the tissue.

Sub-fasciculi
- Each fascicle is made up of 3-20 sub-fasciculi.
- Range between 100-250 micrometres in diameter.

Fibre
- Sub-fasciculi are constituted by fibres with diameters ranging between 1-20 micrometres.

Fibrils
- Each fibre is formed by collagen fibrils, ranging between 20-155 nanometres in diameter.
- Arrangement creates a wavy topography, giving rise to collagen crimp.

Figure 1.6: The hierarchical structure of the anterior cruciate ligament.

The ACL is key in maintaining normal knee kinematics and biomechanics. It acts as a primary restraint to anterior tibial translation and secondary stabiliser to internal tibial rotation [120, 121]. The ACL also provides resistance to hyperextension [122]. The ligament can be easily elongated during normal activity, allowing smooth joint motion, yet increases in stiffness with external loading, preventing excessive movement [123, 124]. The anteromedial and posterolateral bundles help provide anterior and rotational stability [125]. The two collagenous component types described formerly help provide resistance to high tensile stress, while helping maintain the ligament's structure [97, 114].

1.2.2 Biomechanics

The biomechanical behaviour of the ACL exhibits a characteristic non-linear sigmoidal curve under tension (Figure 1.7) [126]. A stress-strain curve obtained from a uniaxial tensile test begins with a toe region, up to circa 4% strain, followed by a linear increase in stress, reaching 12% strain, ending with a short yield and ultimate failure [127]. Briefly, the toe region exhibits low stress per unit strain, with significant elongation under slight load increments. Here, the force is transferred to collagen, as the tissue matrix primary component. The initial, relaxed crimp morphology straightens, aligning with the loading axis subject to stress. In the linear region, collagen fibres are recruited to withstand incremental load and stretching. This occurs through interfibrillar sliding. Stiffness increases as the fibres are taut, while elastic deformation occurs. In the yield region, irreversible deformation occurs, reaching a point where collagen fails by defibrillation. The ligament can no longer comply with its native function, failing after reaching its ultimate tensile load [128–130].

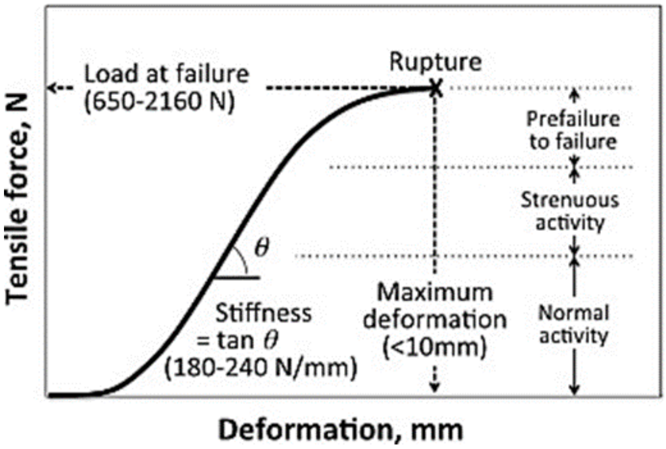

Figure 1.7: ACL load-deformation
curve under tension, from [131].

During normal daily activities, the ACL is mainly subjected to anterior tibial translation and combined rotatory loading [111]. It withstands 169 N walking, 445 N descending stairs and < 100 N ascending stairs or descending inclined paths [123, 132]. ACL stiffness and failure loads revealed an inverse relation with age [123, 133]. As age increases, the mechanical properties of the ACL decrease. A summary of relevant mechanical properties is given in Table 1.9.

Table 1.9: Mechanical properties of native ACL in humans, adapted from [1, 123, 134, 135]

	Elastic modulus (MPa)	**Ultimate load (N)**	**Ultimate stress (MPa)**	**Stiffness (N/mm)**
Young	111 ± 26	2160 ± 157	37.8 ± 9	242 ± 28
Older	65 ± 24	496 ± 85	13.3 ± 5	124 ± 16

Data reported as mean ± standard deviation.

The viscoelastic nature of the ACL is attributed to its composition, and mechanisms occurring within the tissue's ECM. Viscoelastic properties can be obtained from a stress relaxation test [136]. The decrease in stress when the ligament is maintained at a constant displacement is the result of water movement and matrix reorganisation. The friction generated between collagen fibres and other components, on top of that created by water movement between matrix components contributes the ACL's viscoelasticity [137]. At low strain, relaxation occurs through shear between collagen fibres, while at higher strain, fibril reorganisation leads to relaxation [138]. The non-collagenous components provide protection by limiting fatigue and reducing failure stress through hydrating mechanisms. The characteristic viscoelastic nature of the ACL contributes to shock-absorbing and spring energy saving functions [41].

1.2.3 Ruptures

The knee is one of the most heavily loaded joints in the body, subjected to varying yet continuous stress during normal motion. Further, the increasing popularity of sports, both professional and recreational increases the risk of injury [139, 140]. The ACL is the most commonly injured ligament in the knee, accounting for almost half of all knee injuries [141].

Ligament injuries can occur as the result of three mechanisms [142]. Direct contact involves a person or object harming the knee directly; indirect contact refers to contact between an object/person to a part of the body other than the knee which provokes excessive forces to transfer through the knee; noncontact occur when a change in direction or deceleration applies force to the knee, translating the tibia on the femur [142]. The latter is the most common form of ACL rupture.

O'Donoghue identified injuries affecting the ACL also affected the medial collateral ligament (MCL) and medial meniscus (MM), naming it the "unhappy triad". This was reported to occur in 25% of acute athletic knee injuries [143]. It was then observed that the triad was more accurately described as injuries to the ACL, MCL and lateral meniscus (LM) [144]. The "unhappy triad" occurs during contact and noncontact sports as the result of sudden valgus impact with external or internal rotation [145]. More recently, the triad has been found to be more accurately a tetrad, as the "unhappy triad" is accompanied to injury of the lateral compartment, including the anterolateral ligament (ALL) and surrounding capsule [146]. These injuries require reconstruction and repair of all lesions for knee kinematics restoration, taking up to 6 months of recovery time [145]. However, isolated ACL ruptures have been reported to occur more frequently than the "unhappy triad" [147].

1.2.3.1 Epidemiology

It is estimated that 1 – 10 in 1000 people suffer ACL ruptures annually [148]. In the USA alone, more than 200,000 injuries occur, costing around 7 billion dollars [149]. Incidences of 34 per 100,000 in Norway, 38 per 100,000 in Denmark, 32 per 100,000 in Sweden [150] and 30 per 100,000 in the United Kingdom [151] have been reported.

ACL ruptures occur with a higher incidence in young populations [152, 153]. This could be the result of active participation of young individuals in high impact sports, where there is a higher risk of sudden changes in motion direction [141]. The highest incidence rate of ACL injury for both sexes was reported during high intensity rotational landing sports such as gymnastics and obstacle course races [140].

There is a three times higher incidence of ACL rupture in the female population compared to males [154, 155]. This is attributed to anatomical features [156], hormonal fluctuation [157], neuromuscular physiology [158] and associated factors. A summary of relevant factors is given in Table 1.10.

Table 1.10: Factors influencing ACL rupture in men and women [150, 159–161]

Factor	Description	Additional comments
Anatomical	Females have a wider pelvis, influencing knee valgus and instability. Morphological differences between male and female intercondylar notch affect the shearing forces between the ACL and bone. A stable core (including abdominal, back extensor and hip musculature), sometimes poorer in females affects the optimal movement to dynamically stabilise the lower extremity.	Other elements include varying ACL length and width, muscle strength, flexibility and leg misalignment.
Hormonal	Estrogen reduces soft tissue tension by decreasing collagen synthesis and inhibiting ligamentocyte proliferation. Estrogen rises during menstrual cycle are related to ACL strength reduction.	Estrogen also affects the nervous system, altering fine motor skills.
Neuromuscular	Delayed neurological signalling and feedback in females increases risk of injury. Females are less effective in knee stiffening. Muscle recruitment order in females differs from males, initially relying on the quadriceps instead of hamstring for knee stabilisation.	Movement that heavily involves the quadriceps with little or delated balancing action of the hamstring increases the risk of injury.
Environmental	Differences between male and female posture in combination with training techniques increase risk of rupture.	Surface where movement is taking place, shoes, sport type and performance style influence risk of injury.

1.2.3.2 Effects on the knee joint

The impairment of the ACL has a cascading effect on knee kinematics, with suboptimal load transfer and mechanical instability of the knee [162]. ACL deficiency increases anterior tibial translation and internal tibial rotation, accompanied by increased contact stresses [163]. An ACL rupture often results in pathologies of surrounding tissue, as secondary structures are required to resist forces, undergoing abnormally high loads [164]. This creates a higher risk of additional tissue injury, chronic instability and progressive degeneration [164, 165].

The biomechanical changes that follow ACL rupture influence the development of osteoarthritis (OA) [164, 166, 167]. The upregulation of key molecules sustain the progression of OA [168, 169]. A summary of the structures and factors involved in post ACL rupture OA is provided in Figure 1.8. There are different mechanisms that could cause this. For example, without secondary injuries, the initial acute injury commences OA pathogenesis [170, 171]. The mechanical impact of acute trauma affects neighbouring tissue, including cartilage, initiating degenerative processes. Intraarticular bleeding during the initial injury also activates inflammatory processes, and could influence gene expression of molecules involved in OA. The chronic alteration of static and dynamic loading patterns following ACL injury also negatively impact neighbouring tissue [170, 171]. This disrupts homeostasis, increasing the risk of secondary injury and degeneration, accelerating the development of OA.

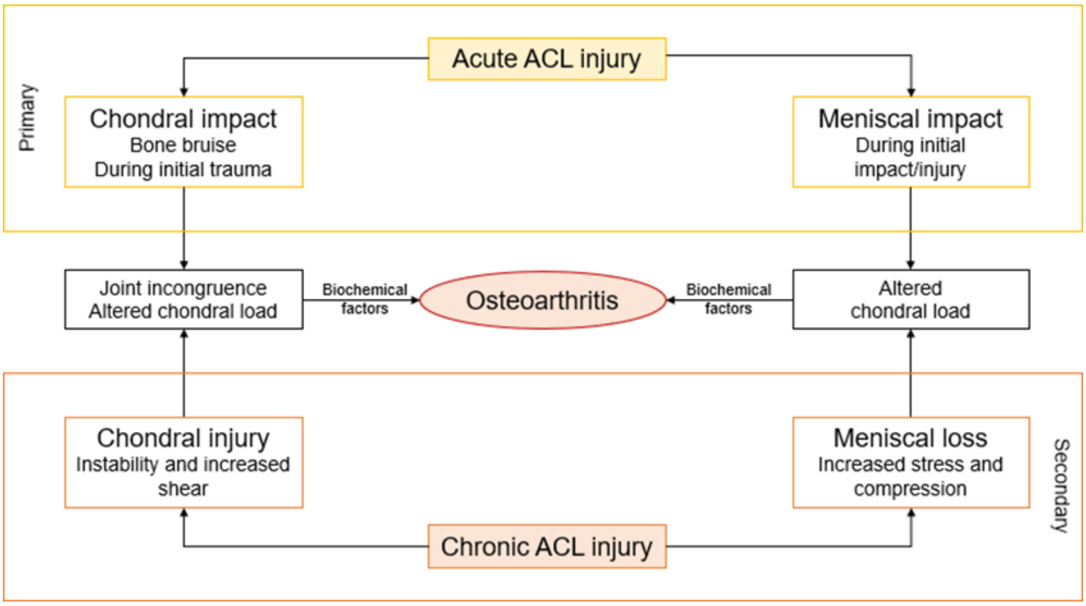

Figure 1.8: OA pathogenesis following ACL rupture,
adapted from [172].

1.2.4 Anterior cruciate ligament reconstruction

ACL reconstruction (ACLR) is a common surgical procedure that replaces the damaged structure to restore functionality and stability in the knee [173]. This requires the use of a graft to substitute the torn ligament [174].

In the United States it is estimated that 120 thousand reconstructions are performed each year [175]. In the United Kingdom, approximately 14 thousand surgeries take place yearly [176]. There have been over 133 thousand ACLRs in England alone between 1997 and 2017, representing a 12-fold increase [151]

Grafts involved in ACLR should comply with the majority of requirements listed in Table 1.11. During reconstruction, autografts or allografts are most frequently used [177]. These must be mechanically superior to native ACL, as ligamentisation can reduce initial strength by up to 50% [178].

Table 1.11: Requirements for grafts to be clinically competent for ACLR [179, 180]

Category	Description
Surgery	-No additional surgeries for harvesting tissue. -Simple technique for implantation. -Minimal morbidity. -Adequate fixation method.
Biocompatibility	-Anatomical dimensions met on a macroscopic place. -Graft material must be biocompatible. -Minimal risk for infection or transmission of disease. -Provide microenvironment which encourages tissue formation and development on a microscopic scale.
Biodegradation	-Occurring at an adequate rate to provide stability after implantation and an appropriate transition to remodelled tissue function in vivo.
Mechanical properties	-Integrity that allows host tissue ingrowth and remodelling. -Mechanical properties should be sufficient to provide stability when implanted. -Physiological function of ACL must be matched as much as possible. -The graft must withstand rehabilitation. -Rapid stabilisation allow patients quality of life and return to normal activities.

Autografts are excised from one part of a patient's body and transplanted to another area of the same patient [181]. This is currently the gold standard for ACLR, as it proves effective in providing stability, particularly in patients who return to sports [182]. The bone-patella tendon-bone graft is one of the most frequently used, given its mechanical strength [183, 184].

Allografts refer to cadaveric tissue, obtained from the same species, but not the same patient [181]. This requires a tissue bank facility with standardised decontamination, storage and sterilisation, incurring in additional costs [185]. Allografts are restricted to the availability of donor tissue, with limited availability, thus less used in ACLR [186]. However, it provides a viable option in patients who have relied on autografts previously [187] .

A summary of the advantages and disadvantages of autografts and allografts is given in Table 1.12.

Table 1.12: Advantages and disadvantages of commonly used grafts in ACLR [112, 142, 188, 189]

Tissue	Advantages	Disadvantages
Autografts: Bone-patella tendon-bone Hamstring tendon Quadriceps tendon	No risk of infection or disease transmission. No immune rejection. Fast incorporation. Quick healing process. Presents satisfactory outcome in young, active patients.	Donor site morbidity. Weakness in muscles after surgery (hamstring or quadriceps). Decrease in physical performance. Risk of quadriceps muscle herniation. Increased time in surgery. In the case of bone-tendon complexes, there is a risk of fracture. In case of tendon only, the graft size is unpredictable. There is risk of harm to medial structures, e.g. damage to patellar cartilage, ruptures or tears of patella tendon, damage to nerves bellow patella.
Allografts: Patellar and Achilles tendon, semitendinosus, fascia lata, hamstring tendon, peroneus longus tendons, quadriceps tendon	No donor site morbidity. Increased availability. Variable configuration, no size limitations. Smaller incision than allograft procedure. Faster surgical procedure. Less discomfort after procedure. In case of bone-tendon complexes, there is bone to bone healing process.	Possibility of infection and disease transmission. Risk of immune rejection. High costs. Storage and sterilisation could adversely impact mechanical properties. Tunnel enlargement. Slow incorporation. Elevated chance of rupture after reconstruction.

Synthetic grafts theoretically could provide biomechanical properties exceeding that of native ACL, while overcoming the disadvantages of autografts and allografts listed above. The use of synthetic materials started in 1914, with silver wire used for ACLR [190]. The first generation of synthetics were knitted, braided or woven materials. The second generation added transverse fibres into the braided or knit structure, also utilising polyethylene terephthalate to facilitate cell proliferation [174]. However, the high incidence of adverse complications, including graft failure, mechanical fatigue, tunnel widening, synovitis, osteolysis, wear particle deposition, arthritic degeneration and osteoarthritis led to their withdrawal [191, 192]. The Ligament Advanced Reinforcement System remains the only synthetic still used by surgeons [193]. However, issues surrounding loosening, graft ruptures, insufficient tendon-bone healing and foreign body reactions do not support its frequent use.

Given the numerous disadvantages to currently used grafts in ACLR, there is a need for an alternative material. A substantial amount of research has been conducted on decellularised biological scaffolds.

1.2.4.1 Decellularised biological scaffolds for anterior cruciate ligament reconstruction

Decellularised xenogeneic tissue presents a viable alternative to autografts and allografts currently used in ACLR [194]. It overcomes many of their limitations, such as donor site morbidity and limited availability. Decellularised scaffolds consist of a biocompatible ECM, without immunogenic components such as cellular material and markers, nucleic acids and antigens (alpha-Gal epitopes) [195]. This reduces the risk of foreign body reaction, inflammation processes and adverse immune response in a host [196]. The ECM structure is highly conserved among species [197], making it recognisable with reduced risk of rejection [198].

The extracellular matrix structure provides an effective scaffold, maintaining the multiscale mechanical function of the tissue along with biochemical and biological cues [199, 200]. Accordingly, it facilitates cell infiltration, proliferation and interaction, ultimately leading to matrix health, renewal and development of new functional tissue by endogenous host cells [201].

1.3 Decellularisation processes

Decellularisation removes cells from their anchors and complexes within a tissue [202]. It is intended that the topography and mechanical properties of the ECM remain post-decellularisation [21, 199]. The decellularisation process is a combination of chemical, physical and biologic methods that carry out the 4 broad steps represented in Figure 1.9. However, any of these methods may result in alterations of the ECM [197].

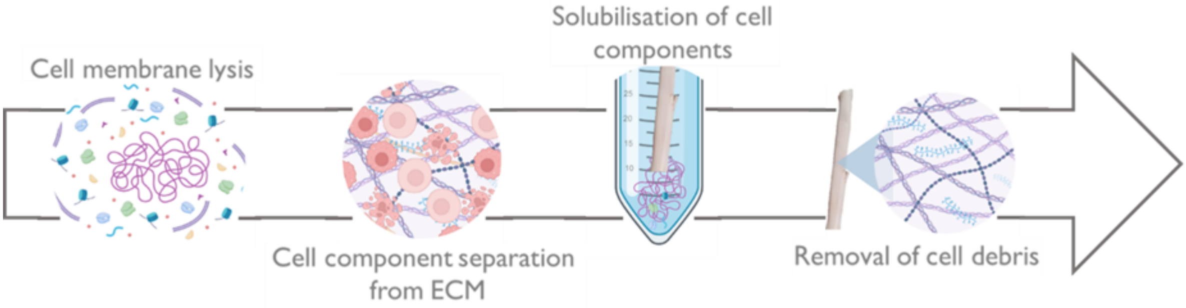

Figure 1.9: General decellularisation process,
created with BioRender.com.

There are three standards to which decellularised tissue must adhere, given the complete removal of cellular material is currently near impossible [203]. Tissue post-decellularisation must contain less than 50 ng/mg of double stranded DNA, and remaining fragments must be no longer than 200 base pairs. Further, there must be no visible nuclear material when histologically assessing the decellularised tissue [204, 205].

Physical methods involve mechanical force, for example freezing, sonication and agitation [197, 204]. Biologic agents include enzymes, chelating agents, protease inhibitors and antibiotics [204]. Chemical methods include acids, bases, hyper- and hypotonic solutions, ionic detergents and solvents [197, 204]. The main disadvantages and possible adverse effects of these methods on tissue matrix are summarised in Table 1.11.

Table 1.13: Decellularisation methods and their potential effects on tissue matrix [197, 204]

Method/reagent	Disadvantage/effet on tissue matrix
Pressure and freezing	Ice crystal formation may impact ECM structure and subtle changes to mechanical properties.
Sonication and agitation	Usually in combination with chemical methods, which may act aggressively on tissue ECM, disrupting its ultrastructure.
Biological agents	Hard to remove fully, which could cause an adverse immune response in the host. Some protease inhibitors may damage ECM ultrastructure.
Acids/bases	Acids could facilitate GAG disassociation, while bases tend to remove growth factors and alter ECM mechanical properties.
Ionic detergents	Disrupt tissue structure, remove growth factors and GAGs, may affect the integrity of collagen.
Solvents	Collagen precipitation or crosslinking which could lead to changes in matrix mechanical properties. Damage to ECM ultrastructure

1.3.1 Decellularised porcine tendon

Decellularised porcine tendon is a protein-rich structure which proves clinically relevant as it is a biocompatible scaffold which replicates the mechanical and biological microenvironment of native tissue [206, 207]. Pigs possess a comparatively similar anatomy and physiology to humans [208], so when implanted, endogenous cells are encouraged to repopulate the graft matrix, synthesising molecules required to remodel the tissue [209, 210]. This reduces the risk of scar tissue formation [211].

Decellularised porcine tendon has been investigated for tendon/ligament tissue engineering. This has been done with various purposes, assessing a range of properties. Research has been conducted on optimisation of decellularisation methods for maintaining scaffold structure and mechanical properties [212]; characterisation of biological, biomechanical and immunological properties of a scaffold [213]; biochemical, in vitro and in vivo biocompatibility of decellularised tendon [214]; asessment of decellularised porcine tendon for ACL replacement in an animal model [215]. Research involving recellularisation of decellularised tendon matrices has not been deemed relevant for the scope of this project.

1.3.2 Porcine superflexor tendon

The *flexor digitorum profundus* (deep digital flexor) can also be referred to as the superflexor tendon, located in hind pig legs. It has been used to represent human tendon in general models of research, particularly in biomechanical studies [216, 217]. This is because of the physiological similarities between porcine and human tissue [208], but mainly due to limited availability of cadaveric tissue. It has been proposed as a xenograft for ACLR, with comparable biomechanics and performance compared to the bone-patella tendon-bone graft [218]. However, immunogenicity proved a major disadvantage. The analogue tendon from chickens has also been investigated as an acellular scaffold for tendon and ligament regeneration [219]. The interest in decellularised superflexor tendon has only increased thereafter.

It is clear why decellularised superflexor tendon has been researched for both tendon and ligament repair. As mentioned in Section 1.1.3, around 50% of MSDs are injuries to these tissues, and 30% represent tendinopathies [102, 103, 106]. As an energy-storing tendon, the superflexor tendon would provide the composition, arrangement and functionality to substitute other energy-storing tendons in the human body.

Research conducted at the University of Leeds has shown decellularised porcine superflexor tendon presents a suitable alternative graft option for ACLR. Assessment of biomechanical, histological, biochemical, biocompatibility and calorimetric properties and behaviour of the tendon has been conducted [220–225]. The performance of the decellularised tendon has also been evaluated in an animal model investigating immunological acceptance and integration [226]. The most relevant aspects of the research conducted to date have been summarised in Table 1.14.

Some of the key findings involve reduced mechanical properties in decellularised tissue compared to native tendon, which are proposed to be a result of loss of GAG content, altered collagen crimp, effects of reagents used during the decellularisation process, swelling and/or subtle changes to the matrix ultrastructure [220–222, 226]. However, there were also reports of comparable biomechanical performance of native and decellularised tissue [222], warranting further investigation. Investigations at the whole tendon scale provided preliminary insight into the consequences of decellularisation on superflexor tendon biomechanical and biological characteristics, yet further insights would be gained from an in-depth analysis delving into a sub-tendon scale. Examining sub-structural mechanics and how these relate to the composition and structural arrangement of the decellularised matrix is key. A hierarchical approach to the experimental research conducted would help better understand the structure-function relationship of tendons. Further, there remains uncertainty in the aspect of loss of ECM molecules post-decellularisation [222], which necessitates investigating. This would provide insight into how the components of the superflexor ECM relate to its biomechanical performance, exploring a more complete mechanical profile, including tensile and compressive biomechanics.

Table 1.14: Research conducted on decellularised porcine superflexor tendon as a potential scaffold for ACLR to date [220–226]

Year	Title	Studies	Variables	Results
2015	A biomechanical characterisation of acellular porcine super flexor tendons for use in anterior cruciate ligament replacement: Investigation into the effects of fat reduction and bioburden reduction bioprocesses	Controlled alteration of the decellularisation process: fat reduction and sterilisation studies. Biomechanical testing: stress relaxation and uniaxial tensile testing.	Acetone vs chloroform-methanol. Antibiotics vs PAA	-Acetone is the preferred solvent for fat reduction compared to chloroform-methanol. -Antibiotics are preferable to PAA for bioburden reduction.
2016	The effects of irradiation on the biological and biomechanical properties of an acellular porcine superflexor tendon graft for cruciate ligament repair	Histology Total and denatured collagen quantification Differential scanning calorimetry In vitro biocompatibility Uniaxial tensile testing	High dose gamma Low dose gamma High dose E-beam Low dose E-beam Fractioned E-beam Control: PAA	-The biomechanical properties of pSFT following varying irradiation dosages are different when compared to PAA alone. -Denatured collagen content and thermal stability is dose dependant, yet this does not affect mechanical integrity. -All grafts were biocompatible. -Storage of grafts for 12 months had no adverse effects.
2017	The effects of irradiation dose and storage time following treatment on the viscoelastic properties of decellularised porcine super flexor tendon	Biomechanical testing: stress relaxation	High dose gamma Low dose gamma High dose E-beam Low dose E-beam Fractioned E-beam Control: PAA	-All treatments affected the viscoelastic properties of the grafts when compared to peracetic acid, but not as a function of the type or dose. -The biomechanical properties of irradiated grafts remain suitable to function as ACL replacement.

2017	Decellularization and Characterization of Porcine Superflexor Tendon: A Potential Anterior Cruciate Ligament Replacement	Histology Immunohistochemistry DNA quantification Collagen quantification GAG quantification alpha-Gal content analysis In vitro biocompatibility In vivo biocompatibility Tensile testing	Native Decellularised	-Decellularised specimens lack cell nuclei and dsDNA, while the architecture of the matrix is similar to native tissue. There is evidence of loss of collagen fibre crimp. GAG content is reduced when compared to native tissue. -Alpha-Gal epitope is reduced but still present. -DNA content abides with standard, with less than 50 ng/mg. -Collagen content is not significantly different after decellularisation, but GAG content is reduced. -In vitro biocompatibility testing shows no effect on cell morphology. -In vivo biocompatibility testing reveals minimal capsule formation and absence of calcification with decellularised implants compared to native. -Biomechanical properties including UTS, failure strain and Young's modulus shows no significant difference between native and decellularised specimens.
2019	Decellularisation affects the strain rate dependent and dynamic mechanical properties of a xenogeneic tendon intended for anterior cruciate ligament replacement	Biomechanical testing: Uniaxial tensile testing and dynamic mechanical analysis	Strain rates: 1, 10, 100% s-1	-Elastic moduli and UTS of decellularised specimens are significantly reduced compared to native. -Increased strain rate does not affect the linear region modulus, UTS or failure strain of native or decellularised grafts. -Dynamic, storage and loss modulus are significantly lower for decellularised tissue compared to native.
2019	Stratifying the mechanical performance of a decellularised xenogeneic tendon graft for anterior cruciate ligament reconstruction as a function of graft diameter	Dynamic mechanical analysis Uniaxial tensile testing	Graft sizes: 7, 8, 9 mm diameters	-Dynamic stiffness is significantly different between all groups. -Dynamic creep differ significantly between 7 and 8 mm, 8 and 9 mm groups. -Linear stiffness is significantly different between all groups, but no differences for failure load. -Increased graft size leads to resistance to failure, and increased suspension device failures.

2021	Integration and functional performance of a decellularised porcine superflexor tendon graft in an ovine model of anterior cruciate ligament reconstruction	Histology DNA quantification Biocompatibility Tensile testing In vivo performance: cytological analysis of synovial fluids, histopathological assessment of tissue and integration, histological and immunohistochemical analysis of graft tissue, tensile testing	Decellularised Allograft (ovine)	-No major differences in performance in vivo. -Inflammatory reaction to both grafts at 4 weeks, reducing after 26 weeks. -Cellular penetration from 12 weeks. -Ligamentisation occurred at osseotendinous junctions. -Grafts failed intra-articularly, showing comparable behaviour between decellularised tendon and allograft.

The decellularisation process used throughout this project was based on the methods of previously conducted research using the superflexor tendon at the University of Leeds (Table 1.14). It also shares the methods of that used in the development of OrthoPure XT, developed by Tissue Regenix Group Ltd. This regenerative medical technology company was spun out of the University of Leeds in 2006, to commercialise the decellularisation process, calling it dCELL technology. The OrthoPure XT is a decellularised, sterile, single use, porcine biological scaffold intended for use in ACLR and other knee ligament procedures [227]. It received CE marking on 1 June 2020 [228]. Human clinical data was presented at the ESSKA Congress in 2022, showing an viable alternative graft choice [229]. The key stages in the decellularisation process used here are shown in Figure 1.10.

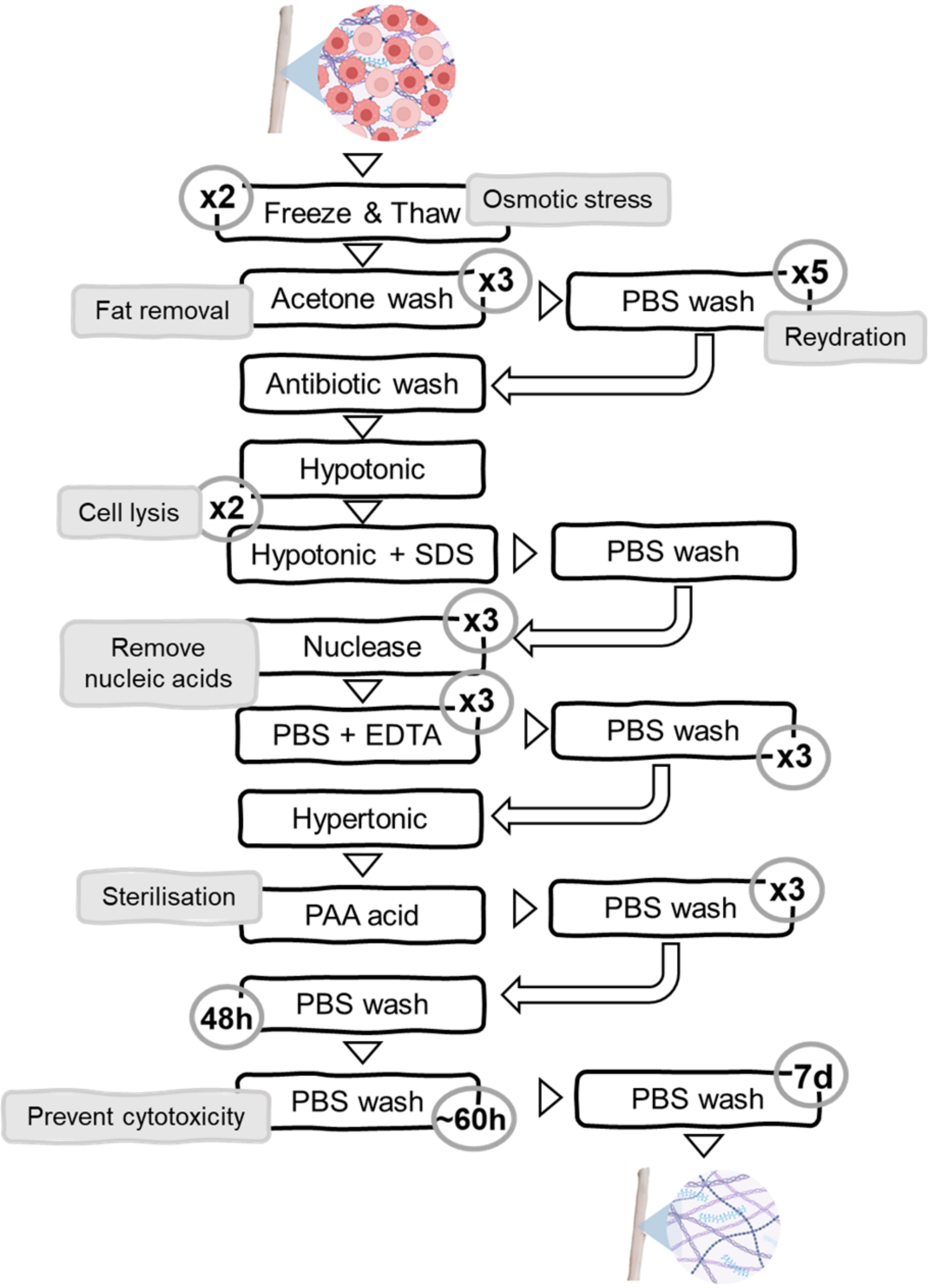

Figure 1.10: Decellularisation methods
used on porcine superflexor tendon throughout this project, totalling 4 weeks to complete, adapted from [220], created with BioRender.com.

1.4 Conclusion and rationale for the study

Decellularised porcine superflexor tendon provides a biocompatible graft for ACLR, with the mechanical strength and biochemical cues to encourage host cell population and tissue remodelling [223]. This overcomes the current disadvantages of using autografts and allografts, primarily in terms of failing to maintain cell viability as a consequence of initial necrosis when implanted [230], and structure degradation which translates to reduced mechanical properties [225].

Decellularised pSFT could potentially constitute an alternative that prevents further injury or ruptures, alleviating the economic burden in healthcare that this represents. It provides an off-the-shelf alternative graft option with similar dimensions to current gold-standard autografts, while exceeding native ACL mechanical properties. Decellularised pSFT could be further stratified depending on patient requirements during ACLR, and also shows promise for other ligament and tendon repair.

However, the decellularisation process has been shown to adversely alter the structure and biomechanics of pSFT [222, 224].

In the research conducted on decellularised pSFT to date, it remains unclear what effect the decellularisation process has on the collagenous and non-collagenous components of the ECM, and how these could play a role in the reduction of pSFT mechanical properties post-decellularisation. It has been proposed that tissue swelling may adversely impact decellularised pSFT [224], occurring as a result of the decellularisation process itself. The biomechanical behaviour of pSFT has been reported only in tension, yet this does not constitute the only loading it could be subject to when acting as a graft for ligament repair. Finally, previous investigations have been conducted on whole tendon, while sub-tendon units may provide key information in terms of the structural, biological and nanomechanical effects of decellularisation on pSFT.

Investigating the biological and biomechanical consequences of the decellularisation process on pSFT using a hierarchical approach would provide extensive insight into the structure-function relationship of tendon at different levels of scale, revealing its suitability to act as a graft for ACLR. With alterations to solutions used in end-stage washes of the decellularisation process, improved mechanical properties may be achieved, while providing information into the effect of different hydrating solutions on swelling and tendon biomechanics. Conducting a thorough biomechanical analysis including tension and compression would deliver a complete mechanical profile of the graft, offering insight into the role of non-collagenous components in pSFT biomechanics. Characterisation of structure, topography and composition of pSFT fascicles would reveal the effects of decellularisation at a sub-tendon scale, and how the interaction between these units contribute to whole tendon mechanics.

1.5 Project aim and objectives

1.5.1 Hypothesis

It is hypothesised that a hierarchical approach comprised of biological and biomechanical methods for investigating the biological and biomechanical consequences of decellularisation on pSFT will help determine its suitability as a graft for ACLR.

1.5.2 Aim

The aim of this project is to investigate the biological and biomechanical consequences of the decellularisation process on pSFT at different levels of scale, proving its suitability to act as a biological graft for ACLR.

1.5.3 Objectives

a) To investigate the biological and biomechanical consequences of decellularisation on whole pSFT.

b) To determine the effect of decellularisation on the collagenous and non-collagenous components of pSFT ECM.

c) To modify the end-stage washes of the decellularisation process to reduce pSFT swelling and adverse effects on its mechanical properties.

d) To assess the compressive behaviour of native and decellularised pSFT.

e) To study the contribution of glycosaminoglycans to tendon mechanics in tension and compression.

f) To characterise the structure and component distribution of native and decellularised pSFT fascicles.

g) To compare the hydration behaviour of pSFT fascicles.

h) To characterise the topography and nanomechanical properties of native and decellularised pSFT fascicles.

Chapter 2

Materials and Methods

2.1 Materials

2.1.1 Equipment

The equipment and suppliers are listed in Appendix A, Table A.1.

2.1.2 Chemicals and reagents

The chemicals and reagents used are listed in Appendix A, Table A.3.

2.2 Methods

2.2.1 Dissection of superflexor tendon

A summary of key stages of porcine superflexor tendon (pSFT) dissection is presented in Figure 2.1. The right hind legs of large white pigs (age 4-7 months; mixed sex; 62-104 kg) were obtained from abattoirs (Yorkshire Farmers, Meadow Quality Ltd, Scotlean Ltd, John Penny & Sons; United Kingdom) within 24 h of slaughter. The deep digital flexor tendon, most commonly referred to as superflexor tendon was dissected using No. 21 and 11 scalpel blades for incisions and removal of connective tissue, respectively.

Upon delivery of the porcine legs, the area where the pSFT was located was cut open, as it is hung from this region in an abattoir. To proceed with dissection, an inspection of the pSFT was conducted, to rule out damage from storage conditions. Once identified, a transverse incision was made across the superficial digital flexor tendon, located directly on top of the pSFT, within the toe region (Figure 2.1a). This revealed the toe region bifurcation of the pSFT underneath. The skin was cut longitudinally distally to the toe region, exposing soft tissues nearer the ankle. The superficial digital flexor tendon was carefully removed longitudinally towards the ankle. A No. 11 scalpel blade was used for removing sheath and connective tissue between the superficial and deep flexor tendons, eliminating as much as possible (Figure 2.1b).

Approximately 4 – 6 cm from the toe bifurcation of the pSFT, an accessory ligament of the deep digital flexor muscle was identified (Figure 2.1c). An incision was made longitudinal to the bulk tissue of the pSFT, releasing it from the accessory ligament. This increased pSFT range of movement while remaining attached at the toe and ankle insertion points, facilitating the removal of fatty and connective tissue enveloping the surface of the pSFT. The external skin layer atop the ankle region was removed perpendicular to the main incision, revealing the insertion site of the pSFT into the deep digital flexor muscle. After performing a thorough removal of remaining sheath connective tissue, an incision was made 1 cm above the myotendinous junction of the pSFT (Figure 2.1d).

The toe attachment site was released with a transverse incision over the fatty interdigital space, above the middle phalanx, deep enough to release the bifurcation of the pSFT from the toe (Figure 2.1e). This was pulled using the initial site of dissection as an anchor, to remove the pSFT from the porcine leg completely. Any muscle tissue on the distal end of the pSFT was removed, obtaining an inverse Y shaped tendon with three main regions: ankle, middle and toe (Figure 2.1f). If pSFTs were not immediately used, they were stored in filter paper soaked with PBS placed in re-sealable plastic bags and frozen at -20 °C until required.

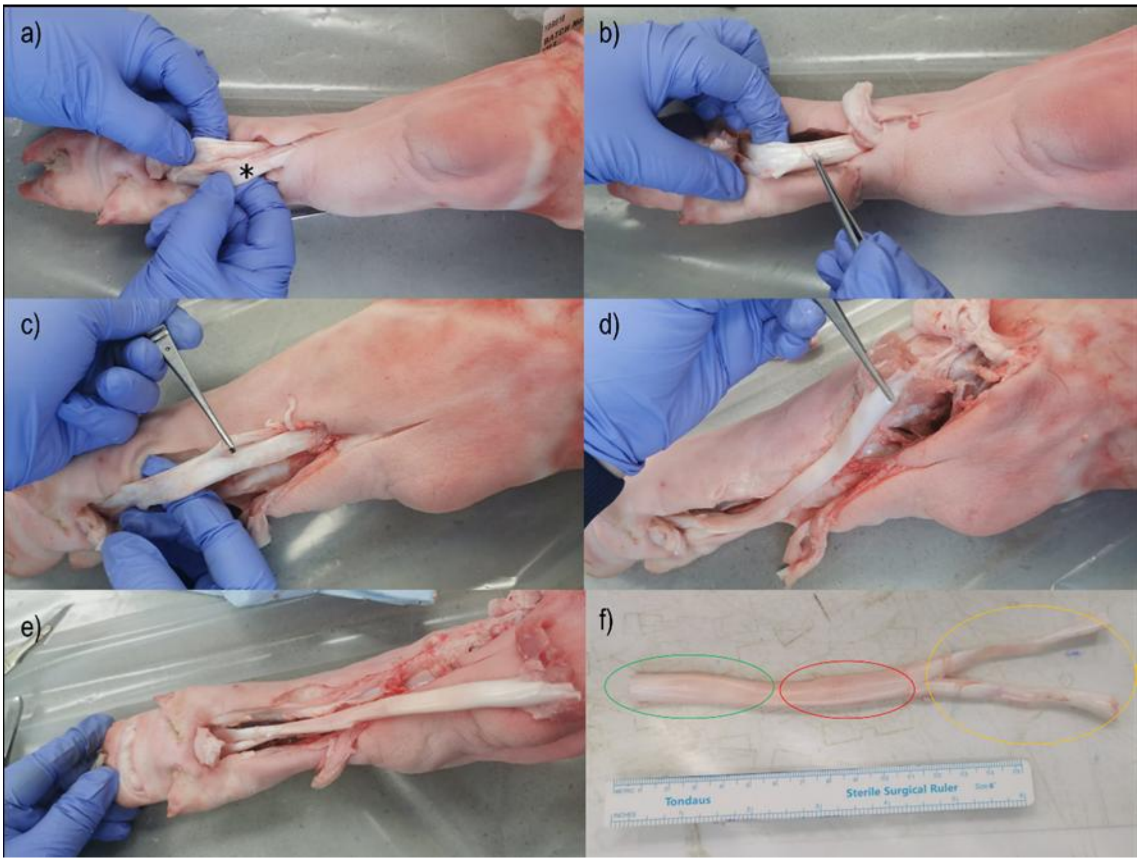

Figure 2.1: Dissection of pSFT from porcine hind leg.
a) After initial longitudinal inicision of porcine skin to reveal soft tissue, distinction between superficial (asterisk) and deep digital flexor tendons near toe region; b) removal of superficial digital flexor tendon and connective sheath tissue enveloping deep digital flexor tendon; c) accessory ligament of deep digital flexor muscle cut by lateral incision to flexor tendon; d) incision at the myotendinous junction releasing flexor tendon from ankle attachment site; e) incision at interdigital space releasing flexor tendon from toe attachment site; and f) whole pSFT with toe (orange), middle (red) and ankle (green) regions.

2.2.2 Decellularisation of superflexor tendon

Decellularisation was achieved using an adaptation of the protocol developed at the University of Leeds [231], previously used on pSFT [222]. Solutions were autoclaved at 121 °C, 15 psi for 20 min, unless otherwise specified.

2.2.2.1 Preparation of decellularisation solutions

Phosphate buffered saline (PBS; pH 7.3)

Ten PBS tablets were dissolved in 1 L of deionised water. pH was measured, ensuring it was within 7.2 – 7.4 range.

PBS containing aprotonin (10 KIU/mL)

Sterile aprotonin (1 mL) was added to 1 L of autoclaved PBS buffer. This was done in a biological safety cabinet (Class II) immediately prior to use. Any remaining solution was discarded.

Antibiotic solution (250 ug/mL amphotericin B, 10,000 U/mL penicillin-streptomycin)

Amphotericin B and penicillin-streptomycin aliquots were thawed 10 min prior to use. Both (6 mL of each) were added to 300 mL of autoclaved PBS buffer in sterile conditions immediately before use. Any remaining solution was left in 1% w/v Virkon for at least 20 min and then discarded.

PBS and EDTA (PBS-EDTA) (0.1% w/v)

Ten PBS tablets and 1 g of EDTA were dissolved in 1 L2.2.6.8 of deionised water using a magnetic stirrer and stirrer bar. Solution pH was adjusted to 7.2 – 7.4 by adding 6 M hydrochloric acid or 6 M sodium hydroxide using a Pasteur pipette while stirring the solution.

PBS-EDTA (2.7 mM) containing aprotonin (10 KIU/mL)

Sterile aprotonin (1 mL) was added to 1 L of autoclaved PBS-EDTA solution. This was done in a biological safety cabinet (Class II) immediately prior to use. Any remaining solution was discarded.

Hypotonic buffer (10 mM tris, 2.7 mM EDTA, 10 KIU/mL aprotonin)

Trizma base (1.21 g) and EDTA (1 g) were dissolved in 1 L of deionised water using a magnetic stirrer and stirrer bar. Solution pH was adjusted to 8.0 – 8.2 by adding 6 M hydrochloric acid or 6 M sodium hydroxide using a Pasteur pipette while stirring the solution. It was then autoclaved. Aprotonin (1 mL) was added in sterile conditions immediately before use. Any remaining solution was discarded.

SDS hypotonic buffer (0.1% w/v SDS, 10 mM tris, 2.7 mM EDTA, 10 KIU/mL aprotonin)

Sterile SDS solution (10 mL) was added to 1 L of autoclaved hypotonic buffer in a biological safety cabinet (Class II) immediately prior to use and mixed gently. Any remaining solution was discarded.

Nuclease solution (50 mM tris, 1 mM magnesium chloride, 10 U/mL Benzonase)

Trizma base (2.2 g) and magnesium chloride (73.1 mg) were dissolved in 360 mL deionised water using a magnetic stirrer and stirrer bar. Solution pH was adjusted to 7.5 – 7.7 by adding 6 M hydrochloric acid or 6 M sodium hydroxide using a Pasteur pipette while stirring the solution. It was then autoclaved. Benzonase (> 90% purity) was added in a biological safety cabinet (Class II) immediately prior to use and mixed gently. Benzonase concentration was revised before adding each time as it varied from batch to batch. The following calculations were to determine the required volume (Equation 2.1), where the volume buffer depended upon the number of tendons being decellularised, and benzonase concentration depended on its batch.

$$V_{buffer}(mL) * 10\frac{U}{mL} \rightarrow \frac{U}{benzonase\ concentration} = uL\ benzonase \tag{2.1}$$

Hypertonic solution (50 mM tris, 1.5 M sodium chloride)

Sodium chloride (87.66 g) and Trizma base (6.06 g) were dissolved in deionised water using a magnetic stirrer and stirrer bar. Solution pH was adjusted to 7.5 – 7.7 by adding 6 M hydrochloric acid or 6 M sodium hydroxide using a Pasteur pipette while stirring the solution.

Peracetic acid solution (0.1% v/v)

Peracetic acid (PAA; 39.9% w/v) was always used for making up the solution. Calculations for the required volume were conducted using Equation 2.2. PAA was added (2.5 mL) to 1 L of autoclaved PBS buffer in a biological safety cabinet (Class II) immediately prior to use and mixed gently. Solution pH was adjusted to 5.9 – 6.2 by adding 6 M hydrochloric acid or 6 M sodium hydroxide using a Pasteur pipette while stirring the solution, maintaining aseptic technique as much as possible. Any remaining solution was discarded.

$$C_1V_1 = C_2V_2 \rightarrow V_1 = \frac{0.1 * 1000}{39.9} \tag{2.2}$$

2.2.2.2 Decellularisation method

Native pSFTs were decellularised in batches of 6 or 9 specimens, following the protocol summarised in Table 2.1. All solutions were prepared a week in advanced. Where aprotonin (10 KIU/mL) and SDS (0.1% w/v) were required, these were added immediately prior to the use of each solution in a biological safety cabinet (Class II) using standard aseptic technique.

pSFTs were thawed at room temperature (20-25 °C) for 3 hours. When fully thawed, the toe bifurcation was removed. The main pSFT, included the middle and ankle regions (Figure 2f), with a length between 9 – 12 cm. Steps 1 – 6 were conducted in 50 mL Falcon tubes. For the thaw and hypotonic freeze cycles, tendons were defrosted from -20 °C storage in a water bath at 30 °C for 30 minutes. Approximately 40 mL of hypotonic buffer containing aprotonin was added to each tube, ensuring the whole pSFT was immersed in the solution. It was then frozen at -20 °C overnight. This was carried out a further two times, and on the final freezing step, the pSFTs were frozen over the weekend for 72 h. The temperature at which the pSFTs were frozen at allowed the formation of large crystals as a consequence of the slow freezing process, which appeared to open the tendon matrix, allowing penetration of solutions during the remaining steps of the process.

The pSFTs were thawed as described above after the 72 h wash (Table 2.1, step 2.1) and the hypotonic buffer was decanted carefully. Each acetone wash used approximately 45 mL to ensure the whole tendon was submerged. The Falcon tubes were organised in a tube rack and placed upright inside a plastic container. The container was placed on an orbital shaker inside a 42 °C incubator and agitated at 240 rpm for 1 h. This was repeated three times to discard as much fat as possible. After the last acetone wash, the Falcon tubes were transferred into a class II safety cabinet. From this point onwards all steps were conducted in sterile conditions. The acetone was decanted and replaced by PBS containing aprotonin for five washes under the same conditions as previously described (42 °C, 240 rpm). Each wash was 5 min long. This helped discard remaining fat and traces of acetone from the pSFTs.

The antibiotic decontamination solution required a sterile-filtered mixture of penicillin and streptomycin (Pen Strep) for antibacterial action, in combination with Amphotericin B (Amp) for antifungal action diluted (1:50) in PBS. The antibiotic aliquots were thawed at 36 °C 10 min before their intended use. The Falcon tubes with antibiotic solution were positioned transverse inside the plastic container, placed on an orbital shaker inside a 37 °C incubator and agitated at 80 rpm for 1 h. The solution was emptied into a container with Virkon solution (1% w/v) and left there for 20 minutes before discarding.

From this point (Table 2.1, step 6) onwards, 150 mL sterile pots were used. The pSFTs were carefully transferred into individual pots where 100 mL of solution would be added for all steps unless otherwise specified. Steps 7 to 10 consisted of hypotonic buffer washes containing aprotonin or aprotonin and SDS (0.1% w/v). Sterile SDS was added immediately before each wash and left for 24 h at 42 °C, agitating at 240 rpm. All pots were placed transverse within the plastic container. To remove SDS from the SFTs, 30 min PBS (containing aprotonin) washes were carried out three times. Each time, PBS was discarded and replaced with fresh PBS in sterile conditions. For thorough removal of SDS and cellular debris, a PBS wash was left over the weekend. This was the last step where aprotonin was added to decellularisation solutions.

Before starting the nuclease step (Table 2.1, step 14), a 30 min PBS wash was carried out to eliminate SDS residue from samples. Benzonase with > 90% purity was the nuclease used for pSFT decellularisation, added immediately prior to each incubation in sterile conditions. Only 60 mL of nuclease solution were used for each pot. The optimum temperature for enzymatic action of Benzonase is 37 °C, so the sample pots were placed in an incubator at this temperature with gentle agitation at 80 rpm for 2h. This was repeated three times. Transverse position of the pots inside the plastic container was preferred as it ensured the tendons were covered by the volume of nuclease solution. The SFTs were washed in PBS – EDTA solution for 30 min, three times and left overnight in a hypertonic buffer. This was all carried out under standard conditions of 42 °C and 240 rpm. Hypertonic buffer was removed by three 30 min PBS washes. The samples were left in fresh PBS overnight.

The peracetic acid sterilisation step required peracetic acid added to PBS immediately prior to use in sterile conditions. The solution was pH to 5.9 – 6.2 using aseptic technique outside of the safety cabinet. Samples were left in this solution for 3 h at 27 °C. To remove the sterilisation solution, samples were washed in PBS for 30 min. This was repeated three times. Steps 21 – 23 consisted of PBS washes to eliminate toxic residue of previously used solutions. These varied in length (as detailed in Table 2.1). The decellularisation process lasted a total of 4 weeks.

Table 2.1: Standard four week porcine pSFT decellularisation protocol

Week	**Step**	**Procedure/ Incubation**	**Additives**	**Temp (°C)**	**RPM**	**Duration**
1	1	Thaw + freeze in hypotonic buffer	Aprotonin	-20	N/A	16 h
	2	Thaw + freeze in hypotonic buffer	Aprotonin	-20	N/A	72 h
2	3	Thaw	No	40	N/A	3 h
	4	Acetone wash	No	42	240	3x1 h
	5	PBS wash	Aprotonin	42	240	5x5 min
	6	Antibiotic wash (in PBS)	v	37	80	1 h
	7	Hypotonic buffer	Aprotonin	42	240	24 h
	8	Hypotonic buffer	Aprotonin, SDS	42	240	24 h
	9	Hypotonic buffer	Aprotonin	42	240	24 h
	10	Hypotonic buffer	Aprotonin, SDS	42	240	24 h

	11	PBS wash	Aprotonin	42	240	3x30 min
	12	PBS wash	Aprotonin	42	240	72 h
3	13	PBS wash	No	42	240	30 min
	14	Nuclease buffer	Benzonase	37	80	3x2 h
	15	PBS - EDTA	No	42	240	3x30 min
	16	Hypertonic buffer	No	42	240	18-20 h
	17	PBS wash	No	42	240	3x30 min
	18	PBS wash	No	42	240	18-20 h
	19	PBS	Peracetic acid	27/RT	240	3 h
	20	PBS wash	No	42	240	3x30 min
	21	PBS wash	No	42	240	48 h
	22	PBS wash	No	42	240	72 h
4	23	PBS wash	No	42	240	1 week
	24	Storage	N/A	-20	N/A	N/A

After discarding the PBS from the week long wash (Table 2.1, step 23), 1 cm of each sample was removed using a scalpel, in sterile conditions, for compression testing. An additional 4 mm of each samples was removed for biological analyses, i.e. histology and biochemical assays. These were placed in bijou tubes, while the bulk tissue samples were stored in filter paper soaked in PBS inside a plastic bag. All samples were stored at -20 °C.

2.2.3 Mechanical characterisation

2.2.3.1 Sample preparation

Samples required shaping into a dumbbell conformation (Figure 2.2) before being subjected to mechanical testing. The dumbbell shape allowed a constant cross-sectional dimension to be maintained and improved gripping (see Section 2.2.3.2) during testing.

The SFTs were thawed at room temperature for approximately 3 h. They were placed on the bottom of a container and flattened manually. Dry ice was emptied into the container, covering the SFTs. They were left for 15 min to ensure freezing occurred. The samples were then placed on top of the dry ice. Fine tip pens were used to mark length and width on the surface of each tendon (Figure 2.2b). The length was 30 mm along the longitudinal axis of the middle region of the pSFT. Width was marked at 4 mm centred within the middle region of each pSFT.

The bulk tissue was removed with a scalpel (No. 21), commencing with the lateral and medial portion of the width marked in the middle region until a dumbbell shape was achieved (Figure 2.2c). A No. 11 blade was then used to remove thinner layers of tissue, getting closer to the marked width lines, ensuring both sides of the gauge length were parallel and as straight as possible. The tendons were placed on the dry ice between tissue removal, ensuring they stayed frozen to facilitate this process.

The interior corners of the dumbbell shaped pSFT were shaped carefully to obtain a smooth curve, eliminating stress concentrations (Figure 2.2d). The final dimensions were 3.5 mm width and natural pSFT thickness, in accordance with British and European standards, including dimensional tolerances of ± 0.18 mm (BS-EN-ISO 6892-1:2019). Shaped samples were stored with filter paper soaked in the appropriate solution, inside resealable plastic bags at -20 °C until mechanical characterisation.

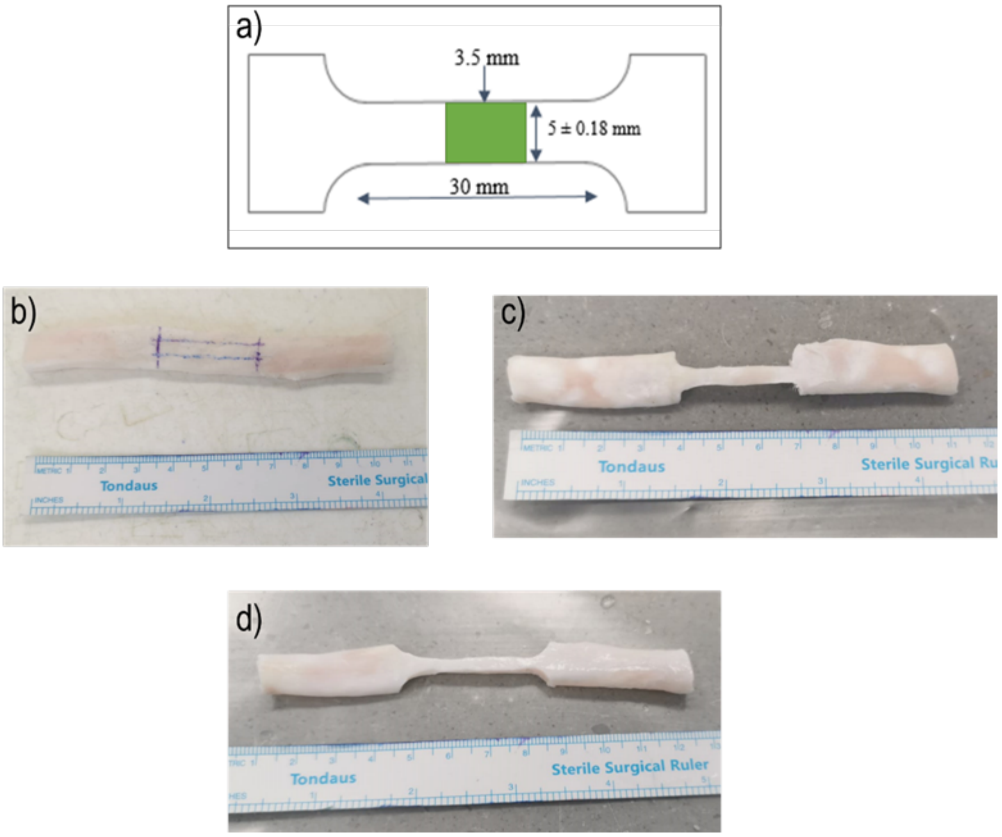

Figure 2.2: Shaping of SFTs in preparation for mechanical characterisation. a) dimensional specification required for pSFT shaping; b) frozen pSFT with length and width measurements; c) removal of bulk tissue leading to dumbbell shape; and d) final pSFT sample.

2.2.3.2 Sample set-up

SFTs were thawed at room temperature for 2 h prior to testing. Each sample was wrapped in filter paper soaked in their respective hydrating solution (PBS, Ringer's solution, saline solution) and placed into individual plastic bags. Each bag was sealed and left to equilibrate for at least 1 h before commencing the test at room temperature. After 1 h dimensional measurements of each sample were taken, repeating width measurements along the gauge length three times, as well as thickness measurements. Digital callipers were used. An average width and thickness (mm) was input into the Bluehill (Bluehill Materials Testing Software, version 2, Instron, USA) testing programme before initiating the experiment.

Cryo-grips (Figure 2.3a, b) were placed inside a freezer at -20 °C to lower material temperature. After 10 min they were transferred into a container with dry ice to reach sub-zero temperature. The cryo-grip compartment was filled with dry ice and shut with its cover, so the sub-zero temperature was maintained for the duration of the test. The detachable jaw faces had been placed face down on the dry ice, ensuring the gripping face was in direct contact with the dry ice, facilitating pSFT gripping. The main body of the cryo-grip was attached to the Instron 3365 testing machine, aligning the gripping faces of top and bottom grips facing front, along the axis of loading. pSFT samples were positioned directly against the gripping face, allowing it to stick. The detachable jaw faces were placed parallel to the exposed pSFT surface and bolts were tightened without excessive force, preventing deformation of the sample. The sample set-up (Figure 2.3c, d) was completed as fast as possible to prevent the tissue from freezing.

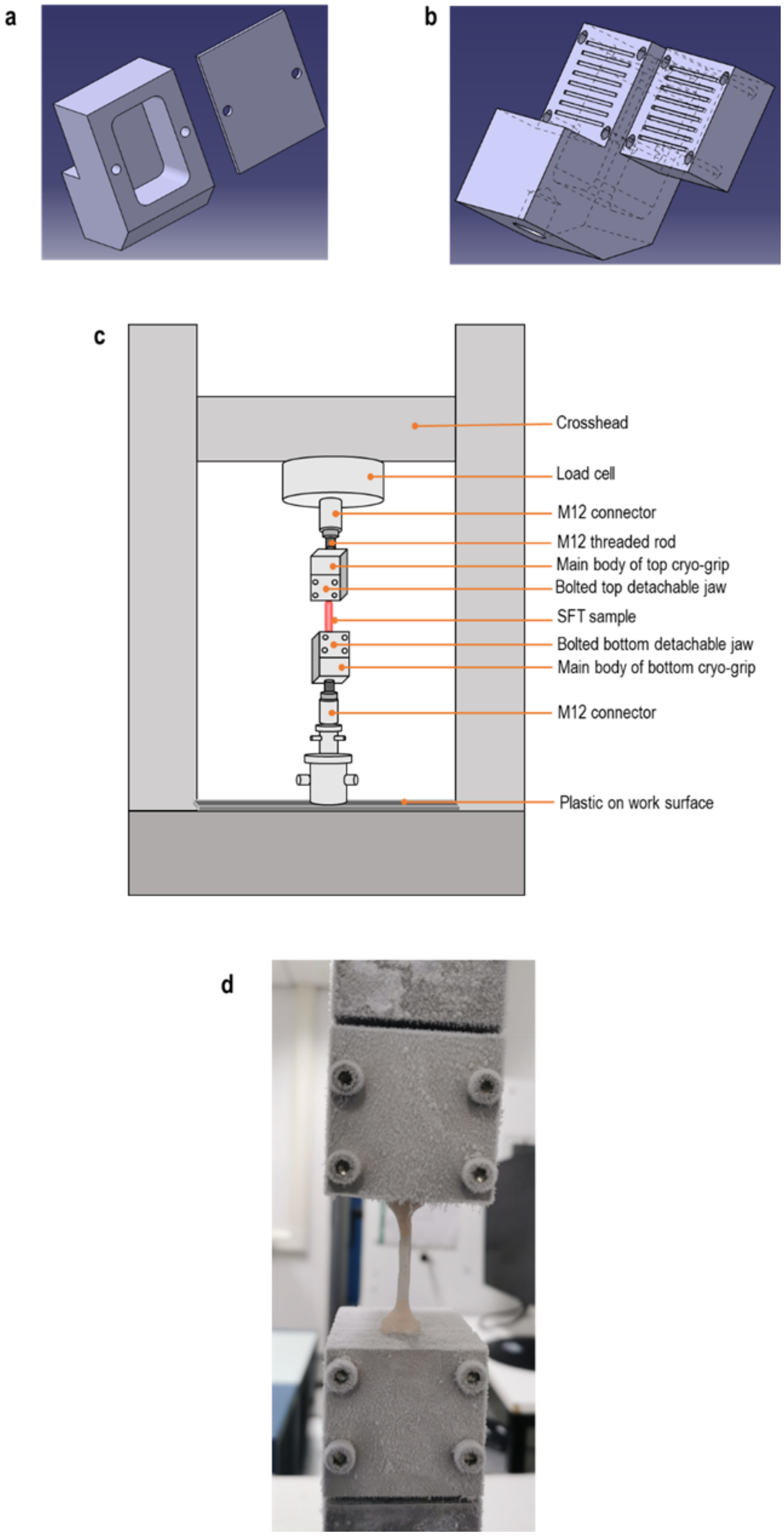

Figure 2.3: pSFT sample set-up using cryo-grips for mechanical characterisation.
a) Main body of the cryo-grip showing the posterior void compartment for dry-ice and its cover; b) detachable jaw and gripping face of the main cryo-grip, between which the pSFT is positioned; c) schematic representation of mounted pSFT sample on Instron testing machine ready for mechanical characterisation and d) pSFT gripped at sub-zero temperature ready for tensile testing.

2.2.3.3 Stress relaxation testing

For stress relaxation testing, a 500 N load cell was used. Immediately after the sample was set up (Section 2.2.3.2), the crosshead of the Instron testing machine was moved at the lowest jog speed (0.01 mm/min) to ensure the pSFT was taut. A pre-load of 0.25 N was applied to maintain consistent tautness between samples, then tared. Specimens were ramp loaded at 100% per min strain rate until a stress of 5 MPa was reached (Herbert et al., 2015). The sample was maintained at the corresponding strain for 180 sec (3 min), allowing stress relaxation to occur. The short duration of the test prevented the gauge length of the pSFT from freezing, caused by the sub-zero temperatures of the cryo-grips (see Section 2.2.3.2), which could influence the outcome of the experiment.

The Instron Bluehill 2 software provided data at a frequency of 0.1 sec (10 Hz), including time, extension, load, tensile strain and stress. The relaxation modulus (E(t)) was calculated as tensile stress divided by tensile strain, as given in Equation 4.

$$E(t) = \frac{\sigma(t)}{\varepsilon} \tag{2.3}$$

The data was fitted to a modified Maxwell-Weichert model (Equation 5) using the non-linear least squares method in Matlab [220]. This provided the quantitative values of time-independent elastic moduli (E_0) and time-dependant elastic moduli (E_1, E_2) used to interpret the mechanical response at their respective relaxation times (τ_1, τ_2), where t_0 corresponds to the time where the maximum stress occurred (˜ 5 MPa). Therefore the model accounts for any stress relaxation that may have occurred during the ramp phase ($0 \leq t \geq t_0$).

$$E(t) = E_0 + \frac{1}{t_0}[E_1\tau_1 e^{-\frac{t}{\tau_1}}(e^{-\frac{t_0}{\tau_1}} - 1) + E_2\tau_2 e^{-\frac{t}{\tau_2}}(e^{-\frac{t_0}{\tau_2}} - 1)] \tag{2.4}$$

2.2.3.4 Strength testing

SFTs were left at least 24 h after stress relaxation characterisation before subjected to strength to failure loading. This allowed sample recovery. For strength testing, a 5 kN load cell was used. Sample set-up and preloading was carried out as described in section 2.2.3.3. Preconditioning was performed to generate a stable viscoelastic response during testing. This consisted of 12x cycles between 0 and 5% strain at a strain rate of 50% per min. This was followed by an extension ramp to failure at a strain rate of 100% per min. Failure was defined as a sudden drop in load, often accompanied by visible and audible partial mid-substance rupture.

The Instron Bluehill 2 software provided data as detailed in section subsec:Stress-relaxation-testing. Ultimate tensile strength (UTS) and strain to failure (ε_{Fail}) were also provided by the software. A bi-linear model was fitted to normalised stress-strain data using the non-linear least squares regression in Matlab R2015a (version 8.5) [232]. The output provided quantitative values of the toe and linear region moduli (E_{toe}, E_{linear}).

2.2.4 Biochemical assessment of matrix components

2.2.4.1 Lyophilisation

Tissue samples of approximately 4 mm height and natural tendon width were macerated using a No. 11 scalpel blade. The tissue was placed into bijou tubes, which had been previously weighed. They were then weighed with the tissue content. The wet weight of the tissue was calculated by subtracting the bijou weight from the weight of the bijou with the tissue content. The bijou tubes were placed inside a freeze-dryer with loose lids. The freeze dryer would then reach -50 °C and 0.15 – 0.2 bar conditions. Tissue was lyophilised to a constant weight (for no less than a 48 h period) and reweighed to give the dry weight of the tissue. Where the lyophilised tissue formed clusters, these were carefully separated using forceps within the bijou tube, to maximise surface area in contact with digestion solutions.

2.2.4.2 GAG quantification

Quantification of GAGs in pSFT matrix was based on a common approach used in different tissues and culture media utilising 1,9-dimethylmethylene blue (DMB) dye. This procedure was first described by Farndale and colleagues in 1982, initially used for cartilage cultures [233]. The cationic DMB dye changes from a characteristic blue to violet colour when it binds to polyanionic substrates like sulfated GAGs [234]. This is a metachromasia phenomenon, where the change in colour is accompanied by an increased absorbance at 525 nm.

Preparation of solutions and reagents

Digestion buffer (5 mM L-cysteine hydrochloride, 5 mM Na2EDTA; pH 6)

For this, 1 L of PBS was previously prepared and autoclaved as per section 1.3.2.1.1, to which 0.788 g L-cysteine hydrochloride and 1.86 g disodium ethylenediaminetetraacetic acid was added. A magnetic stirrer and stirrer bar were used to dissolve the solution before adjusting the pH to 6 by adding 6 M hydrochloric acid or 6 M sodium hydroxide using a Pasteur pipette while stirring the solution. The solution was stored at room temperature and used within the space of six months before discarding.

Papain digestion solution (800 kU/mL casein activity)

Papain (800 kU per mL of digestion buffer) was dissolved in 50 mL of digestion buffer using a magnetic stirrer and stirrer bar. A volume of 3 mL was used per sample. This solution was prepared immediately prior to use. Any remaining solution was discarded.

0.1 M sodium di-hydrogen orthophosphate monohydrate (Solution A)

Sodium di-hydrogen orthophosphate monohydrate (3.45 g) was dissolved in 250 mL of deionised water using a magnetic stirrer and stirrer bar.

0.1 M di-sodium hydrogen orthophosphate (Solution B)

Di-sodium hydrogen orthophosphate (3.55 g) was dissolved in 250 mL of deionised water using a magnetic stirrer and stirrer bar.

GAG assay buffer

Solution A (137 mL) was combined with 63 mL of solution B using a magnetic stirrer and stirrer bar before adjusting the pH to 6.8 by adding 6 M hydrochloric acid or 6 M sodium hydroxide using a Pasteur pipette while stirring the solution. This assay buffer was stored at room temperature and used within the space of three months before discarding.

1 M formic acid solution

For adjusting the pH of the dye solution, 7.9 mL of formic acid was added to 192.1 mL of deionised water inside a fume cupboard.

DMB dye solution

The dye was made by dissolving 16 mg of 1,9 dimethylene blue into 5 mL of 100% ethanol and 2 mL of formic acid using using a magnetic stirrer and stirrer bar. Then 2 g of sodium formate were added and the solution was made up to 1 L by adding deionised water. The pH of the dye solution was checked and if required, adjusted to 3 by adding 1 M formic acid using a Pasteur pipette while stirring the solution. This dye solution was stored at room temperature and used within the space of three months before discarding.

GAG assay standards

The primary standard was made with 10 mg of chondroitin sulphate B dissolved in 10 mL of GAG assay buffer. This was then used to make up standards of varying concentrations (Table 2.3). Briefly, standards of different concentrations were prepared as a 1:1 dilution. The primary standard was stored at -20 °C, used only within the space of a month; all other standards were discarded. Every time a GAG assay was conducted, standards were made fresh.

Table 2.3: Chondroitin sulphate B standards used in GAG quantification assay.

Standard concentration (µg/mL)	Standard solution (µL)	GAG assay buffer (µL)
100	80 of 1 mg/mL (primary standard)	320
50	200 of 100 µg/mL	200
25	200 of 50 µg/mL	200
12.5	200 of 25 µg/mL	200
6.25	200 of 12.5 µg/mL	200
3.125	200 of 6.25 µg/mL	200
1.56	200 of 3.125 µg/mL	200
0	0	200

GAG assay method

Around 55 mg dry weight of pSFT was used for each GAG assay, being lyophilised as detailed in section 1.3.5.1. 3 mL of papain digestion solution was added to each bijou and these were placed in a water bath at 60 °C for 36 h. After 26 h, samples were removed from the water bath briefly and each bijou was vortexed for 10 sec before returning to the digestion process. If after 36 h it appeared the tissue was not yet digested, i.e. with visible clumps of tissue, then the samples were vortexed again and left to digest an additional 24 h. A 40 µL sample of each standard and each unknown (pSFT sample) was pipetted into individual wells of a 96 well plate in triplicate. A blank of assay buffer was used. DMB dye solution (250 µL) was added to each well and the plate was placed on a shaker at 50 rpm for 2 min. Absorbance was measured using a microplate spectrophotometer at 525 nm. Relative GAG content of unknown pSFT samples were calculated by interpolation from the standard curve generated from known concentrations of chondroitin sulfate B, normalising for dilution factor and dry tissue weight, such that final GAG content was expressed in µg/mg dry weight of pSFT. An example of a standard curve used to calculate GAG content is shown in Figure 2.4.

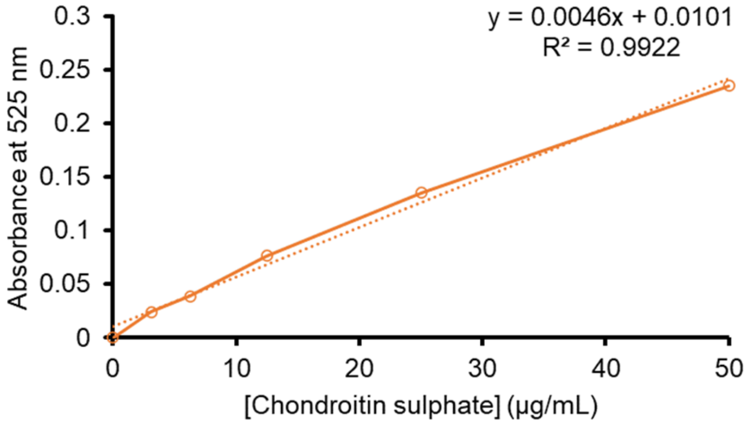

Figure 2.4: Example of a standard curve generated from known concentrations of chondroitin sulphate (CS) B.
Absorbance at 525 nm of known concentrations of CS B used to obtain a linear regression to interpolate the concentration of GAG content in pSFT samples.

2.2.4.3 Hydroxyproline quantification

Hydroxyproline is an amino acid found in collagen, quantifiable based on the assay proposed by Neuman and Logan [235]. Briefly, the colorimetric assay works as a result of the reaction occurring between oxidised hydroxyproline and p-dimethylaminobenzaldehyde (DMAB) [236], also known as Ehrlich's reagent. Hydroxyproline is oxidised by action of chloramine-T, becoming a pyrrole, which reacts with the dye, generating a chromophore with peak absorption at 570 nm [237].

Preparation of solutions and reagents

Assay buffer (158 mM citric acid monohydrate, 140 mM acetic acid, 587 mM sodium acetate trihydrate, 389 mM sodium hydroxide, 20 % v/v propan-1-ol; pH 6.2)

For the assay buffer, 80 mL of propan-1-ol, 13.3 g of citric acid, 3.2 mL of glacial acetic acid, 32 g of sodium acetate trihydrate, 9.1 g of sodium hydroxide and 317 mL of deionised water were mixed using a magnetic stirrer and stirrer bar. Solution pH was adjusted to 6

– 6.5 by adding 6 M hydrochloric acid or 6 M sodium hydroxide using a Pasteur pipette while stirring the solution. This was wrapped in aluminium foil and stored at 4 °C for no longer than two months.

Chloramine-T hydrate solution (50 mM chloramine-T hydrate)

This solution was prepared immediately prior to placing in the well plate for absorbance reading. Chloramine-T (1.13 g) was dissolved in 100 mL of deionised water using a magnetic stirrer and stirrer bar. Remaining solution was discarded.

Erlich's reagent (1 M p-dimethylaminobenzaldehyde, 60% v/v propan-1-ol, 18% v/v perchloric acid)

For Ehrlich's reagent, 7.5 g of p-dimethylaminobenzaldehyde, 30 mL of propan-1-ol, 15 mL of 60% v/v perchloric acid and 5 mL of deionised water were mixed using a magnetic stirrer and stirrer bar. Remaining solution was discarded.

Hydroxyproline assay standards

The primary standard was made by adding 25 mg of trans-4-hydroxy-L-proline to 25 mL of assay buffer. This was mixed by inversion. A secondary standard was made by diluting 1 mL of the primary standard in 9 mL of assay buffer. The secondary standard was used to make up standards of varying concentrations (Table 2.4). Briefly, standards of different concentrations were prepared as a 1:1 dilution. The primary standard was stored at -20 °C for no longer than six months. All other standards were made fresh for each hydroxyproline assay.

Table 2.4: Hydroxyproline standards used in collagen quantification assay.

Standard concentration (µg/mL)	Standard solution (µL)	GAG assay buffer (µL)
50	200 of 100 µg/mL	200
25	200 of 50 µg/mL	200
12.5	200 of 25 µg/mL	200
6.25	200 of 12.5 µg/mL	200
3.125	200 of 6.25 µg/mL	200
1.56	200 of 3.125 µg/mL	200
0	0	200

Hydroxyproline assay method

Around 35 mg dry weight of pSFT was used for each hydroxyproline assay, being lyophilised as detailed in section 1.3.5.1. After reaching a constant weight, the tissue was transferred to a polypropylene universal and 5 mL of 6 M hydrochloric acid was added. The universals were incubated in a block heater at 120 °C overnight. The samples were left to cool down at room temperature before neutralising. Neutralisation was carried out by adding 4.5 mL of 6 M NaOH and then adjusting the pH to 7 ± 0.2 using low concentration HCl or NaOH (1 M, 0.1 M). When the pH was adjusted, the total volume of each sample was recorded as the dilution factor. Samples were diluted 1:20 in assay buffer before assaying. A 50 µL sample of each standard and each unknown (pSFT sample) was pipetted into individual wells of a 96 well plate in triplicate. A blank of assay buffer was used. Chloramine T solution (100 µL) was added to each well and the plate was placed on a shaker at 60 rpm for 5 min. Ehrlich's reagent (100 µL) was added to each well and the plate was covered using a microplate sealing film, then incubated at 60 °C for 45 min. Absorbance was measured using a microplate spectrophotometer at 570 nm. Relative collagen content of unknown pSFT samples were calculated by interpolation from the standard curve generated from known concentrations of hydroxyproline, normalising for dilution factors and dry tissue weight, such that final collagen content was estimated as µg/mg dry weight of pSFT.

2.2.4.4 Denatured collagen quantification

This assay relies on the easy digestion of degraded or unwound collagen by proteolytic enzymes as opposed to the highly resistant digestion of intact collagen molecules. This method was proposed by Bank and colleagues, who simplified the elaborate methods standardly used [238]. It was initially used for quantifying degraded collagen in osteoarthritic cartilage, but applicable to different connective tissue. Briefly, alpha-chymotrypsin is used for selective digestion of degraded collagen, followed by quantification of hydroxyproline in supernatants after hydrolysis is carried out as conducted in the hydroxyproline assay.

Preparation of solutions and reagents

Digest buffer (100 mM Trisma Base, 10 mM Calcium chloride)

Trizma base (1.21 g) and 0.15 g of calcium chloride were dissolved in 100 mL of deionised water using a magnetic stirrer and stirrer bar. Solution pH was adjusted to 7.8 by adding 6 M hydrochloric acid or 6 M sodium hydroxide using a Pasteur pipette while stirring the solution. The solution was autoclaved at 121 °C, 15 psi for 20 min. It was stored at room temperature for no longer than one month.

Alpha-chymotrypsin solution (5 mg/mL)

Alpha chymotrypsin was added at a concentration of 5 mg per mL of digest buffer and mixed using a magnetic stirrer and stirrer bar. Only the amount required for samples was made up prior to use. Any remaining solution was discarded. The assay buffer, standards (primary, secondary and varying concentration standards), chloramine-T and Ehrlich's reagent were prepared as per section 1.3.5.3.1.

Denatured collagen assay method

From 45 – 70 mg dry weight of pSFT was used for each denatured collagen assay, being lyophilised as detailed in section 1.3.5.1. Tissue was transferred to a polypropylene universal and 5 mL of alpha-chymotrypsin solution was added. The universals were incubated in a block heater at 30 °C for 24 h. The samples were left to cool down at room temperature before centrifuging at 600 g for 10 min. The supernatant was transferred to a new universal and 4 mL of 6 M HCl was added. The samples were then incubated in a block heater at 120 °C overnight. The samples were left to cool down at room temperature before neutralising. Neutralisation was carried out by determining the volume of each sample and adding 0.5 mL less than its total volume of 6 M NaOH. After, the pH was adjusted to pH to 7 ± 0.2 using low concentration HCl or NaOH (1 M, 0.1 M). When the pH was adjusted, the total volume of each sample was recorded as the dilution factor. Samples were not diluted before assaying. The hydroxyproline assay was then carried out as detailed in section 1.3.5.3.2, and relative denatured collagen content was expressed in µg/mg dry weight of pSFT.

2.2.5 Thermal stability of porcine superflexor tendon

Differential scanning calorimetry (DSC) is a thermoanalytical technique useful to study alterations in the structural properties of a sample as a function of both temperature and time [239]. From this, transition temperature can be obtained, being the point where 50% of collagen is in native conformation while the rest is denatured. Higher transition temperatures are indicative of a more stable molecule [240]. Moreover, under constant pressure, the heat change in the transition of the sample corresponds to the enthalpy change [241]. Thus, calorimetric enthalpy is given by the integrated zone below the thermogram [242].

Only a small amount of sample is required, no matter if it is in liquid or solid state, for analysis using DSC [243]. Despite being a destructive technique, the sample size requirement proves advantageous.

2.2.5.1 Sample preparation

A 5 x 5 mm section of tissue was taken from the centre of the dumbbell extremity belonging to the toe region of the pSFT (Figure 2.5). The toe region was chosen over the ankle region given natural thickness of pSFT is greater in the toe region. For this, a square of 5 mm width and height was delimitated using a biological tissue marker directly onto the tendon surface. A scalpel (No. 11 blade) was used to remove the tissue from the bulk dumbbell specimen. The peritenon (paratenon and epitenon) was then carefully removed using a scalpel and forceps, leaving a cube of tendon matrix for each sample with an approximate area of 4.5 ± 0.05 mm2. Each sample was obtained after mechanical characterisation. Samples were stored in a bijou at -20 °C until thermal techniques were carried out.

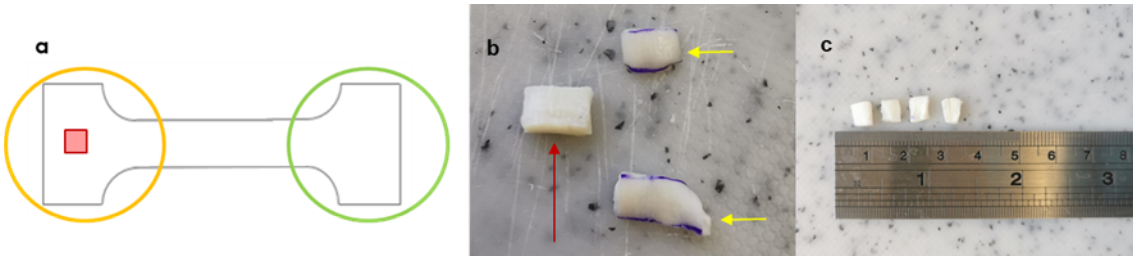

Figure 2.5: Sample preparation for thermal analysis.
a) ankle (green) and toe (orange) region of the dumbbell shaped porcine pSFT with the area of interest in red; b) peritenon (yellow arrows) removed from the surface of the matrix (red arrow); and c) pSFT matrix samples stored for further analysis.

Samples were thawed at room temperature for 20 min. Immediately prior to placing the samples inside the DSC pans, two incisions were made. The first longitudinal incision cut the tendon matrix cube in half. The second transverse incision allowed to obtain a sample that would fit comfortably within the pan. The final pSFT sample dimensions were approximately 2 ± 0.03 mm x 1 ± 0.02 mm. This is displayed in Figure 2.6.

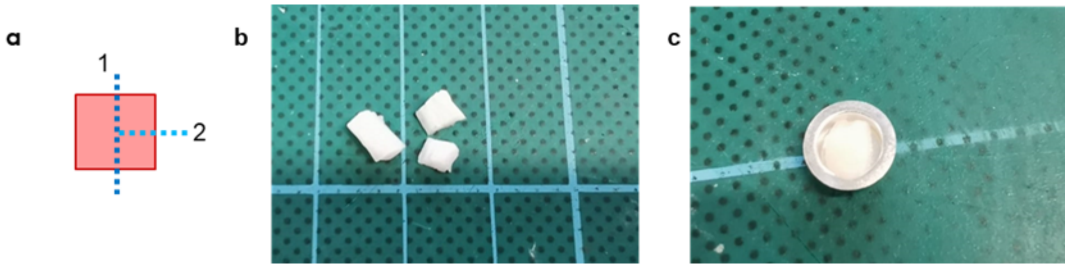

Figure 2.6: Sample preparation for differential scanning calorimetry.
a) representation of initial longitudinal incision made to halve the specimen, followed by a transverse incision to obtain a small cuboidal specimen; b) final sample prior to placing inside DSC pan; and c) pSFT matrix samples inside DSC pan.

2.2.5.2 Differential scanning calorimetry method

Each aluminium pan and lid was weighed and tared before a sample was placed inside it. Samples were then placed inside using forceps, making full contact with the bottom of the pan. Each pan was hermetically sealed and the wet weight was measured prior to calorimetry using a Q2000 DSC Instrument. Samples were equilibrated at 15 °C, then they were subjected to a ramp increasing temperature at a rate of 4 °C per min until 130 °C was reached. Six sample groups were subjected to DSC (n = 6 for each from different tendons). All samples were run on the same day minimising variations that could occur with the calorimeter. Data was analysed using TA Universal Analysis 2000 (TA Instruments), where transition temperature was the temperature at which the heat flow through the sample was the highest [223].

To determine the differences between groups could be attributed to treatment, i.e. decellularisation process, as opposed to inherent tissue variability, a separate experiment was conducted. This compared specimens obtained from the same tendon of the native group (n = 6 cubes) with native specimens from different tendons (n = 6 tendons, 1 cube from each). The same was done for decellularised pSFT. Samples were subjected to DSC under the same conditions.

2.2.6 Qualitative histological analysis

2.2.6.1 Preparation of histological solutions

Alcian blue stain and associated solutions required for the staining protocol were obtained from a commercial kit (detailed in materials). Additional solution preparation is described below.

PBS

Ten PBS tablets were dissolved in 1 L of deionised water. pH was measured, ensuring it was within 7.2 – 7.4 range. The solution was autoclaved at 121 °C, 15 psi for 20 min.

4’, 6-Diamidino-2-phenylindole dihydrochloride (DAPI) dye buffer

Trizma (1.211 g), disodium ethylenediaminetetraacetic acid (372 mg) and sodium chloride (58 mg) were dissolved in 1 L of deionised water using a magnetic stirrer and stirrer bar. The solution was autoclaved. Solution pH was adjusted to 7.4 immediately prior to use by adding 6 M hydrochloric acid or 6 M sodium hydroxide using a Pasteur pipette while stirring the solution. The buffer was stored at room temperature for no longer than six months.

Working DAPI dye solution

DAPI dye solution (aliquot stored at -25 °C wrapped in foil for no longer than six months) (20 µL) was added to 200 mL of dye buffer in a bottle wrapped in foil. This was mixed by inversion. Solution pH was adjusted to to 7.4 by adding 6 M hydrochloric acid or 6 M sodium hydroxide using a Pasteur pipette while stirring the solution. This was prepared immediately prior to staining. Any remaining solution was discarded.

Weigert’s haematoxylin

Equal volumes (500 mL) of solution A and B (obtained from a kit, detailed in materials) were mixed by inversion. The stain was stored at 4 °C for no longer than one month.

Acid alcohol (1% v/v)

Hydrochloric acid (5 mL) was added to 495 mL of 70% ethanol and mixed gently. This was prepared immediately prior to staining.

Acetic acid (1% v/v)

Glacial acetic acid (5 mL) was added to 495 mL of deionized water and mixed gently. This was prepared immediately prior to staining.

Fast green (0.02% w/v)

Fast green (100 mg) was dissolved in 500 mL of deionised water using a magnetic stirrer and stirrer bar. The stain was filtered before use.

Safranin O (0.1% w/v)

Safranin O (500 mg) was dissolved in 500 mL of deionised water using a magnetic stirrer and stirrer bar. The stain was filtered before use. Fresh Safranin O stain was prepared prior to each staining.

Sirius red (0.1% w/v)

Sirius red (100 mg) was added to 100 mL of saturated picric acid solution inside a fume hood. This was dissolved water using a magnetic stirrer and stirrer bar. The stain was filtered before use.

Potassium permanganate (5% w/v)

Potassium permanganate (15 g) was dissolved in 300 mL of deionised water using a magnetic stirrer and stirrer bar. The stain was filtered before use.

Oxalic acid (1% w/v)

Oxalic acid (1 g) was dissolved in 100 mL of deionised water using a magnetic stirrer and stirrer bar. This was prepared immediately prior to staining.

2.2.6.2 Formalin fixation

Tissue fixation and processing have the purpose of preserving the most similar representation of the dynamic, living tissue [244]. To stabilise the microanatomy of the tissue, it was fixed in neutral buffered formalin (NBF), preventing autolysis. Histology cassettes were labelled with pencil. Samples were thawed at room temperature and placed into the individual histology cassettes. These were submerged in an excess of 10% w/v NBF for 26-32 h at room temperature.

2.2.6.3 Tissue processing

After NBF fixation, samples were processed using an automatic tissue processor, following the programme detailed in Table 2.5. The samples were embedded in paraffin wax which facilitates sectioning without altering the structure and architecture of the tissue while providing physical support to the sample [245].

Table 2.5: Tissue processing programme details

Step	Solution	Time
1	10% (v/v) NBF	1 h
2	70% (v/v) ethanol	1 h
3	90% (v/v) ethanol	1 h
4	100% (v/v) ethanol	1 h 10 min
5	100% (v/v) ethanol	1 h 10 min
6	100% (v/v) ethanol	3 h 20 min
7	100% (v/v) ethanol	4 h 20 min
8	Xylene	1 h
9	Xylene	1 h 30 min
10	Xylene	2 h
11	Molten wax	2 h 30 min
12	Molten wax	2 h
	Total processing time	**23 h**

2.2.6.4 Tissue embedding

Embedding of pSFT specimens was conducted in either a transverse or longitudinal orientation (Figure 2.7). This was determined according to the matrix component, structure or characteristic under investigation. Transverse section primarily showed the fascicular matrix , while longitudinal sections revealed collagen crimp structure.

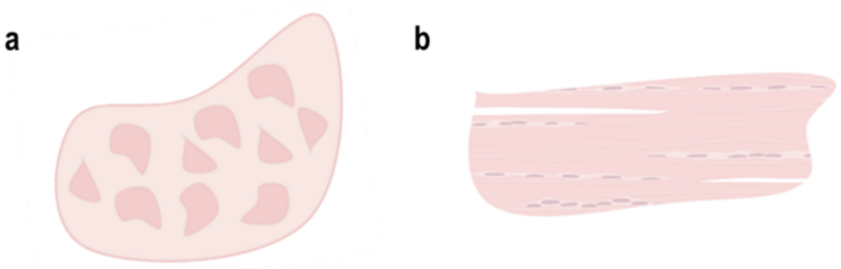

Figure 2.7: Transverse and longitudinal orientation of pSFT specimens for histological evaluation.
a) transverse sectioning would represent the intra- and interfascicular matrix within the peritenon, while b) longitudinal sectioning reveals collagen alignment, crimp and cellular arrangement. Created with BioRender.com.

Paraffin wax embedding

Wax moulds were filled circa 25% with molten wax. Using heated forceps, NBF-fixed pSFT samples were placed in the mould in the required orientation (transverse or longitudinal). The mould was then completely filled with molten wax and the histology cassette base placed on top. Air bubbles were forced out using the heated forceps by pressing down longitudinally along the cassette base. The samples were cooled and set at room temperature overnight. The wax block was then removed from the mould and any excess wax was scraped and discarded. Wax blocks were stored at room temperature away from direct sunlight.

Cryo-embedding

Samples were placed into 1.5 mL Eppendorf tubes. The tubes were dropped into liquid nitrogen to snap freeze. They were left for 2 – 3 min, moving them every 30 sec using forceps. The tubes were removed from the liquid nitrogen and placed into a rack. They were left at – 80 °C for 24 h before transferring to cryo-embedding plastic moulds. The mould was filled circa 90% with OCT mounting medium before placing the sample in the required orientation (transverse). A small amount of OCT was placed on top of the sample. The plastic moulds were placed flat inside the – 80 °C freezer until set. They were then kept at – 20 °C until required for sectioning.

2.2.6.5 Tissue sectioning

Paraffin wax embedded tissue samples

The hotplate and water bath were turned on, ensuring the temperature was 55-60 °C and 45-50 °C respectively. The blocks were trimmed on a microtome and immersed in icy water prior to sectioning. Superfrost plus (positively charged) slides were labelled using pencil. Sample blocks were sectioned at an angle of 0 ° and a thickness of 8 µm. Sections were removed from the microtome using fine tip forceps and transferred onto the water bath long enough for excessive wrinkling to flatten. Sections were placed on superfrost slides (one section per slide unless otherwise stated) and placed onto a hotplate for three hours before leaving to dry at room temperature overnight. Slides were stored in a rack or tray until required for staining.

Cryo-embedded tissue samples

The cryostat was set to – 25 °C. Superfrost plus slides were labelled using pencil. The embedded sample was set onto the chuck using OCT mounting medium and added weight. The chuck was placed into the holder and screwed tight to fasten in place. Samples were sectioned at an angle of 4 ° and initially, a thickness of 45 µm to ensure the blade was in contact with the specimen. Once this was achieved, the thickness was reduced to 15 µm. Multiple sections were placed on superfrost plus slides by touching the section directly onto the slide surface. Slides were placed in a rack kept inside the cryostat until all sectioning was complete. Slides were kept at – 20 °C until required for staining.

2.2.6.6 Dewaxing and hydration of sections

This process was carried out on paraffin wax embedded sections only. Slides were placed into a metallic slide rack and submerged in the solutions detailed in Table 2.1.1.4. Xylene facilitates dewaxing, while ethanol rehydrated sections. Native sections were used as a control for each staining process. Histological stains and solutions were always prepared prior to staining sections (unless otherwise stated), accounting for variation in staining intensities between decellularised groups.

Table 2.6: Details of dewaxing and hydration of paraffin sections

Step	Solution	Time
1	Xylene	10 min
2	Xylene	10 min
3	100% (v/v) ethanol	3 min
4	100% (v/v) ethanol	2 min
5	100% (v/v) ethanol	2 min
6	70% (v/v) ethanol	2 min
7	Running tap water	3 min

2.2.6.7 Histological staining

Haematoxylin and Eosin (H&E)

This is the most commonly used stain analysis of biological material, based on a combination of haematoxylin (blue) and eosin (red). Cell nuclei are stained blue as haematoxylin binds to negatively charged nucleic acids while the cytoplasmic components appear pink/red, counterstained by eosin [245]. Wax embedded sections were dewaxed and hydrated (Section 2.2.6.6). Cryo-embedded sections were thawed at room temperature for 10 min, then immersed in running tap water for 3 min. Subsequent steps were performed on all sections. Slides were immersed in Mayer's haematoxylin for 1 min. They were rinsed under running tap water until the water appeared clear, removing excess stain. They were then immersed in Scott's water for 3 min, followed by tap water for another 3 min. Sections were then stained in eosin for 3 min and rinsed under running tap water for 1 min. Slides underwent dehydration and mounting as detailed in Section 2.2.6.8. Sections were imaged using normal Köhler illumination.

4´,6-diamidino-2-phenylindole (DAPI)

DAPI is a fluorescent stain that allows the visualisation of deoxyribonucleic acid (DNA), by associating with the minor groove of the nucleic acid [246]. It has high affinity for adenine-thymine (AT) clusters, and has the advantage of increased photostability compared to alternative fluorescent stains [246]. The working dye solution was prepared immediately prior to staining. After sections were dewaxed and hydrated (Section 2.2.6.6), they were immersed in the working solution. This was placed inside a drawer to ensure darkness and room temperature conditions remained constant for 10 min. Slides were washed in PBS for 10 min. PBS washes were performed three times. Sections were mounted using Dako fluorescence mounting medium on glass coverslips. Slides were stored at 4 °C in the dark for 48 h. Native and decellularised sections were imaged under fluorescent illumination with a DAPI filter prism (460 nm) with the same settings. This maintained staining intensities constant enough for comparison between groups.

Safranin O/Fast Green

Safranin O is a cationic dye used for staining proteoglycans and glycosaminoglycans [247] red. Fast Green acts as a counter stain and haematoxylin stains cell nuclei purple/blue. Sections (Section 2.2.6.4) were stained 24 h after sectioning to ensure consistent staining of glycosaminoglycans. After sections were dewaxed and hydrated (Section 2.3.7.5), they were immersed in Weigert's haematoxylin for 3 min. Slides were washed in tap water for 10 min before differentiating in 1% acid alcohol for 1 min. Slides were washed in tap water for 3 min and transferred into 0.02% w/v Fast Green for 5 min. They were briefly washed in 1% v/v acetic acid and drained, removing excess solution. Sections were stained in 0.1% Safranin O for 4 min. Slides underwent dehydration and mounting as detailed in Section 2.2.6.8. Sections were imaged using normal Köhler illumination.

Alcian Blue/PAS Stain

Alcian blue is used to identify the presence of sulphated glycosaminoglycans, used in combination with Periodic acid-Schiff (PAS) stain which highlights glycogen, glycoproteins and neutral mucosubstances in pink/red [248]. The protocol from a commercial staining kit (Atom Scientific) was followed. After sections were dewaxed and hydrated (Section 2.2.6.6), they were immersed in Alcian Blue for 10 min and washed with deionised water. Slides were immersed in 1% periodic acid for 5 min and washed using deionised water to remove excess solution. They were then immersed in Schiff reagent for 20 min and washed in running tap water for 8 min until sections were visibly magenta. Sections were stained in haemalum Mayer for 1 min and rinsed in running tap water. They were differentiated in 1% acid alcohol for no longer than 5 sec and washed in running tap water before dehydration and mounting (Section 2.2.6.8). Sections were imaged using normal Köhler illumination.

Sirius Red

Picrosirius red staining (PSR F3BA) is an anionic dye with sulfonic groups which react with amino acids in collagen molecules. Given the high specificity of this reaction, and the alignment of the dye with respect to collagen fibres, Sirius red staining optimises the birefringence of collagen under polarised light [249]. After sections were dewaxed and hydrated (Section 2.2.6.6), they were immersed in 5% potassium permanganate for 5 min and washed in deionised water until excess solution was removed. Slides were immersed in 1% oxalic acid for 2 min and washed in deionised water for 1 min, then this was repeated in fresh water for 4 min. Slides were immersed in 95% ethanol for 1 min before being stained using Miller's stain for 1 h. Slides were washed using 95% ethanol until excess stain was removed, then immersed in 70% ethanol for 1 min. Ethanol was removed by washing in tap water for 2 min. Sections were then stained in Weigerts haematoxylin for 10 min and washed in tap water for 1 min. Sections were differentiated in 1% acid alcohol for 11 min and washed in deionised water for 30 sec before staining in picro Sirius red for 1 h. Slides were washed using deionised water and blotted dry. Slides underwent dehydration and mounting as detailed in Section 2.2.6.8. Sections were imaged using normal Köhler illumination and polarised light.

2.2.6.8 Dehydration and mounting

Following histological staining, slides were dehydrated in ethanol and prepared for mounting in xylene as detailed in Table 2.7. A drop of DPX mountant was placed on a glass coverslip using a Pasteur pipette. The coverslip was then placed face down onto the section attached to the superfrost slide using forceps. Air bubbles were pushed out by applying gentle pressure on the middle of the coverslip with forceps. Slides were left to dry overnight at room temperature before imaging.

Table 2.7: Details of dehydration and mounting of paraffin sections

Step	Solution	Time
1	70% (v/v) ethanol	5 sec
2	100% (v/v) ethanol	1 min
3	100% (v/v) ethanol	2 min
4	100% (v/v) ethanol	3 min
5	Xylene	10 min
6	Xylene	10 min

2.2.6.9 Confocal microscopy imaging

An upright Axio Imager M2 microscope (Carl Zeiss Microscopy) was used for viewing histologically stained sections. Köhler (bright field) illumination was used for visualising sections unless otherwise stated. Microscope calibration was carried out prior to use.

All sections stained with a specific stain were imaged on the same day under the same conditions (exposure time) to minimise variation between groups. When required, polarising filters were used. Fluorescent illuminators were used when fluorescent microscopy was required. Images were captured digitally with the associated AxioCam MCr5 digital camera and computer software (Zen version 2). Magnification of representative images are specified combining the objective lens and camera lens magnification.

Chapter 3

The consequences of decellularisation process modification on the biomechanical and biological properties of porcine superflexor tendon

3.1 Introduction

In previous studies [220–224], it has been reported that the decellularisation process used on pSFT does not significantly reduce the biomechanical strength of porcine superflexor tendon. However, minor changes have been found, including a reduction in stress relaxation parameters and dynamic mechanical properties, and changes in the toe region of decellularised specimens [220, 224]. Furthermore, some inconsistencies were reported in the collagen and non-collagenous components of the decellularised matrix [222], including a significant GAG loss. Also, a loss of collagen crimp has been reported post-decellularisation [220, 222]. This warrants an in-depth analysis of the consequences of decellularisation on the structure, composition and biomechanical behaviour of porcine superflexor tendon.

During decellularisation, phosphate buffered saline (PBS) is used, primarily due to its comparability to interstitial fluid, given it is an isotonic solution, with physiological pH and osmolarity [250]. It is also used as a hydrating solution during mechanical testing. PBS has been shown to increase water content in tendon and ligament, swelling the tissue, adversely affecting its tensile mechanical properties, including Young's modulus and tensile strength [251–256].

The mechanisms through which matrix components interact and withstand loads are affected by hydrating with PBS, proven further by studies conducted at smaller levels of scale [257–261]. Consequently, adjusting the in vitro conditions for mechanical testing may prove beneficial [251, 252]. The effect of swelling has not yet been studied in porcine superflexor tendon, yet has been proposed to have occurred resulting in a reduction of material properties [224], including tensile strength. Due to the extensive use of PBS during decellularisation and mechanical testing, the potential adverse effects on tissue mechanics require investigating.

PBS not only swells tendon, but also has this effect on other musculoskeletal tissues

[261]. Alternative solutions containing the physiological concentration of sodium [262] as the main cation of extracellular fluid, could be used during end stage washes of the decellularisation process, which aim to remove residual reagents. They could also be used for tissue hydration during subsequent mechanical testing. Ringer's solution has been used as a hydrating medium on human tendon previously [263], while saline solution is clinically relevant, used for irrigation during surgical procedures. It was therefore hypothesised that by substituting PBS with alternative physiological fluid-like solutions in both decellularisation and testing methods, tissue swelling could be reduced, reducing structural and biomechanical changes post-decellularisation.

3.1.1 Aim and objectives

3.1.1.1 Aim

The aim of this Chapter was to investigate the effect of the decellularisation process on the structure, composition and biomechanics of pSFT and to explore how alternative solutions to PBS used in the end stages of the decellularisation method affected tissue properties.

3.1.1.2 Objetives

The specific objectives were as follows:

a) To introduce alternative solutions to PBS during end-stage washes of the decellularisation method, including 25% Ringers, 100% Ringers and 0.9% saline solution.

b) To determine the effects of using different solutions during the decellularisation process on pSFT swelling, then investigate whether the same behaviour occurs on native pSFT.

c) To characterise the biomechanical behaviour of decellularised pSFTs using their solution (25% Ringers, 100% Ringers and 0.9% saline solution) as a hydrating medium during testing.

d) To quantify the loss of collagenous and non-collagenous (GAGs) components from pSFT matrix as a consequence of decellularisation.

e) To assess the quality and stability of the collagen in decellularised pSFT.

f) To qualitatively evaluate the structural and compositional changes in pSFT architecture following decellularisation.

g) To investigate the consequences of decellularisation on collagen crimp by analysing crimp parameters.

3.2 Methods

3.2.1 Dissection of superflexor tendon

Dissection was carried out as per Chapter 2, section 2.2.1

3.2.2 Decellularisation of superflexor tendon

Standard decellularisation was carried out as detailed in Chapter 2, section 2.2.2.

3.2.3 Modification to decellularisation method

Due to the swelling effect PBS has on tendon, alternative solutions were used during end-stage washes of the decellularisation process (Table 2.1, step 21 onwards). Ringers solution was used at 25% as it shares a similar potassium chloride concentration to PBS at quarter strength, while sharing the sodium chloride concentration at 100% (full strength). Further, this allowed to provide insight into the effect of salt/solute concentration on tissue swelling. Saline solution was used due to its clinical use during ACLR, sharing sodium chloride concentration with PBS. For solution composition, refer to Table 3.1.

3.2.3.1 Preparation of decellularisation solutions

Solutions were prepared as detailed in section 2.2.2.1. Additional solutions required were prepared as follows.

Quarter strength Ringer's solution (2.25 g/L sodium chloride; 25%)

Two Ringer's tablets were dissolved in 1 L of deionised water. It was stored for no longer than one month.

Full strength Ringer's solution (9 g/L sodium chloride; 100%)

Four Ringer's tablets were dissolved in 1 L of deionised water.

Saline solution (9 g/L sodium chloride)

Saline solution for irrigation (Baxter) was autoclaved (1 L).

3.2.3.2 Modified decellularisation method

The decellularisation protocol was carried out as described in Section 2.2.2.2 until finishing the last PBS wash (Table 2.1, step 20) after peracetic acid sterilisation. From this point until the end of the protocol (Table 2.1, steps 21 – 23), alternative solutions were used for the last washes. These solutions are listed in Table 3.1. Temperature, agitation speed and time of each wash was carried out as detailed in Table 2.1.

Table 3.1: Alternative solutions to PBS used in end stage washes of decellularisation protocol.

Solution	**Contents (g/L)**	
Quarter strength (25%) Ringer's solution	Sodium chloride	2.25
	Potassium chloride	0.105
	Calcium chloride 6H2O	0.12
	Sodium bicarbonate	0.05
Full strength (100%) Ringer's solution	Sodium chloride	9.0
	Potassium chloride	0.42
	Calcium chloride 6H2O	0.48
	Sodium bicarbonate	0.2
Saline Solution	Sodium chloride	9.0

3.2.4 Tissue swelling after decellularisation

Tissue dimensions for each specimen were taken at two different time points (see below) during the decellularisation process. Measurements were carried out using digital callipers, measuring tendon width and thickness in triplicate in each region along the length of each specimen (Figure 3.1), totalling 9 measurement for each specimen. The first measuring time point was immediately before placing the pSFTs in the first hypotonic wash (see Table 2.2.2.2, step 1). This did not require aseptic conditions. The second measuring time point was after the week long solution wash, before storing of the specimens (see Table 2.2.2.2, step 23). Following aseptic technique, measurements were performed within the safety cabinet, having previously sterilised the callipers to minimise tissue contamination. This was considered pSFT dimensions post-decellularisation. Swelling was therefore considered the change in width and thickness at the final time point, and comparisons were made between decellularisation groups.

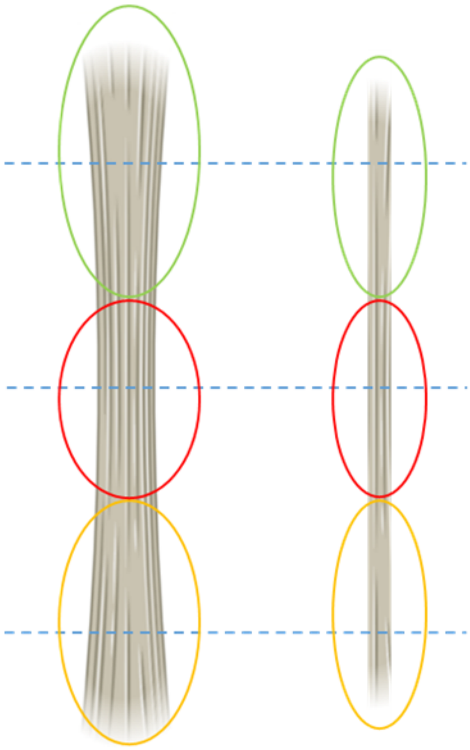

Figure 3.1: Representation of dimensional measurements taken for each pSFT during the decellularisation process.
Toe (orange), ankle (green) and middle (red) region of pSFT. Width measurements taken as depicted in the frontal plane (left) of the specimen and thickness measurements as represented in the sagittal plane (right) of the specimen. Created with Biorender.com.

3.2.4.1 Water uptake and swelling in native pSFTs

Preparation of solutions

All solutions were prepared as detailed in section 2.2.2.1. and 3.2.3.1, adding aprotonin and antibiotic as follows.

Amphotericin B and penicillin-streptomycin aliquots were thawed 10 min prior to use. Both (2 mL of each) were added to 100 mL of autoclaved solution. Sterile aprotonin (100 µL) was added in sterile conditions immediately before use.

Hydration method

To determine the effect of each solution (PBS, 25% Ringers, 100% Ringers, saline solution) on native pSFT swelling, a hydration experiment was conducted. Swelling was considered the change in width and thickness. This experiment would help find a relationship between the increase in weight/water uptake and tissue dimensions (width, thickness) over time, while hydrating in different solutions. Further, it would provide information on whether swelling was caused by the use of the solution itself, or if there was an effect of the decellularisation process and the solution used during the end-stage washes (PBS, 25% Ringers, 100% Ringers, 0.9% saline). Tissue dimensions were taken as described in Section 3.2.4. The first measurements were taken after tissue equilibration.

Prior to this, all tendons used (n = 3 for each group) were stored wrapped in PBS soaked filter paper at − 20 °C. This presented the same storage conditions of tendons subjected to decellularisation, minimising variability where possible. It also facilitated a baseline and consistent hydration level across all tendons. The tissue was then placed into 150 mL sterile pots, which had been previously weighed. They were then weighed with the tissue content. The dry weight of the tissue was calculated by subtracting the pot weight from the weight of the pot with the tissue content. The appropriate solution (100 mL) was added to each pot and left incubated at 37 °C and 240 rpm, similarly to the washes carried out during decellularisation. A solution change was conducted after 24 h, 48 h, and 1 week. At each time point, tissue dimensions and wet weight were measured. Water uptake was calculated using Equation 3.1, where dry weight was taken as initial baseline weight and wet weight changed according to each time point.

$$\%Water\ uptake = \frac{W_w - W_d}{W_d} * 100 \tag{3.1}$$

3.2.5 Biochemical assessment of matrix components

Quantification of GAGs, collagen and denatured collagen were carried out as per Chapter 2, section 2.2.4.

3.2.6 Thermal stability of porcine superflexor tendon

Assessment of thermal stability was conducted as detailed in Chapter 2, section 2.2.5.

3.2.7 Qualitative histological analysis

Histological techniques were conducted as detailed in Chapter 2.

3.2.7.1 Cryosections image analysis

ImageJ software was used to carry out image analysis on cryosections of native and decellularised pSFT. Images of the medial fascicular matrix areas of the tissue section at the same magnification from both groups were used. Briefly, images were binarised, making all tissue pixels black and all background white. The area of black and white pixels was obtained to calculate their ratio. Tissue to white space ratio was reported for both groups to assess the openness of the matrix in a quantitative manner.

3.2.8 Collagen crimp analysis

Image analysis was conducted on sections stained with Sirius Red, using ImageJ software (National Institutes of Health, USA; version 1.53e). Images were converted to grayscale (16 bit), ensuring the option of scale when converting was set up. Images were rotated at various angles depending on the original direction of the image using the transform function. This was simplified given the preview option in combination with an existing grid (Figure 3.2a). Intensity information was analysed by hovering the cursor over a given area in the image, as the pixel intensity is provided on the toolbar (Figure 3.2b). Bands of the least pixel intensity (< 45) were determined as a peak or trough. Sectioned tendon commonly presents an open matrix, facilitating observational analysis. Thus, it was concluded a streak was either a peak or a trough depending on the direction of the wavy tissue contrasted against the background (Figure 3.2c). In addition, the invert function was used to corroborate the observations made were accurate, indicative of peaks and troughs of the crimp pattern (Figure 3.2d).

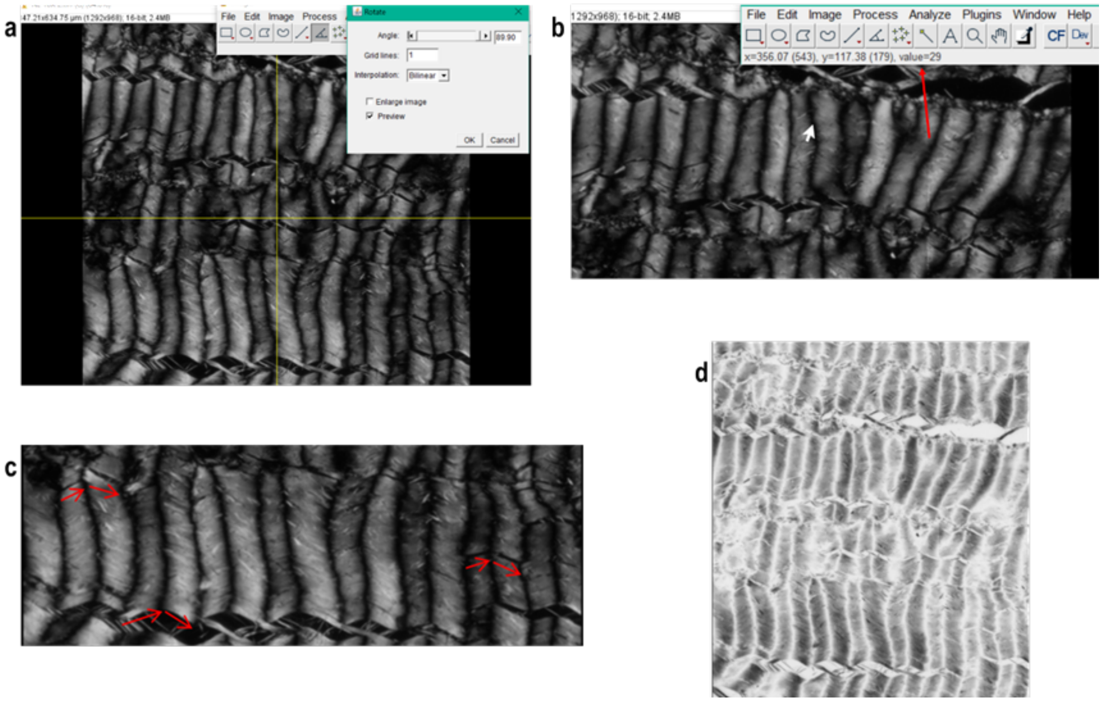

Angle: 89.90
Grid lines: 1
Interpolation: Bilinear
☐ Enlarge image
☑ Preview

x=356.07 (543), y=117.38 (179), value=29

Figure 3.2: First stage of image analysis using ImageJ software.
Images of tendon sections were prepared following a simple process to ensure consistency between subsequent steps of the quantitative analysis. This process briefly consisted of rotation (a), identification of peaks and troughs (b & c) and validation of direction of crimp pattern (d).

Each image was divided into three areas, and a crimp pattern was chosen within each area, subsequently referred to as the region of interest (ROI). The image was then exported to Adobe Photoshop (version 22.0.0) to draw over the crimp pattern of the ROI, to ease subsequent quantitative analysis. Drawing was carried out using the curvature pen tool, adjusting the wave morphology as much as possible (Figure 3.3). A total of seven peaks was drawn for each ROI. This was conducted in triplicate, to ensure measurements did not vary greatly within the same ROI. Images were then exported to ImageJ again, where measurements would be taken for ROI crimp parameters.

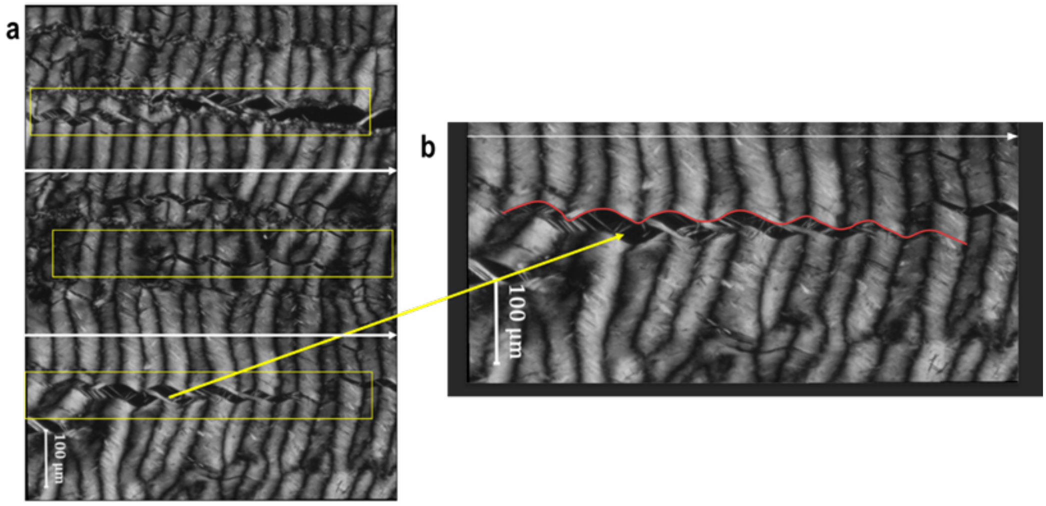

Figure 3.3: Second stage of image analysis using Adobe Photoshop
Areas of tissue section for crimp pattern analysis. a) The section image, divided into three areas (separated by white arrows), with a region of interest (ROI) within each area in yellow; b) drawing of the crimp pattern of interest in red, carried out using Adobe Photoshop, of a single ROI (bottom with yellow arrow).

The crimp morphology parameters of interest were period, angle and amplitude, allowing comparison between tendons decellularised using standard and modified processes. Period was measured as the length between crimp peaks, obtaining seven values for each ROI. Measurements were then taken for the triplicates within each ROI, ensuring variability was not significantly different, but only six values selected from each area, giving a total of eighteen crimp period values for each tissue section. Amplitude was measured by drawing a straight line between troughs and measuring the length between the line and the crimp peak. This value was then divided by two, equivalent to half the peak to trough distance [264]. Again, this was compared to other crimp patterns within the same ROI before selecting values for each area. Finally, angle was measured with the angle tool by placing the first point on the peak, the second on the trough immediately to the left and the third as a straight line in direction to the trough immediately to the right. The same comparison within the ROI of each area was carried out before selecting angle values for each area. This analysis was conducted on three different tissue sections, i.e. different tendons, from each sample group. A schematic of how crimp parameters of interest were analysed is represented in Figure 3.4.

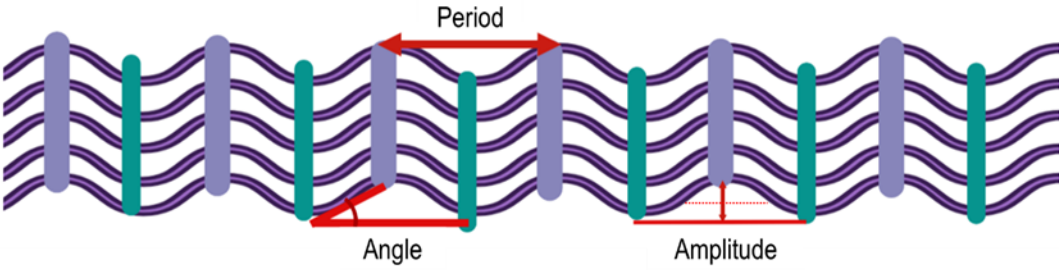

Figure 3.4: Graphical representation of crimp parameters
Wavy pattern of collagen in purple, representing waviness observed in Sirius red stained longitudinal sections of tendon. Peaks are represented in lilac, while troughs are represented in green. In red, representation of how crimp period, angle and amplitude were obtained using a combination of ImageJ and Adobe Photoshop software. Created with BioRender.com.

3.2.9 Mechanical characterisation

Mechanical characterisation was carried out as per Chapter 2, section 2.2.3.

3.2.10 Statistical analysis

Statistical analysis was carried out using GraphPad Prism (version 8, GraphPad software). Prior to analysis, data was checked for normal distribution using the Kolmogorov-Smirnov normality test. For comparing two means an unpaired Student's t-test was used. This was carried out on independent sample groups. For comparing the mean of multiple groups, a one-way ANOVA with Tukey post hoc test was conducted. For assessment of water uptake, the overall effects of solution, time and interaction between both factors were assessed through a two-way ANOVA and Sidak's correction for multiple comparisons. P values lower than 0.05 were deemed to be significant.

3.3 Results

3.3.1 Tissue swelling after decellularisation

Width and thickness tissue measurements of decellularised pSFT using modified processes are summarised in Table 3.2. Measurements of pSFT width and thickness prior to decellularisation showed no significant differences between groups, thus establishing consistency of preparation between specimens. Final tissue measurements could then be attributed to the effect of the solutions used during the decellularisation process, allowing to identify the solution causing the greatest swelling. Swelling was taken as the increase in width and thickness post-decellularisation. Width and thickness of decellularised groups showed maximum swelling in the PBS group, followed by 100% Ringers and saline groups. The tissue with smallest width and thickness post-decellularisation was 25% Ringers group. This modified group presented ~ 28% less width and ~ 50% less thickness compared to the standard PBS group.

Table 3.2: Gross tissue pSFT measurements (mm) before and after decellularisation using modified processes.

DC group	Pre-decellularisation	Post-decellularisation
PBS	10.37 ± 0.58	12.49 ± 0.56^{a}
	4.87 ± 0.17	6.63 ± 0.41^{d}
25% Ringers	10.41 ± 0.32	8.94 ± 0.48^{b}
	5.11 ± 0.39	3.35 ± 0.40^{e}
100% Ringers	10.61 ± 0.34	12.02 ± 0.40^{ac}
	4.94 ± 0.24	5.96 ± 0.29^{f}
Saline	10.45 ± 0.58	11.45 ± 0.27^{c}
	5.10 ± 0.39	5.74 ± 0.36^{f}

Data is presented as mean (n = 6) ± 95% CI, a total of 9 measurements were conducted along pSFT length. Width (top) and thickness (bottom) post-decellularisation were compared between groups using different solutions. Data were analysed using one-way ANOVA followed by Tukey's post hoc test. Groups that do not share the same superscript for width are significantly different. Groups that do not share the same superscript for thickness are significantly different.

3.3.1.1 Water uptake in native pSFTs

Measurements of pSFT width and thickness at time 0, representative of a consistent baseline hydration level showed no significant differences between groups. The width and thickness of pSFT hydrated in different solutions over time is presented in Figure 3.5. Width was compared across groups at each time point, showing no significant differences at time point 0. After only 24 h, there was a significant increase in the width of pSFT hydrated in PBS and saline compared to 25% Ringers. This occurred at each time point, demonstrating similar swelling profiles in pSFTs hydrated in PBS and saline solutions. Thickness was compared across groups at each time point, revealing no significant differences at 24 and 48 h, but a significant increase in thickness of pSFT hydrated in PBS and saline compared to pSFT hydrated in 25% Ringers (˜ 1 mm) after 1 week. All groups, except the 25% Ringers showed an increase at each time point.

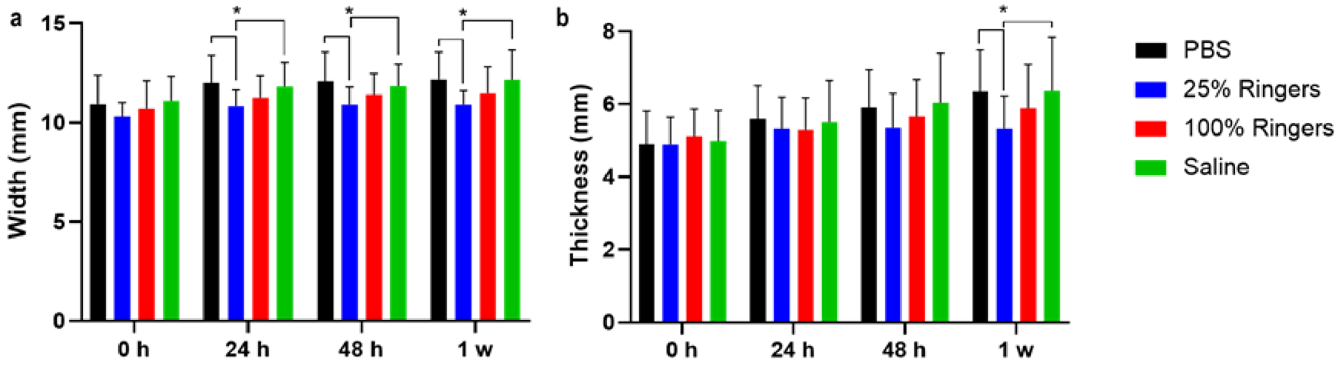

Figure 3.5: Width (a) and thickness (b) of native pSFT hydrated in different solutions over time.
No differences in tissue dimensions at timepoint 0 h, revealing consistent baseline hydration level. a) Significantly increased width for PBS and saline groups compared to 25% Ringers. b) No differences at 0 h, 24 h or 48 h. Significant reduction in pSFT thickness hydrated in 25% Ringers compared PBS and saline after 1 week. Data is presented as mean (n = 3) ± 95% CI, a total of 9 measurements were conducted along pSFT length. Data was analysed using one-way ANOVA followed by Tukey's post hoc test. * indicate significant difference between groups.

Using pSFT weight at different time points, water uptake was calculated (Table 3.3). A two-way ANOVA with the solutions and time as factors revealed only the solution had a significant effect. There was no significant interaction. The largest water uptake was observed in the PBS group after 24 and 48 h, exceeded only by the saline group at the 1 week time point. The group with least water uptake was the 25% Ringers group at all time points. Sidak multiple comparisons at each time point revealed a significantly lower water uptake for the 25% Ringers group compared to PBS and saline groups. No differences were found between 25% and 100% Ringers groups.

Table 3.3: Percent water uptake (%) of native pSFT hydrating in different solutions over time.

DC group	24 h	48 h	1 Week
PBS	65.93 ± 37.16^{a}	69.61 ± 14.14^{a}	58.41 ± 12.26^{a}
25% Ringers	27.03 ± 6.25^{b}	26.41 ± 4.75^{b}	23.74 ± 2.68^{b}
100% Ringers	$40.58 \pm 5.90^{a,b}$	$44.13 \pm 11.95^{a,b}$	$48.23 \pm 7.96^{a,b}$
Saline	58.43 ± 8.64^{a}	64.92 ± 1.60^{a}	75.17 ± 4.79^{a}

Data was calculated using equation 3, using time point 0 as dry weight. Data is presented as mean (n = 3) ± 95% CI. Data was analysed using a two-way ANOVA with Sidak's correction for multiple comparisons. Groups in each column that do not share the same superscript are significantly different

The isoelectric point of collagen lies between 7.2 – 7.8 [265, 266], whereby swelling of collagenous tissue increases the further the pH is from it. The pH of each solution was measured resulting in the pH of saline at 6.83, PBS at 7.35, 25% Ringers at 8.62 and 100% Ringers at 9.00. However, the most basic solution (100% Ringers) did not result in a significant increase in pSFT water uptake compared to PBS, which was the solution closest to the isoelectric point of collagen (Figure 3.5). Saline, with a pH close to the isoelectric point of collagen led to the highest water uptake, while 25% Ringers with a basic pH led to the lowest water uptake over time.

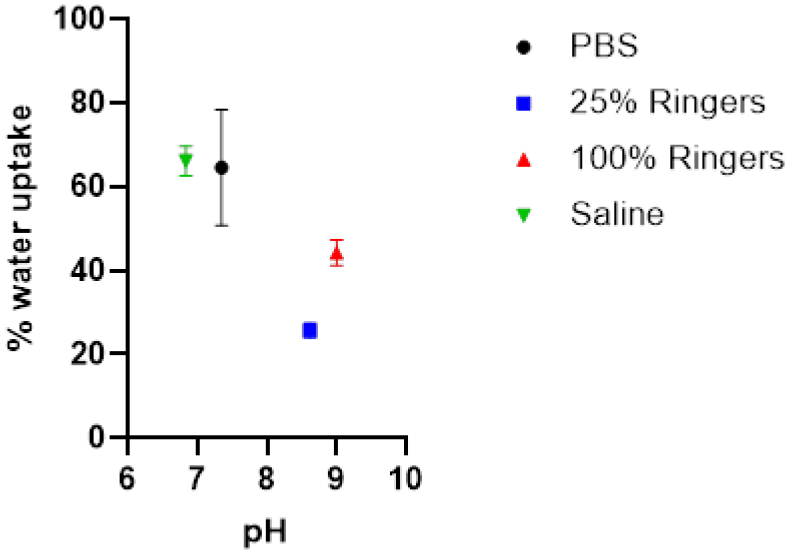

Figure 3.6: Water uptake of pSFT in solutions of different pH.
PBS (pH 7.35) as the solution closest to the isoelectric point of collagen resulted in considerable swelling of pSFT over time, similarly to saline (pH 6.83). 100% Ringers (pH 9.00), with a pH furthest from the isoelectric point of collagen did not present increased swelling. Data is presented as the mean ± 95% CI water uptake (%) of all time points.

3.3.2 Relative quantification of matrix components

No significant loss of GAGs occurred during any decellularisation process, independent of the solutions used in end-stage washes, as shown in Figure 3.7. GAG content was not statistically different between decellularised groups, and was not significantly different from native pSFT.

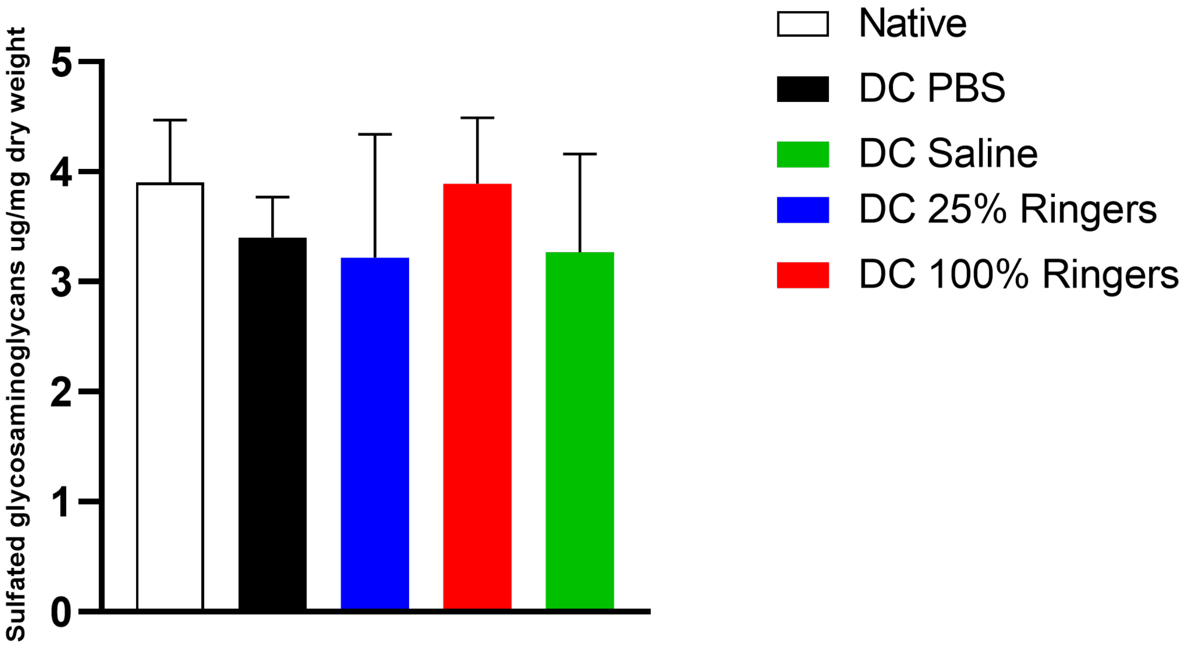

Figure 3.7: Relative sulfated GAG (ug of GAGs per mg of dry tissue weight) assay results for native and decellularised (DC) groups.
No significant difference between groups independent of solution composition. Data is presented as mean (n = 6) ± 95% CI. Data was analysed using one-way ANOVA followed by Tukey's post hoc test.

No loss of collagen content post-decellularisation as all groups showed no statistical reduction compared to native pSFT (Figure 3.8a). The saline group resulted in a significantly higher collagen content compared to all groups. Quantification of denatured collagen in decellularised groups showed no significant increase compared to native pSFT (Figure 3.8b), independently of the solution used during the decellularisation process. The sensitivity of this assay is given by the calibration curve conducted separately for each of the assays. Given the standard known concentrations used (see Table 2.4), it is capable of detecting hydroxyproline content between 0 and 50 µg/mL.

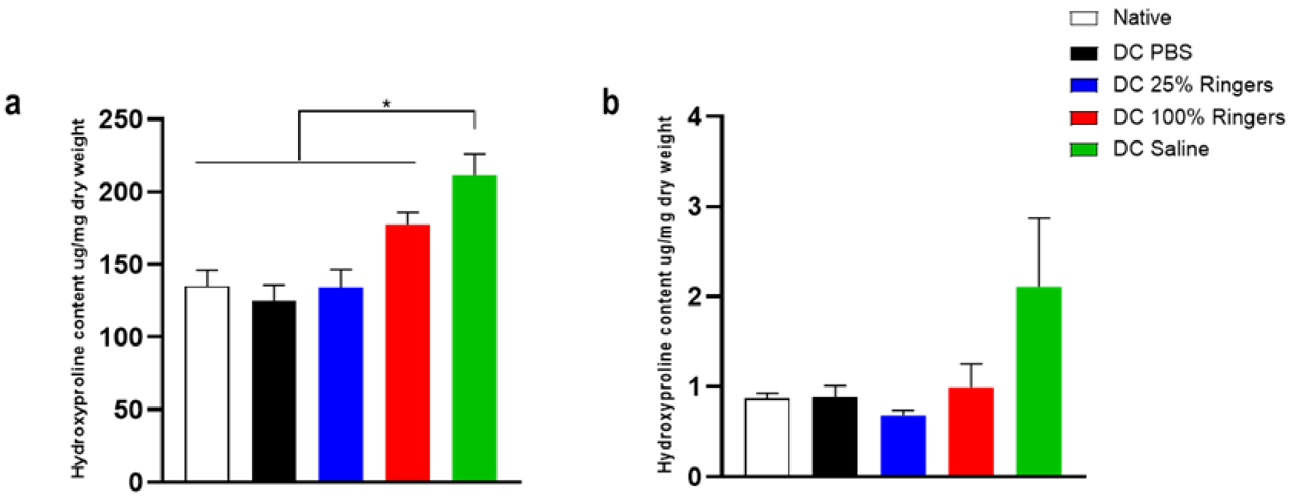

Figure 3.8: Relative collagen and denatured collagen content (ug of hydroxyproline per mg of dry tissue weight) assay results for native and decellularised (DC) groups.
a) Significant increase in collagen content of DC saline group compared to all other groups, while there are no statistical differences between collagen of remaining DC groups or when compared to native pSFT; b) No significant difference between native and DC groups. No significant difference between DC groups independent of solution composition. Data is presented as mean (n = 6) ± 95% CI. Data was analysed using one-way ANOVA followed by Tukey's post hoc test. * indicate significant difference between groups.

3.3.3 Thermal stability of superflexor tendon

Validation of transition temperature differences attributed to group treatment was achieved as there were no statistical differences between native specimens procured from different pSFT samples compared to specimens procured within the same pSFT. The same occurred with decellularised specimens, indicating potential differences between native and decellularised groups with modified methods could be attributed mainly to the effects of decellularisation on collagen, as opposed to inherent biological variability of pSFT tissue. This is represented in Figure 3.9.

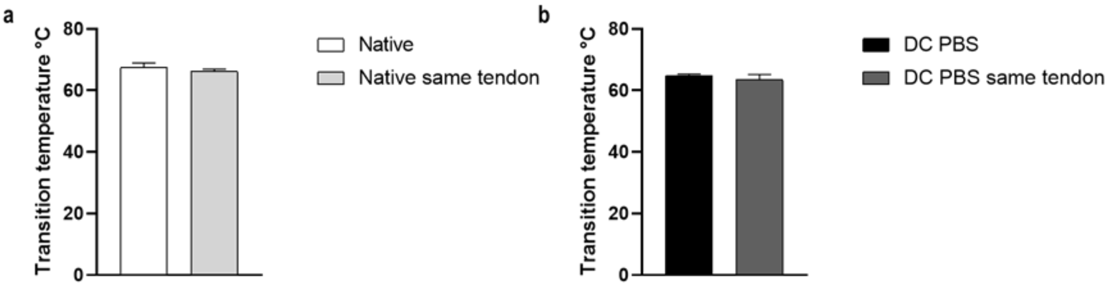

Figure 3.9: Thermal stability of native and decellularised groups comparing specimens obtained from different tendons and specimens obtained from same tendon.
No significant differences between native groups or decellularised groups. Data is presented as mean (n = 6) ± 95% CI. Data was analysed using an unpaired t-test.

The thermal denaturation scan of native and decellularised (PBS) specimens (Figure 3.10) showed an alteration in the peak shape of the thermogram, with a slight reduction in transition temperature of standard decellularised pSFT.

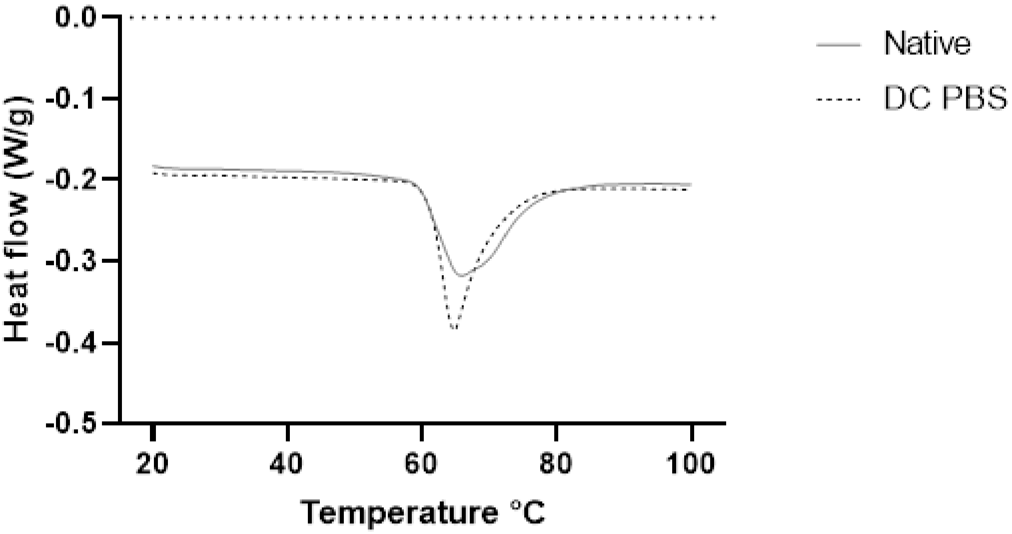

Figure 3.10: Thermal denaturation scans of native and decellularised (DC) pSFT.
DC specimens tested in PBS show a reduction in transition temperature compared to native specimens. Data is presented as mean (n = 6) for each group.

Transition temperature and enthalpy of denaturation are presented in Table 3.4, showing native pSFT as the tissue with the most stable collagen content. All decellularised groups showed a significant reduction in transition temperature. Enthalpy of denaturation was only significantly reduced for the decellularised specimens using 100% Ringers and saline compared to native specimens; however, no statistical differences were found between native and decellularised specimens using PBS and 25% Ringers.

Table 3.4: Characteristic thermal parameters of the denaturation of native and decellularised pSFT.

	Native	Decellularised			
		PBS	25% Ringers	100% Ringers	Saline
Transition temperature (°C)	67.44 ± 1.47^{a}	$64.75 \pm 0.54^{b,c}$	65.76 ± 0.83^{b}	65.34 ± 0.87^{b}	63.61 ± 0.41^{c}
Enthalpy (J/g)	19.36 ± 1.08^{a}	$18.32 \pm 1.68^{a,b}$	$16.66 \pm 1.2^{a,b}$	15.31 ± 2.01^{b}	15.48 ± 3.2^{b}

Data are presented as means (n = 6) ± 95% CI. Groups in each row that do not share the same superscript are significantly different.

3.3.4 Histological evaluation

3.3.4.1 H&E staining

Images of native sections (Figure 3.11A & C) showed characteristic cell nuclei stained purple/blue, within a pink stained extracellular matrix. Cell distribution was a combination of individual cells throughout the matrix, with some cell aggregation or clusters where endotenon would surround fascicular matrix (black arrows). The standard process of decellularisation (using PBS) revealed a pink extracellular matrix with no cells or cellular debris (Figure 3.11 B & D). This suggests the decellularisation process was effective in removing cellular material. The histoarchitecture of native and decellularised sections was similar, with a slightly more open matrix in decellularised section (B & D) compared to native sections (A & C).

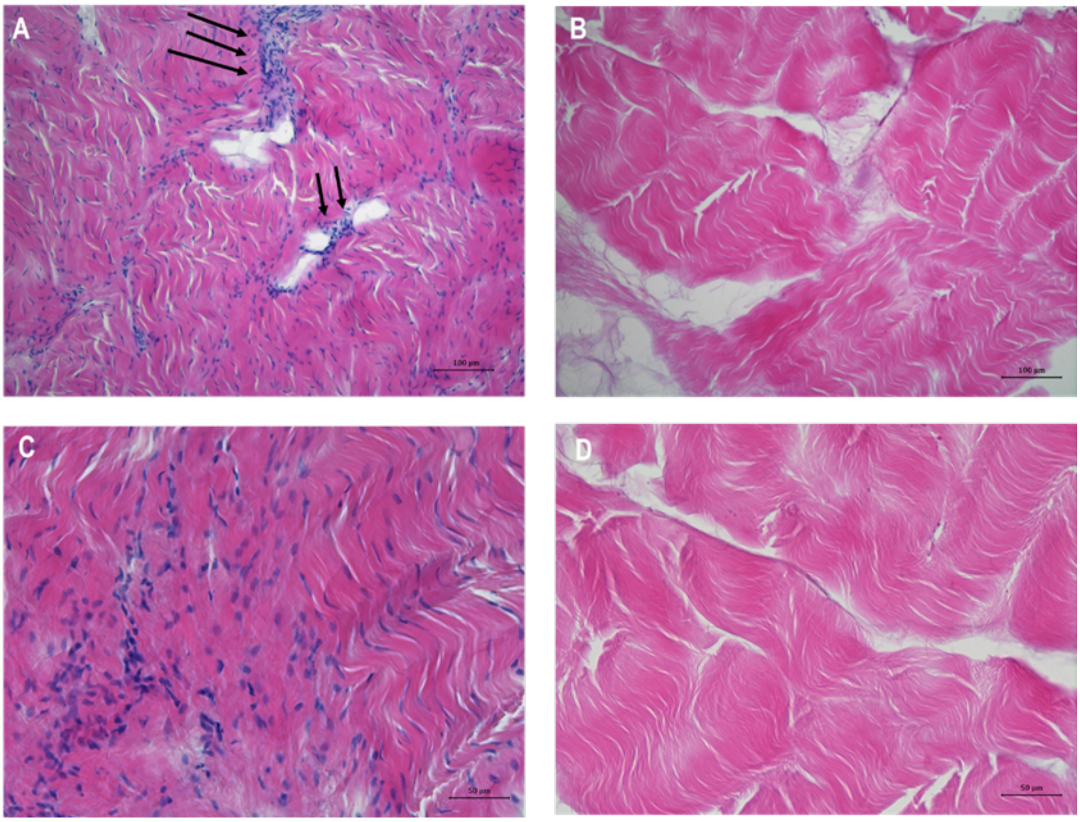

Figure 3.11: Representative micrographs of native and decellularised (DC) pSFT sections stained with H&E.
Transverse sections of native (A, C) sections show characteristic blue/purple nuclei, conglomerating mainly in endotenon channels (arrows in A). DC sections (B, D) with PBS show no visible nuclei or cellular debris, even at higher magnification (D). Images (A, B) were taken at 100x magnification (scale bar 100 µm), while images (C, D) were taken at 200x magnification (scale bar 50 µm).

The effectiveness of modified decellularisation processes was assessed using H&E staining of NBF fixed, wax embedded pSFT sections. There were no cells or cellular material in decellularised sections using 25% Ringers (Figure 3.12 A & B) 100% Ringers (Figure 3.12 C & D) or saline solution (Figure 3.12 E). The native pSFT section (Figure 3.12 N) showed characteristic blue/purple staining of cell nuclei, which aggregate where endotenon surrounded fascicle structures (black arrows). The IFM channels, clearly visible in all decellularised sections (A – E), showed no substantial cellular debris. The histoarchitecture of decellularised sections showed a more open matrix compared to native tendon (N). Further, sections of tissue decellularised using 25% Ringers (A & B) and saline solution (E) show a similar matrix, while decellularised sections using 100% Ringers (C & D) appeared slightly less open, more similar to native sections (N).

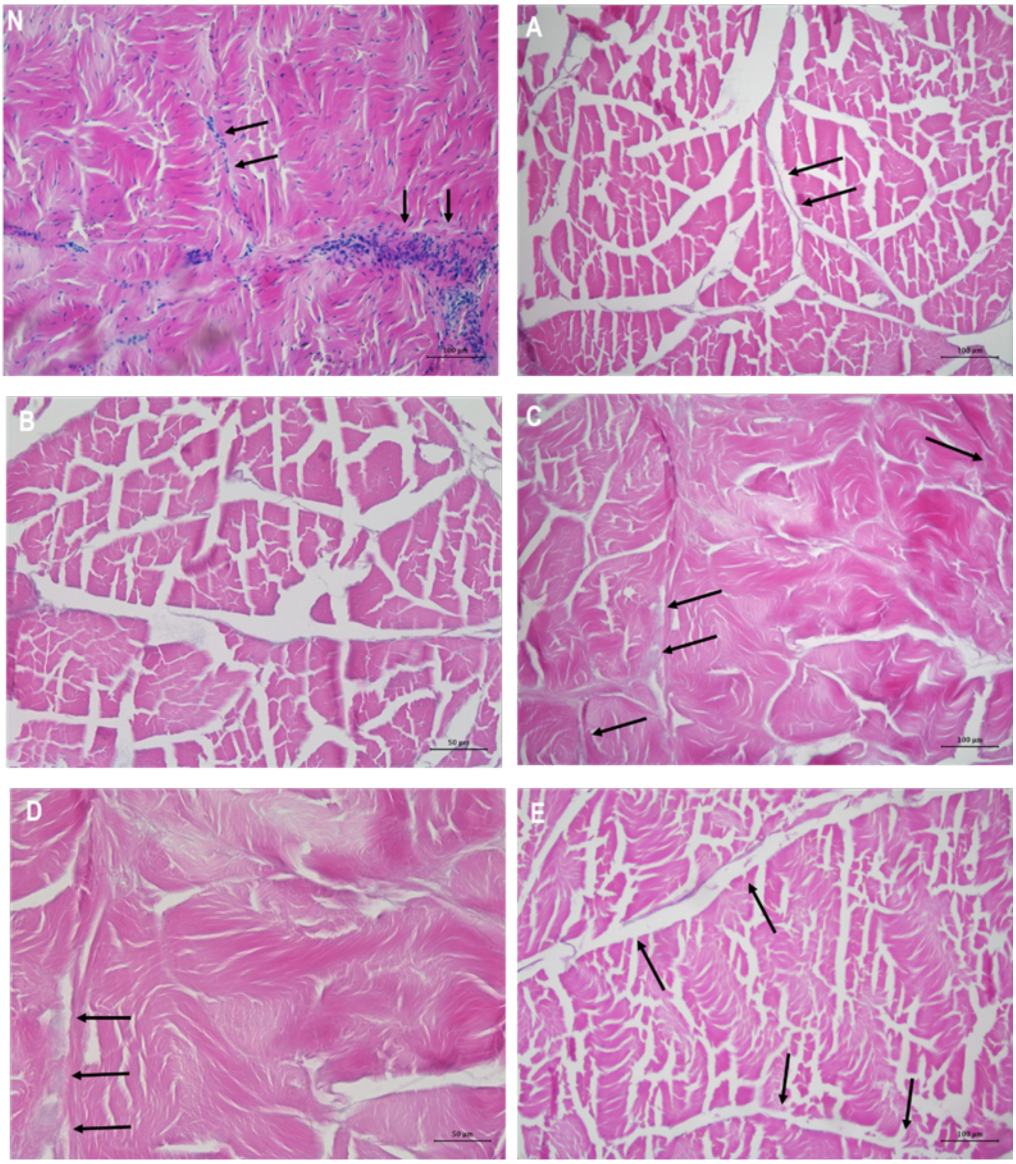

Figure 3.12: Representative micrographs of native and decellularised (DC) pSFT sections stained with H&E.
Transverse sections of native (N) pSFT to facilitate comparison with characteristic blue/purple nuclei, conglomerating in endotenon channels (arrows). DC sections (A - E) using modified processes show no visible nuclei or cellular debris in endotenon channels (arrows). DC with 25% Ringers group (A, B) show more open matrix compared to DC with 100% Ringers group (C, D). DC with saline group (E) show similar matrix architecture to DC 25% Ringers group. Images (A, C, E, N) were taken at 100x magnification (scale bar 100 µm), while images (B, D) were taken at 200x magnification (scale bar 50 µm).

Figure 3.13 shows native pSFT cryosections stained with H&E, with a fully preserved peritenon (Figure 3.13 A – C) and dense fascicular matrix (Figure 3.13, D – F). Cellular distribution was more apparent, both throughout the fascicular matrix and endotenon. Cellularity was denser and more organised toward the periphery of the pSFT, along the epitenon, while clusters were observed in areas surrounding fascicle structures (IFM). Fascicle substructures were observed (Figure 3.13 B), with a less open matrix compared to NBF fixed sections (Figure 3.11 A, C & 3.16 N).

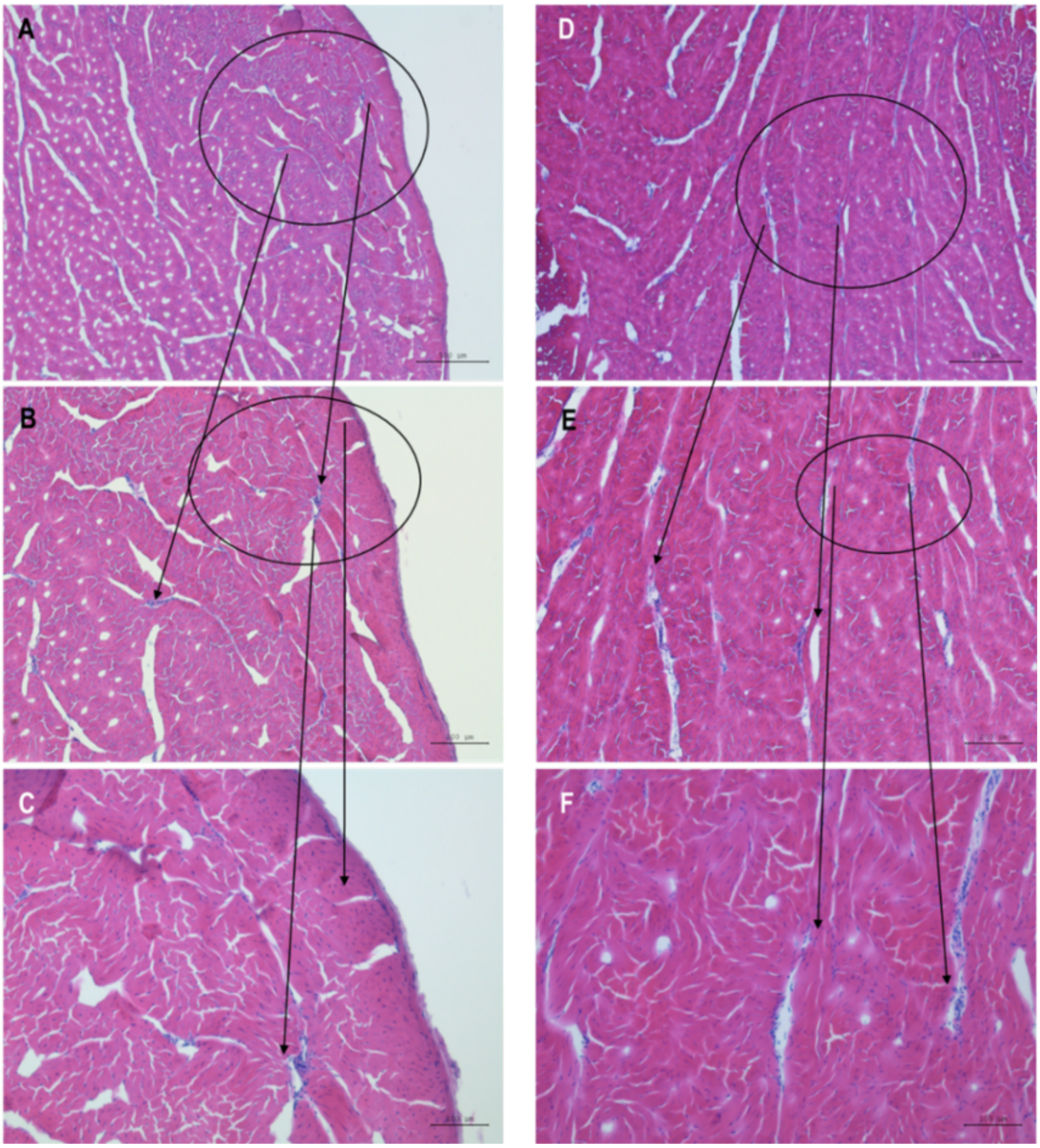

Figure 3.13: Representative micrographs of native pSFT cryoembedded sections stained with H&E.
Transverse sections of peritenon region (A – C) and fascicular matrix (D – F). Circles and arrows show the area that was magnified. Tendon histoarchitecture appears unaffected by cryoembedding and cryosectioning, showing a less open matrix compared to NBF fixed and wax embedded sections stained with H&E. Cells appear distributed throughout the matrix, as well as conglomerated along the epitenon. Cells cluster in endotenon channels. Images (A & D) were taken at 25x magnification (scale bar 500 µm); images (B & E) were taken at 50x magnification (scale bar 100 µm); images (C & F) were taken at 100x magnification (scale bar 50 µm).

Figure 3.14 shows decellularised pSFT cryosections stained with H&E, showing a fully preserved peritenon (Figure 3.14 A & B). The matrix (Figure 3.14 C & D), though more open compared to native cryosections (Figure 3.13), appeared less open compared to decellularised NBF fixed sections (Figure 3.12). The openness of pSFT matrix was more apparent toward the periphery (A & B) compared to the fascicular matrix (C & D). Cells were removed during the decellularisation process, with no purple/blue staining throughout the matrix, especially evident along the peritenon region (B), compared to the cellularity observed in native cryosections (Figure 3.12, A – C). There was minimal cellular debris in the matrix (Figure 3.14 D), mainly occurring in IFM areas, while no cellular debris was observed on the periphery of the tissue.

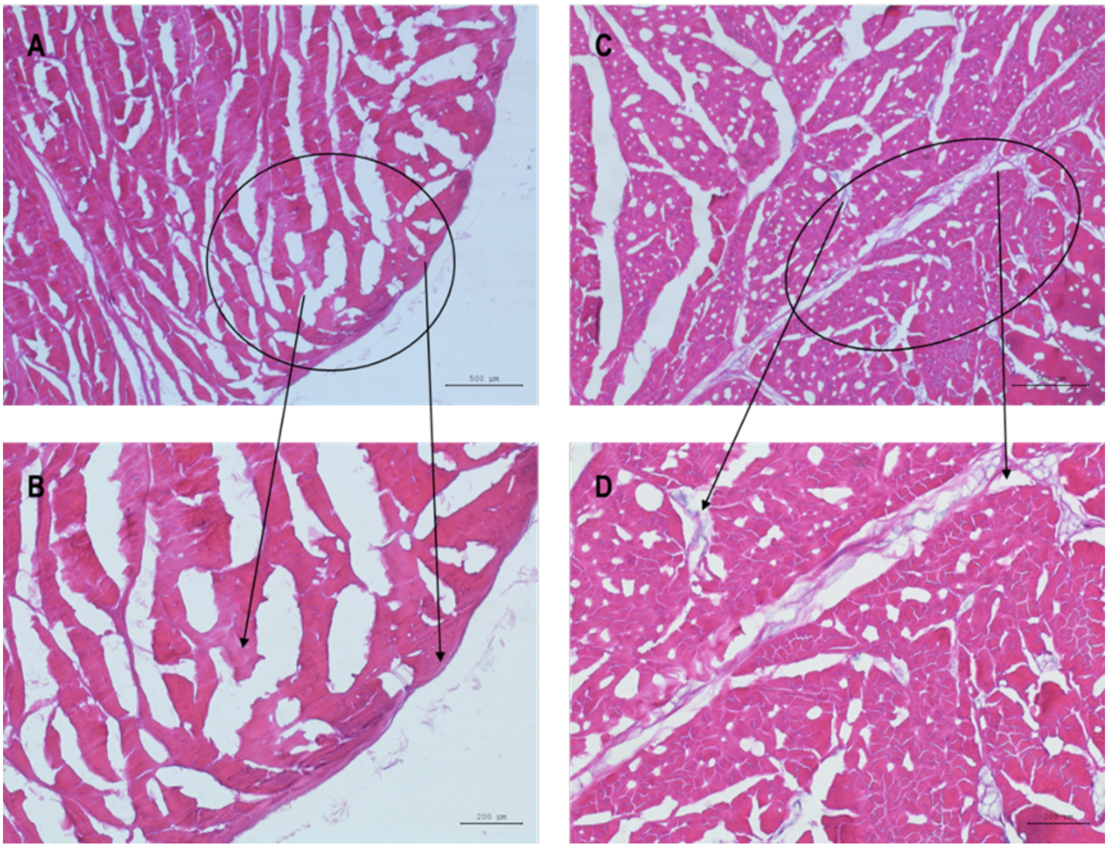

Figure 3.14: Representative micrographs of decellularised (DC) pSFT cryoembedded sections stained with H&E.
Transverse sections of DC peritenon region (A & B) and DC fascicular matrix (D & E). Circles and arrows show the area that was magnified. Tendon histoarchitecture shows a more open matrix compared to native cryoembedded sections. However, matrix histoarchitecture appears more dense compared to NBF fixed and wax embedded DC sections stained with H&E. No cells throughout the fascicular matrix or along the epitenon. Some cellular debris appears purple mainly in IFM channels (D). Images (A & D) were taken at 25x magnification (scale bar 500 µm); images (B & E) were taken at 50x magnification (scale bar 200 µm).

The tissue to white space ratio of decellularised matrix in cryosections was significantly reduced ˜ 27 % compared to its native counterpart, as presented in Figure 3.15.

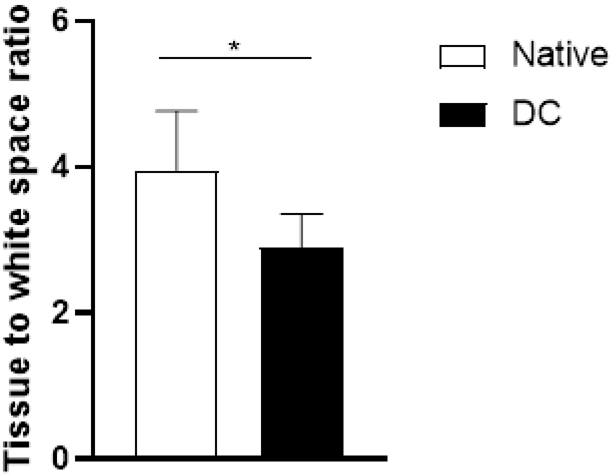

Figure 3.15: Tissue to white space ratio of native and decellularised (DC) pSFT cryosections.
Significantly reduced ratio for DC cryosections, indicating a more open matrix compared to native pSFT. Data are presented as means (n = 6) ± 95% CI. Data were compared using an unpaired Student's t-test, asterisk indicates significant difference between groups.

3.3.4.2 DAPI staining

Native sections (Figure 3.16 A) showed clearly stained nuclei fluorescing across the tissue matrix. Cell distribution corresponded with H&E stained sections (Figure 3.11 & 3.17), with individual nuclei throughout the matrix, with some cell clusters organised along IFM channels (Figure 3.16 A, white oval). The standard process of decellularisation, using PBS (Figure 3.16 B), revealed an absence of nuclei throughout the tissue matrix, with no evidence of fluorescence.

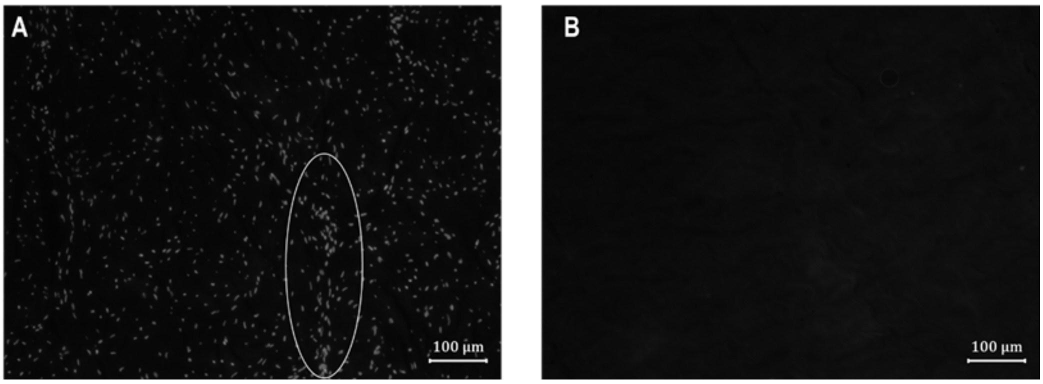

Figure 3.16: Representative micrographs of native and decellularised (DC) pSFT sections stained with DAPI.
Significantly reduced ratio for DC cryosections, indicating a more open matrix compared to native pSFT. Data are presented as means (n = 6) ± 95% CI. Data were compared using an unpaired Student's t-test, asterisk indicates significant difference between groups.

DAPI staining of decellularised tissue using modified methods showed a lack of nucleic acids and viable cell nuclei, with no fluorescence throughout tissue matrix (Figure 3.17 A – C). This is evident when comparing to native tissue (Figure 3.17 N).

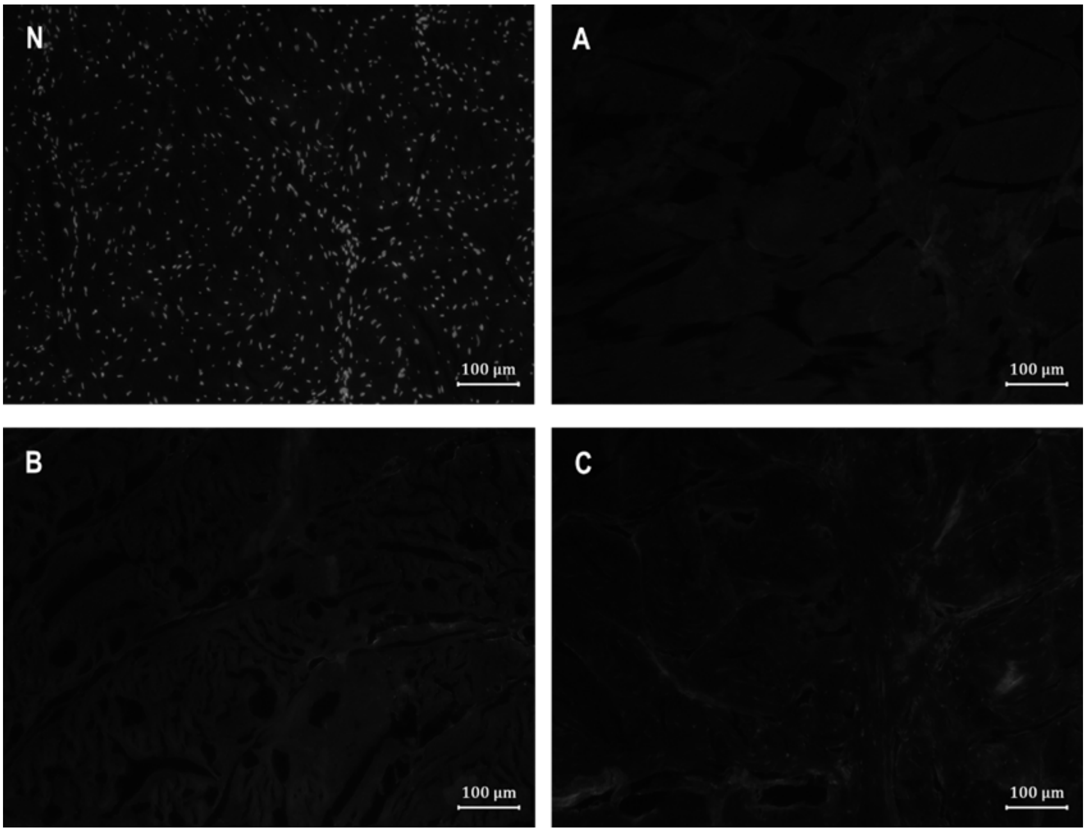

Figure 3.17: Representative micrographs of modified decellularised (DC) pSFT sections stained with DAPI.
Transverse sections of native (A) section to facilitate comparison with characteristic fluorescent nuclei. Decellularised (DC) sections (A – C) using modified processes show no fluorescence. DC with 25% Ringers (A), 100% Ringers (B) and saline (C) show no signs of cell nuclei. Images were taken at 100x magnification (scale bar 100 µm).

3.3.4.3 Alcian blue staining

Transverse sections of native pSFT (Figure 3.18 A – C) showed differences in staining colour and intensity within the same batch (A & B) as well as batch to batch variation (C). While both (A & B) showed some GAGs mainly located near endotenon channels, there was less presence in (A) compared to (B), while the matrix appeared a more intense purple in (A). Native section (C) showed an abundant presence of GAGs distributed throughout the fascicular matrix, as well as increasingly towards the surrounding endotenon area. This section also revealed cell structures, whereas (A & B) showed no cellular presence. Decellularised sections (Figure 3.18 D & E) showed similar shades of blue and purple throughout the fascicular matrix, making GAG presence and matrix staining indistinguishable. There was no presence of cellular material. The histoarchitecture was more open compared to native sections (A – C), yet no other similarities were observed between groups.

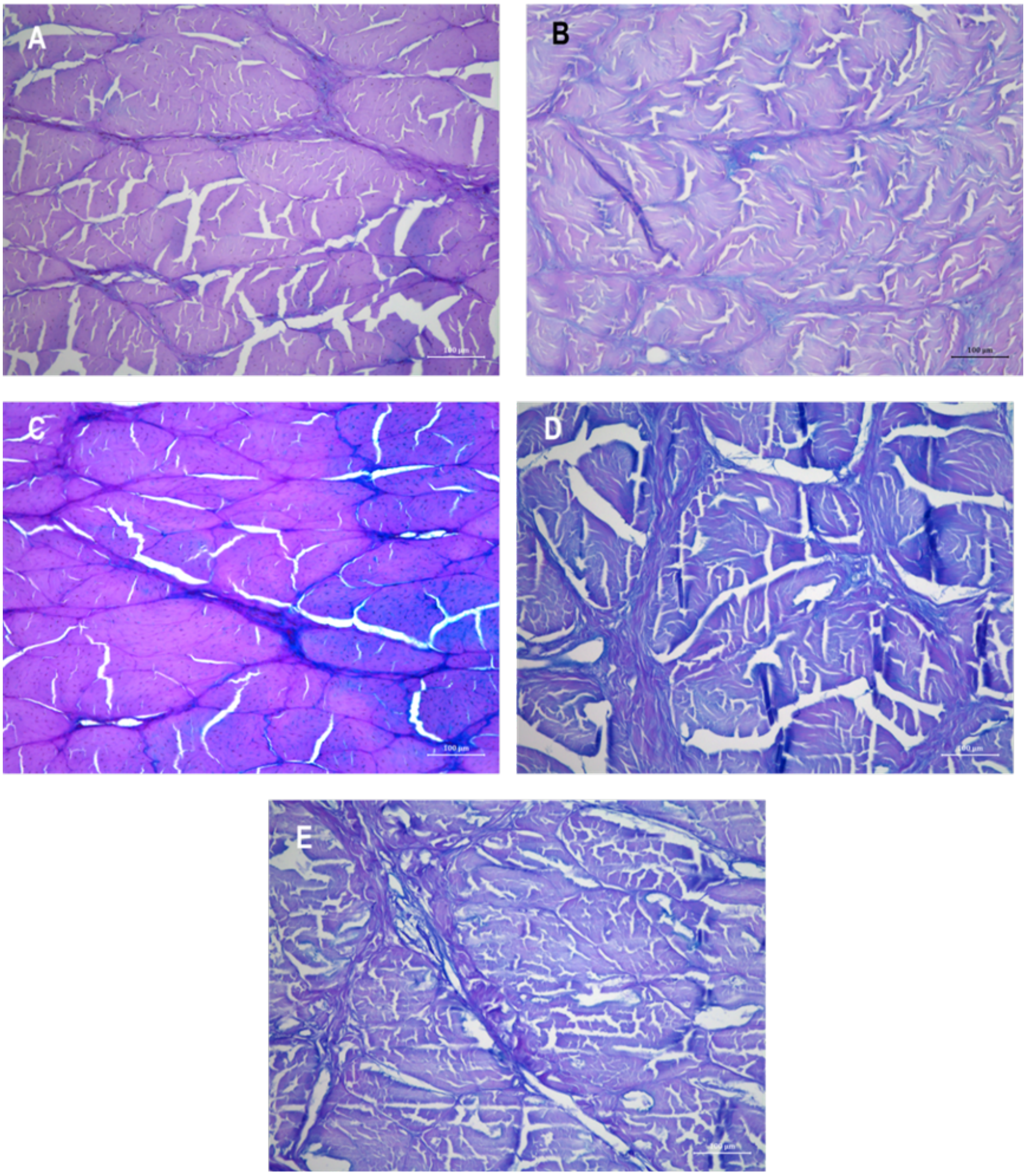

Figure 3.18: Representative micrographs of native and decellularised (DC) pSFT sections stained with Alcian blue.
Native sections show different tones of purple and blue staining within the same staining batch but different sections (A & B). Evidence of blue GAGs distributed throughout the matrix, while aggregating near IFM channels in (B), but almost no blue staining in (A). Native sections stained separately (C) show a different distribution of blue GAGs, with strong blue staining along IFM channels, while also throughout the fascicular matrix. Cells also appear visible in (C). DC sections (D & E) show similarity between tones of purple and blue, making it hard to distinguish between GAGs and matrix architecture. Stain appears to bind to denser areas of tissue section, presenting as streaks. No similarity between DC and native sections. Images were taken at 100x magnification (scale bar 100 µm).

Native longitudinal sections (Figure 3.19 A & C) showed a dense purple matrix with dark blue GAGs throughout the matrix, increasing towards the peritenon (A, bottom). The characteristic wavy pattern of collagen or crimp was observed throughout native matrix architecture, especially at a higher magnification (C). Collagen fibrils were in close proximity to one another. GAGs were located between crimp structures. Dense GAG content was observed in the form of thick blue streaks, evenly spaced out (Figure 3.19 C, white arrows). There was also evidence of GAGs between them. Decellularised sections (Figure 3.19 B & D) revealed unspecific binding of the stain to the matrix, making it difficult to differentiate GAGs from the counterstain. An apparent higher abundance of GAGs was seen in (B) compared to native sections (A & C). The matrix of decellularised pSFT (D) showed a similar alignment of GAGs between collagen fibrils compared to native sections, albeit the denser localisation of GAGs seen in (C) was lost. Immediacy between collagen was reduced, resulting in increased interfibrillar spacing.

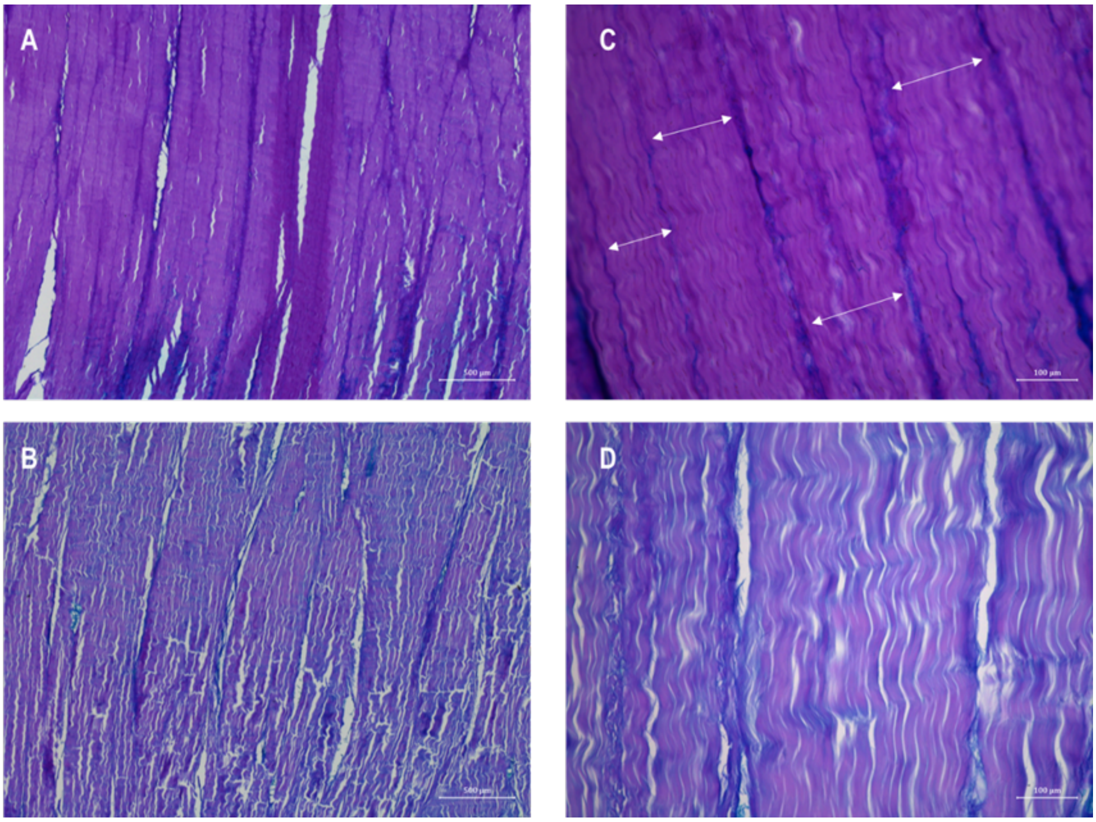

Figure 3.19: Representative micrographs of native and decellularised (DC) pSFT sections stained with Alcian blue.
Longitudinal sections of native (A & C) and DC (B & D) pSFT show different tones of purple within same staining batch. Matrix architecture appears more dense in native sections compared to a more open matrix in DC sections. Blue staining longitudinally along collagen arrangement, with an increase in apparent GAGs towards the peritenon region of native pSFT (A). Staining of (B & D) shows unspecific binding of the blue dye, accumulating on collagen crimp peaks and along interfascicular spaces. Images (A & B) were taken at 25x magnification (scale bar 500 µm), while images (C & D) were taken at 100x magnification (scale bar 100 µm).

3.3.4.4 Safranin O/Fast green staining

Safranin O was used as an alternative method for GAG staining, with a more optimal counterstaining of pSFT matrix. There were no differences in staining intensities of native and decellularised sections, showing a blue/green matrix with pink/red GAGs (Figure 3.20). Native sections (Figure 3.20 N) showed an abundant presence of GAGs throughout the matrix. Fascicle structures were identified in native sections (N) delineated by the a denser cell population (black arrows), while pink/red cells were observed throughout the matrix. Decellularised sections (Figure 3.20 A – D) showed no cell nuclei, while GAGs were distributed throughout the matrix with evidence of a higher GAG content toward areas where IFM surrounded the fascicular structures. This was also observed in Figure 3.18 and 3.19. The histoarchitecture of decellularised sections was consistently more open compared to native sections. Fascicle structures were preserved best in the group which used 25% Ringers (C), some shown with blue ovals. The PBS group (A) showed a similar matrix to the saline group (D), whereas the groups using 25% (C) and 100% Ringers (B) also showed likeness in matrix architecture.

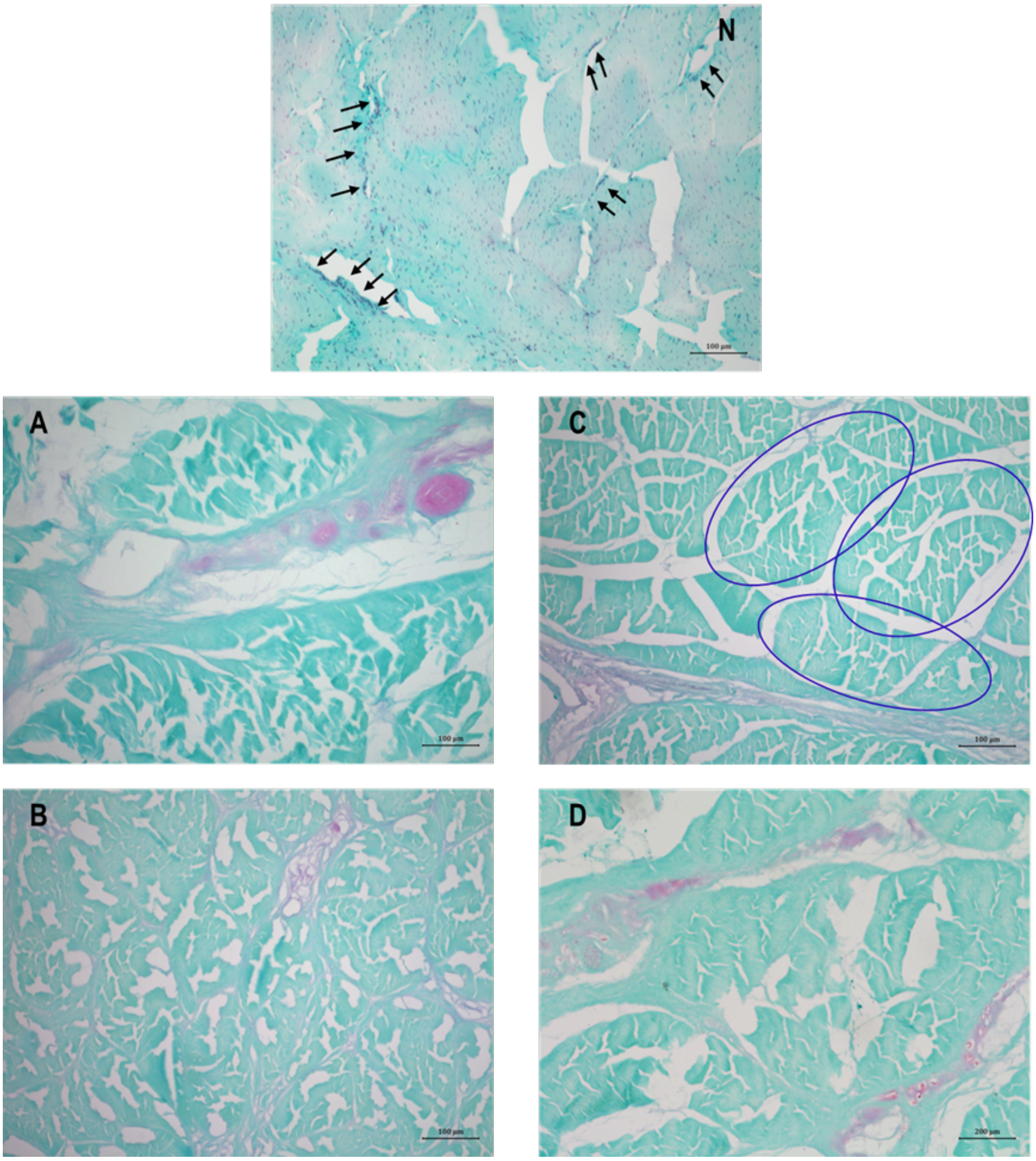

Figure 3.20: Representative micrographs of native and decellularised (DC) pSFT sections stained with safranin O/fast green.
Transverse sections of native (N) pSFT to facilitate comparison, showing pink-red GAGs throughout the matrix, delineating fascicle structures (black arrows). Purple cells apparent. DC sections (A – D) using modified processes show pink-red GAGs throughout a more open matrix, with no evidence of cellular material. DC with 25% Ringers (C) and 100% Ringers (B) show similar openness of matrix, while DC with PBS (A) and saline (D) show similar matrix architecture. DC with 25% Ringers (C) show preserved fascicle structures (blue ovals). Image (D) was taken at 50x magnification (scale bar 200 µm), while images (N, A – C) were taken at 100x magnification (scale bar 100 µm).

3.3.4.5 Sirius red staining

Transverse sections of native pSFT (Figure 3.21 A & D) showed a dense matrix, with clear substructure architecture, showing tendon fascicles (D) in a green colour and IFM in red.

Transverse sections of decellularised pSFT (Figure 3.22 A) showed a similar organisation of tissue matrix, with visible fascicular structures, yet less presence of IFM accompanied by increased interfascicular spacing. The openness of the matrix was evident there was more background (black) compared to native sections (Figure 3.21 A & D). Longitudinal sections of native (Figure 3.21 B & E) and decellularised (Figure 3.22 B – E) showed collagen fibre alignment was mainly retained post-decellularisation. There were differences in collagen spatial arrangement, with increased intrafascicular and interfascicular spacing in decellularised sections. Collagen crimp did not appear affected by decellularisation, with a similar pattern for the groups which used 25% Ringers (Figure 3.22 D), 100% Ringers (C) and saline solution (E). The standard decellularisation process using PBS produced a section with a more extended crimp pattern (B).

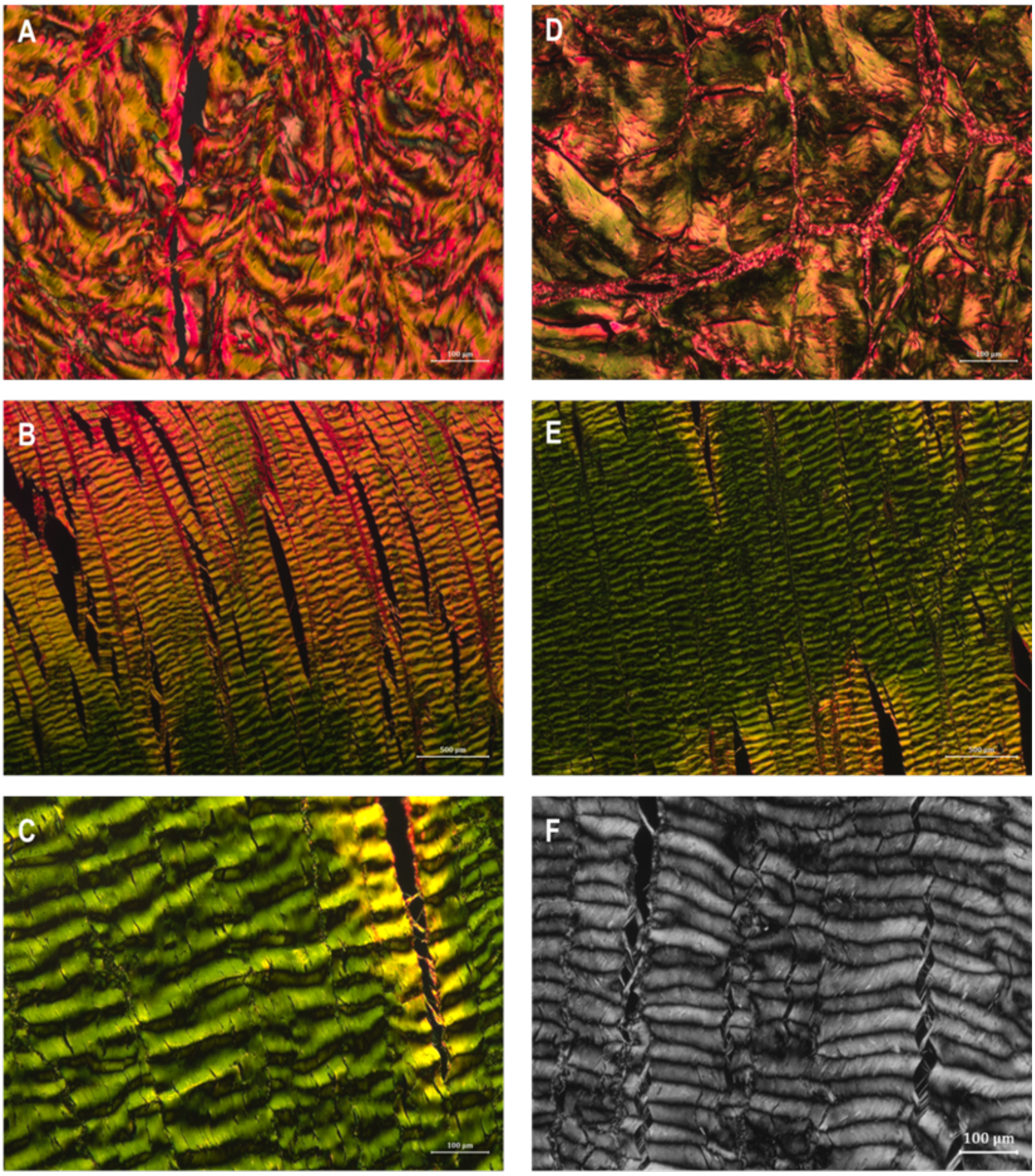

Figure 3.21: Representative micrographs of native pSFT sections stained with Sirius red.
Transverse (A & D) and longitudinal (B, C, E, F) sections of native pSFT. Fascicular matrix histoarchitecture is better showed in transverse sections, with evidence of abundant collagen throughout the matrix. Longitudinal sections show clear collagen crimping throughout the matrix (E, C, F) and towards the peritenon region (B). Imaging in black and white facilitates the identification of collagen crimp peaks and troughs (F). Images (B & E) were taken at 25x magnification; images (A, C, D, F) were taken at 100x magnification (scale bar 100 µm).

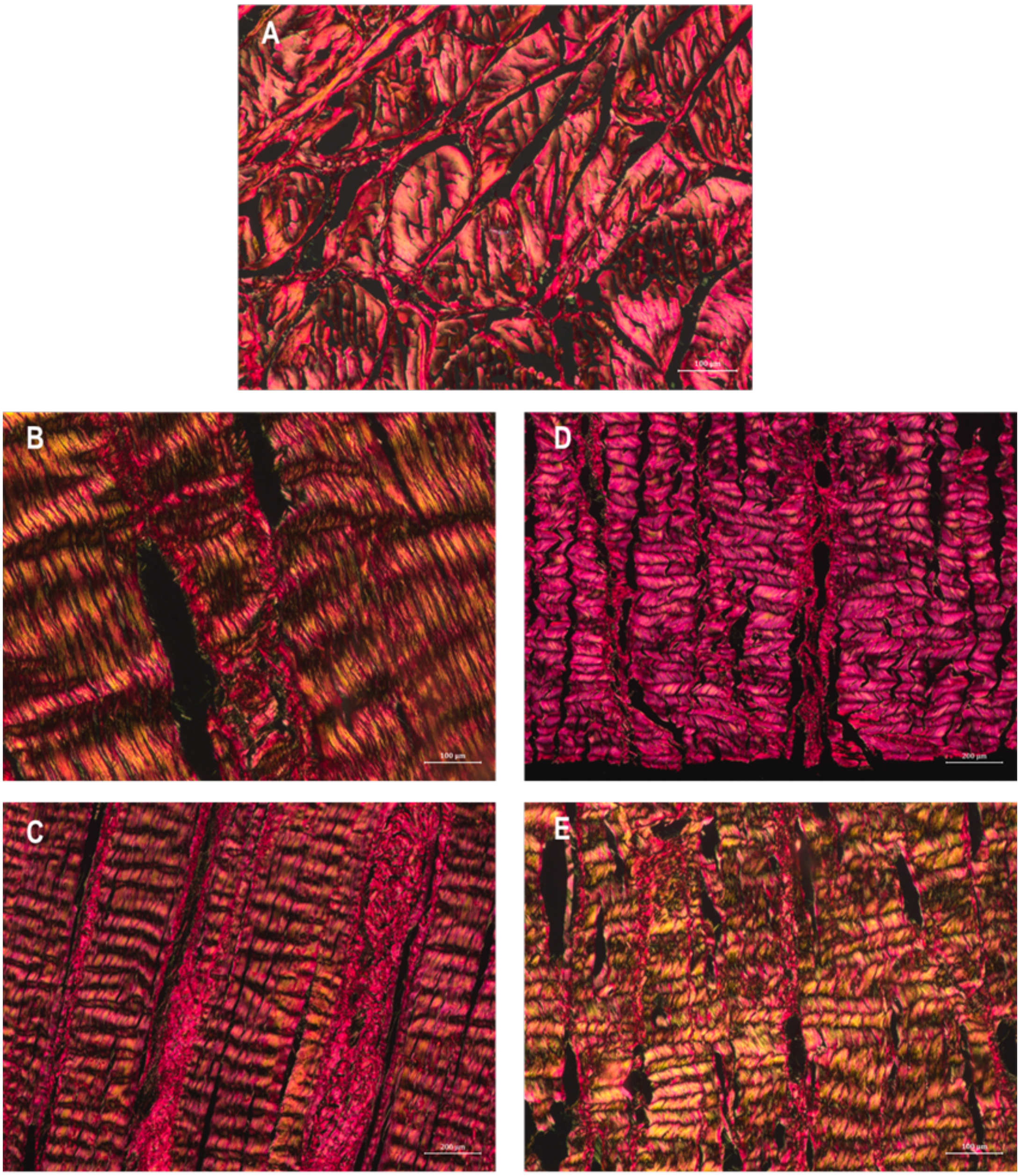

Figure 3.22: Representative micrographs of decellularised (DC) pSFT sections stained with Sirius red.
Transverse (A) and longitudinal (B – E) sections of DC pSFT show a more open matrix compared to native sections. Images (C – E) using modified processes show no apparent differences in matrix openness. DC with 25% Ringers group (D), 100% Ringers (C) and saline (E) show a similar crimp pattern throughout the matrix. DC with PBS (B) show a more extended crimp. Images (C & D) were taken at 50x magnification (scale bar 200 µm); images (A, B, E) were taken at 100x magnification (scale bar 100 µm).

3.3.5 Collagen crimp parameters

Crimp period was not significantly different in the decellularised PBS or 100% Ringers group, yet a significant increase was observed in the 25% Ringers and saline groups compared to native sections (Figure 3.23a). There were no significant differences in crimp amplitude of decellularised groups compared to native pSFT, with the exception of the 25% Ringers group. This group observed a statistically higher amplitude compared to native, 100% Ringers and PBS decellularised groups.

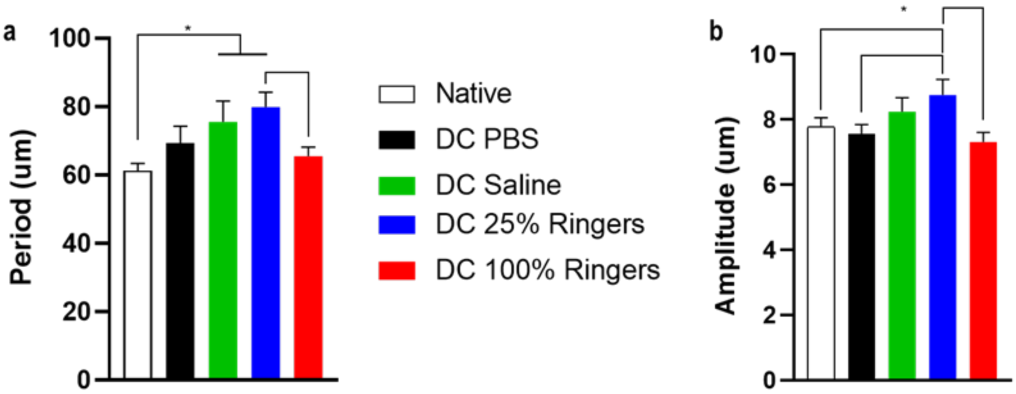

Figure 3.23: Collagen crimp parameters period and amplitude of native and decellularised (DC) groups.
a) significant increase in the period of DC saline and DC 25% Ringers group compared to native pSFT. DC 100% Ringers group period was significantly reduced compared to DC 25% Ringers, but not significantly different from native pSFT. DC PBS group showed no statistical differences in crimp period compared to native group; b) only DC 25% Ringers had a significant increase in crimp amplitude compared to native pSFT, while remaining DC groups showed no statistical difference compared to native group. DC 25% Ringers amplitude was also significantly higher than DC 100% Ringers and DC PBS groups. Data is presented as mean (n = 3) ± 95% CI. Data was analysed using one-way ANOVA followed by Tukey's post hoc test. * indicate significant difference between groups.

Crimp angle was significantly reduced for all decellularised groups, with a significant reduction in the 25% Ringers group compared to the standard decellularised group (PBS). No other differences were found across decellularised groups (Figure 3.24).

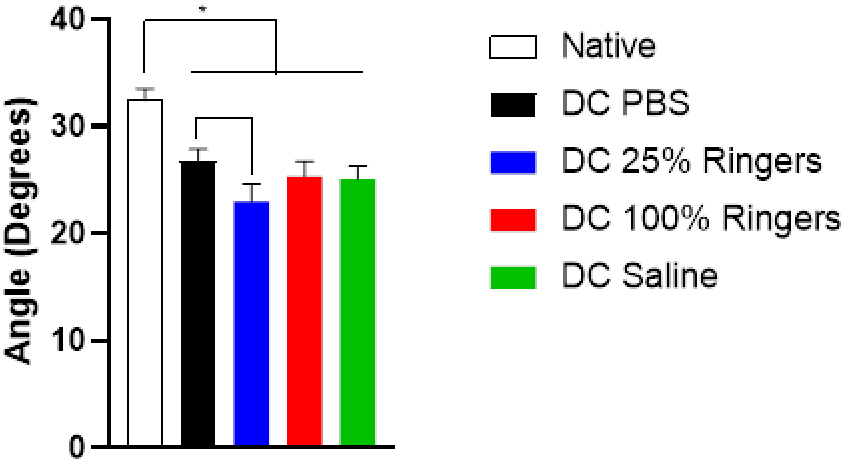

Figure 3.24: Collagen crimp angle of native and decellularised (DC) groups. Reduction in collagen crimp angle was observed in all DC groups compared to native pSFT. Further there was a significant reduction in DC 25% Ringers crimp angle compared to DC PBS. There was no significant differences between DC groups using PBS, 100% Ringers and saline. Data is presented as mean (n = 3) ± 95% CI. Data was analysed using one-way ANOVA followed by Tukey's post hoc test. * indicate significant difference between groups.

3.3.6 Mechanical characterisation

The tensile moduli revealed decellularised groups using PBS and 25% Ringers had a significant reduction in E_{toe}, while groups using 100% Ringers and saline solution were not significantly different to native tissue. Contrary to its low E_{toe}, the 25% Ringers group had the highest E_{linear}, not significantly different from native pSFT. All other decellularised groups' E_{linear} was significantly reduced (Figure 3.25).

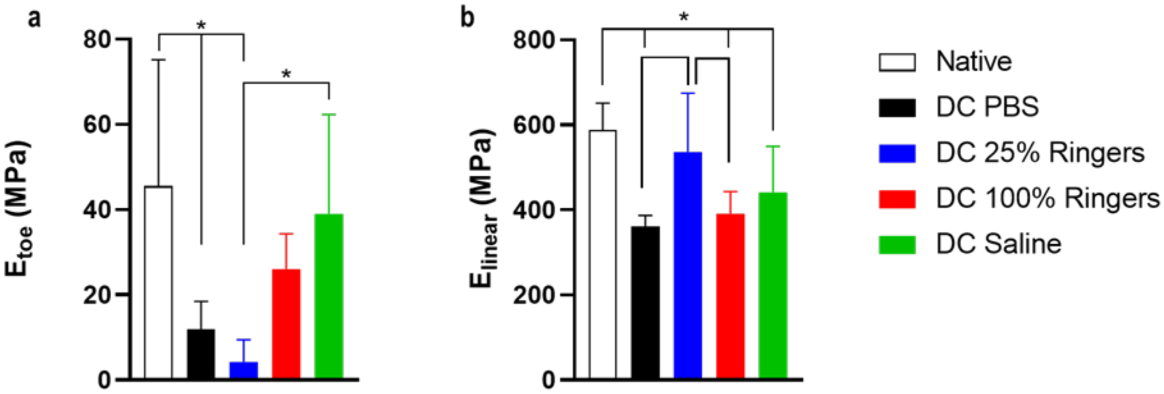

Figure 3.25: Toe (a) and linear (b) moduli of native and decellularised (DC) groups.
a) Significant reduction in DC PBS and DC 25% Ringers groups' toe modulus compared to native pSFT, while DC 100% Ringers and DC saline groups were not significantly different from native tissue; b) all DC groups had a significantly reduced linear moduli compared to native tissue, except DC 25% Ringers. Data is presented as mean (n = 6) ± 95% CI. Data was analysed using one-way ANOVA followed by Tukey's post hoc test. * indicate significant difference between groups.

The UTS (Figure 3.26) of all decellularised groups shared the same trend as the linear modulus (Figure 3.25b), where the lowest UTS was seen in the PBS group, followed by the 100% Ringers group and the saline group, all significantly reduced compared to native pSFT. There was no significant difference for UTS between the 25% Ringers and native groups, with only ˜ 9% reduction. Finally, there were no differences between groups' ε_{fail}, ranging between 0.19 – 0.22 mm/mm.

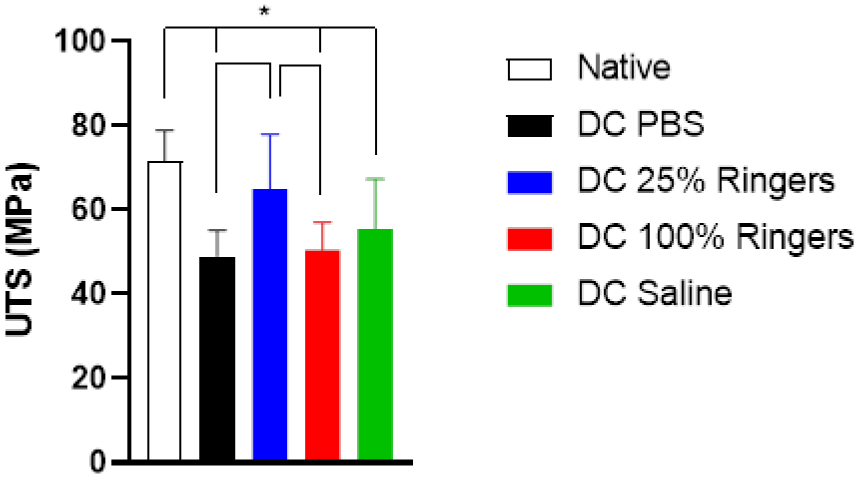

Figure 3.26: Ultimate tensile strength (UTS) of native and decellularised (DC) groups.
All DC groups had a significantly reduced UTS compared to native tissue, except DC 25% Ringers. Data is presented as mean (n = 6) ± 95% CI. Data was analysed using one-way ANOVA followed by Tukey's post hoc test. * indicate significant difference between groups.

The time-independent (E_0) and time-dependent (E_1 & E_2) moduli of pSFT are summarized in Table 3.5. There was a significant reduction in all moduli for decellularised groups compared to native pSFT. There were no statistical differences between decellularised groups.

Table 3.5: Stress relaxation parameters of native and decellularised (DC) pSFT.

	Sample group	E_0 (MPa)	E_1(MPa)	E_2 (MPa)	τ_1 (s)	τ_2 (s)
	Native	124.30 ± 14.41^a	23.41 ± 7.65^a	16.91 ± 6.14^a	2.87 ± 0.41^a	45.05 ± 14.42^a
	PBS	73.15 ± 14.62^b	9.56 ± 3.14^b	5.56 ± 2.53^b	2.99 ± 1.16^a	29.37 ± 8.64^a
D	**25% Ringers**	64.44 ± 8.13^b	9.06 ± 1.44^b	4.65 ± 2.58^b	$1.89 \pm 0.85^{a,b}$	21.18 ± 10.53^b
C	**100% Ringers**	65.53 ± 6.91^b	7.89 ± 0.58^b	5.565 ± 1.70^b	2.68 ± 0.81^a	30.25 ± 9.55^a
	Saline	84.45 ± 19.89^b	7.40 ± 2.38^b	1.76 ± 2.06^b	1.12 ± 0.52^b	6.64 ± 3.15^b

Data is presented as mean (n = 6) ± 95% CI. Data was analysed using one-way ANOVA followed by Tukey's post hoc test. Groups in each column that do not share the same superscript are significantly different.

3.4 Discussion

3.4.1 Tissue swelling after decellularisation

The hypothesis that by substituting PBS with alternative physiological fluid-like solutions in both decellularisation and testing methods, tissue swelling could be reduced was proven, as all modified decellularised groups showed a reduction in specimen width (Figure 3.5a) and thickness (Figure 3.5b), albeit not statistically reduced for the 100% Ringers group in both instances (Table 3.2). Increased swelling induced by PBS does not only occur at a whole-tendon scale, but has also been reported in tendon fascicles [127, 257]. This suggests PBS could play a role in increasing intrafascicular and interfascicular spacing within pSFT, temporarily affecting the intricate arrangement of collagenous and non-collagenous matrix components. This could translate into changes to the biomechanical properties of decellularised pSFT, discussed in section 3.4.6.

Similarities in tendon swelling occurred in the decellularised groups using solutions with the same 9 g/L NaCl concentration (100% Ringers, saline). Both tissue dimensions were significantly greater than the 25% Ringers group (2.25 g/L NaCl). This could suggest tissue swelling is proportional to NaCl concentration, with hypertonic solutions increasing swelling. However, hypertonic solutions have been reported to do the opposite in tendon [261] and other connective tissue, such as cartilage [267]. The similarities between the swelling behaviour of 100% Ringers and saline groups could indicate that the remaining components of Ringer's solution, including potassium chloride, calcium chloride and sodium bicarbonate, play no significant role in swelling tendon. However, PBS contains disodium hydrogen and potassium dihydrogen phosphates, which could influence tissue swelling, explaining the significant increase compare to remaining groups. There is no information on the effect of phosphates in connective tissue swelling; however, phosphate ions have been shown to affect the dynamics of water molecules in tendon and cartilage [268], potentially translating into the excessive swelling observed in pSFT.

The trend observed in tissue weight and water uptake aligned with tissue dimensions over time, suggesting swelling can be represented by the increase in pSFT width and thickness, as stated in section 3.3.1. The swelling behaviour of pSFT hydrated in the different solutions during this experiment was not always representative of the behaviour observed post-decellularisation using the same solutions during end-stage washes. There was a demonstrated difference in the swelling of pSFT hydrated in saline compared to its decellularised group, while the 25% Ringers group aligned with the least swelling observed in its decellularised group (see Figure 3.5). Therefore, decellularisation in combination with the solution used during end-stage washes appears to influence the swelling of pSFTs.

The main protein in tendon, collagen I, is an ampholytic protein, meaning above its isoelectric point it is polyanionic, and below it is polycationic [269]. The isoelectric point of collagen I has been reported between 7.2 [266] and 7.8 [265]. It has been stated that swelling of collagenous tissue increases the further the pH is from collagen's isoelectric point. This is attributed to the repelling force of charged protein chains which results in an increased influx of surrounding water into the tissue [270], thus increasing swelling. Swelling and water uptake are therefore considered interchangeable terms. It was shown, using rat tail tendon, that solutions with pH values closer to the isoelectric point of collagen lead to the lowest swelling ratio [271], yet this did not occur with pSFT. Maximum and least swelling did not show a relation to the pH of the solution (Figure 3.6). This shows a negligible effect of pH on the swelling behaviour of pSFT, therefore not impacting the results obtained post-decellularisation in Section 3.3.1.

3.4.2 Relative quantification of matrix components

The standard decellularisation protocol used here was initially developed for porcine meniscus [231], yet the removal of cellular and nucleic acid material was accompanied by a significant reduction (˜ 59.4%) in meniscus GAG content. Similarly, when osteochondral plugs were subjected to the decellularisation process [272], a reduction in GAG content and increased deformation of tissue matrix were reported. Previous GAG quantification on decellularised pSFT using the standard process also resulted in significant GAG loss [222]. Therefore, analysis of GAG content was performed on standard and modified decellularised groups, revealing no GAG loss occurred as a consequence of the decellularisation process and/or solution used during end-stage washes of the method. Contrary to what was hypothesised in previous studies [220, 224], the results of this study suggest any reductions in tensile mechanical properties of decellularised pSFT cannot be solely attributed to GAG loss.

Quantification of collagen content has been conducted on decellularised pSFT before, reporting no significant difference compared to native tissue [222]. This is in agreement with the results presented in section 3.3.2, supporting that no removal of extracellular matrix collagenous components are caused by decellularisation or the different solutions end-stage washes. The significant increase observed in the saline decellularised group

(Figure 3.8a) may be caused by inherent variability of porcine tissue [273], not associated with the decellularisation process. Studies conducted on a range of decellularised tendon procured from diverse animals have also reported no adverse effects on collagen composition or structure [212, 274–282]. Further assessment of collagen content, structure and arrangement in pSFT post-decellularisation was analysed in section 3.3.5. An undisturbed collagen network in decellularised pSFT fascicular matrix is also consistent with the immunohistochemical techniques conducted by [222], showing similar staining patterns for collagen type I and III when compared to native sections.

Denatured collagen quantification has been conducted on pSFT before, revealing similar low levels across samples [223]. Denatured collagen refers to an evident uncoiling in collagen's triple-helix, which could occur as a consequence of the physical, chemical and enzymatic methods pSFT is subjected to during decellularisation. This uncoiling has also been called micro-unfolding [283]. Native undamaged collagen molecules are tightly wound and packed into fibrils, which prove highly resistant to enzymatic cleavage. However, when micro-unfolding events occur, uncoiled regions within collagen molecules are susceptible to cleavage by alpha-chymotrypsin. There was no evidence of significant micro-unfolding post-decellularisation, suggesting firstly that the collagen triple helix is unaffected by the process itself, and secondly, that whole tendon swelling does not adversely impact the intramolecular and intrafibrillar spacing of collagen within pSFT fascicular matrix. Finally, a tendency is apparent in the proportion of denatured collagen to total collagen content (Figure 3.8). This is hypothesised to be naturally occurring, as a consequence of collagen development and self-assembly within the pSFT [284], whereby inhomogeneous and random uncoiled sites exist within collagen triple helices, proportionate to total collagen content.

3.4.3 Thermal stability of superflexor tendon

The narrowing of the peak observed in the thermogram between native and decellularised groups (Figure 3.10) may be attributed to a reduction in configurational freedom as a consequence of matrix swelling caused by the PBS [285]. However, this minor change was better analysed in combination with transition temperatures and enthalpy of denaturation.

The consistency found between groups in Table 3.4 signifies roughly the same amount of energy was required for collagen denaturation of native and decellularised pSFT. This is likely attributed to a certain stability in enthalpy of denaturation in tendon, as it remains unaltered even by tensile overload [286]. This has been attributed to a negligible effect of conformational alterations of matrix structure, excluding the destabilisation of collagen water bridges.

Further, enthalpy is influenced by hydration, i.e. water surrounding collagen fibres [287]. Decreases in enthalpy have been associated to dehydrated collagen fibres [288–290]. Given the consistency between sample storage and preparation, it could be hypothesised that decellularised specimens belonging to the 25% Ringers, 100% Ringers and saline groups showed a reduction in enthalpy in relation to their water content, notable compared to native pSFT. A more dense tissue could translate to a network of closely aligned collagen fibrils, displacing water, thus influencing the values of enthalpy obtained. This reduction was not observed in the decellularised PBS group, given its water content was higher compared to remaining decellularised groups.

Despite the statistical differences between groups, the transition temperatures and behaviour of native and decellularised tissue subjected to thermal denaturation was very similar (see Figure 3.10). Thermal studies have been conducted on pSFT before, comparing irradiated and non-irradiated decellularised tissue c, showing a significant dose-dependent decrease in transition temperature of 8 – 11 °C. Here, the decrease ranges between 1.7 – 3.8 °C, which could suggest collagen's molecular organisation, i.e. bonding within the peptide chain and/or cross-linking arrangement between fibrils is not adversely altered by the decellularisation process. Despite the statistical analysis revealing differences between groups, there is lacking evidence of speed and ease in reaching the thermal denaturation transition state post-decellularisation. This suggests no evidence of molecular disruption of collagen in pSFT fascicular matrix. Further, the effect of swelling caused by the different solutions used in end stage washes of the decellularisation process, appears to have no effect on the transition temperature of pSFT. Despite there being evidence of significant tissue swelling (see Section 3.3.1) in the PBS group, it seems insufficient to cause adverse dissociation of the collagen structure, which in turn would result in a significant decrease in denaturation temperature, reported before in swollen collagen thermal behaviour [285].

3.4.4 Histological evaluation

Histology is the microscopic study of biological material through a process of sectioning, staining and microscopy imaging [291, 292]. The staining methods allow the evaluation of specific characteristics, components and structures of a given section. Histology was carried out on native and decellularised pSFT samples firstly to determine the effectiveness of the decellularisation process, and assess potential architectural changes to tendon matrix. Figures 3.11 and 3.12 showed removal of cellular content and cellular debris independently of the solution used during end-stage washes. This suggest PBS is interchangeable with the solutions used in this Chapter (see Table 3.1) during end stage washes without affecting the efficiency of the decellularisation process. Figures 3.16 and 3.17 showed no fluorescence in decellularised tissue sections, further proving nucleic acids were effectively removed with all the solutions used during modified methods. This outcome abides by one of the three criteria that determines the decellularisation of biological tissue, including no visible cellular/nuclear material in histological analyses with H&E or DAPI [197, 203, 204].

There was evidence of variability in the histoarchitecture of NBF fixed, wax embedded pSFT sections stained with H&E, even within native specimens. It was empirically observed that tissue fixing varied between 24 – 36 h. Successful fixation can occur within the given time range, but can often result over-fixed after 24 h. This could be attributed to natural tendon thickness; however, has not been investigated further. It was hypothesised that fixation influenced the histoarchitecture of pSFT sections, potentially affecting the openness of the matrix when comparing native and decellularised sections. Therefore, cryo-embedding and cryo-sectioning of native and decellularised samples was conducted, to further assess tendon matrix architecture. It has been reported that cytological features and tissue architecture of cryo-embedded sections are inferior to wax embedded sections due to the formation of ice crystals [293]; however, this did not occur with pSFT cryosections. The histoarchitecture of native pSFT appeared less disturbed by the process of cryo-embedding and cryo-sectioning. There was minimal disruption attributed to the formation of ice crystals which appeared as circular openings throughout the sections (Figure 3.13 & 3.14). Preserved architecture and cell density of cryosections has also been reported in brain and spinal cord tumour [294]. The minimal cellular debris observed in decellularised cryosections (Figure 3.14 D) can be attributed to the thickness or density of pSFT [295], as it is more difficult for decellularisation solutions to penetrate the tissue reaching the fascicular matrix, completely washing out cellular debris.

Decellularised pSFT matrix has been qualitatively described as more open and porous [220]. By conducting a tissue to white space ratio analysis (Figure 3.15), a more quantitative approach of matrix openness comparing native and decellularised tissue was obtained. The significant reduction for decellularised sections indicate that the openness of the matrix increased post-decellularisation, with less area corresponding to matrix pixels, and more area corresponding to white space or background pixels. This was observed qualitatively in cryosections (Figure 3.13 & 3.14) and wax embedded sections (Figure 3.11 & 3.12) of decellularised pSFT and aligns with previous histological analyses [220]. This can be attributed mainly to the removal of cellular material, and the rearrangement of fascicular matrix that ensued.

The first stage of histological evaluation helped determine the effectiveness of the decellularisation process and architectural changes in matrix post-decellularisation. The next step consisted in analysing specific matrix components, i.e. GAGs. It was previously shown that there were no differences in GAG content of native and decellularised pSFT (see Section 3.3.2). Alcian blue and safranin O staining of transverse sections revealed GAGs throughout fascicular matrix, while higher quantities arranged along surrounding endotenon. IFM is vascular-rich [296], and GAGs are mainly distributed throughout the endotenon network. Further, the presence of GAGs increasing towards the peritenon agrees with a high GAG and proteoglycan concentration in tendon areas primarily subject to compression [80, 297]. Alcian blue staining of native and decellularised pSFT has been conducted before in [222], in longitudinally orientated sections. This approach was replicated. GAGs were characteristically situated between collagen [298]. Decorin, the main proteoglycan in tendon, associated with dermatan sulphate is commonly located between collagen fibrils [299]. This is exemplified in Figure 3.19 C. Further, the dense GAG staining observed is likely IFM. This explains the consistent spacing between streaks (Figure 3.19 C, arrows), whereby the fascicular matrix, with a lesser amount of GAGs (thin blue streaks) is tightly packed between a looser IFM, which is known to contain a higher amount of GAGs and PGs [300, 301]. This suggests a highly structured organisation of GAGs in native pSFT matrix.

The dissimilarities between staining shades of native and decellularised sections obtained using alcian blue also occurred in a previous study using porcine Achilles tendon [214], and pSFT [222]. Despite the unspecific staining, it was evident that there was a loss of the dense GAG content arrangement seen in native tissue (see Figure 3.19 C & D). This, combined with the increased openness of the matrix histoarchitecture may indicate that IFM components are affected as a consequence of the decellularisation process. Given there was no GAG loss post-decellularisation (see Section 3.3.2), this component remained in the pSFT matrix, yet likely in different locations throughout the fascicular matrix, possibly leading to the random blue staining seen in Figure 3.19 B and D. This is hypothesised to have occurred as a consequence of a structural rearrangement. Disruptions to the IFM of decellularised pSFT were also observed in sections stained with Sirius red (Figure 3.22).

Collagen crimp has been hypothesised to be affected by standard decellularisation in pSFT, demonstrated through histological loss of crimp in decellularised longitudinal sections [220, 222]. Therefore, it resulted crucial to investigate if this occurred in standard and modified decellularised groups. Sirius red staining was carried out on NBF fixed, wax-embedded sections of native and decellularised pSFT, as it is currently the standard for collagen detection in histological sections of tissue [302]. It was used to analyse the entirety of the collagenous components of pSFT ECM, not distinguishing between collagen types. Imaging of sections stained with Sirius red at different angles produces different colours unable to accurately discern collagen type I and III [249, 302].

Crimp loss was not apparent in decellularised group, with the exception of the PBS group, which showed a more extended crimp (Figure 3.22 B), likely representing the crimp loss present past studies [220, 222]. The changes to the IFM observed with alcian blue staining were also evident in Figure 3.21, where fascicle structures were visible, yet interfascicular spacing was more noticeable compared to native sections (Figure 3.21 D). The characteristic red shade of the IFM located between fascicular structures was apparent only in longitudinal sections (Figure 3.22 B, C & E), with a less arranged structure compared to native pSFT. A disruption to the IFM as a consequence of decellularisation may induce a more dramatic rearrangement of the fascicular matrix, possibly leading to the minor changes observed in collagen crimp. If collagen is less tightly packed due to an increase in interfascicular spacing, collagen fibres could lose crimp tightness intra-fascicularly. This is further discussed in section 3.4.5. It may also relate to the biomechanical changes observed in decellularised pSFT, discussed in section 3.4.6.

3.4.5 Collagen crimp

Contrary to the hypothesised tighter crimping with decreasing hydration, this study observed the opposite as the two groups with statistically greater crimp period (25% Ringers and saline) were the two groups with least swelling post-decellularisation (see Section 3.3.1). An alternative hypothesis is that while crimp morphology was not significantly affected by the decellularisation process, extended crimp (periodicity) may be a consequence of matrix component loss. The removal of cellular components, accounting for circa 20% of total tendon composition [1], in addition to the hypothesised loss of IFM (seen in section 3.3.4), may provide more space within the confinement of the peritenon, as well as within individual fascicular structures. Crimp can then further extend, presenting itself as more relaxed. The increase in distance between peaks would therefore be attributed to a spatial reconfiguration post-decellularisation. This would further support the unaltered crimp pattern observed in decellularised porcine Achilles tendon [214]. Furthermore, it may be that due to the minor swelling in the 25% Ringers and saline groups (see Section 3.3.1), less water molecules occupied space within the fascicular matrix, allowing further relaxation of collagen crimp, resulting in the significant increase in crimp period for both groups.

The significant reduction in crimp angle for all decellularised groups could be attributed to the spatial reconfiguration described above. It has been postulated that a smaller crimp angle is related to earlier fibre failure [68], which could explain the reduction in UTS for decellularised groups compared to native pSFT (see Figure 3.26). The smallest crimp angle was observed in the 25% Ringers group, which aligns with the greatest period and amplitude, shown in Figure 3.23. This is also consistent with the significantly reduced toe modulus presented in Figure 3.25a, yet does not account for the better mechanical properties it presents compared to the remaining decellularised groups. This may be largely due to the effects of the solution used during mechanical testing, discussed more in detail in section 3.4.1 and 3.4.6.

It has been reported that crimp angle measurement largely depends on the sectioning plane and crimp propagation plane [303], which may have influenced the crimp angles reported here; however, crimp angles of rat tail tendon collagen fibres have been reported between 12.5 – 20 degrees [304], not significantly dissimilar to the angles obtained in pSFT sections.

Analysis of collagen crimp has been investigated before, but focused more on the mechanisms of crimp loss during mechanical loading, and increasing strain [305, 306]. The study used as reference to design this method provided no comparable data, as it characterised crimp of different equine tendon types [67]. Crimp analysis has not been conducted on decellularised tendon before.

3.4.6 Mechanical characterisation

The characteristic sigmoidal curve representing tendon mechanics under tension, begins with a non-linear toe region. This initial, low stiffness region ends at approximately 4% strain [307], followed by a high stiffness linear region. The initial toe region has been related to range of motion, given physiological loading *in vivo* operates within the initial 4% strain [308]. Therefore, E_{toe} provides valuable information on the mechanical behaviour of decellularised pSFT within the physiologically relevant region. The nonlinear region is characterised by collagen withstanding stress through a combination of mechanisms, including gradual loss of its characteristic waviness, referred to as crimp [306], accompanied by increasing fibre realignment [128–130].

Based on the highly complex architecture of tendon, and its capability to experience multiaxial loads, pSFT possesses an inhomogeneous array of substructures, including fascicles and fibres. This translates into a complex distribution and alignment of both, which undergo realignment under initial loading. This is consistent with findings on the human supraspinatus tendon [298]. The groups with a significant reduction in E_{toe} (Figure 3.25a) correspond to the tissue with greatest and least swelling (see Table 3.3). This suggests that hydration levels of pSFT impact collagen fibre alignment during the low stiffness toe region. Excessive swelling may lead to increased free water in the extracellular matrix, occupying all free space within the pSFT, hindering collagen fascicle and fibre realignment. Conversely, reduced water content results in a matrix so dense, fibre movement for realignment simply cannot occur. Moreover, the groups using solutions with 9 g/L NaCl concentration showed similarity in E_{toe} (Figure 3.25a), yet were higher than the PBS group. This could suggest that the excessive swelling caused by PBS, independently of NaCl concentration, adversely impacts tissue mechanics in the physiologically relevant region under tensile loads. Accordingly, the phosphates in PBS could alter collagen mechanics [309]. This could occur through water dynamic mechanisms, affecting tendon's ability to organise the fibre collagen network to withstand stress.

Collagen crimp contributes to tendon nonlinear behaviour [310]. It was suggested by [220] that increased crimp, could explain the reduction in initial stiffness observed in decellularised pSFT, therefore requiring greater strain to reach the linear region. The lowest E_{toe} (25% Ringers group), could be a consequence of tissue water content. The tightly packed crimping pattern could be attributed to decreased hydration, rather than the effect of the decellularisation process itself. Crimp has been reported to be affected by decellularisation processes in bovine saphenous veins [311] and porcine aortic valve leaflets [312]. Contrarywise, decellularised porcine Achilles tendon showed no alterations in crimp pattern [214]. Such inconsistencies warranted the investigation of potential changes in collagen crimp characteristics post-decellularisation presented in section 3.3.5.

The linear region of the load curve occurs after recruitment and realignment [313] of collagen fibres during initial loading. Collagen fibres then withstand increasing load through interfibrillar sliding mechanisms [128–130]. However, swelling, and in particular, a recurring use of PBS, has been proposed to affect, firstly, collagen fibre recruitment [256]. This would affect the intrafascicular mechanisms leading up to the linear region, producing a cascade effect on tendon mechanics under increasing loads. Indeed, excessive hydration and swelling has been proven to reduce the modulus of diverse tendons at different levels of scale, as observed here (Figure 3.25b). At the whole-tendon level, an inverse relation was found in human iliotibial bands, with increasing linear modulus and tensile strength with decreasing water content [314]. Similarly, rat tail tendon incubated in PBS showed a reduced modulus accompanied by evidence of microscale damage [256]. Consistent with such results, the reduction of mechanical properties in relation to levels of swelling was apparent across all decellularised groups (see Table 3.2 & Figure 3.25).

At lower levels of scale, fibrils have been studied likely due to the rationalisation that fibrillar properties are key to tendon mechanics, potentially governing the sub-failure response [315]. This is supported by findings using rat tail tendon fibrils, where swelling not only resulted in a reduction in modulus and tensile strength[257], but also provided evidence of enlarged fibril diameters, altered morphology, increased interfibrillar spacing and diminished fibril density [256]. This suggests an adverse effect on interfibrillar contact, compromising tendon ability to withstand tensile load through shear. It likely also impacts at a sub-fibril level, where specific interactions between collagen molecules such as salt bridges, may affect collagen stability. This effect has been studied before on bovine Achilles tendon [258], where a higher salt concentration resulted in increased modulus, only exceeded by tissue dehydration. Linear modulus obtained across decellularised groups (Figure 3.25b) only align with improving mechanical properties according to lower hydration, but not with the modification of salt concentration in the solutions used. These results are further consistent with studies conducted at a fibril level [259, 316].

The tensile strength of decellularised groups shown in Figure 3.26, shared the trend observed in linear modulus. The level of swelling within decellularised groups appeared to influence the mechanical strength of each group, such that the least swelling (25% Ringers) resulted in the highest UTS, not significantly different from native tissue. The trend continued, such that UTS decreased with increasing swelling, with the lowest UTS observed in the PBS group. Previous tensile testing conducted on decellularised pSFT have reported no significant reduction in tensile strength compared to native pSFT [220, 222], suggesting the decellularisation process itself may not be solely responsible for changes in tendon mechanical properties, but is primarily a consequence of tissue hydration and the impact of swelling on multiscale structure and mechanics.

The linear modulus for human ACL in young patients has been reported to be circa 111 MPa, and around 65 MPa in older patients [123, 134, 135]. The UTS has been reported circa 38 MPa in young patients and 13 MPa in older patients [123, 134, 135, 317]. Despite the significant reduction for both mechanical properties in all decellularised groups using solutions with physiologically relevant NaCl concentrations (see Table 3.1), they exceed native ACL values. Ideally, the mechanical properties of the graft should complement the surrounding biomechanical environment of the tissue it aims to substitute, avoiding an overcompensation or degradation of surrounding tissue [318]. An equivalence is optimal but not strictly required for the graft to be successful, mainly due to the remodelling that occurs in vivo, a structural adaptation to the mechanical stresses it is subject to when implanted [319]. The graft should allow for the stretch and recoil that native ACL demonstrates, such that the ultimate strain is similar, reducing risk of rupture under normal loading in the body. This property was not affected by decellularisation, with similar strain to failure properties between native and decellularised pSFT. Further, the decellularised pSFTs' UTS resulted almost equivalent to the gold standard human patella tendon graft used during ACLR, of circa 68 MPa [320]. However, an initial degradation of the graft associated with loss of mechanical properties [321] occurs as part of the integration process, so a higher linear modulus (see Figure 3.25) would prove beneficial for this to not adversely impact graft performance. Thus, the mechanical properties obtained remain acceptable for decellularised pSFT to meet clinical requirements, proving a suitable graft. Furthermore, it has been reported that tendon has lower hydration *in vivo* than in saline solution *ex vivo* [315]. It could be, in fact, that the 25% Ringers group, having the lowest hydration, represents the biomechanical behaviour of decellularised pSFT graft *in vivo* following implantation.

It has been debated that proteoglycans (PG) and GAGs influence the viscoelastic behaviour of tendons. This has been explained through the component's high affinity to water and interactions with collagenous matrix components [322]. At a fascicular level, it has been shown that GAG depletion reduces relaxation rate [323]. Similarly, a relation between decorin content and relaxation rate was found in mouse tail tendon [324]. However, this has been disproven at different levels of scale by studies conducted on rat tail tendon fascicles [325] and human medial collateral ligament [326], finding PGs and GAGs play no significant role in regulating viscoelastic properties. In pSFT, decellularisation did not remove GAG content (see Section 3.3.2), suggesting their loss is not a factor in the changes in viscoelasticity observed. However, this leads to consider additional non-collagenous components found within decellularised pSFT matrix. The IFM, also called endotenon, is a combination of elastin, PGs, GAGs and some collagen[300, 301]. It is a porous structure, thus highly hydratable, which can interact accordingly with fluids encountered within the fascicular matrix [327]. It has been proposed previously, that the IFM is essential in mediating the viscoelastic behaviour of tendons [137], thereby possibly altered by the decellularisation process with ensuing changes in pSFT viscoelasticity.

The reduction in E_0 of decellularised pSFT (Table 3.5) may be attributed to changes in fluid flow within the IFM, previously observed in bovine deep digital flexor tendons [327]. A relation between water content and rate and amount of relaxation have been reported previously [252, 253], showing increased water or swelling resulted in greater, faster relaxation. This has also been seen in ligaments [251]. The changes in fluid flow could be a product of altered biochemical composition or structural organisation of the IFM. Knowing that collagen and GAG content were unaltered post-decellularisation (see Section 3.3.2), a change to the structure, size or location of elastin fibres, glycoproteins and possibly collagen itself, may have resulted in a different IFM structure. The IFM could provide a different control of fluid flow within decellularised pSFT matrix, contributing to the creation of a relaxation response unlike native tendon. Qualitative changes in IFM of decellularised pSFT were observed through histological techniques (see Section 3.3.4). There remain some inconsistencies regarding the water content of the decellularised groups showing the fastest relaxation (25% & 100% Ringers); however, this could be a result of the fluid flow behaviour during mechanical testing, as opposed to that quantified post-decellularisation. This was influenced additionally, by the removal of cellular material. Higher permeability due to the loss of the matrix's cellular component may have resulted in more relaxation.

The reduction in long-term relaxation of decellularised pSFT represented by E_2 in Table 3.5 supports the hypothesis that the decellularisation process may have affected the IFM, independently of the solution used. However, it has been postulated that plasticity of the IFM, along with the spatial conformation of tendon fascicular matrix is primarily involved in long-term viscoelasticity [327]. This corresponds to the mechanical response of the solid components of the IFM. Despite the GAGs and collagen being retained within the fascicular matrix of decellularised pSFT (see Section 3.3.2), their molecular structure and spatial distribution within the IFM remains unknown. The mechanical integrity of these components may have been affected by decellularisation, and should be further investigated. In addition, the reagents used during decellularisation could have altered or partially reduced elastin, PGs and/or glycoproteins, leading to the structural changes observed in Figure 3.22 A, where a decrease in IFM density was observed, potentially contributing to changes in mechanical behaviour. These potential changes to decellularised pSFT endotenon may have contributed to the reductions in short- and long-term relaxation moduli observed.

3.5 Conclusion

In summary, through the work presented in this chapter it was shown that the alternative solutions used during end-stage washes of the decellularisation process did not reduce the effectiveness of the process, while reducing pSFT swelling. The biomechanical properties of the modified decellularised groups improved compared to the standard PBS group, likely attributed to a reduction in tissue swelling, while the 25% Ringers group showed most native-like properties. Decellularisation did not remove collagen or GAG content from pSFT matrix, but likely altered IFM structure and components, also observed qualitatively through histological techniques. The function and mechanical contribution of collagenous and non-collagenous matrix post-decellularisation requires investigating. Finally, though transition temperature was reduced for all decellularised groups, there was no indication of a loss in collagen quality and stability, but rather changes to the crimp morphology were observed, including increased periodicity, likely a consequence of cellular content removal. This initial study instigated the development of the methods used in the following chapter, for obtaining a more complete mechanical profile of decellularised pSFT, involving compressive as well as tensile loads.

Chapter 4

Biomechanical behaviour and structure-function relationships of porcine superflexor tendon in tension and compression

4.1 Introduction

Chapter 3 presented the effects of decellularisation on the content of ECM components and pSFT biomechanics under tension. It introduced a modification to the end-stage washes of the decellularisation process, providing insight into the influence of swelling on the tensile mechanical properties of tendon. However, the consequences of decellularisation methods and associated swelling on the biomechanical behaviour of pSFT under compression has not yet been studied. Further, the function of the GAGs and their contribution to tendon mechanics following decellularisation remain unclear.

Biomechanical studies on pSFT have focused on its properties under tension, as this seems the main state of deformation under physiological conditions. However, tendon may also experience lateral compressive loads[328], given complex in vivo loading conditions [329], therefore subject to multiaxial states of stress [330]. Terminal regions of tendons[31, 331] are subject to both longitudinal tension and transverse compression [332]. Limited studies on compressive properties of tendon exist in the literature [329, 333–336]. Compression characterisation of decellularised tendon has not been conducted to date.

Compression is also relevant for a material intended to act as a graft for ACLR, due to fixation mechanisms. Interference screws are the most commonly used direct mechanical fixation method in ACL replacement [337]. Compression occurs between bone-screw, screw-tendon and tendon-bone interfaces [338, 339], transverse to the longitudinal axis of the graft. This indicates that a potential graft should be capable of undergoing compressive forces normal to the main axis of collagen fibre alignment, to ensure adequate fixation. The effect of swelling in compressive properties of tendon has not been studied in detail. The impact of swelling occurs not only in tendon, but other connective tissues, where it has been shown to alter the mechanical behaviour of cartilage under compression [267, 340]. Therefore, the consequences of pSFT swelling on its compressive properties require investigating.

Tendon ECM is predominantly comprised of collagen [1], constituting approximately

60% of its dry mass [68]. Collagen has been extensively studied [306, 341–343]. However, tendon matrix also includes a small amount of non-collagenous contributors ($<$ 20% of extracellular matrix), which remain to be investigated in depth [17, 73, 344]. Within this non-collagenous matrix, the distribution, characterisation and mechanical function of GAGs is less understood, particularly following the process of decellularisation.

GAGs are often associated to the compressive response of connective tissue. The main GAGs in tendon, dermatan sulphate and chondroitin sulphate [78], are vastly electronegative, contributing significantly to tissue hydration [345, 346]. GAGs water-binding function help maintain tendon integrity [78, 80, 347], potentially enabling tissue matrix to support compressive loads. The mechanical role and contribution of GAGs in bearing compressive loads in pSFT warrant investigation, particularly after being subjected to the decellularisation process.

GAG degrading enzymes have helped provide insight into their role within tissue in the literature. Previous studies have used ChABC for GAG depletion to study consequences on tendon swelling [333], viscoelastic properties of human ligament [326], and contribution of GAGs to tendon fascicle and fibril mechanics in tension [323, 325, 348, 349]. Only one study has focused on the contribution of GAGs in compression [350], conducted on porcine medial collateral ligament. The contribution of GAGs to the tensile and compressive mechanical properties of pSFT has not been studied to date.

4.1.1 Study 1: Aim and objectives

4.1.1.1 Aim

The aim of Study 1 was to provide a complete mechanical assessment of decellularised pSFT, building upon the results presented in Chapter 3, with particular interest in the function of GAGs in decellularised matrix.

4.1.1.2 Objectives

The specific objectives were as follows:

a) To develop a method for compression testing of pSFT.

b) To characterise the compressive mechanical properties and behaviour of native and decellularised tendon.

c) To characterise the compressive mechanical properties and behaviour of decellularised pSFTs using their solution (PBS, 25% Ringers, 100% Ringers and 0.9% saline solution) as a hydrating medium during testing.

d) To determine the effects of swelling on the biomechanics of decellularised pSFT in compression.

e) To investigate the function of GAGs in decellularised pSFT subjected to compression.

It was hypothesised that despite GAG content remained unchanged post-decellularisation, the function of the component was compromised. Therefore it became imperative to investigate GAG contribution to tendon mechanics. The role of this non-collagenous matrix component is not yet completely understood, specifically regarding its contribution to load bearing mechanisms [351], both in tension and compression.

4.1.2 Study 2: Aim and objectives

4.1.2.1 Aim

The aim of Study 2 was to gain a better understanding of GAG function and their contribution to pSFT mechanics by investigating the consequences of GAG removal from pSFT matrix on its biomechanical behaviour in tension and compression.

4.1.2.2 Objectives

The specific objectives were as follows:

a) To efficiently remove GAG content from pSFT matrix.

b) To assess the effect of GAG depletion on the quality and stability of the collagen in pSFT.

c) To characterise the compressive mechanical properties and behaviour of GAG-depleted pSFT.

d) To characterise the tensile mechanical properties and behaviour of GAG-depleted pSFT.

4.2 Methods

4.2.1 Study 1

4.2.1.1 Experimental design

The experimental design for the characterisation of the compressive mechanical properties of native and decellularised pSFT is summarised in Figure 4.1. Tendons were subjected to decellularisation (see Section 2.2.2) using different solutions during end-stage washes. These included PBS (standard decellularisation method), 25% Ringers, 100% Ringers or 0.9% saline solution. Cylindrical plugs were then obtained as detailed subsequently in section 4.2.1.4 using a biopsy punch. A total of n = 6 specimens were tested for each decellularised group. Native specimens underwent the same sample preparation process (n = 6), hydrated in PBS throughout the experiment. The cylindrical specimens were hydrated in filter paper soaked in the solution used during the end-stage washes of their decellularisation process, and then subjected to compression testing hydrated in the same solution. The biomechanical behaviour of native and decellularised pSFT in compression was obtained, providing insight into the effect of tissue swelling and hydrating solutions on tendon mechanical properties. Further, the function of GAGs and their role in withstanding compressive loads in decellularised tissue was assessed.

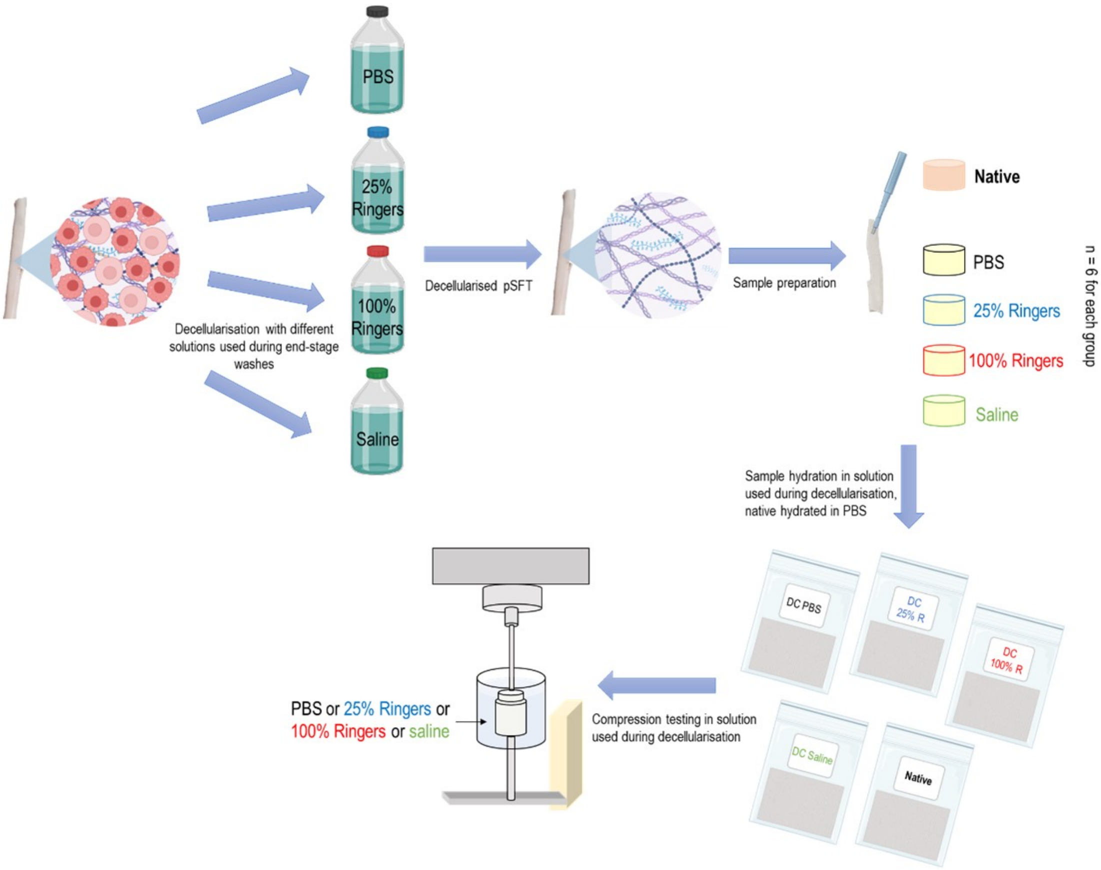

Figure 4.1: Experimental design for the characterisation of the compressive mechanical properties of native and decellularised pSFT,
and the effect of swelling on tendon mechanical behaviour in compression. Native pSFT was subjected to standard and modified decellularisation methods, using different solutions during end-stage washes, including PBS, 25% Ringers, 100% Ringers and 0.9% saline solution. Specimen preparation to obtain cylindrical plugs required a biopsy punch. Samples were hydrated in the same solution used during their decellularisation process, and subjected to compression testing in the same hydrating solution.

4.2.1.2 Dissection of superflexor tendon

Dissection was carried out as per Chapter 2, section 2.2.1.

4.2.1.3 Decellularisation of superflexor tendon

Standard decellularisation was carried out as detailed in Chapter 2, section 2.2.2. Modified decellularisation methods (including the use of PBS, 25% Ringers, 100% Ringers and 0.9% saline solution) followed the methods detailed in Chapter 3, section 3.2.3.

4.2.1.4 Confined compression characterisation

Sample preparation

For compression testing a single sample was removed from the mid-substance of the ankle insertion point (ankle region) of each pSFT using a 6 mm diameter biopsy punch (Sigma-Aldrich 6mm Harris Uni-Core). The punch was oriented normal to the lateral anatomical surface of the tendon. This produced cylindrical specimens with collagen fibres orientated normal to the test axis, i.e. transverse plane. The cylindrical plug specimens are presented in Figure 4.2 To prepare consistent specimens, the mechanism for punch biopsies used in healthcare was mimicked. This is based on pushing the punch into the tissue using rotatory movements until the required depth is achieved [352]. Specimen height (H) was taken as pSFT natural thickness, measured at two points using Vernier callipers and averages calculated (Figure 4.2a). Samples were stored at -20 °C in bijous with filter paper dampened with solution according to their sample group until required for testing.

Figure 4.2: Cylindrical 6 mm diameter pSFT plugs for compression characterisation
obtained using a biopsy punch, where height was measured as represented in a), showing a perpendicular view of a specimen in b) and a transverse view in c).

Test apparatus and sample set-up

All specimens were tested in a custom-designed apparatus. This consisted of a confining cylindrical chamber (50 mm diameter) manufactured in Delrin polymer material. The top chamber with a simple 6 mm diameter hole. The bottom chamber with a cavity (25.4 mm diameter, 2.1 mm depth) for the porous platen to lie, and a centred 6 mm hole. The top and bottom chamber were held together using M4 bolts.

The specimen was placed within the 6 mm hole and pushed down using a thin, cylindrical wooden rod. This process was slow and careful to not damage the sample, while ensuring the bottom surface of the specimen was in contact with the porous platen (Figure 4.3a).

A stainless steel plunger (6 mm diameter, 120 mm length) was manufactured, along with a lock nut or connecter (same material) which allowed it to mount onto the Instron 3365 materials testing machine. This plunger was aligned with the chamber hole to compress the sample during testing, confining the sample to impermeable surfaces above and around, with the only porous surface below. The porous platen (Porous 316L SS disc Media Grade 5; Mott Corporation) with uniformly sized and distributed pores allowed fluid flow downwards during compression. Finally, a Delrin spacer was fitted onto a stainless steel base of 40 mm diameter, which facilitated mounting onto the bottom part of the Instron.

Once the specimen was placed inside the confining cylindrical chamber, it was placed on top of the delrin spacer and submerged inside a bath. The centre hole was aligned with the plunger. The experimental set up is represented in Figure 4.3b.

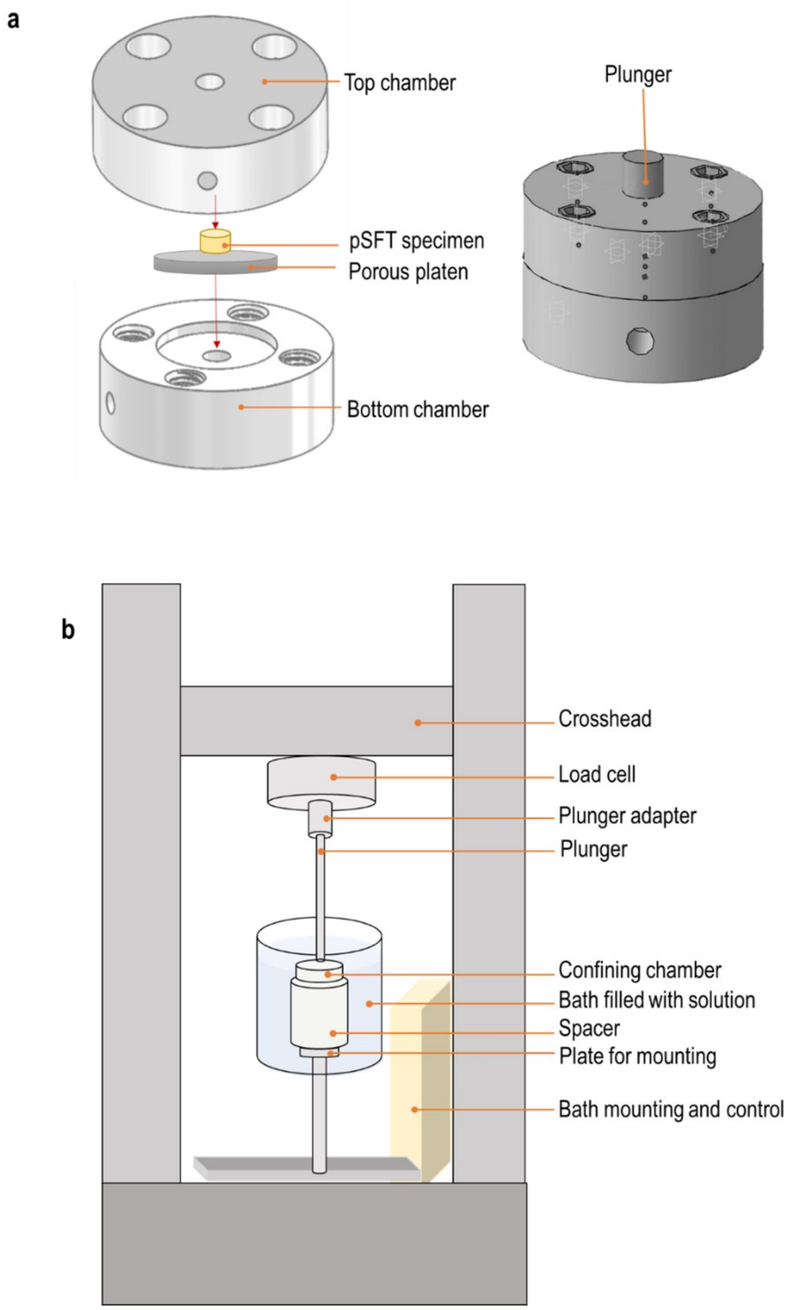

Figure 4.3: Specimen set-up inside confining chamber (a) mounted on Instron for compressive characterisation (b).
Confining delrin chamber with cylindrical pSFT specimen confined within (a), showing relative position of specimen within top and bottom chamber on the left; confining chamber held together by M4 bolts with pSFT specimen inside on the right. Elements mounted onto Instron 3365 material testing machine (b), with confining chamber equilibrating inside bath, ready for compressive loading by action of the plunger.

Standardised confined compression method

Method development was carried out on pSFT to determine the optimal conditions for tissue equilibration and confined loading conditions. After initial attempts and a pilot study conducted on native and decellularised specimens, a standardised, repeatable method was achieved. The pilot study method and results were not included in the present Chapter. However, the significantly higher loads reached during the pilot study resulted in changing the load cell to a 5 kN load cell for the remainder of the compression testing.

Specimens were thawed at room temperature for 30 min, then hydrated with their respective solution (PBS, 25% Ringer's, 100% Ringer's, 0.9% saline), according to the modified decellularised method used. Each individual specimen was wrapped in solution-soaked filter paper and placed inside sealed plastic bags for approximately 1 h. During this time, the bath was filled with the solution required for each group and gradually heated until reaching 37 °C. Specimens were placed carefully inside the confining chamber, as represented in Figure 4.2, and submerged in the temperature-controlled (37 °C) 2 L bath containing the solution they were previously decellularised and hydrated with.

Specimens were allowed to equilibrate in confined conditions, submerged in the bath for 15 minutes. The crosshead was lowered until a small load > 0 N was registered, ensuring contact between the plunger and specimen surfaces, and removed in < 30 sec. A preconditioning load of 2.5 N was applied for 60 sec and then removed, followed by a tare load of 0.25 N for 300 sec. This was followed by a ramp to 10% compressive strain at a rate of 1% per sec, left at a constant displacement for 600 sec. Each test lasted 981 (± 2) sec. Data was recorded at a frequency of 10 Hz. Displacement, force, compressive strain and stress were provided by the BlueHill software, determined by the surface area (6 mm diameter specimen).

Given the lack of compression testing conducted on tendon, the 10% strain was based on extensive compression experiments conducted on cartilage. Healthy knee cartilage undergoes average strains under 10% during physiological motion [353]. There is evidence of peak strains up to 17%, yet physiologically relevant behaviour lies below this [354, 355]. Therefore, 10% strain was considered physiologically suitable for the compression characterisation conducted here. A representation of the method conducted during compressive characterisation of tendon is presented below (Figure 4.4).

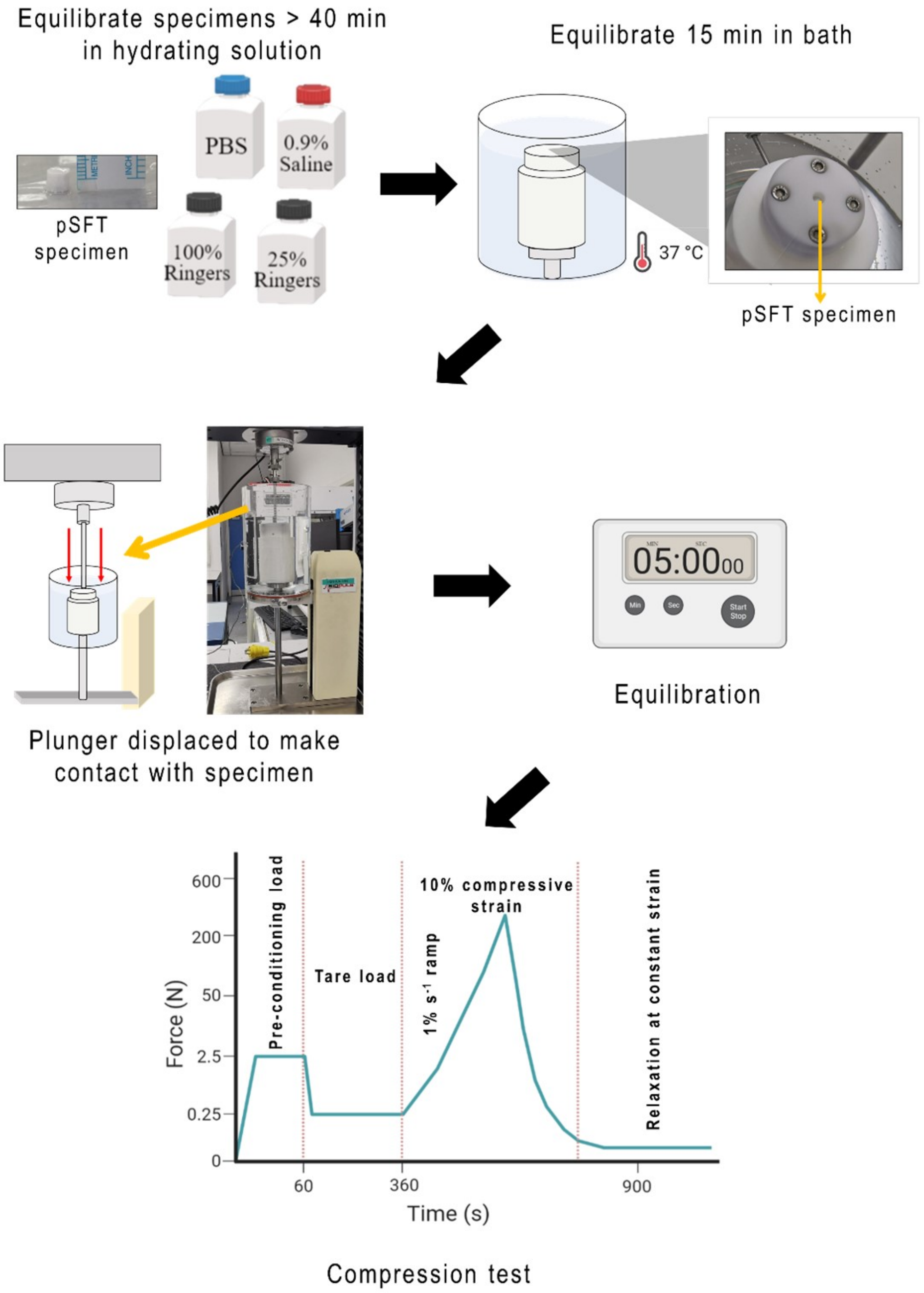

Figure 4.4: Confined compression standardised method.
Specimens were equilibrated at room temperature prior to testing. Within the compression chamber, specimens were equilibrated in the bath at 37 °C for 15 min, then subject to pre-conditioning and tare loads (˜ 360 s) before undergoing compressive loading.

Peak stress was taken as the stress value occurring at 10% strain, being the maximum stress value throughout the test. Equilibrium stress was calculated as an average stress calculated over the final 30 s of the hold period of the test.

4.2.1.5 Statistical Analysis

Statistical analysis was performed using GraphPad Prism (version 8, GraphPad software). Native and decellularised pSFT compressive properties in different hydration solutions were initially assessed using Sidak's correction for multiple comparisons following a two-way ANOVA. The overall effects of solution, decellularisation and interaction between both factors were assessed through a two-way ANOVA. P values lower than 0.05 were deemed to be significant.

4.2.2 Study 2

4.2.2.1 Experimental design

The experimental design for GAG removal and subsequent testing is summarised in Figure 4.5 A total of 12 pSFT procured from porcine legs within 24 h of each other (slaughter date within the same week) were divided into control and treated groups (n = 6 in each group). The treated group was subjected to GAG-depletion using the enzyme ChABC, the control group followed the same incubations without the enzyme (see Figure 4.5).

A cylindrical plug was taken from the ankle region of each pSFT as per section 4.2.1.4. The remaining bulk tendon was normalised to a consistent height for all specimens. Excess tendon was removed using a scalpel (No. 11) from the toe region of the pSFT. The bulk pSFT was then shaped to a dumbbell conformation as per section 2.2.3.1. This would allow wet weights to be comparable at different time points. Both dumbbell and cylindrical specimens were placed in an individual 150 mL sterile pots which had been previously weighed. The weight of each pot with tissue was recorded. The wet weight of the tissue was calculated by subtracting the pot weight from the weight of the pot with the tissue.

Compression testing was then conducted on the cylindrical specimens of the treated group, and stress relaxation (non-destructive) testing was conducted on the dumbbell specimens of the treated group. This would provide information regarding the mechanical performance of the tissue prior to being subject to GAG depletion by ChABC action, guaranteeing the mechanical properties obtained after GAG depletion would be attributed to the treatment and removal of GAGs from the matrix, and not due to biological variability or compromised mechanical integrity due to destructive loading.

The process of enzymatic degradation of GAGs involved subjecting the specimens to equilibration and treatment, detailed subsequently. Wet weights were recorded again at two different time points during this process. Once the enzymatic treatment was over, specimens were subjected to mechanical testing as per Figure 4.4 Cylindrical plugs were loaded in confined conditions following the standardised method described in section 4.2.1.4, whereas the dumbbell specimens were subjected to stress relaxation testing first (see Section 2.2.3.3), before allowing a period of 24 h before it was subjected to strength testing. Finally, GAG quantification assays were conducted on cylindrical and dumbbell specimens as detailed in section 4.2.2.2.

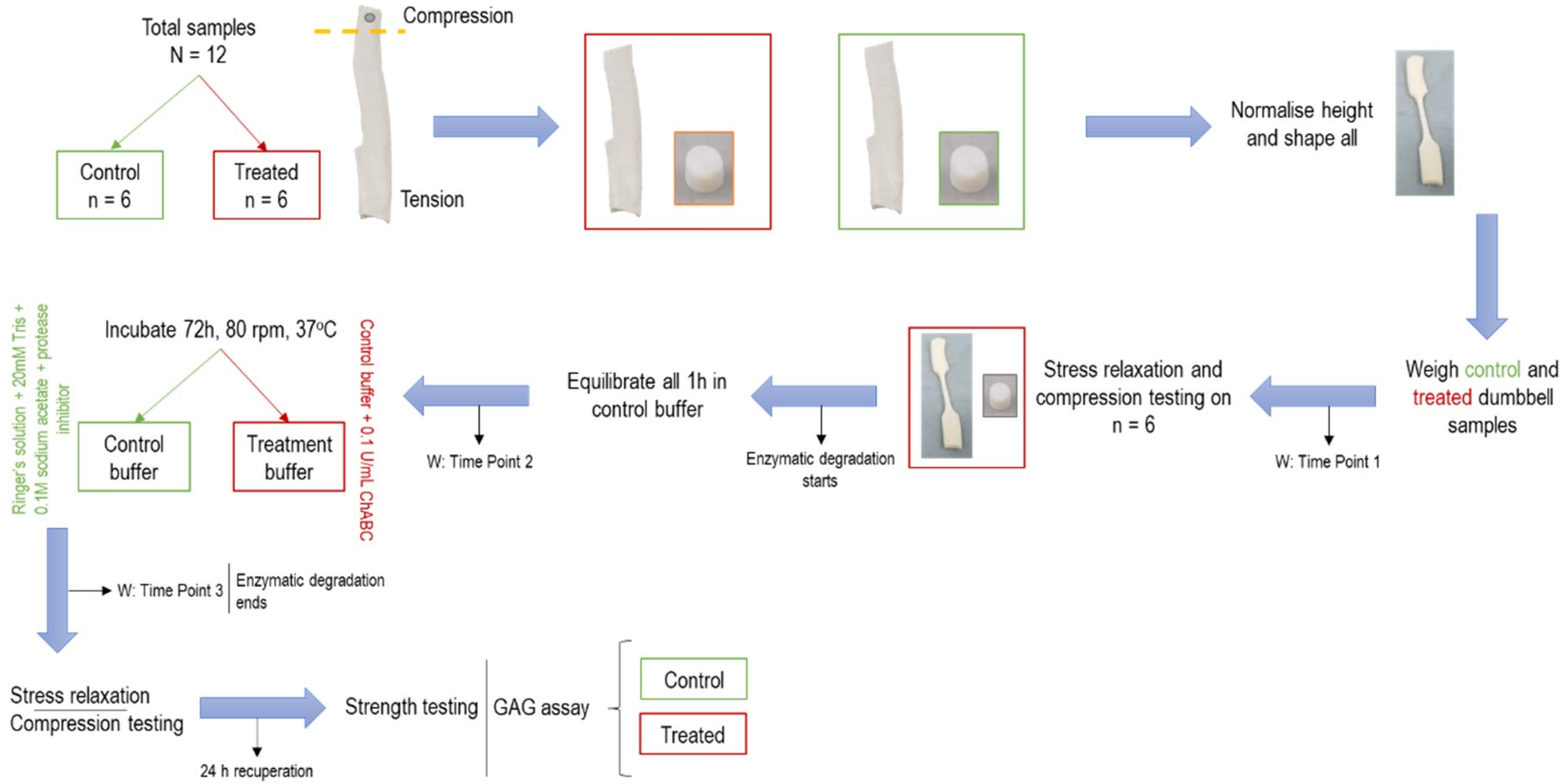

Figure 4.5: Experimental design for effect of GAG removal on biomechanics of pSFT in tension and compression. Control (green) and ChABC treated (red) pSFTs were divided into bulk tissue (for tensile testing) and cylindrical plugs (for compression testing). The bulk tissue was adjusted to maintain a consistent height between samples before shaping into dumbbells. Both groups were weighed at different time points during the process for swelling monitoring. Enzymatic degradation was carried out with an initial equilibration for both groups in control buffer, followed by their respective treatment for 72 hours. Mechanical testing was conducted after treatment and GAG quantification was performed for both groups.

4.2.2.2 GAG removal from superflexor tendon matrix Preparation of solutions

Control buffer (20 mM Tris, 0.1 M sodium acetate, 10 KIU/mL aprotonin)

Eight Ringer's solution tablets, 2.42 g of Trizma, and 9.8 g of sodium acetate were dissolved in 1 L of deionised water using a magnetic stirrer and stirrer bar. Solution pH was adjusted to 7.2 – 7.4 by adding 6 M hydrochloric acid or 6 M sodium hydroxide using a Pasteur pipette while stirring the solution. It was then autoclaved at 121 °C, 15 psi for 20 min. Aprotonin (1 mL) and Pen Strep (20 mL) were added immediately prior to use in sterile conditions, inside a biological safety cabinet.

Bovine Serum Albumin (0.01% w/v BSA)

Bovine serum albumin (0.1% w/v, 1 mL) was diluted in 9 mL of deionised water. It was then filtered using 5 mL syringes and a 0.22 µm filter, transferring it into a polypropylene universal. This was performed in sterile conditions, inside a biological safety cabinet (Class II). The solution was stored at -20 °C until it was used (within 24 h).

Chondroitinase ABC buffer (0.1 U/mL ChABC)

The ChABC (10 U) was reconstituted by adding 500 µL of 0.01% w/v BSA solution. The reconstituted solution was then transferred into a polypropylene universal and the volume made up to 5 mL using the 0.01% w/v BSA solution. The ChABC (5 mL) was added to 95 mL of control buffer (0.1 U/mL) immediately prior to use. This was performed in sterile conditions, inside a biological safety cabinet.

GAG removal method

Enzymatic degradation was adapted from (Henninger et al., 2010), beginning with an equilibration of all specimens in 60 mL of control buffer. This was added to each pot with an individual specimen in sterile conditions, inside a biological safety cabinet. The pSFTs were left in the buffer at 37 °C, with gentle agitation using an orbital shaker (80 rpm) for 1 h. Specimens of the ChABC treated group and control group (n = 6 in each group) were then transferred into a single 250 mL sterile pot and 100 mL of their respective solution (control buffer or ChABC solution) was added to each pot in sterile conditions. This was left for 72 h at the same agitation and temperature as previously stated. After 24 h, amphotericin B (2 mL) was added to each 250 mL pot in sterile conditions, before resuming agitation.

4.2.2.3 Validation of GAG removal

For validation of GAG removal using ChABC, two sets of specimens were subject to quantification methods. The specimens subjected to confined compression were macerated and lyophilised (see Section 2.2.4.1) 24 h after testing. Bulk tissue (6 ± 1 mm height, 3.5 ± 0.1 width, natural thickness) was taken from the dumbbell shaped specimen 24 h after being subject to tensile testing and lyophilised using the same method. The specimens used as controls during ChABC treatment were also separated into the two specimen groups described previously. This allowed direct comparison of native, control and ChABC treated groups. In addition, it helped determine compression loading had no adverse effect on GAG content within pSFT, such that variations were due to the treatment of each group and not influenced by external factors.

GAG quantification

GAG quantification was carried out as per section 2.2.4.2.

Histological evaluation

Native, control and ChABC treated specimens (3.5 mm height, natural width and thickness) were taken from the ankle insertion point (ankle region). Histological analysis using Safranin O/Fast green was carried out as per section 2.2.6.7. Longitudinal and transverse sections were analysed.

4.2.2.4 Tissue swelling during GAG removal process

Wet weights of control and ChABC treated groups were recorded at three time points during the GAG depletion process. The first time point was prior to equilibrating the specimens in control buffer for 1 h. The second time point was after the equilibration. Then the control group specimens were placed in control buffer and left agitating at 37 °C for 72 h while the treatment group was placed in ChABC treatment buffer in the same conditions for the same period of time. The final time point was after this occurred. Gross observations of each specimen were also made at each time point, including width and thickness measurements as described in Section 3.2.4. Bulk swelling tests have been conducted on tendon, reporting an impact on the tissue's material properties [328], so by recording wet weights and gross observations, a monitoring of pSFT swelling throughout the GAG depletion process was conducted. Swelling could therefore be disregarded as an influencing factor in the mechanical properties of GAG-depleted tendons.

4.2.2.5 Thermal stability of GAG depleted superflexor tendon

Thermal stability of GAG depleted tendon followed section 2.2.5.

4.2.2.6 Mechanical characterisation in compression

Confined loading was conducted on native, decellularised and GAG-depleted specimens as per section 4.2.1.4. Biphasic theory parameters aggregate modulus (H_A) and zero-strain permeability (k_0) were determined using a combined solving approach, employing FEBio (v 2.8) and custom Matlab algorithms and fitting ramp and hold phase data using a Nelder-Mead scheme [356].

The FEBio software is a nonlinear implicit finite element framework designed for analysis in computational solid biomechanics [357], which was used to develop a nonlinear biphasic poroviscoelastic finite element model with strain dependent permeability [358, 359]. The Nelder-Mead simplex method is an optimising technique used to obtain optimal values of k_o [360].

This was conducted through a collaboration with Dr Phil Riches from the University of Strathclyde, Glasgow.

4.2.2.7 Mechanical characterisation in tension

Sample preparation (see Section 2.2.3.1) was carried out during the initial phase of the GAG depletion process. Mechanical characterisation was conducted as per section 2.2.3.3 – 2.2.3.4.

4.2.2.8 Statistical analysis

Statistical analysis was carried out using GraphPad Prism (version 8, GraphPad software). Prior to analysis, data was checked for normal distribution using the Kolmogorov-Smirnov normality test. For comparing the mean of multiple groups, a one-way ANOVA with Tukey post hoc test was conducted. P values lower than 0.05 were deemed to be significant.

4.3 Results

4.3.1 Study 1

4.3.1.1 Statistical analysis

The mean compressive strain obtained at a frequency of 10 Hz (0.1 sec) of each decellularised group (n = 6 pSFT per group) was plotted against time resulting in Figure 4.6. All decellularised groups showed stress responses with well-defined ramp, peak and hold phases.

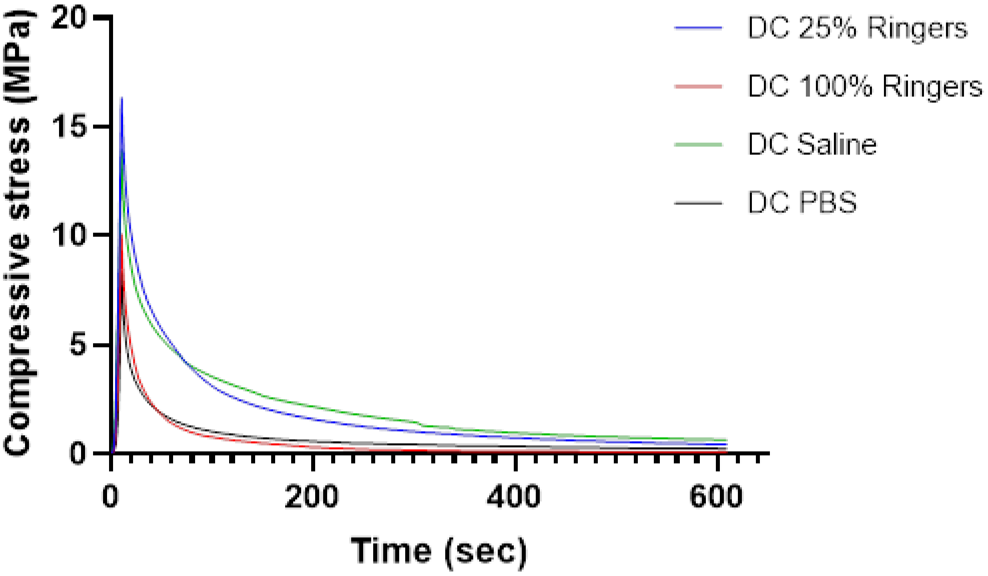

Figure 4.6: Mean compressive stress over time of decellularised (DC) groups. DC specimens tested in different hydration solutions, according to their modified decellularisation protocol, show different peak stress values and relaxation over time. Data is presented as mean (n = 6) for each group.

Peak stress of native pSFT ranged between 12.5 and 16 MPa, while decellularised pSFT ranged between 8 and 16.5 MPa (Figure 4.7). There were no significant differences between the heights of all specimen plugs prior to confined loading. There were no significant differences between native groups tested in different solutions, or decellularised groups tested in different solutions. The PBS decellularised group resulted in a significant reduction of almost half native peak stress value.

A two-way ANOVA with decellularisation and the different hydrating solutions as factors revealed a significant interaction effect (p = 0.0076) on the peak stress of pSFTs under compressive loads. This indicates that the effect of the solution used during testing differs between native and decellularised specimens, but neither has a significant effect alone. This is evident as the highest compressive peak stress for native pSFT occurred using PBS as the hydrating solution, followed by saline and 25% Ringers with similar peak stresses. This trend was not present in decellularised specimens.

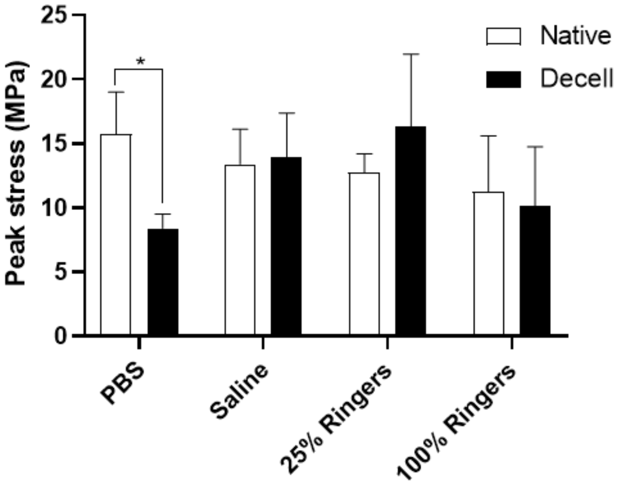

Figure 4.7: Compressive peak stress of native and decellularised (DC) pSFT in different solutions.
Significant decrease in compressive peak stress of DC PBS group compared to its native counterpart. Data was analysed using a two way ANOVA with Sidak's correction for multiple comparisons. Data is presented as mean (n = 6) ± 95% CI. * indicate significant difference between groups.

Equilibrium stress of native pSFT ranged between 0.21 and 0.34 MPa, while decellularised pSFT ranged between 0.1 and 0.67 MPa (Figure 4.8). There were no significant differences between the equilibrium stress of native groups tested in different solutions, or decellularised groups tested in different solutions. The saline group showed a significant increase in the decellularised specimens compared to its native counterpart, being almost twice the value of native pSFT tested in saline solution.

A two-way ANOVA analysis on equilibrium stress of all groups revealed again a significant interaction (p = 0.0045) effect. From the two factors, the solution resulted to significantly affect the results, while the decellularisation process itself appeared to have no significant effect.

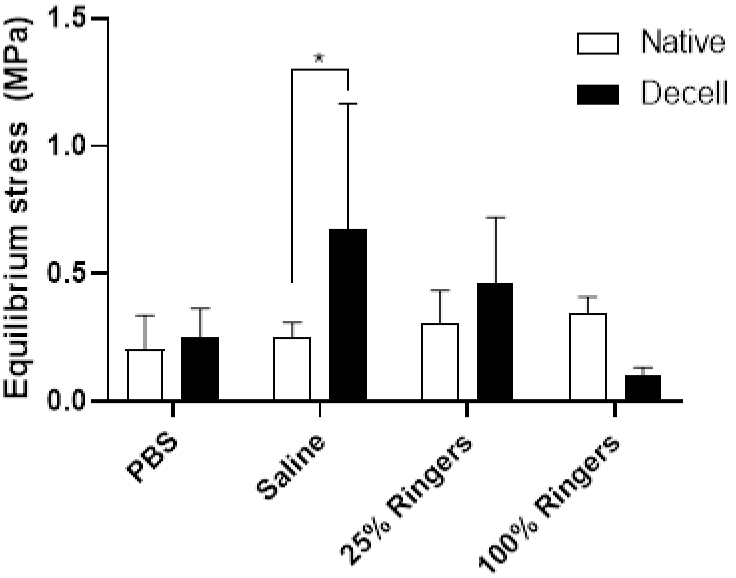

Figure 4.8: Compressive equilibrium stress of native and decellularised (DC) pSFT in different solutions.
Significant increase in compressive equilibrium stress of DC saline group compared to its native counterpart. Data was analysed using a two way ANOVA with Sidak's correction for multiple comparisons. Data is presented as mean (n = 6) ± 95% CI. * indicate significant difference between groups (right).

4.3.2 Study 2

4.3.2.1 Evaluation of GAG removal from superflexor tendon matrix

Relative GAG quantification

There were no differences in GAG content between native and control groups, both significantly higher than the GAG-depleted group (Figure 4.9). Native pSFT contained 3.46 ± 0.38 µg/mL, control pSFT from bulk and plug specimens (n = 6 for each specimen type, i.e. bulk and plug) contained circa 3.37 and 3.28 µg/mL, respectively. Following incubation with ChABC, GAG content was reduced significantly circa 85% with respect to the control group, with a GAG content of only ˜ 0.52 µg/mL. The two type of specimens (n = 6 for bulk and plug) used for GAG depletion validation revealed no significant differences within both the control group and the GAG-depleted group, showing compressive and/or tensile loading does not remove GAGs from pSFT matrix. Quantification of GAG content across different regions (ankle, middle regions) evidenced this matrix component appears consistent throughout the length of the tendon, barring the toe region, which was not specifically assessed at this time.

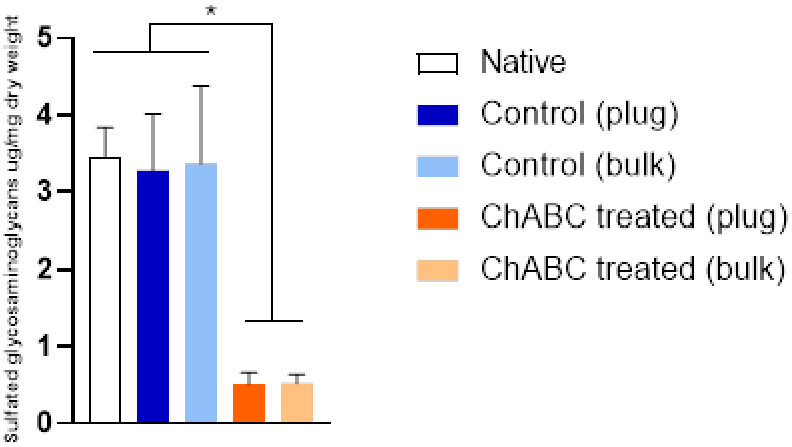

Figure 4.9: Relative sulfated GAG (ug of GAGs per mg of dry tissue weight) assay results for native, control and ChABC treated groups.
No significant difference between specimen groups (bulk tissue and cylindrical plugs) of both control and ChABC treated groups. Significant reduction post ChABC treatment compared to native and control groups. Data is presented as mean (n = 6) ± 95% CI. Data was analysed using one-way ANOVA followed by Tukey's post hoc test. * indicate significant difference between groups.

Histological evaluation

Native sections (Figure 4.10 A & D) showed an abundant GAG content throughout the matrix, particularly towards the peritenon. GAGs were largely distributed throughout the fascicular matrix in transverse sections (Figure 4.11 A), while aligned between the collagen in longitudinal sections (Figure 4.11 D). Similarly, GAGs were present in control sections (Figure 4.10 B & E), with no differences in matrix structure with respect to native tissue. GAG-depleted sections (Figure 4.10 C & F) showed no presence of GAGs. No cells were observed transverse (Figure 4.10C) or longitudinal (Figure 4.10 F) sections. No gross changes in the collagenous matrix were apparent post GAG-depletion (Figure 4.10 C & F).

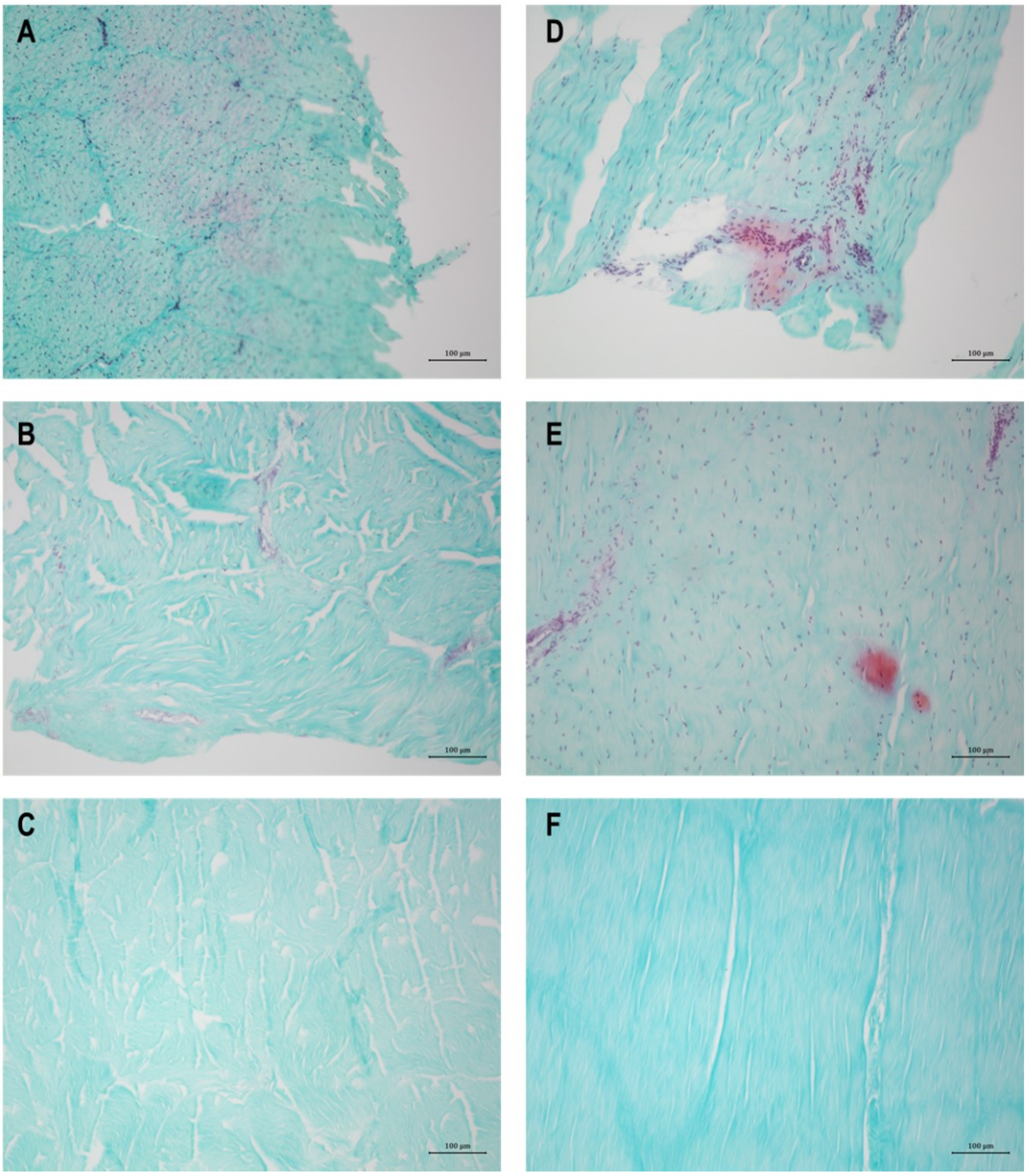

Figure 4.10: Representative micrographs of native, control and GAG-depleted sections of pSFT stained with Safranin O/Fast green.
Transverse (A - C) and longitudinal (D - F) sections of native (A, D), control (B, E) and GAG-depleted (C, F) pSFT show presence of pink-red GAGs in native and control sections but not in ChABC treated sections. Presence of cells in native and control section, but none apparent in GAG-depleted sections. Images were taken at 100x magnification (scale bar 100 µm).

4.3.2.2 Thermal stability of GAG depleted superflexor tendon

The thermal denaturation scan of native and GAG-depleted specimens (Figure 4.11) showed a reduction in transition temperature for GAG-depleted pSFT.

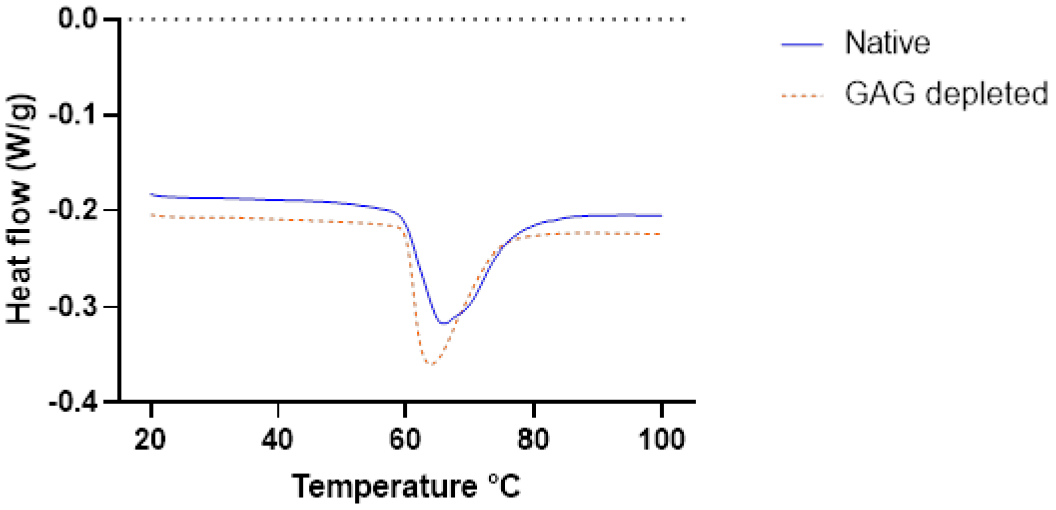

Figure 4.11: Thermal denaturation scans of native and GAG-depleted pSFT. GAG-depleted specimens show a reduction in transition temperature compared to native specimens. Data is presented as mean (n = 6) for each group.

Transition temperature and enthalpy of denaturation are presented in Table 4. There was a with significant reduction in the transition temperature of the GAG-depleted group of circa 3 °C. No statistical differences were found in the enthalpy of native and GAG-depleted groups.

Table 4.1: Thermal stability of native and ChABC treated groups.

	Native	**GAG-depleted**
Transition temperature (°C)	67.44 ± 1.47^a	64.17 ± 0.41^b
Enthalpy (J/g)	19.36 ± 1.08	18.24 ± 1.28

Thermal parameters of the denaturation of native and GAG-depleted pSFT. Significant decrease in transition temperature of GAG depleted pSFT. Data was analysed using an unpaired Student's t-test. Groups in each row that do not share the same superscript are significantly different. Data is presented as mean (n = 6) ± 95% CI.

4.3.2.3 Tissue swelling during GAG removal process

Wet weights of the three time points (TP) for control and ChABC treated groups increased with a similar trend. Wet weights prior to equilibration were not different between groups. A one-way ANOVA revealed both groups increased significantly from TP1 to TP2 and from TP1 to TP3. Control and ChABC treated specimens had similar wet weights at TP2 (post-equilibration), with a mean increase of ˜ 36% and 31% from TP1, respectively.

Gross observations did not reveal major variations in tissue swelling profiles of one group over the other. A mean increase of 35% and 40% occurred from TP1 to TP3 for control and ChABC treated groups, respectively (Figure 4.12). Wet weights at TP3 were not statistically compared between groups as this data was used to monitor swelling after ChABC treatment [349, 361]. Total percent increase in wet weight suggested water content did not significantly influence the mechanical properties obtained from these specimens.

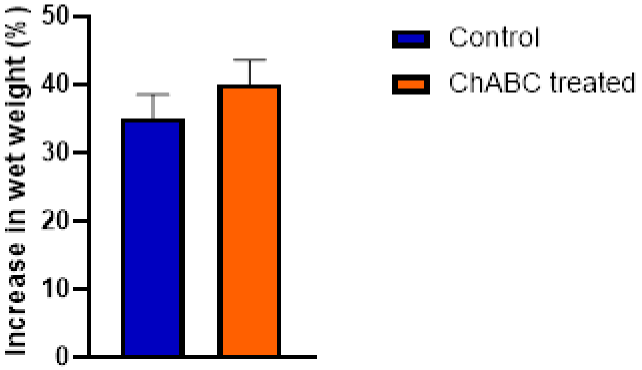

Figure 4.12: Tissue swelling percentage increase from TP1 to TP3.
TP1 – prior to equilibration in control buffer, TP3 – after 72 h incubation in control/treatment buffer. Control and ChABC treated groups increased 35% and 40% from TP1 to TP3. Data is presented as mean (n = 6) ± 95% CI.

4.3.2.4 Contribution of glycosaminoglycans to superflexor tendon mechanics in compression

There were no significant differences between the heights of all specimen plugs prior to testing. The mean compressive strain obtained at a frequency of 10 Hz (0.1 sec) of each group (n = 6 pSFT per group) was plotted against time resulting in Figure 4.13. Native, decellularised and GAG-depleted specimens showed stress responses with well-defined ramp, peak and hold phases. Peak phase of native and GAG-depleted specimens showed most discrepancy.

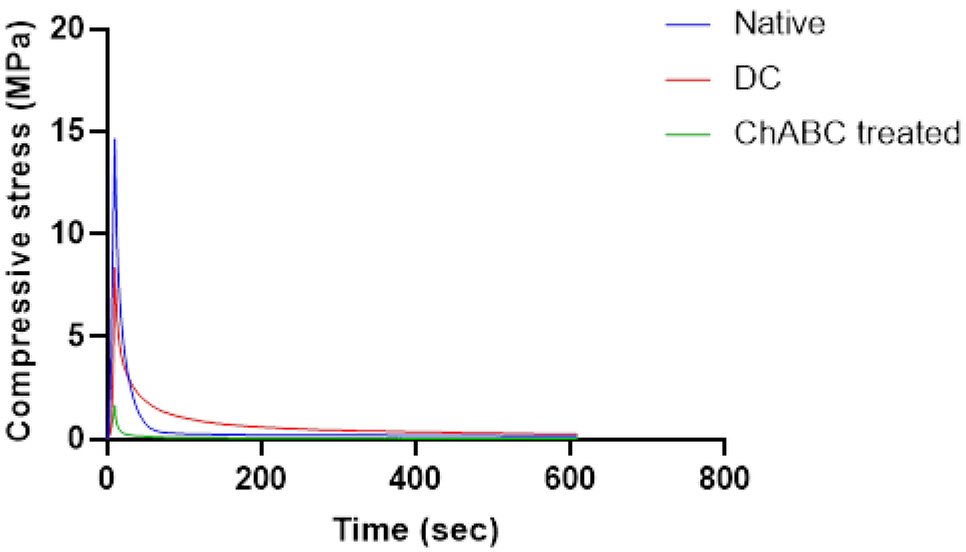

Figure 4.13: Mean compressive stress over time of native, GAG-depleted and decellularised (DC) pSFTs.
Notable difference between the peak phase and relaxation over time of the three groups, with a reduction in GAG-depleted specimens compared to native. Data is presented as mean (n = 6) for each group.

Peak stress of native pSFT was significantly higher than GAG-depleted and decellularised specimens. A drastic statistically significant reduction was observed in the GAG-depleted group. GAG-depleted specimens achieved circa 11% of native peak stress (Figure 4.14a), reduced compared also to decellularised specimens. Equilibrium stress of native specimens had ˜ 100 kPa variation towards the end of the hold phase (Figure 4.14b), not significantly different from GAG-depleted or decellularised specimens. GAG-depleted specimens had a significantly reduced equilibrium stress compared to decellularised specimens. The final 30 s of the hold phase saw less than 113 kPa change in stress.

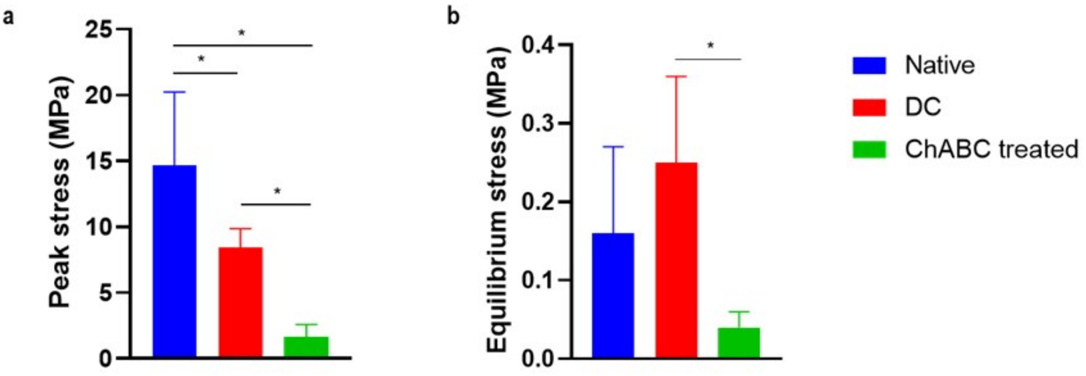

Figure 4.14: Peak and equilibrium stress of native, GAG-depleted and decellularised (DC) pSFTs.
Significantly reduced peak stress (a) of GAG-depleted specimens compared to native and DC pSFTs. Significant reduction in equilibrium stress (b) of GAG-depleted group compared to DC pSFTs. Data is presented as mean (n = 6) ± 95% CI. Data was analysed using one-way ANOVA followed by Tukey's post hoc test. * indicate significant difference between groups.

The aggregate modulus of native, decellularised and GAG-depleted groups is shown in Figure 4.15. Native specimens' aggregate modulus was significantly higher than the GAG depleted group. Aggregate modulus decreased with GAG content, with a reduction ˜ 74% compared to native pSFTs. Decellularised specimens had a similar aggregate modulus to native specimens, significantly higher compared to GAG-depleted pSFTs.

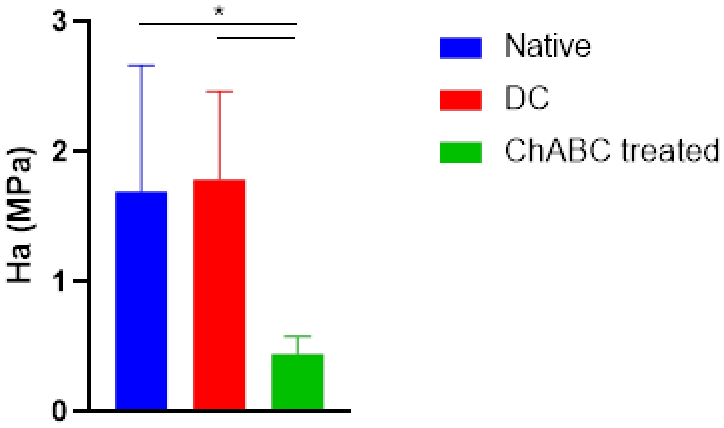

Figure 4.15: Aggregate modulus of native, GAG-depleted and decellularised (DC) pSFTs.
Significant reduction in aggregate modulus of GAG-depleted group compared to both native and DC pSFTs. Data is presented as mean (n = 6) ± 95% CI. Data was analysed using one-way ANOVA followed by Tukey's post hoc test. * indicate significant difference ($p < 0.01$) between groups.

Contrary to the aggregate modulus, the zero-strain permeability of GAG-depleted specimens was significantly higher than decellularised pSFTs, though not statistically different from native specimens. Permeability thus appears to be affected by the decellularisation process, with a mean reduction of ˜ 93% compared to native pSFTs, as seen in Figure 4.16.

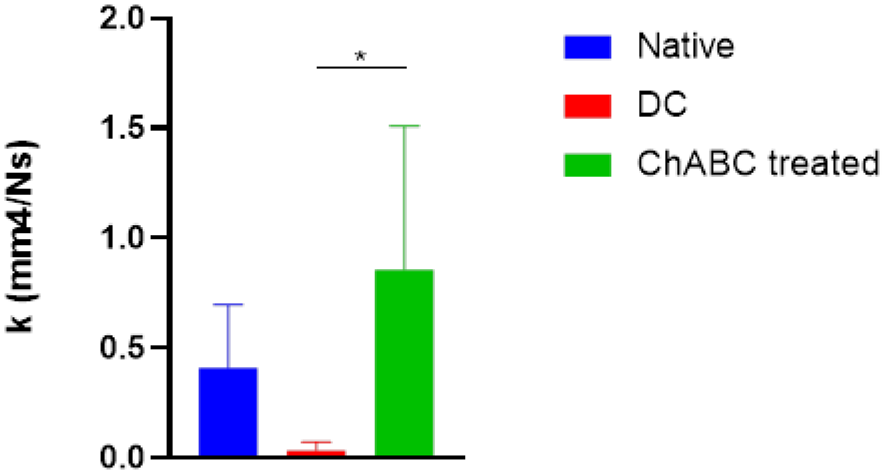

Figure 4.16: Zero-strain permeability of native, GAG-depleted and decellularised (DC) pSFTs.
Significant increase in permeability of GAG-depleted pSFTs compared to DC. Data is presented as mean (n = 6) ± 95% CI. Data was analysed using one-way ANOVA followed by Tukey's post hoc test. * indicate significant difference between groups.

4.3.2.5 Contribution of glycosaminoglycans to superflexor tendon mechanics in tension

When subjected to strength testing, mid-substance failure of all specimens was achieved. There were no significant differences between native and GAG-depleted specimens (Table 4.2). There was a significant reduction in E_{linear} of decellularised specimens compared to both native and GAG-depleted groups. Similarly, UTS was significantly reduced for decellularised specimens compared to GAG-depleted, but not different from native pSFT.

Table 4.2: Strength testing parameters determined by uniaxial tensile testing.

	E_{toe} (MPa)	E_{linear} (MPa)	UTS (MPa)	ε_{Fail} (mm/mm)
Native	78.20±18.29	585.77±111.18^{a}	67.40±9.06^{a,b}	0.18±0.02
Decellularised	38.94±17.78	441.06±82.86^{b}	55.53±11.84^{b}	0.20±0.03
GAG-depleted	110.35±86.41	611.03±86.08^{a}	79.37±15.53^{a}	0.17±0.02

Data were compared using one-way ANOVA followed by Tukey's post hoc test. Groups in each column that do not share the same superscript are significantly different. Data are presented as means (n = 6) ± 95% CI.

Stress relaxation parameters (Table 4.3) showed no significant difference in the time-independent relaxation moduli (E_0) between native and GAG-depleted groups. However, there was significant reduction in the decellularised group when compared to remaining groups. The time-dependent relaxation moduli, E_1, of GAG-depleted specimens was significantly higher compared to native and decellularised groups, while decellularised specimens had a significantly reduced E_1 compared to its native counterpart. The time-dependent relaxation moduli, E_2, was significantly reduced for decellularised specimens compared to GAG-depleted, but not different from native pSFT.

Table 4.3: Stress relaxation parameters.

	E_0 (MPa)	E_1 (MPa)	E_2 (MPa)	T_1 (s)	T_2 (s)
Native	207.90 ± 45.60^{a}	14.94 ± 7.24^{a}	$6.52 \pm 3.08^{a,b}$	0.84 ± 0.32	4.10 ± 3.50
Decellularised	84.04 ± 19.84^{b}	6.98 ± 2.21^{c}	1.97 ± 2.40^{a}	0.96 ± 0.43	7.97 ± 3.12
GAG-depleted	209.03 ± 37.65^{a}	24.03 ± 3.23^{b}	10.45 ± 6.61^{b}	0.92 ± 0.71	7.64 ± 7.18

Data were compared using one-way ANOVA followed by Tukey's post hoc test. Groups in each column that do not share the same superscript are significantly different. Data are presented as means (n = 6) ± 95% CI.

4.4 Discussion

4.4.1 Confined compression characterisation of native and decellularised superflexor tendon

The trend in the compressive mechanical behaviour of all groups aligns with their tensile mechanical behaviour. The decellularised 25% Ringers group showed the highest compressive peak stress compared to other decellularised specimens (Figure 4.7). Similarly, the decellularised 25% Ringers group had the highest linear modulus and tensile strength under tension (see Section 3.3.6, Table 3.5). The decellularised PBS group resulted in the lowest compressive peak stress of all decellularised specimens, similarly to the lowest linear modulus and tensile strength obtained for this group during tensile characterisation (Table 3.5). The remaining groups (100% Ringers, saline), containing the same NaCl content, displayed similar compressive peak stresses between native and decellularised specimens, whereby similarities in the tensile properties of decellularised specimens belonging to these groups were observed (toe and linear moduli, UTS; Table 3.5).

GAGs, an important component of tendon matrix, are situated in areas mainly subject to compressional force [362], and are also sparsely distributed between collagen fibrils throughout the endotenon [80]. Their contribution to load bearing mechanisms remains debated [351], yet GAGs associated with PGs may facilitate tendon matrix resistance to high compressive forces [300]. This can be explained through tissue hydration mechanisms, as the charged molecules in the tissue resist the exudation of fluid. Therefore, the mechanical and water-binding function of GAGs in decellularised pSFT matrix appeared not to be affected by decellularisation, as all but one group showed comparable compressive peak stresses to their native counterpart. Having proven GAG content remained post-decellularisation (see Section 3.3.2), the characterisation of decellularised pSFT in compression helped show the GAGs appear to maintain intact functions pertaining load bearing. However, this warranted further investigation, provided by Study 2. Finally, decellularised pSFT appears mechanically competent when compared to native tissue in compression, as well as in tension (Chapter 3).

The compressive peak stress of all decellularised groups aligns with the swelling observed in tissue post decellularisation (see Section 3.3.1). This indicates swelling may play a significant role in the mechanical behaviour of tendinous tissue subjected to compressive loads. It has been shown that PBS-induced swelling increases fibril diameters and inter-fibrillar distances [257], affecting the interactions between matrix components from a sub-fibril and fibril level, affecting tendon hierarchically to the macroscale. Increasing the distance between GAG chains as consequence of tissue swelling, could affect their ability to interact with collagen, disturbing matrix structural integrity. Accordingly, the ability of the tissue to withstand compressive loads is compromised. This is observed in the significant reduction in compressive peak stress observed in decellularised PBS group, compared to native specimens. Further, compressive peak stress decreased with increasing swelling, suggesting the extent to which the mechanical capabilities of decellularised tissue in compression are affected, may depend on intra- and inter-fascicular organisation, including collagenous and non-collagenous component interactions influenced largely by swelling of pSFT.

The effect of swelling in compressive properties of tendon has not been studied in detail. However, the influence of cartilage swelling on its mechanical behaviour under compression has been investigated [267, 340, 363], relating to the salinity of hydrating solutions. The outcomes report a reduction in compressive and equilibrium moduli with increasing bath salinity. This is in agreement with the results presented, having the highest compressive peak stress in the 25% Ringers group, with the lowest salinity compared to remaining solutions. PBS appears to adversely affect tendinous tissue likely combining increased swelling of the tissue with a disruption to the matrix, component interactions and water-matrix interactions, leading to the significant reduction in compressive peak stress observed.

Studies analysing tissue swelling in tendon [261], cartilage[267, 340, 363–365], aorta [366] and skin tissue [367], it has proven a consensus that a hypotonic medium, with a lower concentration of solute (NaCl) or least salinity, increases water content and thus swelling. Conversely, lesser swelling and water content occurs in a hypertonic medium. The mechanisms underlying this phenomenon are various, including the negatively charged GAGs within the tissue, which attract positively charged ions creating a Donnan osmotic pressure, helping maintain tissue hydration, thus contributing to swelling. The interactions between PGs/GAGs occurring through repulsive forces between the negatively charged molecules, as well as electrostatic and mechanical interactions between matrix components also contribute to swelling. However, the inverse phenomena is true for decellularised pSFT (see Section 3.3.1), where the lowest salinity reduced tissue swelling. Given collagen and GAG content were not affected by the decellularisation process, it may be that removing the cellular content from tissue matrix imbalanced the mechanisms described previously.

The compressive equilibrium stress is based on stress decaying during the relaxation phase of the experiment until it reaches an asymptotic value, which proves informative pertaining tissue deformation [368]. A higher equilibrium stress is indicative of tissue with a greater capability to resist deformation. A characteristic property of equilibrium stress is that when relaxation under specific loading stops, the load may be maintained at constant strain indefinitely, and the stress on the material would reach the steady state stress, or equilibrium stress [356, 368]. Native specimens showed similar values irrespective of the hydrating solutions, showing consistency in native pSFT tissue deformation under compressive loading. Decellularised specimens resulted dissimilar between groups, yet with higher stress values compared to native counterparts, suggesting their ability to withstand deformation under compression remained unaffected post-decellularisation.

The compressive equilibrium stress of native specimens tested in different solutions showed little discrepancies between groups, contrary to the values obtained in pSFT post-decellularisation, which suggests the solution itself does not solely affect the fluid flow and ultimate equilibration of tendinous tissue after being subjected to compressive loading. Removing the cellular components from pSFT matrix appears to influence the mechanisms in which the tissue exudes fluid and reaches equilibrium after compression. Further, the decellularised matrix appears to interact differently to the different solutions used, with a more apparent distinction between the compressive mechanical behaviour among decellularised groups. It was discussed in Chapter 3 that the IFM interacts with fluids as a result of being highly hydratable [327]. The hypothesised rearrangement or disruption caused by the decellularisation process may have altered the manner in which the matrix interacts with the different solutions, ensuing greater variability in both the peak and equilibrium stresses when comparing decellularised groups. Finally, it may be of interest to further investigate the inhomogeneous compressive properties of pSFT. Physiological compression would occur in localised areas of the tendon, namely terminal regions [31, 331], so this behaviour would be relevant to characterise. Limited studies have been conducted to date, proposing an inhomogeneous nature of tendinous tissue [335, 336].

Peak and equilibrium stress of decellularised pSFT remains comparable to native tendon, proving capable of withstanding compressive loads, providing a more complete mechanical profile, essential for a potential biological graft.

4.4.2 Evaluation of GAG removal from superflexor tendon matrix

ChABC treatment removed circa 85% of GAGs with respect to native pSFT (Figure 4.9). This significant reduction was likely due to cleaving of chondroitin sulfate A, C, dermatan sulfate and hyaluronic acid chains [345]. ChABC removes chondroitin and dermatan sulfate from both large and small proteoglycans in tendon [369]. Generally, the most abundant proteoglycan in tendon is decorin [370], possessing a single dermatan or chondroitin sulfate chain, possibly involved in maintaining interfibrillar spacing [371].

While ChABC treatment removed most GAGs in pSFT matrix, it is likely that the remaining 15% of GAGs in the GAG-depleted specimens accounts for keratan sulfate of heparan sulfate chains [127, 257], along with partially cleaved GAGs that may have not been fully removed during washing steps. However, the mechanical integrity and overall function of these remaining GAGs remained unknown. By subjecting GAG-depleted pSFT to tensile and compressive loading (Study 2), their contribution to the mechanical integrity of the tissue was investigated.

Finally, GAG content was not reduced in the control group (Figure 3.7), signifying GAG-depletion was in fact a result of enzymatic degradation. Histological evaluation was carried out using Safranin O staining as the most optimal for GAG visualisation (see Section 3.3.4). Native and decellularised sections showed GAG presence (Figure 4.10), whereas GAG-depleted sections showed only a green-stained matrix. The lack of cellular content was attributed to the role GAGs play in cell to cell and cell to extracellular matrix adhesion [372–374]. The mechanisms in which these adhesions occur were disrupted when GAGs and associated proteoglycans were cleaved during ChABC treatment. This resulted in the loss of cellular material during the GAG-depleting process. During subsequent fixing, processing and staining processes, cellular loss continued to occur, thus leaving an otherwise unaffected matrix with no cellularity. Furthermore, the unaltered histoarchitecture of pSFT matrix following ChABC treatment suggests the enzymatic action during incubation had no adverse effects on collagen structure, organization or content. This translates as minimal proteinase activity in the samples, attributed to the use of aprotonin during incubation periods. The subsequent analysis of mechanical behaviour in tension and compression can therefore be attributed to the effects of GAG depletion in isolation.

4.4.3 Thermal stability of GAG depleted superflexor tendon

The change in the shape of the thermal denaturation peak of GAG-depleted samples (see Figure 4.11) may be a consequence of minor changes in the structural state of the collagen network caused by GAG-depletion. However, both sharp denaturation endotherms are characteristic of the collagen triple helix structure [375], suggesting no adverse effects on collagen molecule quality or crosslinking occurred during enzymatic degradation. The baseline shift observed may due to a decrease of the thermal capacity of GAG-depleted tissue caused by the loss of bound water clusters [375].

Enthalpy of denaturation derives from the energy required to disrupt hydrogen bonds within collagen molecules that provide its characteristic secondary structure, in addition to breaking hydrophobic interactions with water [376]. This indicates enthalpy is influenced by an intrinsic composition of collagen and water presence around said molecule [287]. DSC revealed enthalpy was not significantly different between native and GAG-depleted groups. This suggests no adverse effect on the collagen in pSFT matrix occurred during GAG-depletion processes. Despite the water-binding role of GAGs, it appears their loss did not reduce water content enough to produce adverse effects on enthalpy of denaturation.

Transition temperatures of native and GAG-depleted pSFT are within a range comparable to previously conducted differential scanning calorimetry methods [223]. The significant reduction in the GAG-depleted specimens (Table 4.1) is in fact comparable to the transition temperatures obtained in decellularised pSFT (see Section 3.3.3). Removing GAGs from the extracellular matrix of pSFT did not lead to a significant alteration of the packing density of collagen molecules. However, it is possible a minor change in the conformational freedom of collagen, by removal of a matrix component, may have caused an almost negligible reduction in thermal stability [377], translated as the statistical difference between the transition temperature of native and GAG-depleted pSFT.

4.4.4 Contribution of glycosaminoglycans to superflexor tendon mechanics in tension and compression

Having demonstrated that GAG content is unaffected by decellularisation (see Section 3.3.2), and with the insight provided in the compressive mechanical assessment of decellularised specimens in Study 1 (see Section 4.3.1), an alternative mechanism may be responsible for the difference in compressive peak stress following cellular and nucleic acid removal. A potential effect of decellularisation on collagen is unlikely to be solely responsible for the reduced compressive peak stress, given its mechanical contribution to bearing compressive loads is less prevalent than non-collagenous ECM components [336]. A similar trend regarding the mechanical contribution of collagenous and non-collagenous components to withstand compressive loading is observed in cartilage [378]. One hypothesis is that the decellularisation process may instigate a change in the three-dimensional architectural network of endotenon through a rearrangement of collagen-GAG interactions. Further, the reagents used throughout the decellularisation process could affect the peritenon structure of pSFT. This is a thin layer of connective tissue, composed of paratenon and epitenon, which envelop the endotenon [13, 26, 300, 379]. It acts like a tube, stabilising the matrix components within it [336]. The collagen and elastic fibres of which it is comprised helps maintain the structural integrity of the tube. An alteration to these structures would compromise their ability to resist deformation under compression, perhaps resulting in a reduced compressive peak stress.

Both peak and equilibrium stresses demonstrated significant reductions relative to GAG content, further proving this matrix component plays a key role in bearing compressive forces. The reduction in peak stress is in agreement with previous findings involving porcine ligament [350]. GAG-depleted specimens' peak stress was reduced circa 89% compared to native pSFT. As negatively charged molecules, GAGs play a role in maintaining the structural integrity of tissue matrix [78, 80, 347]. Sodium and water are attracted to GAGs, which are then bound by them. Thus, a water molecule shell is formed enveloping the GAGs. When a load is applied, the water molecules are released, yet the shell is re-formed as the load is removed [80]. GAG depletion reduces the ability of tendon matrix to bind water, through a change in osmotic swelling pressure that can no longer occur as a result of an absence of negatively charged GAGs. The water molecule shell can no longer be formed, so when a load is applied, the exudation of water is faster. This reduces the ability to support compressive loads, explaining the reduction in both peak and equilibrium stress.

The aggregate modulus is a flow-independent measure of stiffness, i.e. intrinsic stiffness of the solid matrix. As aggregate modulus increases, tissue resists deformation under load with more ease [380]. This property provides insight into the mechanical function of GAGs in compression. The aggregate modulus of native and decellularised groups was similar, with no statistical difference between groups. Given GAG content is not reduced with decellularisation, this suggests that the mechanical role of this matrix component in withstanding compressive loads also remains post-decellularisation. Decellularised pSFT appears to withstand compressive loads as effectively as its native counterpart. However, the aggregate modulus of GAG-depleted specimens was drastically lower than both native and decellularised pSFT, decreasing with GAG content. This is indicative of the crucial contribution of GAGs in resisting compressive forces, which is likely carried out via the shell mechanism described previously. The ChABC action mechanism targets chondroitin sulfate A, C, dermatan sulfate and hyaluronic acid chains [345]. It could therefore be hypothesised that dermatan and chondroitin sulfate are the primary GAGs involved in compressive load bearing, as their removal led to a drastic reduction in tissue stiffness. Chondroitin sulfate has been found to resist compressional forces in cartilage matrix [381], concurring with this hypothesis. The remaining 14% of GAGs post-ChABC treatment, likely keratan sulfate of heparan sulfate chains [127, 257] could then play a less important role during compression.

A comparable aggregate modulus or stiffness to native tendon poses not only an obvious mechanical advantage for decellularised tissue, but also relates to cell behaviour [356]. Cells require a solid material to adhere to, referred to as anchorage dependence [382]. Stiffness has been shown to play a role in cell anchorage, as cells actively probe and respond to mechanical cues in their immediate environment [383]. Significant changes to tissue stiffness could therefore impact cell adhesion, growth and gene expression [382]. Stiff adhesion materials have been related to well spread, phenotypically and morphologically sound cells, whereas more flexible materials lead to irregularly shaped and less stable cells and associated cellular activity [384]. As a potential graft for ACL reconstruction, decellularised pSFT stiffness would provide consistent mechanical cues to cells that attempt to repopulate the graft once implanted into a host. This would lead to desirable cell behaviour, facilitating attachment and proliferation, ultimately leading to matrix renewal through neo-tissue development.

Permeability provides information regarding resistance to fluid flow through tissue matrix [380]. GAG-depleted pSFT resulted twice as permeable as native pSFT, signifying increased velocity and ease in water exudation with reduced GAG content, likely attributed to the water binding function GAGs carry out in tissue ECM, which was previously described. A study involving porcine ligament also reported a significant increase in transverse permeability after GAG depletion [350]. This study presented similar results in cartilage. Cartilage appears less permeable with tissue maturity [385]. The reduction in permeability may also occur as a consequence of the structural and conformational alterations following the removal of cellular material during decellularisation. In Chapter 3 (see Section 3.4.6), the IFM or endotenon was postulated as potentially undergoing such changes during decellularisation, translating to altered tendon mechanics under tensile loading. The IFM is constituted by glycoproteins, mainly from the small leucine-rich proteoglycan family (SLRP), including decorin, lumican, biglycan and fibromodulin [23], along with some collagenous components. These proteins create interfibrillar bridges between GAGs and collagen microfibrils, assembling structures throughout the tendon [386]. Such organisation may be disrupted during the decellularisation process, caused by any chemical, enzymatic or mechanical methods. This in turn could have influenced the interaction of the IFM with fluids, resulting in a lower permeability.

It should be mentioned that these results do not fully align with the increased fluid flow and permeability post-decellularisation reported in Chapter 3, and in previous studies [220, 224]; however, only tensile loading was studied thus far, and therefore, the results obtained under compression may warrant further investigation.

There were no differences in the stress-strain profile and classical material properties of GAG-depleted specimens compared to native pSFT, suggesting the removal of GAGs has no major effect on tendon capacity to withstand tensile loads. In the linear region of loading, collagen fibres withstand incremental loads through interfibrillar sliding mechanisms, involving interfibrillar PGs and interaction with collagen fibres [387]. Dermatan sulfate bridges interfiribrillar spacing more so than other GAGs present in tendon [388]. Through the enzymatic action of ChABC, this GAG was likely removed completely, suggesting this and additional GAGs involved in interfibrillar sliding mechanisms play no major role in withstanding tension. This aligns with a study conducted on human medial collateral ligament, where tensile material properties resulted unaffected after targeted removal of dermatan sulfate [389]. Even at lower levels of scale, GAG removal has been shown to have a small influence on tensile mechanical properties in tendon [348, 349, 390]. It can therefore be suggested that collagen is the principal ECM component contributing to the tensile mechanical properties of tendon, likely supported in some minor capacity by non-collagenous matrix components other than PG-GAGs.

Long collagen fibrils may be capable of transferring loads between one another without the presence of interfibrillar GAGs [351]. It is possible that due to collagen length in the specimens used, tensile loading was achieved, almost comparably to that of native tissue, without requiring GAGs to aid in load-bearing mechanisms. Moreover, removal of GAGs may have led to a rearrangement in the fibrillar and non-fibrillar network of components in pSFT matrix. By removing GAGs, the matrix in which collagen lies may have been altered in such a way that fibres were more easily and readily recruited under increasing tensile loading. The re-orientation of collagen fibres would be facilitated, with less impediments from the surrounding endotenon [391]. However, the increase in the toe modulus of the GAG-depleted group may be related to an increase in stiffness influenced by GAG removal. While GAGs normally facilitate collagen fibril sliding in tension [349], their removal may have increased interfibrillar contact and friction [392] in the early stages of loading, leading to a rise in stiffness. This did not result in a statistical difference between toe moduli, perhaps attributed to the GAG-collagen ratio in pSFT matrix.

Stress relaxation parameters, with the exception of the time-dependent relaxation modulus, showed no difference between native and GAG-depleted specimens, suggesting GAGs do not play a significant role in the viscoelastic behaviour of tendon. This could be explained through the structural integrity and organisation of the collagen network, which compensates for the lack of non-collagenous components and interactions within pSFT matrix. This aligns with the conclusions drawn from studying human medial collateral ligament, which showed no relation between GAG and collagen interactions with viscoelastic mechanics [326]. It is possible that GAGs influence the long-term viscoelastic behaviour of pSFT, explained through the effect of water content in the tissue [251]. An increase in water content would allow freer matrix rearrangement and movement. However, it is difficult to conduct a test for analysing long-term viscoelastic behaviour of pSFT using the set-up described for stress-relaxation methods (see Section 2.2.3.2). The results presented here provide a short viscoelastic response.

4.5 Conclusion

The mechanical behaviour of native, GAG-depleted and decellularised pSFT in confined compression conditions was investigated for the first time. Similarly to the tensile mechanical properties (Chapter 3), the compressive properties of decellularised groups aligned with their level of swelling, with PBS showing reduced peak stress, while 25% Ringers group showed more native-like properties. Effective GAG removal resulted in a more compliant tissue with drastically reduced compressive aggregate modulus, but no reduction in tensile properties. Decellularisation did not reduce pSFT aggregate modulus but reduced its zero-strain permeability, likely related to changes occurring in the IFM as a consequence of the decellularisation process. Therefore, the mechanical integrity of GAGs in decellularised pSFT was proven, resulting a crucial component in compressive load bearing while playing a less significant role in withstanding tensile loads. Finally, the biomechanical properties of decellularised pSFT are mostly similar to native tissue in both tension and compression, capable of resisting loading as a graft, particularly surrounding fixation in vivo.

Chapter 5

Effect of decellularisation processes on the biomechanical and biological properties of porcine superflexor tendon at a sub-tendon scale

5.1 Introduction

The research conducted in Chapter 3 and 4 provided information about the consequences of decellularisation on the structure, composition and biomechanics of pSFT at the whole-tendon scale. In addition, previous research conducted on decellularised pSFT has also focused on whole tendon [220–225]. However, investigating at the sub-tendon scale is hypothesised to provide key information in terms of the structural, biological and nanomechanical effects of decellularisation on pSFT.

Similarly, the compositional and mechanical consequences of GAG depletion were explored in Chapter 4, revealing pSFT to be more compliant under very small loads. This is likely a structural consequence of GAG removal and worthy of investigating at the sub-tendon scale.

Fascicles are the functional units of tendon, constituted by tightly packed fibres and separated by endotenon or interfascicular matrix [393, 394]. Fascicles have not yet been studied in pSFT, and to the author's knowledge, there is no information on fascicle arrangement, structure and composition in decellularised or GAG-depleted tendon.

The mechanical properties of whole tendon are strongly influenced by the composition and organisation of the ECM at each hierarchical level [17]. Therefore, investigating at the fascicle level proves useful in better understanding structure-function relationships, and gaining insight into the causes of biomechanical and compositional changes occurring at the whole-tendon scale.

The outcomes of Chapter 3 and 4 led to the hypothesis that pSFT IFM was affected by the decellularisation process, likely influencing the biomechanical changes and swelling behaviour observed. Studying at the fascicle level will allow looking into pSFT IFM in more depth. It has been suggested that mechanical adaption is largely dependent on IFM composition [21, 395]. It is therefore relevant to investigate whether this constituent of pSFT was affected by decellularisation and in what ways.

Finally, in future studies conducted on decellularised pSFT involving cells, this research will help understand the underlying reasons of cell-matrix interactions and infiltrations. It may help predict if cell behaviour will be any different as a consequence of changes occurring at the sub-tendon and whole tendon scale.

5.1.1 Aim and objectives

5.1.1.1 Aim

The aim of this Chapter was to investigate the consequences of decellularisation and enzymatic GAG depletion on the composition, structure and mechanics of pSFT fascicles and interfascicular matrix.

5.1.1.2 Objectives

The specific objectives were as follows:

a) To develop a method for fascicle dissection and isolation from pSFT.

b) To characterise the structure of fascicles from native, decellularised and GAG-depleted pSFTs.

c) To qualitatively assess the composition of native, decellularised and GAG-depleted pSFT fascicles.

d) To characterise the hydrating behaviour of native, decellularised and GAG-depleted pSFT fascicles.

e) To investigate the topographical structure and features of native and decellularised pSFT fascicles.

f) To determine the mechanical properties of native and decellularised pSFT fascicles.

g) To characterise topographical structure and features of native and decellularised IFM.

h) To determine the mechanical properties of native and decellularised IFM.

5.2 Methods

5.2.1 Fascicle dissection

Fascicle dissection was carried out on native, decellularised and GAG depleted pSFTs, summarised in Figure 5.1. For native specimens, dissection of pSFTs from right hind legs was previously carried out per section 2.2.1. If fascicle dissection did not take place on the same day, whole pSFTs were stored at -20 °C wrapped in filter paper dampened with PBS until required. For decellularised specimens, decellularisation was carried out as described in section 2.2.2, using PBS solution throughout the process. For GAG depleted pSFTs, GAG removal was carried out per section 4.2.2.2, using low concentration ChABC. Both decellularised and GAG depleted pSFTs were stored as described above for native pSFTs until fascicle dissection.

Specimens were thawed at 37 °C for 20 min, then placed on a dissecting board and hydrated with no more than 15 mL of 0.9% saline solution, using a Pasteur pipette. The tendon was then left at room temperature for 5 – 7 min. The toe region bifurcation was removed using a scalpel (No.10). This left the bulk of the pSFT of approximately 12 cm length (Figure 5.1a). From this point on the tendon was referred to as divided into three regions: toe, ankle and middle (Figure 5.1b). Fascicles were isolated from the mid-substance of the middle region of the pSFT, flanked by the toe and ankle region. A single incision (scalpel No. 11) was made distally from the ankle insertion point leaving approximately 4 cm intact towards the toe region (Figure 5.1c). This provided an anchor point to prevent the left (1) and right (2) portions of the tendon to rotate or move excessively during dissection. It also facilitated moving the whole tendon with forceps clamping the toe region when required during the process. A second incision was made bilaterally in the respective midsection (Figure 5.1d; 1a, 1b; 2a, 2b). Fascicles appeared visible under 1.75X lamp magnification (3 diopter) (Figure 5.1e).

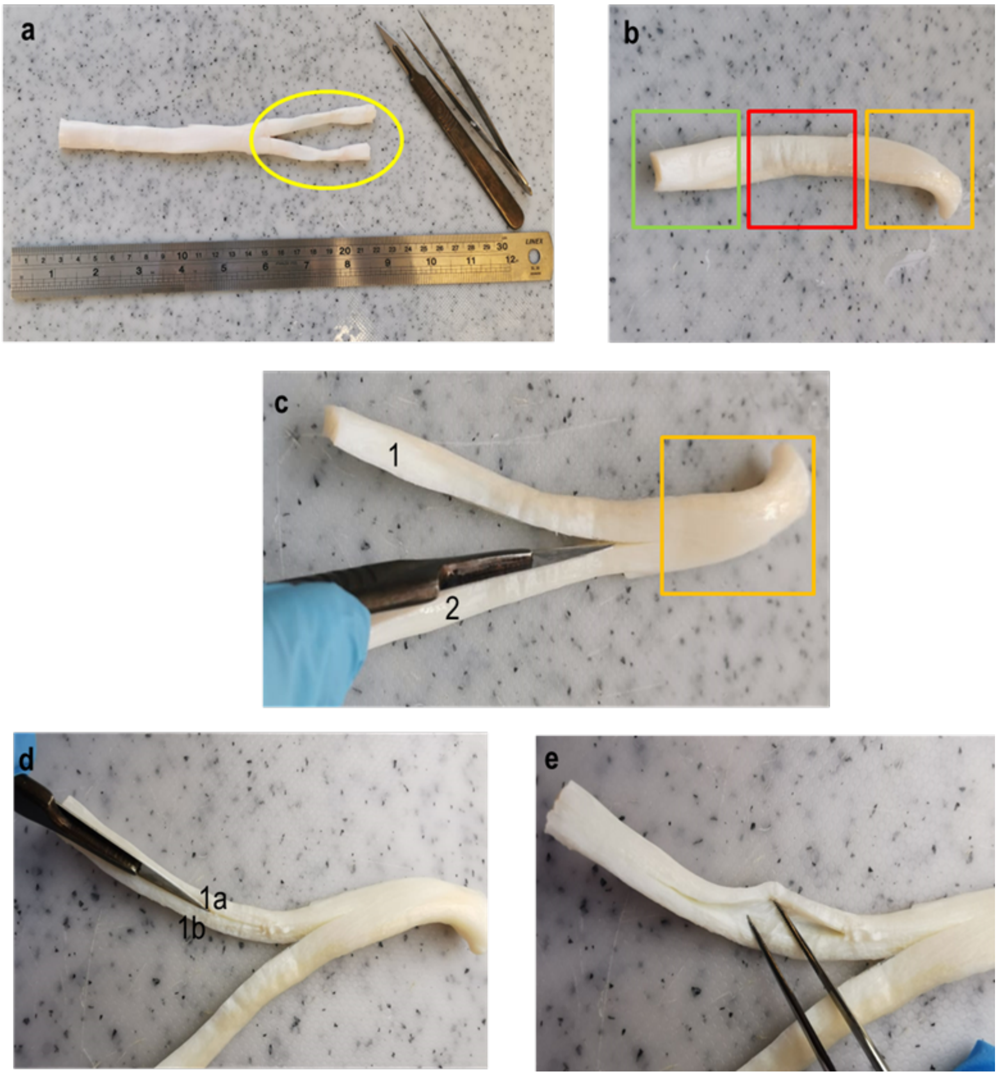

Figure 5.1: Dissection of sub-tendon structures or fascicles from porcine SFT. a) whole pSFT with toe region bifurcation shown in yellow; b) bulk of pSFT with toe (orange), middle (red) and ankle (green) regions; c) division of pSFT distally from ankle region into portions 1 and 2; d) division of mid-substance of section 1 into subsections 1a and 1b where the same incision was made on section 2; and d) visualisation of fascicles within middle region of pSFT.

Microdissection forceps were used to separate the fascicles from one another, beginning with section 1 (Figure 5.1c). Gentle force was required to insert the tip of the forceps into the mid-substance of subsection 1a and a similar force was used to pull perpendicularly. This rapidly made IFM visible. IFM was removed carefully, longitudinally along the fascicle structure, with the aid of a scalpel. It was common that more than one fascicle was being held by the forceps at this point. A second set of microdissection forceps would further allow the isolation of a single fascicle from a group, while the scalpel cut away the IFM between parallel fascicles. If the fascicle appeared to have suffered damage or loss of attachment to 1a at this point during the dissection, it was discarded and a new fascicle was isolated. This prevented micro-damaged fascicles to be analysed further.

Before removing the fascicle from its attachment sites within 1a, the scalpel cut away as much IFM as possible to retain a clean, undamaged tubular structure. The fascicle was then isolated with a single incision on both extremities. The first incision would release the fascicle from the toe region leaving it carefully on the dissection board until the end anchored proximal to the toe region was cut. This would allow the detachment from section 1 to take place first, taking extreme care not to compromise the integrity of the fascicle. It was less challenging to make an incision above the attachment site to the mid-substance without damaging the structure of the fascicle.

Dissected fascicles never exceeded 20 mm length, given previous attempts to gain lengths greater than 20 mm had a high chance of causing micro-damage during dissection. Each dissected fascicle was then moved into a hydrating saline solution – no more than 2 mL previously pipetted onto the dissection board –using forceps for 30 – 45 seconds and then placed carefully on a glass slide as straight as possible. The cohesive properties of the solution on the glass slide facilitated fascicle immobilization for imaging.

The same process was conducted at least twice on each subsection (Figure 5.1d; 1b, 2a, 2b). At least six fascicles were obtained from each pSFT. Between the successful dissection of one fascicle and the next, the whole tendon was rehydrated using a Pasteur pipette and saline solution. It was then left at room temperature for 5 minutes before the process was resumed. It was discovered that if hydration was constant and/or excessive, the fascicles became fragile, suffering damage quickly with gentle forces applied. In contrast, if tendons were kept dehydrated for longer than 20 minutes, the fascicles became more difficult to see and therefore isolate, with ruptures at various time-points during dissection.

5.2.2 Structural characterisation of fascicles

A qualitative characterisation of fascicles from native, decellularised and GAG-depleted pSFT was conducted based on microscopic observation.

A total of six fascicles were obtained from 3 pSFT from each group. A total of 18 fascicles from each group were imaged and diameter measurements were conducted (see Section 5.2.2.1) to ensure they were not sub-fasciculi.

For microscopy, four fascicles of varying diameter were selected randomly, with the condition that their structural integrity was observable, to remove the effect of damage occurring during dissection from influencing the characterisation of each specimen. Similarly, for staining evaluation, three fascicles were selected. Sample size (n) therefore refers to the number of fascicles used for each method.

5.2.2.1 Microscopy

Fascicles from native, decellularised and GAG-depleted pSFTs were isolated (see Section 5.2.1) and imaged on the same day to ensure dissection and imaging techniques remained as consistent as possible between groups. An upright Axio Imager M2 microscope (Carl Zeiss Microscopy) was used for viewing fascicles placed on a glass slide as described above. Köhler (bright field) illumination was used. Medial regions of the fascicles were imaged, in addition to areas where particular characteristics were observed. This could refer to possible damage caused by dissection techniques, visualisation of collagen crimp, possible presence of IFM or sub-fascicles. This is further described in section 5.3.1. Images were captured digitally with the associated AxioCam MCr5 digital camera and computer software (Zen version 2). Magnification of representative images are specified combining the objective lens and camera lens magnification. A summary of the method is schematically represented in Figure 5.2.

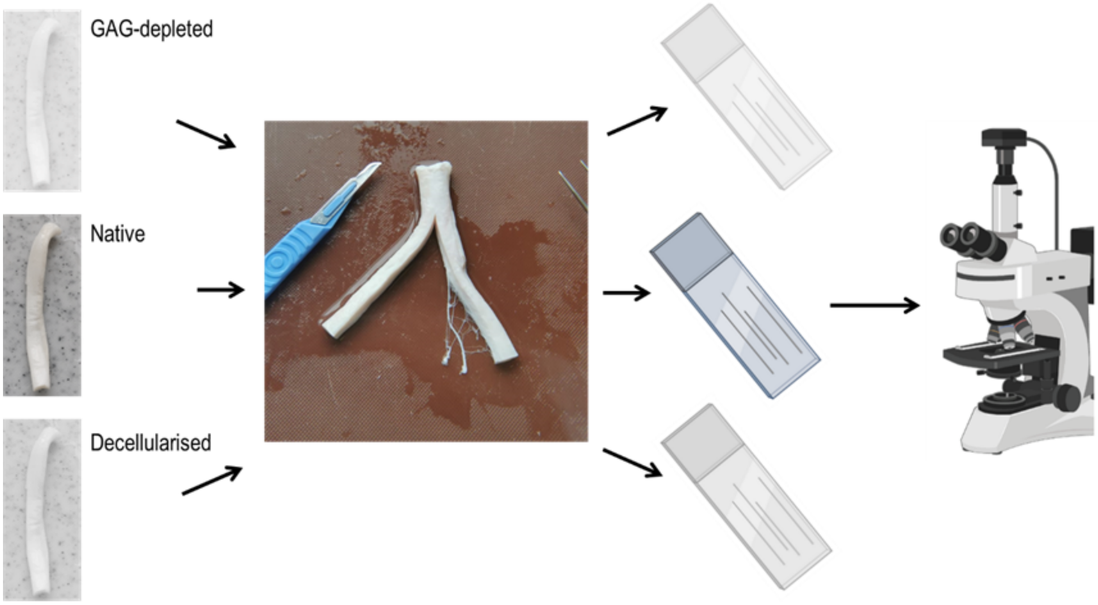

Figure 5.2: Fascicle dissection and imaging for structural characterisation. Fascicles were dissected from native, decellularised and GAG-depleted pSFTs. Multiple fascicles were isolated at one time, given dissection techniques would sometimes render specimens unusable. Slides were visualised using an upright microscope and fascicle areas were imaged for subsequent description. Created with BioRender.com.

Observable characteristics of fascicle structure and arrangement, as well as diameter measurements form part of the characterisation presented in section 5.3.1. Diameters were measured using ImageJ software (Figure 5.3a). The image was divided into 6 sections of equal size. Within each section, a straight line was drawn from one end of the fascicle to the other, and its length was deemed representative of the diameter of an otherwise cylindrical pSFT fascicle. The end of any given fascicle was determined by a defined border, not including adjoined IFM, fascicular matrix or any other ECM (Figure 5.3b). Measurements were therefore repeated 6 times along the length of the medial region of each fascicle. The diameter was calculated as mean ± 95% CI for each fascicle. Fascicles used throughout this Chapter had a diameter within the range 50 – 500 µm [396].

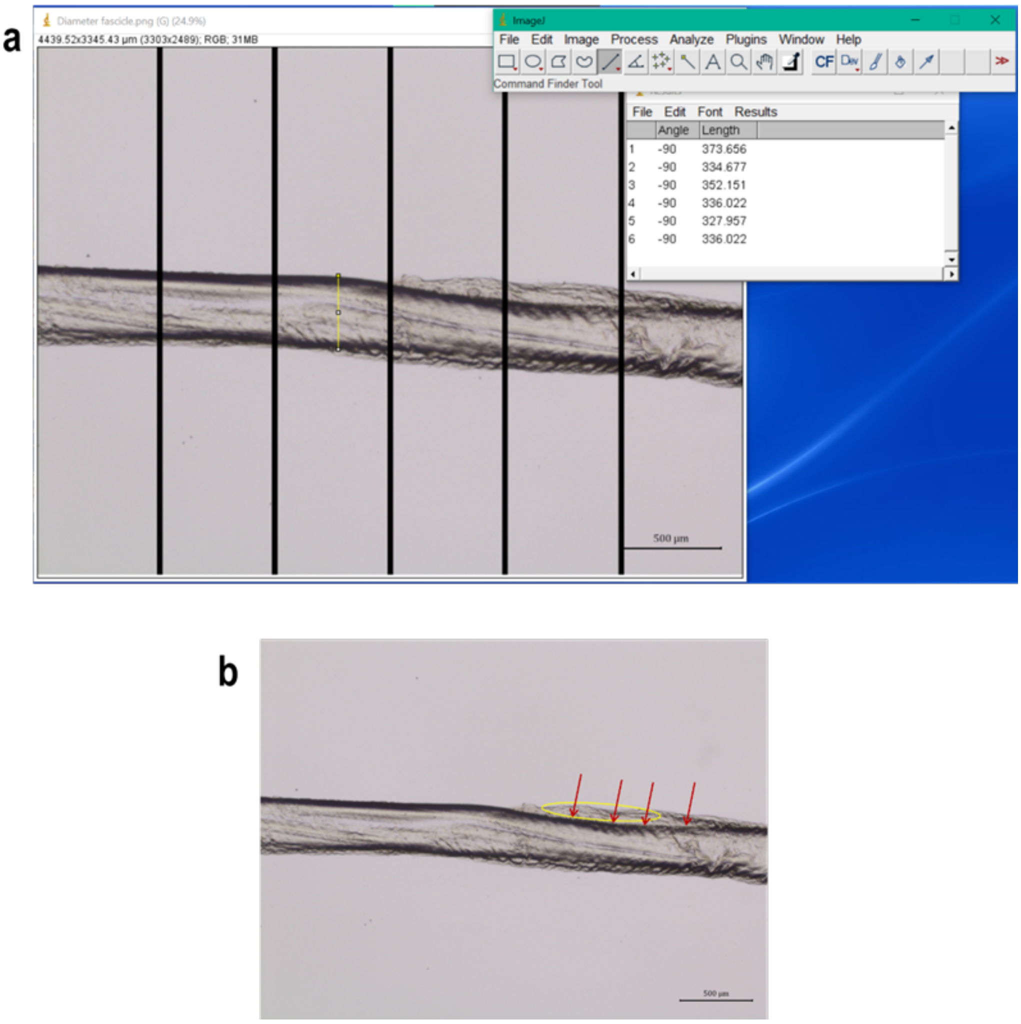

	Angle	Length
1	-90	373.656
2	-90	334.677
3	-90	352.151
4	-90	336.022
5	-90	327.957
6	-90	336.022

Figure 5.3: Diameter measurements for pSFT fascicles.
a) Fascicle micrographs were divided into 6 equal sections, where a single straight line (yellow) was drawn transversally and its length measured; b) each fascicle had distinguishable borders (red arrows) from which the diameters were measured, not taking into account IFM or ECM adhered to it (yellow). Images were taken at 25x magnification (scale bar 500 µm).

5.2.2.2 Staining evaluation of matrix component distribution

The characterisation of the compositional aspects of fascicles from native, decellularised and GAG-depleted pSFT were analysed through histological staining techniques, conducted on whole fascicle units. This was hypothesised to provide information into the matrix component distribution in fascicles, with particular focus on potential changes occurring as a consequence of decellularisation and GAG depletion processes. The histological dyes were selected to gain insight into the location and distribution of GAGs, proteoglycans and lipids.

5.2.2.2.1 Preparation of histological solutions

Solutions required for Safranin O/Fast green and Alcian blue staining were prepared as detailed in section 2.2.6.7. Sudan black stain and associated solution required for the staining protocol were obtained from a commercial kit (detailed in Appendix A, Table

II).

5.2.2.2.2 Specimen preparation

Fascicle dissection was carried out on native, decellularised and GAG depleted pSFTs as per section 5.2.1. Seven to ten fascicles were obtained from each group and placed on a positively charged glass slide. Fascicles were visualised and imaged as described in section 5.2.1. Three fascicles were selected from each group and rehydrated using a Pasteur pipette and saline solution. They were then transferred using forceps to a new glass slide and placed parallel to one another. Once the fascicles were aligned as straight as possible, a single drop of medium viscosity superglue (Loctite, USA) was placed at either end of each fascicle to immobilise it (Figure 5.4). This reduced risk of movement during the staining process, or potential loss of the fascicle.

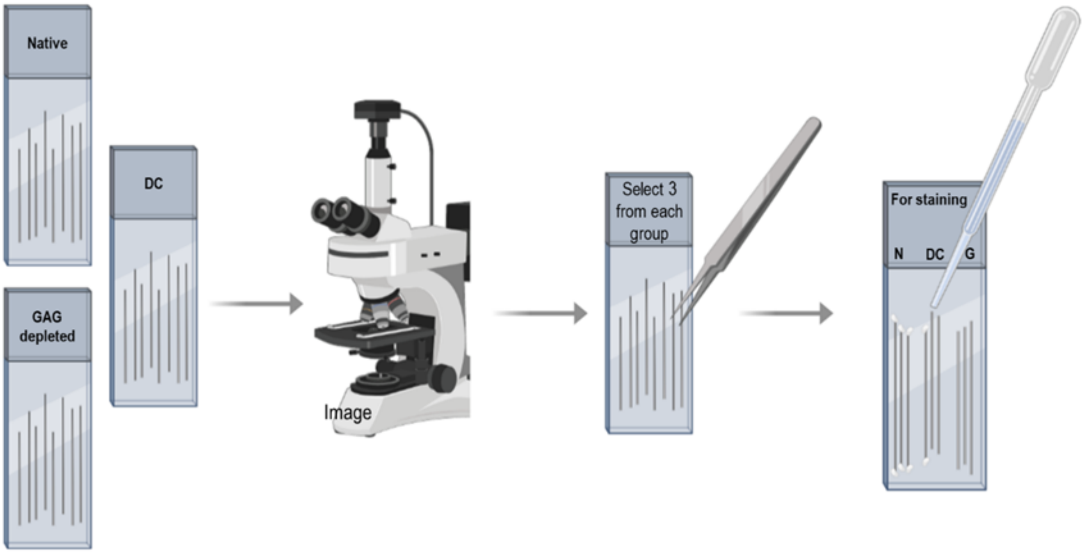

Figure 5.4: Fascicle preparation for staining processes.
Fascicles from native, decellularised (DC) and GAG depleted pSFTs (7-10 fascicles) were imaged using an upright Zeiss microscope equipped with Köhler (bright field) illumination at 50x magnification. Three fascicles were chosen from each group to transfer onto a new slide, placing them parallel before immobilising with a drop of superglue at either end. Created with BioRender.com.

5.2.2.2.3 Staining optimisation process

Specimen preparation was carried out as detailed in section 5.2.2.2.2. Native and decellularised fascicles were used for optimisation processes. This consisted in determining the ideal time during which a specific stain could be used on the fascicles to show adequate component staining, i.e. Safranin O stain for 4, 6 or 8 min to visualise proteoglycans and GAGs. This was carried out for each of the staining processes, as it was the first time histological stains were used on fresh sub-tendon units. Once the time required for adequate staining of a specific component was determined, the staining process was conducted on native, decellularised and GAG-depleted fascicles, following specimen preparation as above. For all staining processes, solutions and stains were added dropwise using Pasteur pipettes directly onto the fascicles, unless otherwise stated. The lid of glass staining jars were used to place the slide where the fascicles were immobilised, preventing excessive movement, while an additional glass lid was placed on top to prevent evaporation of solutions used during staining.

5.2.2.2.4 Safranin O/Fast Green

Fascicles were stained within 24 h from dissection to ensure consistent staining of glycosaminoglycans. Slides were hydrated briefly with deionised water. Weigert's haematoxylin was added and left for 3 min. Fascicles were washed in tap water for 10 min, then excess water was removed. This was carried out by placing the slide inside a glass staining jar containing water and shifting the slide gently 3 times during the 10 min. Differentiation with 1% acid alcohol was performed for 1 min. Fascicles were washed in tap water for 3 min, then 0.02% w/v Fast Green was added for 5 min. A brief 5 sec wash was performed with 1% v/v acetic acid and excess solution removed. Fascicles were stained with 0.1% Safranin O for 4, 6 and 8 min. This helped determine how long the stain was required to be left on the fascicles for it to penetrate enough to visualise glycosaminoglycans. After the staining optimisation process, 4 min resulted the optimum time for fascicle staining with Safranin O.

5.2.2.2.5 Alcian Blue/PAS stain

Fascicles were stained within 24 h from dissection to ensure consistent staining of glycosaminoglycans. Slides were hydrated briefly with deionised water. Alcian blue was added dropwise directly onto the fascicles and left for 10, 15 and 20 min to determine the required time for fascicle penetration and staining of glycosaminoglycans. The stain was then washed off with deionised water. Fascicles we subject to a 5 min 1% periodic acid wash before removing excess solution with deionised water. Schiff reagent was added for 20 min, then fascicles were washed in running tap water for 8 min. This was carried out by placing the slide inside a glass staining jar with a gentle flow of water angled at the corner of the jar. Excess water was removed and haemalum Mayer was added for 1 min. Fascicles were then washed in running tap water to remove excess stain. Fascicles were subject to 1% acid alcohol for 5 sec and then washed in running tap water for 2 min. After the staining optimisation process, 10 min was found to be the optimum time for fascicle staining with alcian blue.

5.2.2.2.6 Sudan Black

Sudan Black B is a lipophilic dye, with a high affinity to lipid compartments. It has been used to react against lipofuscin, which is a combination of oxidised proteins, metals and lipids [397]. The dye stains in dark colours, being blue/black for neutral fats, and a grey colour for phospholipids. Ethanol (70% v/v) was added to the fascicles for 30 sec. Sudan Black B solution was then added dropwise directly onto the fascicles and left left for 1.5 and 2 h to determine the time required for penetration and adequate staining of lipids. The dye was then washed using 70% v/v ethanol for 3 min. The fascicles were then washed in tap water for 2 min. This was carried out by placing the slide inside a glass staining jar containing water and shifting the slide gently once during the 2 min. The slide was blotted dry using tissue paper in the areas surrounding the fascicles, while gently applying pressure directly onto the fascicles to remove excess solutions. Neutral red solution was added for 3 min and then excess stain was washed using tap water. After the staining optimisation process, 2 h was found to be the optimum time for fascicle staining with Sudan Black B.

An additional optimisation stage was performed, where formalin vapour fixation was carried out prior to the staining process. For this, 5 mL of formaldehyde (36.5 – 38%) solution was poured into a coplin jar. Tissue roll had previously been placed in the base of the jar, acting as an absorbent material. The slide with the immobilised fascicles was placed inside the coplin jar in such a way that these did not touch the base, preventing direct contact with the formaldehyde solution. The coplin jar was covered, and the slide was left to fix in vapours for 10 min. After removing the slide from the coplin jar, staining with Sudan Black B was carried out as detailed previously.

5.2.2.2.7 Confocal imaging

After staining, the slide was left to dry at room temperature for 24 hours before imaging. No coverslip was placed on the fascicles. Microscopy imaging was carried out as detailed in section 2.2.6.9, using an upright Axio Imager M2 microscope (Carl Zeiss Microscopy) equipped with Köhler (bright field) illumination. All fascicles stained with a specific stain were imaged on the same day under the same conditions to minimise variation between fascicle groups. However, exposure time was adjusted according to the objective lens that was used.

5.2.3 Fascicle hydration

The water uptake and swelling behaviour of whole pSFT was investigated in Chapter 3 (see Section 3.3.1). An analysis into the water uptake or hydration of the fundamental unit of pSFTs was therefore considered relevant to gain insight into the swelling behaviour at the sub-tendon scale, revealing hierarchical similarities or discrepancies and their effect on pSFT biomechanics.

5.2.3.1 Preparation of solutions

Deionised water was autoclaved before use and absolute ethanol ($\geq$ 99.8%) was used directly from supplier (Fischer Scientific) as hydrating and dehydrating solutions respectively.

5.2.3.1.1 Phosphate buffered saline (PBS)

Five PBS tablets were dissolved in 500 mL of deionised water. pH was measured, ensuring it was within 7.2 – 7.4 range. The solution was autoclaved at 121 °C, 15 psi for 20 min. It was used within one week.

5.2.3.1.2 Quarter strength Ringer's solution (2.25 g/L sodium chloride; 25%)

A Ringer's tablet was dissolved in 500 mL of deionised water. The solution was autoclaved at 121 °C, 15 psi for 20 min. It was used within one week

5.2.3.1.3 Full strength Ringer's solution (9 g/L sodium chloride; 100%)

Ringer's tablets (2) were dissolved in 500 mL of deionised water. The solution was autoclaved at 121 °C, 15 psi for 20 min. It was used within one week.

5.2.3.1.4 Sodium chloride solution (0.9%)

The sodium chloride for irrigation solution (250 mL) was placed in a Duran bottle and autoclaved at 121 °C, 15 psi for 20 min. It was used within a week.

5.2.3.2 Hydration of tendon fascicles

Fascicle diameters were measured using ImageJ software (Figure 5.5). Each fascicle image was divided into three areas (Figure 5.5b). In each area, two topographical landmarks were allocated to carry out measurement in the same location thereafter (Figure 5.5c). A straight line was then drawn from one end of the fascicle to the other, and its length was deemed representative of the diameter of an otherwise cylindrical pSFT fascicle. This was carried out in duplicate in each area of the fascicle image (Figure 5.5d). Fascicle diameters were analysed prior to commencing the experiment to confirm there were no significant differences within or between groups.

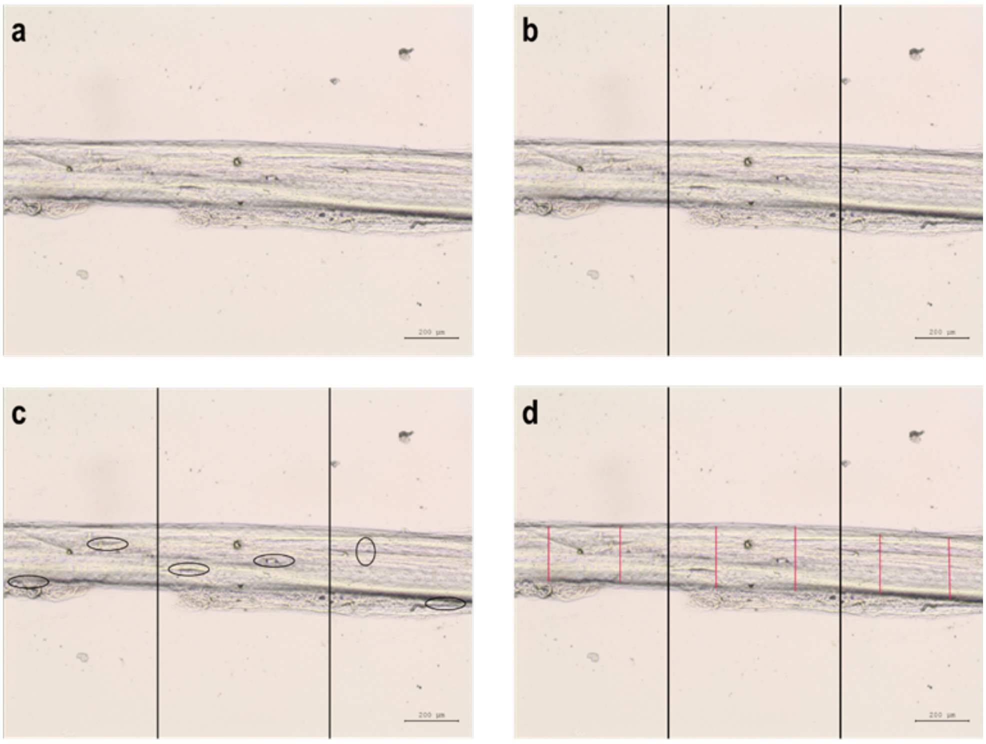

Figure 5.5: Diameter measurements for fascicle hydration analysis.
Images of fascicles from native, decellularised and GAG-depleted pSFT (a) were divided into 3 areas (b) where 2 topographical landmarks (c) were used as reference points for diameter measurements (d) using ImageJ software. Images were taken at 50x magnification (scale bar 200 µm).

Fascicles (n = 3) from native, decellularised and GAG-depleted pSFT were placed on a glass slide and immobilised at either end using a drop of clear all-purpose adhesive (Loctite, USA). The hydration or dehydration processes with different solutions described subsequently were carried out using a sterile Pasteur pipette (5 mL), placing 3 drops along the length of the fascicle. All fascicles were dehydrated using absolute ethanol to establish a consistent baseline between samples. Fascicles were hydrated with the same solutions used in the modified decellularisation methods (Chapter 3), including PBS, 25% Ringers, 100% Ringers and saline solution.

The fascicle was hydrated in each solution for 3, 5 and 10 min. Excess solution was removed placing filter paper on the left inferior corner of the slide where the fascicle was immobilised immediately prior to fascicles imaging using the confocal microscope. A dehydration step was carried out between the different time intervals of each solution.

This consisted of air drying the slide for 2 min, agitating it for the first 25 sec. Absolute ethanol was then added to the fascicles and left for 3 min and until it evaporated at room temperature. The same solution was then added for the second and third time interval (5, 10 min). Fascicle diameters were measured using the same method described above. Fascicles were left to equilibrate 24 h after a final dehydration step before moving onto the next solution. An example of fascicle imaging after hydration in different solutions is presented in Figure 5.6.

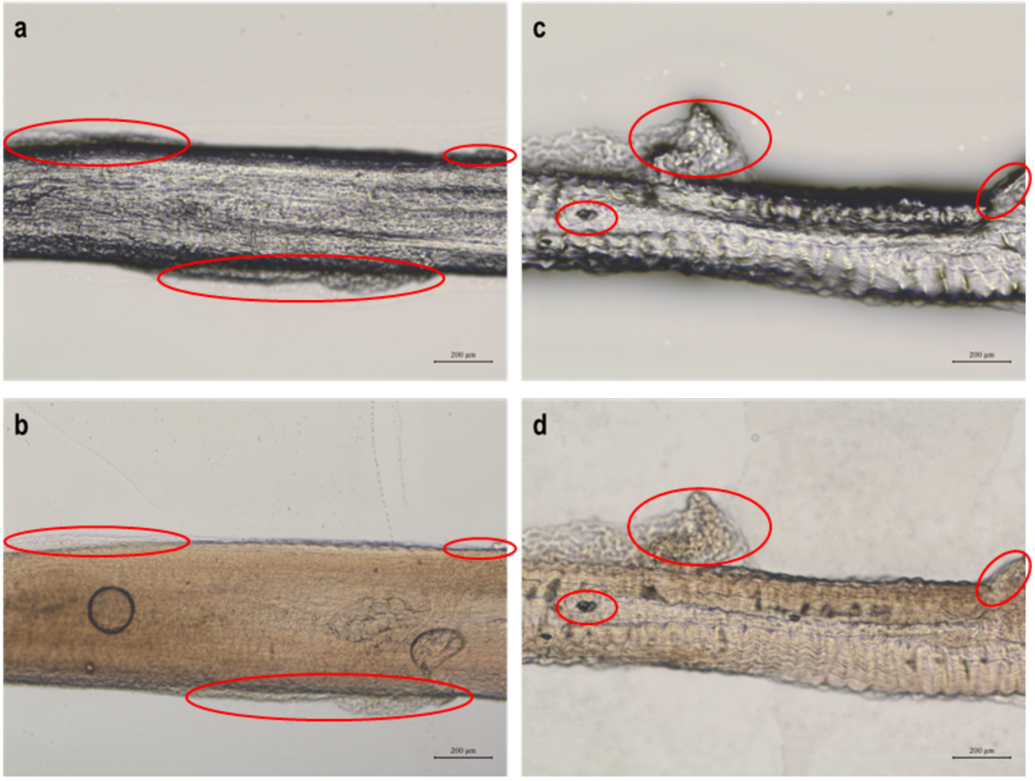

Figure 5.6: Native (a & b) and decellularised (c & d) pSFT fascicles after being dehydrated in ethanol (a, c) and hydrated in PBS (b, d) for 3 min. Topographical landmarks (red ovals) facilitated diameter measurements were taken consistently after each time interval. Images were taken at 50x magnification (scale bar 200 µm).

5.2.3.3 Microscopy imaging

Fascicles were imaged immediately after hydrating for 3, 5 or 10 min in each solution. Topographical landmarks facilitated imaging the same area of each fascicle to measure diameters consistently for each group in the different hydrating solutions. No coverslip was placed on the fascicles. All imaging was carried out at 50x magnification (scale bar 200 µm).

5.2.4 Fascicle analysis

Atomic force microscopy (AFM) is a technique capable of imaging inert and biological surfaces in 3D at very high resolution. Using a tiny but sharp probe to scan across surfaces, it is capable of exploring at the molecular scale in either vacuum, air or liquid environments with equal ease [398]. It provides qualitative and quantitative information on physical properties such as morphology, roughness and size [399]. It can also provide data surrounding mechanical properties, adhesion strength and magnetic forces [400]. This technique was used to conduct a characterisation of the topographical surface and mechanical analysis of fascicles at the nanoscale.

Fascicles of native and decellularised pSFT were dissected following as described in section 5.2.1. Given only small sections (< 10 mm) would be required as analyses would be conducted at a nanoscale, dissected fascicles of variable sizes were used in the first stage of dissection and imaging.

A total of three fascicles were obtained from 3 native and decellularised pSFT. A total of 9 fascicles (sub-divided into smaller sections; Figure 5.9) were imaged and diameter measurements were conducted. For AFM methods, two fascicle sections with the least rugged surface were selected, ensuring they were from different pSFTs. Sample size (n) therefore refers to the number of fascicle sections used.

5.2.4.1 Sample preparation

One of the main requirements for AFM sample preparation is the immobilisation of samples on a flat substrate. Fascicles for AFM imaging were chosen based on multiple preliminary sessions carried out prior to the standardisation of sample preparation described subsequently. In these preliminary sessions, fascicles were dissected following section 5.3.1 and sections of circa 5 – 7 mm length were placed onto round glass coverslips (Figure 5.6). A thin layer of PVA glue had been flattened onto the surface of the coverslip using a scalpel blade whereby the positioning of the fascicle would lead to its immobilisation. Fascicles were imaged once immobilised to determine whether the PVA glue enveloped the fascicle and if there was enough surface area in the medial region to image using AFM. Imaging was carried out in air, as PVA glue would be washed out if imaged in liquid (PBS) and the fascicle would no longer be immobilised, rendering the imaging difficult. During this stage, the topography of the fascicles obtained with AFM allowed subtle changes to be implemented during the fascicle dissection stage, to achieve the most ideal fascicle sample possible. It also became evident that an alternative mode of sample immobilisation was required to allow imaging in air and liquid.

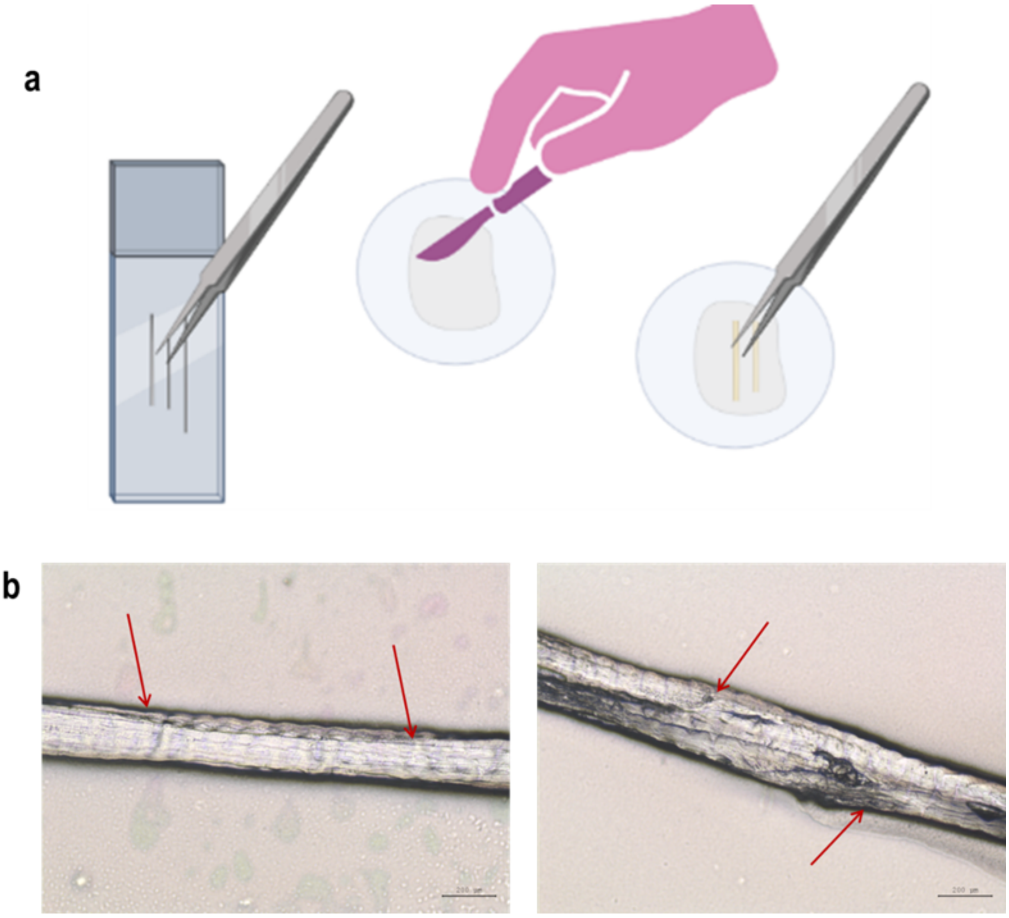

Figure 5.7: Preliminary fascicle preparation for AFM imaging.
Fascicles were dissected and imaged prior to being transferred to a glass coverslip. a) A thin layer of PVA glue coated the surface of the coverslip, evened out using a scalpel. Fascicle sections were placed atop the PVA glue using forceps for immobilisation; b) fascicle images show some evidence of the glue enveloping the fascicle (red arrows). Images were taken at 50x magnification (scale bar 200 µm). Created with BioRender.com.

A number of superglue (Loctite, USA) and industrial grade (Everbuild Building Products Ltd, UK) glue options were experimented with, applying different techniques for accomplishing a thin layer upon which fascicles could be placed without being completely enveloped. However, it became evident (Figure 5.8) this was not a viable option. After experimenting with a range of supporting materials and adhesives, a standardised method for sample preparation was implemented.

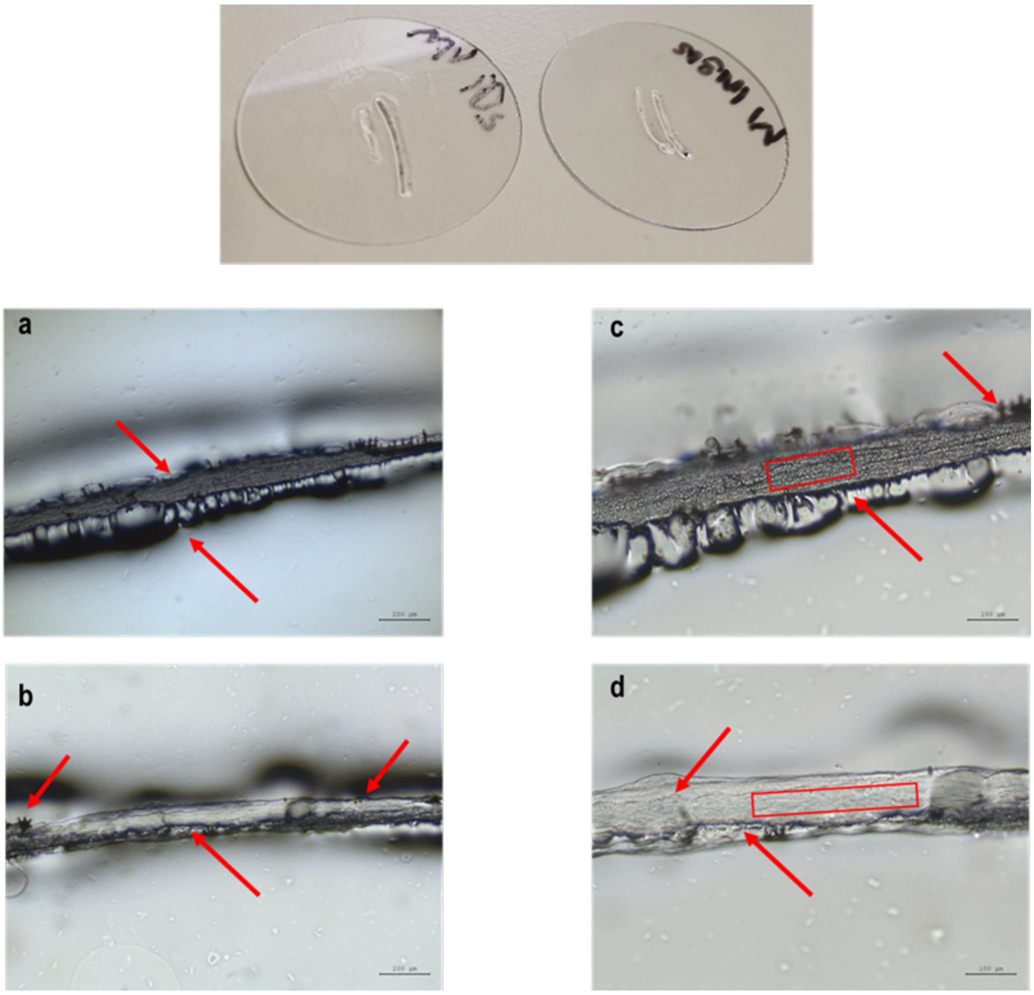

Figure 5.8: Fascicle immobilisation using a range of adhesives.
Despite the different techniques applied to ensure a thin, even layer of adhesive on the coverslips (top), the fascicle specimens were always enveloped (red arrows). Some areas were uncoated by glue and therefore viable to image using AFM (red rectangles). The thick edges of the adhesive layer made it difficult to image the surface as it interferred with the movement of the AFM probe. Images (a & b) were taken at 50x magnification (scale bar 200 µm), while images (c & d) were taken at 100x magnification (scale bar 100 µm).

The dissected fascicles were placed on the glass slide following section 5.2.1. The slide had previously been marked for dividing into 6 mm length sections (Figure 5.9). This would assist sectioning the fascicle into smaller lengths. Room temperature dehydration of the fascicle happened in under 3 minutes of being placed onto the glass slide. A scalpel (No. 11) was then used to divide the fascicle into smaller sections. The fascicles were then imaged without a coverslip, and the fascicles with the least rugged surface were chosen for further preparation. This was based on the interaction required between specimen surface and probe for imaging to render useable data.

Fascicle sections were rehydrated using a drop of saline solution to facilitate its transfer onto a clear, waterproof adhesive tape (Gorilla Glue Company, USA) using forceps. A 2 x 2 mm grid had been printed onto transparent, printable, adhesive vinyl (Evergreen Goods Ltd, UK) and placed onto the non-adhesive surface of the adhesive tape. The fascicle, once air dried at room temperature was placed carefully on the adhesive surface of the adhesive tape, as straight as possible. Fascicles from native and decellularised pSFT were placed on the same tape to optimise AFM imaging times. Fascicles were immobilised at both ends using liquid superglue (Loctite, USA), placing a miniscule amount using a biopunch applicator stick (circa 2 mm diameter). Fascicles were finally imaged using the upright microscope, where the grid functioned to subsection the fascicle, imaging the different regions along its length. Once in the AFM, this subsection imaging allowed a speedy positioning of the probe on the least uneven region within each fascicle specimen.

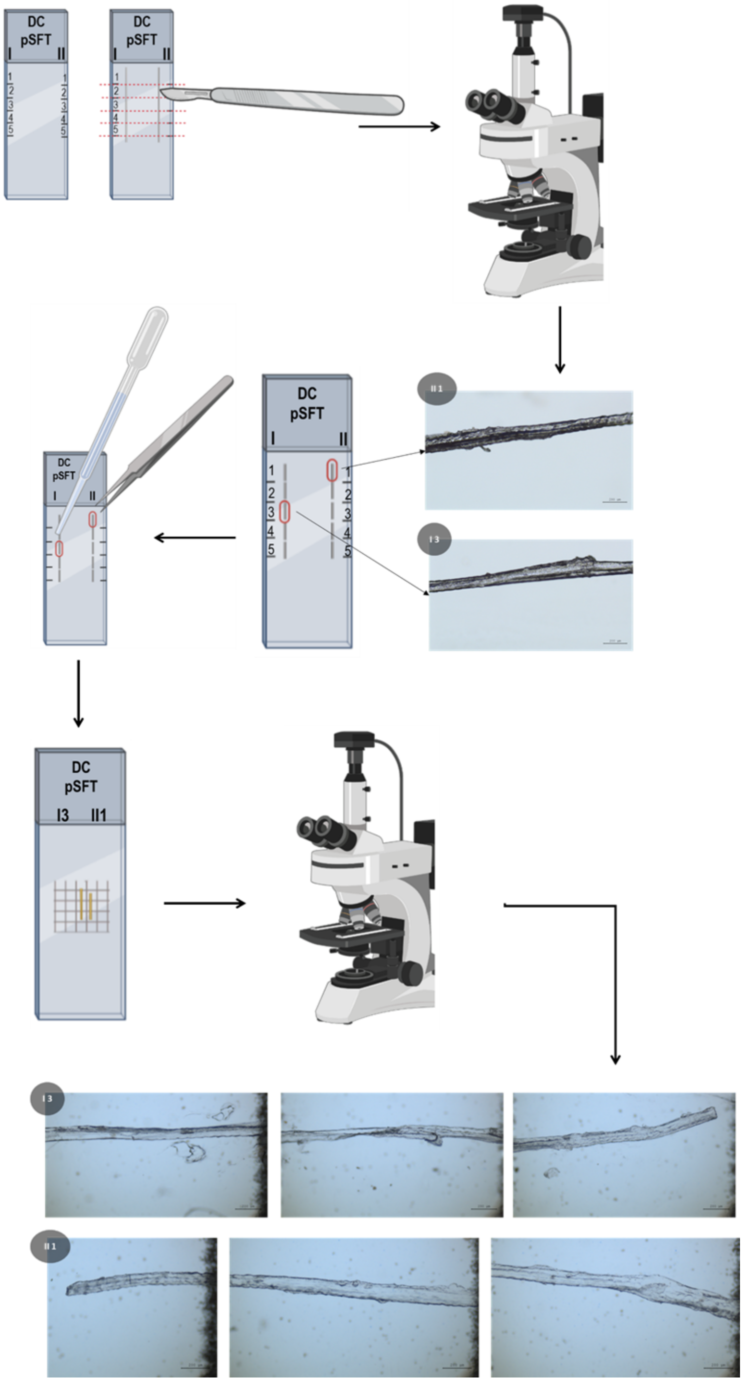

Figure 5.9: Fascicle preparation optimised for AFM imaging.
Dissected fascicles from native and decellularised (DC) pSFT were divided into sections and imaged using microscopy to determine the section (1 – 5 on glass slide) deemed suitable for imaging using AFM. The selected sections (red ovals) were then rehydrated using saline solution and transferred onto adhesive tape using forceps. These were imaged again using microscopy, where the grid facilitated the location of an area the probe could interact with the specimen encountering the least resistance. Images were taken at 50x magnification (scale bar 200 µm). Created with BioRender.com.

Ethanol treatment

Fascicle imaging revealed a layer enveloping mainly native fascicles, while present only to a lesser extent in decellularised fascicles. This is described in more detail in section 5.3.4. During the hydration experiments, it was observed that fascicle dehydration using absolute ethanol allowed crimp to be observed more clearly, particularly in decellularised fascicles. This is described in more detail in section 5.3.3. Consequently a dehydration step was implemented during sample preparation. The hypothesis was that by dehydrating the fascicle, the external enveloping layer would adhere to the intrafascicular matrix, making its topography more visible so the AFM probe would encounter less resistance during tapping of the sample.

Fascicle isolation, imaging and selection was carried out as per the standardised method described previously. Prior to transferring the chosen fascicles from native and decellularised pSFT to the adhesive tape, they were carefully placed on a glass coverslip using forceps. A 1 mL syringe was filled with absolute ethanol. Ethanol was placed atop each fascicle section dropwise through the syringe needle, with enough volume to cover the entirety of its length (2 – 4 drops). This was left for 10 min, and then specimens were left to dry at room temperature for 1 h. Fascicle sections were then transferred to the adhesive tape using forceps and immobilised using superglue. Imaging was carried out as described in the standardised method. A summary of the method is presented in Figure 5.10.

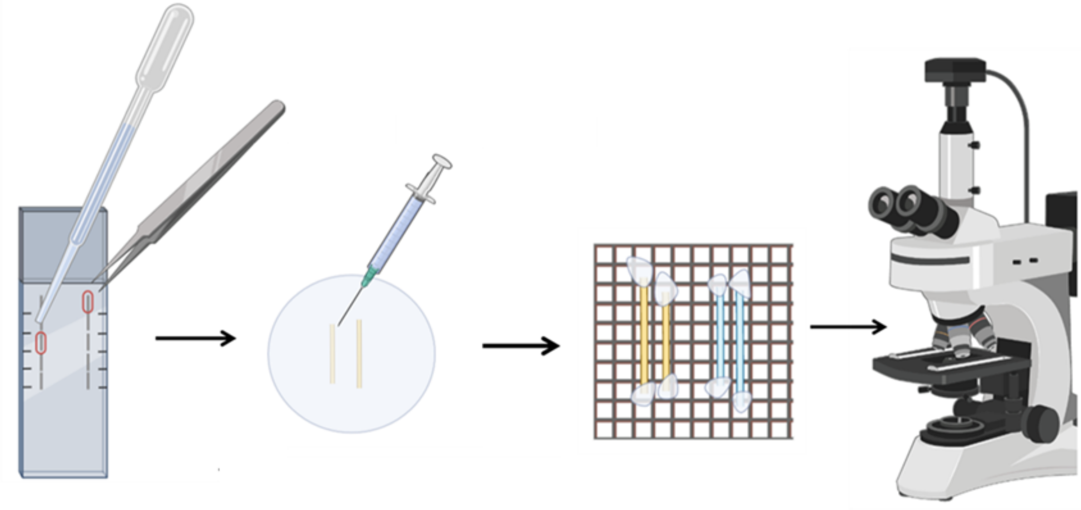

Figure 5.10: Fascicle dehydration with absolute ethanol.
Selected fascicles were subjected to a 10 min immersion in ethanol, followed by a 1 h air drying period at room temperature. Dehydrated fascicles were then transferred to the adhesive tape using forceps, immobilised at either end and imaged as per the standardised method prior to AFM imaging. Created with BioRender.com.

The ethanol treatment was always carried out on the same day AFM imaging took place. This ensured the natural humidity of the environment did not counteract the dehydrating effect of the absolute ethanol. Sample that underwent this treatment were only used for topographical imaging.

5.2.4.2 Topographical imaging using atomic force microscopy

In air All experiments conducted on the AFM were carried out in collaboration with Dr Lekshmi Kailas and Dr Simon Connell (School of Physics and Astronomy). As chief experimental officer in AFM, Dr Lekshmi provided much guidance regarding sample preparation optimisation. The tape with fascicle specimens was placed, with forceps, onto a metallic sample mounting disc of 15 mm diameter using double sided tape (Figure 5.11a). The disc was then mounted onto the sample stage of a Dimension FastScan Asyst AFM (Bruker, USA) (Figure 5.11b). From this point on, Dr Lekshmi conducted the necessary preparations. Silicon tip on silicon nitride cantilever probes were used for imaging in air and liquid (FastScan A probes in air; FastScan D probes in liquid, Bruker). FastScan A probes have a force constant of ˜ 18 N/m and a resonance frequency of approximately 1400 kHz, while FastScan D probes have a force constant of ˜0.25 N/m and a resonance frequency of approximately 110 kHz in liquid. All probes were calibrated manually. Each specimen was imaged in tapping mode at scan rates between 0.8 Hz – 2 Hz depending on the interaction between the probe and the specimen surface. Due to the uneven surface, specimens were imaged in different locations attempting to find a relatively flat area. Images of the region are provided in alongside the topographical outcomes (see Section 5.3.4). The NanoScope (version 9.7) software from Bruker was used for acquiring images.

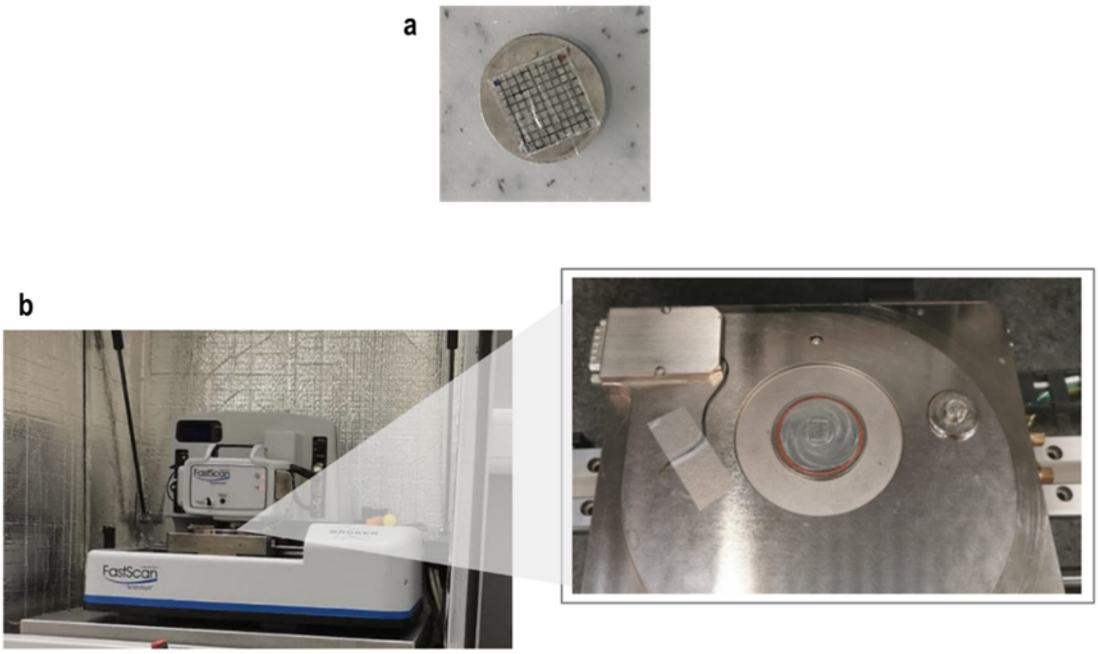

Figure 5.11: Sample mounting on AFM.
Fascicles specimens immobilised on adhesive tape as per section 5.2.4.1 were placed on mounting disc (a), which was then mounted on the AFM (left) stage via an integrated magnetic holder (right). The stage was then manually controlled using the NanoScope software to locate the probe on top of the specimen.

Height, phase and amplitude error data were captured in 3D and analysed using NanoScope Analysis software (version 1.90, Bruker). A 1st order flatten function was executed on all height images before further image analysis to remove tilt. Section analysis was conducted to gain insight into the surface topography, i.e. collagen D-spacing. The 3D image function rendered a topographical mapping of the specimen surface in three planes, where light pitch and intensity could be modified subtly to visualise detail. The roughness analysis determined average roughness, skewness which measures the distribution of features relative to the mean and kurtosis which is sensitive to the sharpness of peaks or valleys [401] of the surface imaged.

In liquid

When imaging in liquid, autoclaved PBS was used. Once the tape with fascicle specimens was mounted on the metallic disc as described in above, PBS was pipetted (200 µL) covering the fascicle specimens completely. These were left for 15 min to hydrate. The disc was then mounted on the AFM stage. A drop of PBS was placed on the probe to cover the tip using the same pipette for imaging in a liquid environment.

Fibril width and collagen D-spacing measurements

2D height images were used for measurements. Using the section analysis function, the image was analysed in 3 areas (Figure 5.12a), then magnification was used within each area to visualise individual fibrils more clearly (Figure 5.12b). The measure tool on the image software was then used to measure either the width of collagen fibrils within each area (Figure 5.12c), or the collagen D-spacing (Figure 5.12d). Width measurements from 6 different fibrils were taken in each of the areas of the image. Collagen D-spacings were measured along the length of 6 different fibrils in each of the areas of the image. This was conducted on two images of two different pSFT fascicles (n = 2) due to limited data obtained using AFM.

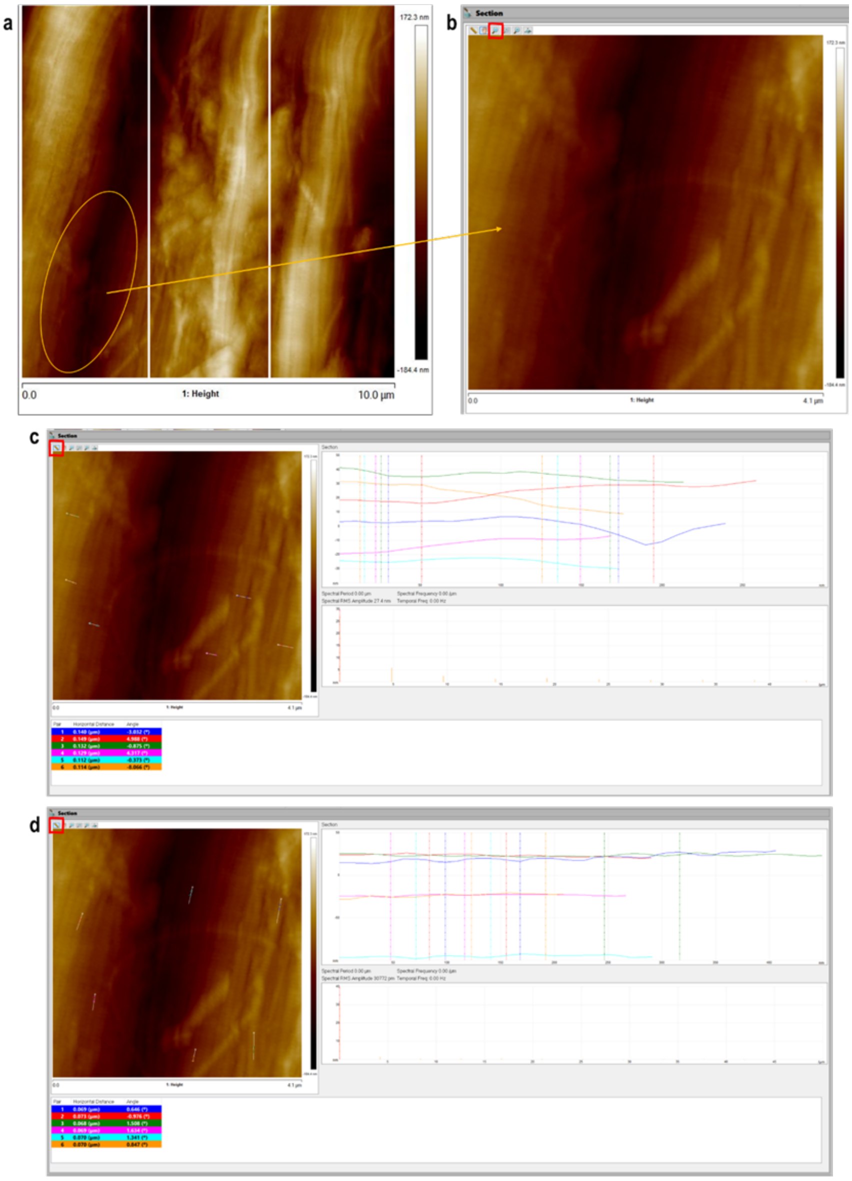

Pair	Horizontal Distance	Angle
1	0.140 (µm)	-3.032 (°)
2	0.149 (µm)	4.988 (°)
3	0.132 (µm)	-0.875 (°)
4	0.129 (µm)	4.317 (°)
5	0.112 (µm)	-0.373 (°)
6	0.114 (µm)	-8.066 (°)

Pair	Horizontal Distance	Angle
1	0.069 (µm)	0.646 (°)
2	0.073 (µm)	-0.976 (°)
3	0.068 (µm)	1.508 (°)
4	0.069 (µm)	1.634 (°)
5	0.070 (µm)	1.341 (°)
6	0.070 (µm)	0.847 (°)

Figure 5.12: Measurement of fibril width and collagen D-spacing of pSFT fascicles.

All measurements were conducted using the NanoScope Analysis software. Each height image was divided into 3 areas (a), within which magnification helped visualise fibril structures (b). Using the measure tool, the width of 6 different collagen fibrils (c), and the collagen D-spacing was measured (d). The image used as an example is a decellularised pSFT fascicle imaged in air.

5.2.4.3 Nanomechanical characterisation using atomic force microscopy

Images were acquired using peak force quantitative nanomechanical mapping mode (PF-QNM NanoScope, Bruker). In PF-QNM mode, a very fast force curve is collected at every pixel in the image which enable the quantitative assessment of nano-scale material properties such as modulus, adhesion, deformation and dissipation.

Super sharp silicon nitride lever probes were used for QNM in air (Model PEAKFORCE-HIRS-SSB, Bruker). Probes had a force constant of ˜ 0.12 N/m and a resonance frequency of approximately 110 kHz. Before imaging the tendon sample surface, probes were calibrated using polydimethylsiloxane (PDMS) (2.5 ± 0.7 MPa) or fused silica (72.9 GPa) with known Young's modulus. Specimens were then mounted on the AFM stage. Images were acquired using peak force quantitative nanomechanical mapping mode (PF-QNM NanoScope, Bruker).

Data files including height, Peak force error and Log DMT modulus were analysed using NanoScope Analysis software (version 1.90, Bruker). The main parameter of interest was the modulus. The Young's modulus (E*) was obtained using the Derjaguin-Muller-Toropov (DMT) model [402], given by:

$$F_{tip} = \frac{4}{3}E^{*}\sqrt{Rd^{3}} + F_{adh} \tag{5.1}$$

Where F_{tip} is the force on the tip, F_{adh} is the adhesion force, R is the tip radius and d is the separation between the tip and the sample. This is why it is referred to as DMT modulus. The output given by the AFM was the Log DMT modulus. It is inaccurate when changed to modulus (without logarithmic scale) within the NanoScope software, so used as Log modulus for subsequent steps.

The Analysis tool of the NanoScope Analysis software was used, where a depth analysis was conducted using the log Modulus image of specimens which rendered a histogram of the logarithmic value of the moduli corresponding to each point across the imaged area of each fascicle. A maximum and minimum value of the log Modulus was also obtained. Where a complete area of fascicle specimens was not clearly imaged, at least two areas were selected to create a histogram of the log Modulus, and obtain a minimum and maximum value.

5.2.5 Preliminary analysis of the interfascicular matrix of porcine superflexor tendon

It was hypothesised in previous chapters that the IFM may be affected by decellularisation processes, whereby the structural and compositional changes may influence the biomechanical behaviour and properties of pSFT. AFM was used to provide qualitative and quantitative information regarding the IFM of native and decellularised pSFT, revealing possible changes that could relate to fascicular and whole-scale tendon biomechanics. Histological staining of elastic fibres, a component found in high quantities in tendon IFM [22] was used to determine if decellularisation processes led to the loss of this component.

5.2.5.1 Millers elastin

Millers stain was used for visualisation of fine and coarse elastic fibres [403, 404]. After sections were dewaxed and hydrated (Section 2.2.6.6), they were immersed in 5% potassium permanganate for 5 min. Slides were then washed in deionised water, before submerging into 1% oxalic acid. Slides were then rinsed in deionised water for 1 min, and then for 4 min. Slides were immersed in 70% ethanol for 1 min before leaving submerged in Miller's stain for 1 h. Slides were then washed in 95% ethanol until running clear, then 70% ethanol for 1 min and tap water for 2 min. Slides were immersed in Weigert's haematoxylin for 10 min and then rinsed in tap water for 1 min, followed by acid alcohol for 1 min and tap water again for 1 min. Slides were immersed in van Gieson stain for 3 min, then washed in tap water for 1 min and finally deionised water for 30 sec. Slides underwent dehydration and mounting as detailed in Section 2.2.6.8. Sections were imaged using normal Köhler illumination.

5.2.5.2 Sample preparation for atomic force microscopy imaging

The topographical characterisation of native and decellularised fascicular matrix, including intra- and interfascicular matrix was attempted using transverse sections of pSFT. Cryo-embedded specimens were used, where 100 µm thick cryosections were immobilised by placing on different adhesive materials, ultimately selecting adhesive vinyl (Evergreen Goods Ltd, UK) and waterproof adhesive tape (Gorilla Glue Company, USA). These were imaged using an upright microscope. Transverse sections of fresh native and decellularised pSFT were also used as an alternative specimen for imaging. This due to the risk of the adhesive interfering with the probe when imaging the cryosections. For fresh transverse sectioning, pSFTs were used from storage at -20 °C, left to thaw at room temperature for 10 min. A no. 11 scalpel was then used to cut a section of circa 4 mm thickness as straight as possible. It was at the stage between completely frozen and thawed where this could be carried out optimally, given that when the pSFT thaws, it becomes impossible to cut a transverse section straight. Specimens were immobilised on waterproof adhesive tape or using liquid superglue (Loctite, USA) atop a glass coverslip. This is summarised in Figure 5.13.

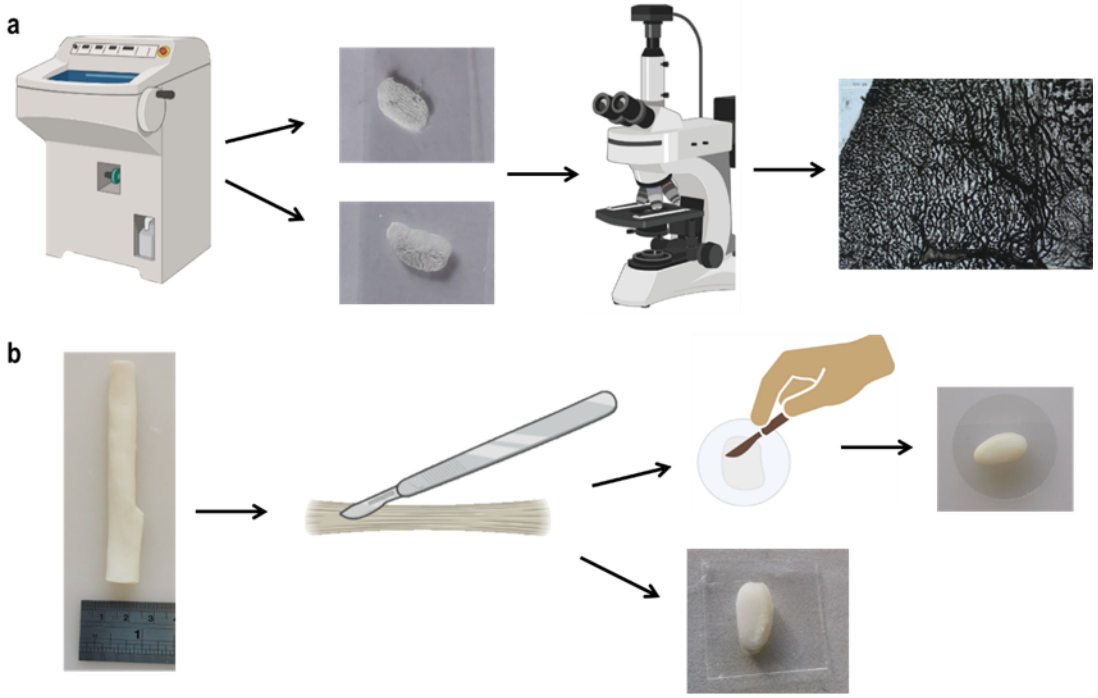

Figure 5.13: Sample preparation for AFM imaging of transverse sections of native and decellularised pSFT.
a) Cryo-embedded tissue was sectioned (100 µm) and placed on adhesive vinyl (top) or waterproof tape (bottom). Sections were imaged at 25x magnification (scale bar 500 µm); b) fresh pSFT was left to thaw at room temperature from frozen (-20 °C) and a scalpel used to cut sections as straight as possible. Specimens were either immobilised using waterproof tape (bottom) or a thin, even layer of liquid superglue on the surface of a glass coverslip (top). Created with BioRender.com.

An optimisation of the sample preparation occurred after the first attempts at imaging the transverse sections. The reasoning is detailed further in section 5.4.6. The new method consisted of obtaining fresh sections of native and decellularised pSFT, removing the peritenon, leaving a small cuboidal section with the surface as flat as possible (Figure 5.14). A scalpel (no. 11) was utilised, whereby all sectioning occurred after 10 min of the pSFTs thawing at room temperature from a frozen state. Specimens were left to dehydrate at room temperature 48 h prior to imaging. Specimens were immobilised using the same superglue method atop a glass coverslip described above.

Figure 5.14: Sample optimisation for transverse imaging using AFM.
Fresh native pSFT specimens after removing peritenon, leaving a cube-shaped section of fascicular matrix. Specimens were left to air dry at room temperature for 48 h prior to immobilising and imaging.

5.2.5.3 Topographical imaging using atomic force microscopy

Imaging was conducted as per section 5.2.4.2, the least uneven region, where it was found that suitable sample-probe interaction occurred, was used.

5.2.6 Statistical analysis

Prior to analysis, data was checked for normal distribution using the Kolmogorov-Smirnov normality test. For comparing two means an unpaired Student's t-test was used. For the hydration experiment, the overall effects of solution, treatment (decellularisation, GAG-depletion, no treatment) and interaction between both factors were assessed through a two-way ANOVA and Sidak's correction for multiple comparisons. P values lower than 0.05 were deemed to be significant.

5.3 Results

5.3.1 Structural characterisation of superflexor tendon fascicles

Micrographs of native pSFT fascicles of varying diameters (108 – 484 µm, see Table 5.1) are presented in Figure 5.15. The tubular structure of native fascicles is clearly delineated (Figure 5.15 a, c & d) with only some showing the wavy outline occurring due to collagen crimping (Figure 5.15b, red arrows). The surface of the fascicular matrix appeared smooth with collagen fibrils visible only in some areas (black asterisks). The greenish/white collagen fibrils appeared longitudinally aligned with little crimp. The remaining areas appeared to be covered with a layer (red asterisks), masking the sub-structures, likely providing the smoothness of the fascicular surface. The layer, likely IFM attached to the fascicle, can also be observed outside of the fascicle unit itself (Figure 5.15d, black arrows).

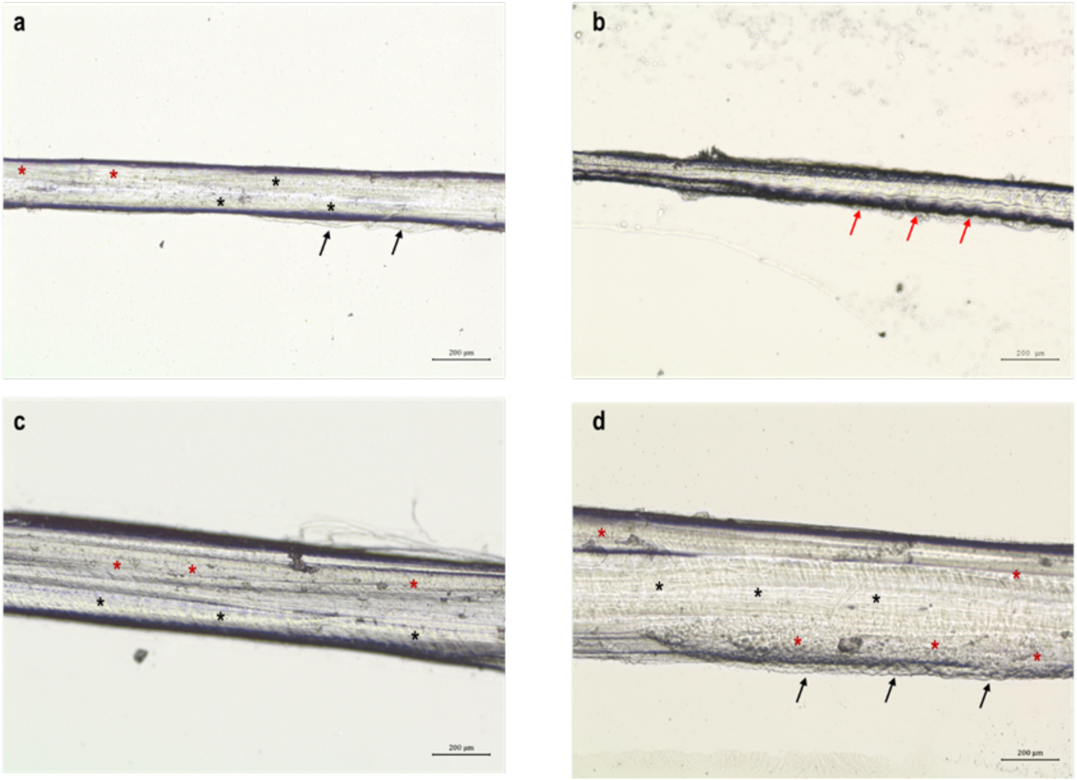

Figure 5.15: Representative micrographs of native pSFT fascicles.
Fascicles that constitute native pSFT with varying diameters. Tubular structures clearly delineated (a, c, d) with (b) showing a wavy outline characteristic of collagen crimp (red arrows). Smooth surface along fascicle length (red asterisks) with some greenish collagen fibrils visible (black asterisks). Smooth surface appears to be a protective sheath masking underlying substructures. Evidence of IFM (black arrows). Images were taken at 50x magnification (scale bar 200 µm).

Micrographs of decellularised pSFT fascicles of varying diameters (61 – 374 µm, see Table 5.1) are presented in Figure 5.16. Collagen crimp is clearly visible along decellularised fascicles, throughout the fascicular matrix, while also showing a characteristic waviness delineating the structure (Figure 5.16 b & d). Fascicle substructures including fibres and subfascicles are evident (Figure 5.16 a & c, red rectangles). Collagen fibrils are clearly visible, primarily visible in a light green colour. The clarity with which substructures are observed suggests the enveloping sheath observed in native fascicles may be thinner or not present in decellularised fascicles.

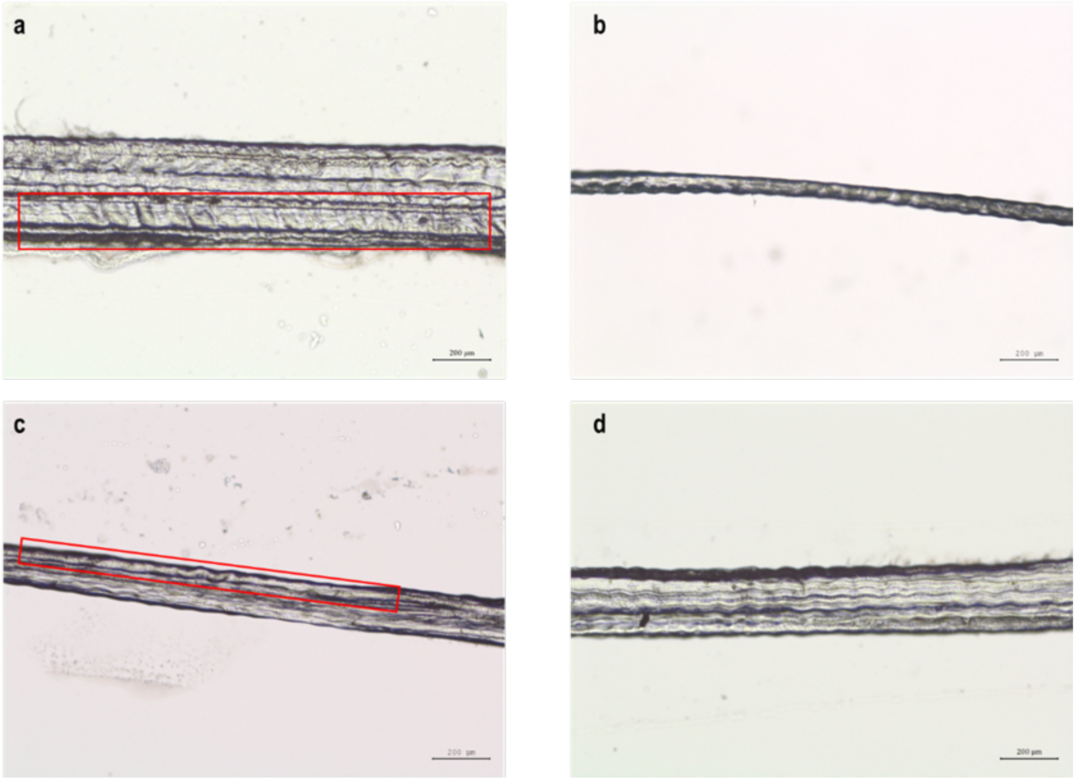

Figure 5.16: Representative micrographs of decellularised pSFT fascicles. Fascicles that constitute decellularised pSFT with varying diameters. Collagen crimp visible along fascicle length as well as delineating the fascicle structure itself (b, d). Substructures (red rectangles) within fascicles were observable (a, c). Images were taken at 50x magnification (scale bar 200 µm).

Micrographs of GAG-depleted pSFT fascicles of varying diameters (213 – 452 µm, see Table 5.1) are presented in Figure 5.17. Tubular structure less defined, with a soft, compliant fascicular matrix. Smooth surface along fascicle length, with the protective layer enveloping the fascicle structure, similar to native pSFT fascicles (Figure 5.15). Some peaks and troughs observed on the edges of the fascicle unit (Figure 5.17 a – c, blue arrows). Substructures, including collagen fibrils mainly masked by the protective layer, with some collagen fibrils visible in a greenish colour (black asterisks). Fibrils appeared to have a less organised arrangement longitudinally aligned along fascicle length (Figure 5.17b). Collagen fibrils and likely IFM attached to fascicles visible on either end of the structure (Figure 5.17 a – c, black arrows).

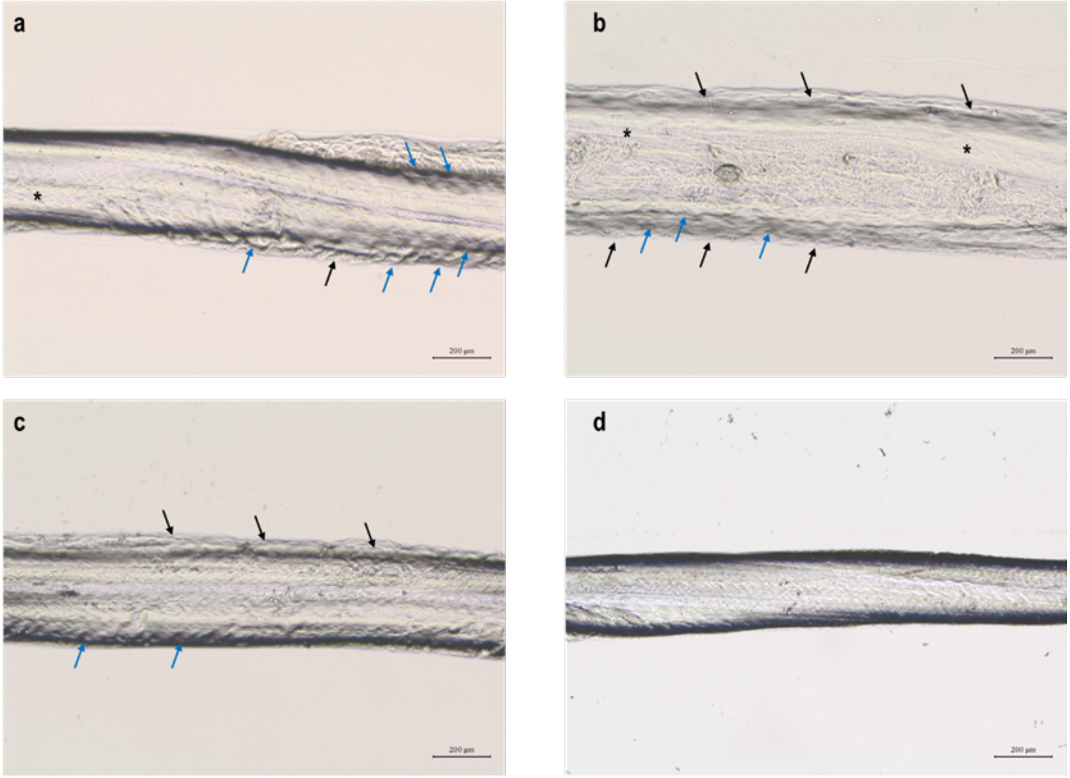

Figure 5.17: Representative micrographs of GAG-depleted pSFT fascicles. Fascicles that constitute GAG-depleted pSFT with varying diameters. Less defined fascicle units with a compliant, soft matrix. Smooth surface, with a seemingly protective sheath enveloping the fascicle. Some collagen fibrils visible (black asterisks), with a less longitudinally aligned arrangement (b). Peaks and troughs visible on edges of fascicle structure (a – c, blue arrows). IFM at either ends of the fascicle (black arrows). Images were taken at 50x magnification (scale bar 200 µm).

Fascicles from the native, decellularised and GAG-depleted pSFT varied in size, with fascicles of different diameters. The diameters of 20 fascicles from each group were measured as described in Section 5.2.2.1 (data not shown). Native fascicles had diameters between 69 – 487 µm; decellularised fascicles between 58 – 467 µm, and GAG-depleted fascicles between 224 – 440 µm.

The diameters of the 4 fascicles presented in Table 5.1 correspond to the measurements conducted on the individual fascicles observed in Figures 5.15 – 5.17 (a – d). These were obtained using using ImageJ software (see Section 5.2.2.1). They correspond to modal diameters obtained from each sample group. It is noteworthy to recognise the differences in the diameters of fascicle units within each sample group, for example, native b & d as well as decellularised a & b (Table 5.1). This is why the diameter data was not pooled and presented as a mean for each group, as it did not appear representative of the array of fascicles present within the tissue.

The structure of native and decellularised fascicles allowed the diameter to be easily measured, as the structure was clearly delineated. GAG-depleted fascicle had a less defined structure (Figure 5.16). All groups presented fascicles of different diameters within a single pSFT and between pSFTs of a single group.

Table 5.1: Diameters of native, decellularised (DC) and GAG-depleted pSFT fascicles.

	Diameter (µm)			
	a	**b**	**c**	**d**
Native	173.56 ± 16.18	130.52 ± 23.05	322.34±26.92	451.26±32.75
DC	355.16 ± 18.85	70.39 ± 9.43	149.09±18.02	228.96±24.70
GAG-depleted	305.72 ± 28.86	426.20 ± 26.00	314.52±15.54	243.41±30.50

Measurements obtained according to the method detailed in section 5.2.2.1 using ImageJ software. Measurements were taken from each micrograph presented above (Figures 5.15 – 5.17), where (a – d) correspond to each micrograph in each Figure, relating to separate specimens from each group. Data is presented as mean (n = 4) ± 95% CI, where 6 measurements were taken along fascicle length.

Features of native and decellularised fascicle surfaces are presented in Figure 5.18. The native fascicle (338.08 ± 18.83 µm diameter) continued to show a protective sheath enveloping the structure (Figure 5.18a), with a seemingly smooth surface (yellow asterisks), making it difficult to visualise the collagen structures within the fascicle. This layer, possibly in combination with collagen may have been damaged during the dissection process giving rise to the recoiled area (black arrows). Collagen fibril damage was evident as some thin fibril-like structures appear torn and superposed on the fascicle with an orientation unlike the longitudinal fascicle structure (red arrows). The decellularised fascicle (202.07 ± 26.14 µm diameter) did not show evidence of the sheath enveloping the fascicle (Figure 5.18b), with a clearly visible presence of collagen crimp waviness along the fascicle length. Further, the characteristic crimp of collagen fibrils was also evident (green asterisks) suggesting the fascicular matrix was more exposed compared to the native fascicle. The subfascicle in focus was contained within a fascicle unit (orange arrows) with substructures (fibre) also visible (yellow arrows).

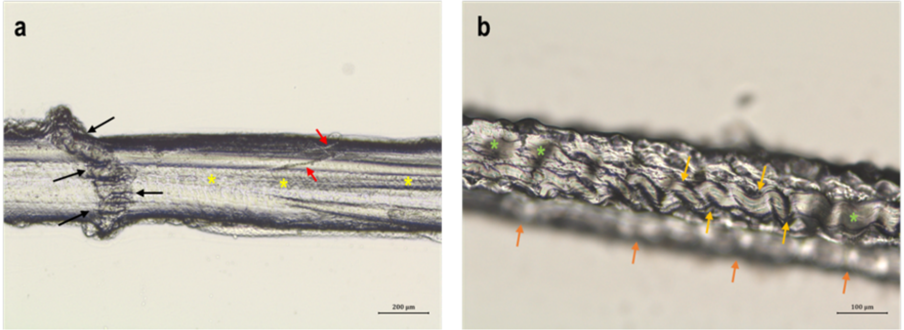

Figure 5.18: Representative micrographs of features on native and decellularised fascicle surfaces.
Native fascicle (a) with possible damage caused during dissection evident as collagen or enveloping sheath recoil (black arrows). Damage to collagen fibrils which appear orientated randomly atop the longitudinally aligned fibrils (red arrows). Sheath enveloping structures within the fascicular matrix appears to cover the length of the fascicle, with a seemingly smooth surface (yellow asterisks). Decellularised fascicle (b) with a subfascicle structure in focus, where the whole unit (orange arrows) appears blurred. Collagen crimp and characteristic waviness is evident throughout fascicle length, with collagen fibril waviness visible (green asterisks). No evidence of sheath covering the fascicular matrix. Collagen fibre substructure apparent (yellow arrows), also showing well defined crimp pattern. Image (a) was taken at 50x magnification (scale bar 200 µm), while image (b) was taken at 100x magnification (scale bar 100 µm).

A higher magnification image of native (Figure 5.19a) and decellularised (Figure 5.19b) fascicles provided qualitative features of the fascicle structure and surface features. The native fascicle (65.06 ± 3.20 µm diameter) showed a clear, defined tubular structure with some irregularities on the surface, observed as peaks and troughs, giving rise to a uneven morphology. The collagen fibres within the densely packed fascicle were somewhat apparent, but not clear. The surface seemed to be representing a protective sheath enveloping the fascicular matrix, where characteristic collagen crimp was hard to distinguish. The decellularised fascicle (64.48 ± 2.61 µm diameter) had a wavy outline delineating its structure, representing the characteristic crimp of collagen. Collagen fibres and fibrils observed within the structure appear more exposed compared to the native fascicle. The surface had no clear evidence of the peaks and troughs described in the native surface, possibly with a thinner or no protective sheath enveloping the fascicular matrix.

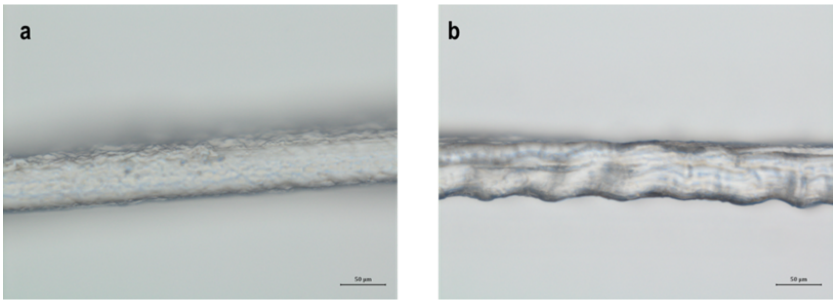

Figure 5.19: Representative micrographs of native and decellularised pSFT fascicles.
Surface features more apparent due to higher magnification. The native (a) fascicle shows a well-defined tubular structure with a waviness on the surface, created by small peaks and troughs. The decellularised (b) fascicle shows a wavy outline to the structure, where collagen fibres are evident within. Images were taken at 200x magnification (scale bar 50 µm).

5.3.2 Component distribution within superflexor tendon fascicles

Safranin O staining of native, decellularised and GAG-depleted fascicles is shown in Figure 5.20. Each micrograph corresponds to separate fascicles. Staining revealed GAGs located mainly in the envelope of fascicle structures, with a strong pink/red staining surrounding the fascicle structure of native and decellularised specimens (Figure 5.20 A – D). The green/blue matrix in Figure 5.20 A, C, D was hypothesised to be fascicular matrix that unravelled due to dissection techniques. Diameter measurement revealed the distinct tubular structures had a diameter > 50 µm (A: 82.41 ± 5.82 µm; C: 177.90 ± 15.65 µm; D: 96.67 ± 7.15 µm), indicating these likely corresponded to pSFT fascicle units. Variation between fascicle diameters within a group was observed, as previously mentioned in Section 5.3.1.Cellularity observed in native specimens (A, B), with some stained GAGs aligning longitudinally along fascicle length in Figure 5.20 B. Similar GAG staining observed in decellularised specimens (C, D) compared to native (A, B), with some distributed along collagen fibre arrangement in Figure 5.20 D. No evidence of cells in decellularised fascicles. No clear pink/red staining in GAG-depleted fascicles (E, F), with a smooth green/blue stained matrix, showing no evidence of cellular material.

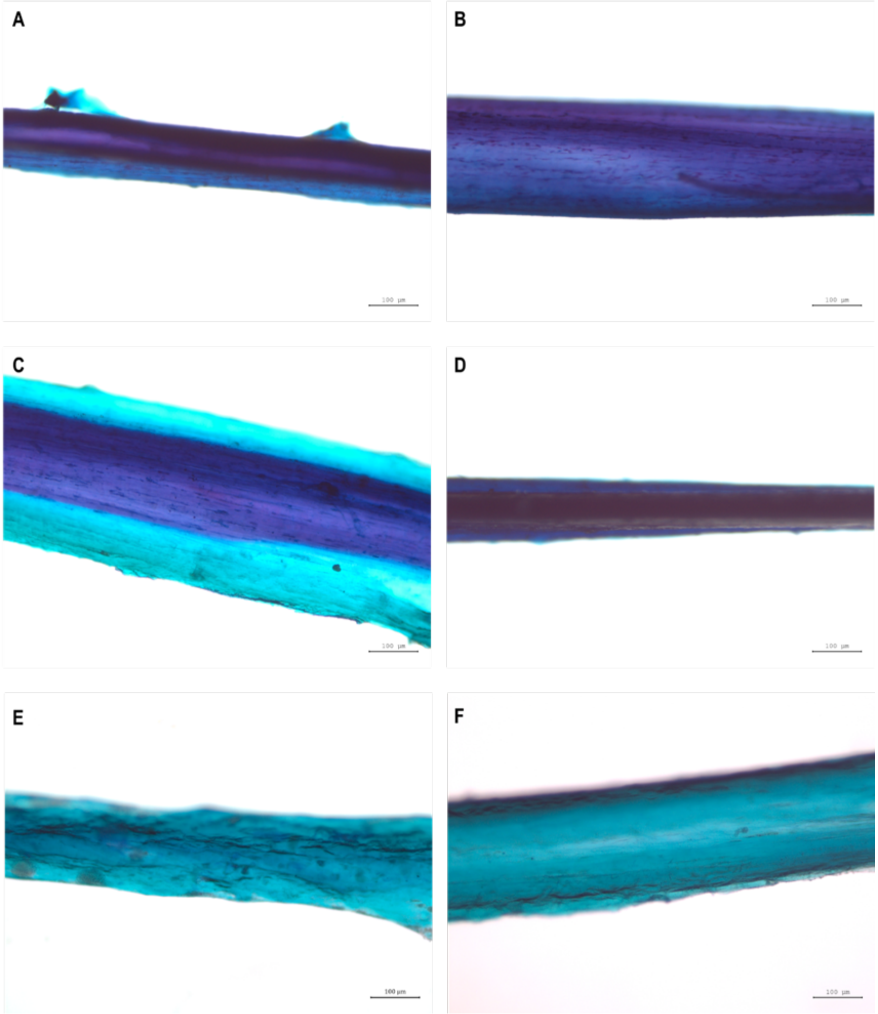

Figure 5.20: Safranin O/fast green staining of native, decellularised and GAG-depleted fascicles.
Micrographs correspond to different fascicles of native (A, B), decellularised (C, D) and GAG-depleted (E, F) groups. In native and decellularised groups, red stained GAGs surrounding fascicle structure, hypothesised to be IFM. Evidence of cellularity in native fascicles, while no cells visible in decellularised fascicles. Fascicular matrix stained green/blue in native (A) and decellularised (C) fascicles possibly unravelled matrix as a consequence of dissection techniques. No evidence of GAGs within fascicle or surrounding IFM in GAG-depleted fascicles (E, F). Images were taken at 100x magnification (scale bar 100 µm).

Alcian blue staining of native, decellularised and GAG-depleted fascicles is shown in Figure 5.21. Characteristic waviness of collagen is observed in native and decellularised fascicles (Figure 5.21 A – D). Native specimens (A, B) observed blue stained GAGs aligned longitudinally between the collagen fibre/fibril network. A dense blue staining was observed on the edges of the fascicle structure in (A). A more open fascicle structure observed in (B) shows a more evenly distributed arrangement of GAGs. Decellularised fascicles (C, D) with a similar GAG distribution compared to native specimens, aligned longitudinally along fascicle length. Areas of denser staining hypothesised to correspond to higher GAG content in areas between collagen fibres within the fascicle. Damage to fascicle observed in (C). GAG-depleted specimens (E, F) show no GAGs and a smoother fascicle surface compared to native and decellularised specimens.

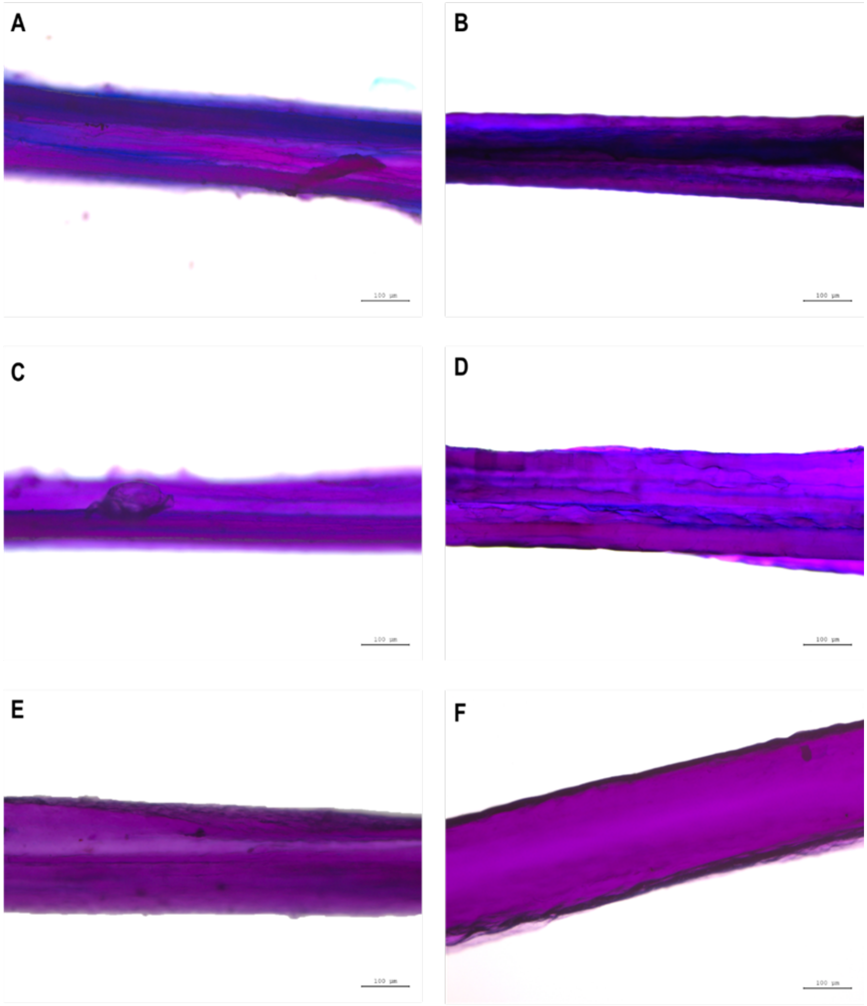

Figure 5.21: Alcian blue staining of native, decellularised and GAG-depleted fascicles.
Blue GAGs in native (A, B) and decellularised (C, D) fascicles, aligning longitudinally along collagen fibre's main axis of loading, with some evidence of collagen crimp. No evidence of GAGs in GAG-depleted (E, F) fascicles, with a smoother surface of purple-stained matrix. Images were taken at 100x magnification (scale bar 100 µm).

Sudan black staining of native, decellularised and GAG-depleted fascicles is shown in Figure 5.22. Some black staining mainly in the envelope surrounding the fascicle structure of native specimens (A). Grey and blue stained lipids were observed in (B), distributed across the fascicular matrix and also in the tissue attached to the bulk of the fascicle. Evidence of cellular presence in native fascicles with red stained nuclei (A, B). Decellularised fascicles (C, D) showed less grey/black staining localised in the edges of the fascicle structure (C), likely corresponding to the envelope surrounding the fascicular matrix. Figure 5.22 D showed a more evenly distributed blue staining across the fascicular matrix and black staining observed in the matrix attached to the bulk fascicle structure. The distribution of lipids/lipoproteins was similar between native and decellularised specimens, with less intense staining in decellularised fascicles. No evidence of red cellular material in decellularised specimens. GAG-depleted specimens

(E, F) showed a primarily black and grey staining across the fascicular matrix, with more visible staining on the edges of the fascicle structure (F). Redness observed in (E), suggesting the presence of cellular material.

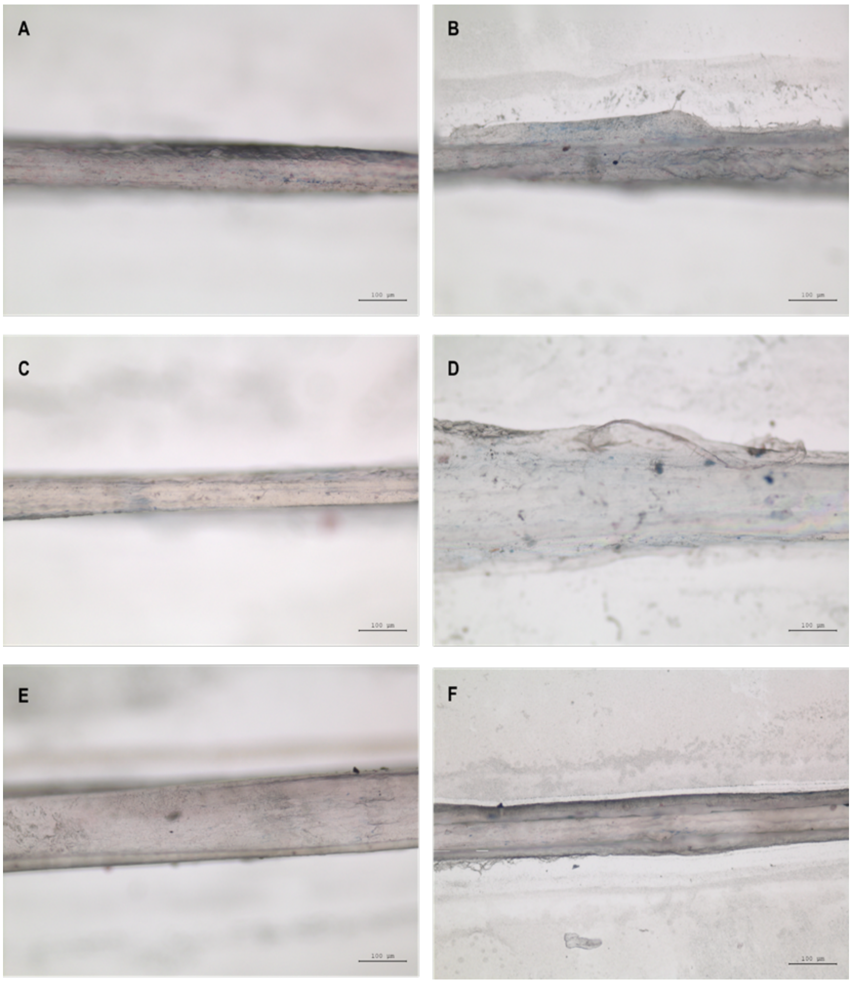

Figure 5.22: Sudan black staining of native, decellularised and GAG-depleted fascicles.
Black and blue staining of lipids where dense black staining is observed along the enveloping area of the fascicle in (A). Grey and blue staining in (B) mainly in matrix attached to bulk fascicular matrix of the native fascicle. Evidence of cellularity (red) in native fascicles (A, B). Lesser black and grey staining around decellularised fascicles (C), with some blue lipid presence in the fascicular matrix in (D), and some black stained lipids in the matrix attached to the fascicle, hypothesised to be IFM. No evidence of cellular content in decellularised fascicles (C, D). Black and blue stained lipid in envelope surrounding GAG-depleted fascicles, while also in fascicular matrix (E, F). Some redness indicating cellular presence, with no clear nuclei. Images were taken at 100x magnification (scale bar 100 µm).

5.3.3 Hydration behaviour of superflexor tendon fascicles

The hydration behaviour of native, decellularised and GAG-depleted fascicles after 3, 5 and 10 min is presented in Figure 5.23. Fascicle diameters prior to hydration showed no statistical differences between groups. After 3 min, there was increased swelling in the native fascicles hydrated with PBS compared to those in ethanol. No other differences within groups were found. Increased swelling occurred in GAG-depleted fascicles hydrated with deionised water, 25% Ringers and 100% Ringers compared to decellularised fascicles (a). After 5 min, there was increased swelling in decellularised fascicles hydrated with deionised water and saline compared to those in ethanol. In GAG-depleted fascicles, significantly higher swelling occurred in all solutions compared to ethanol. No other differences within groups were found. Increased swelling occurred in GAG-depleted fascicles hydrated with deionised water compared to native fascicles, with PBS and 25% Ringers compared to both native and decellularised fascicles, and with 100% Ringers compared to decellularised fascicles (b). Finally, after 10 min, there were no differences within groups. Increased swelling occurred in GAG-depleted fascicles hydrated with deionised water and saline compared to both native and decellularised fascicles, and with ethanol and 100% Ringers compared to decellularised fascicles (c).

The 2-way ANOVA revealed both treatment (none, decellularisation, ChABC treatment) and solution had a significant effect on the outcomes of this experiment, but no interaction.

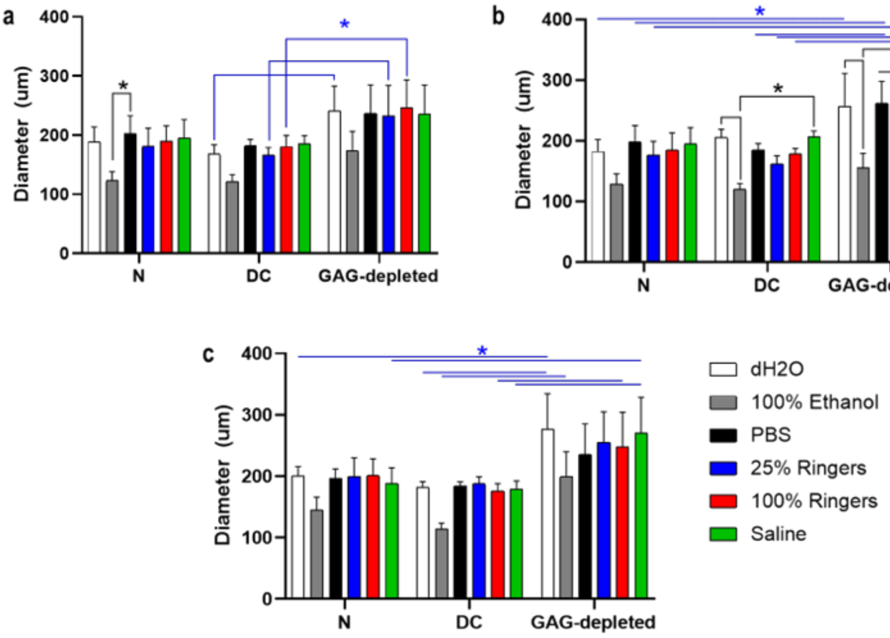

Figure 5.23: Hydration behaviour of native (N), decellularised (DC) and GAG-depleted fascicles in different solutions.
N fascicles showed significant swelling in PBS compared to ethanol after 3 min (a). No other differences were found within the N group. DC fascicles revealed significant swelling in deionised water and saline solution compared to ethanol after 5 min (b). No other differences were found within the DC group. GAG-depleted fascicles showed significant swelling when hydrated in all solutions compared to ethanol after 5 min (b). No other differences were found within the GAG-depleted group. a) Increased swelling in GAG-depleted fascicles hydrated in deionised water, 25% and 100% Ringers compared to DC fascicles after 3 min; b) increased swelling in GAG-depleted fascicles hydrated in deionised water compared to N, PBS and 25% Ringers compared to both N and DC, and 100% Ringers compared to DC fascicles after 5 min; c) increased swelling in GAG-depleted fascicles hydrated in deionised water and saline compared to both N and DC, and ethanol and 100% Ringers compared to DC after 10 min. Data is presented as mean (n = 3) ± 95% CI, where 6 measurements were taken along fascicle length. Data was analysed using a two-way ANOVA with Sidak's correction for multiple comparisons. * (black) indicate significant difference within groups and * (blue) indicate significant difference between groups.

5.3.4 Topographical characterisation of superflexor tendon fascicles by atomic force microscopy

5.3.4.1 In air

The native pSFT fascicles imaged under AFM in air are presented in Figure 5.24. The optical images of the areas of different fascicles scanned by the AFM tip area shown (Figure 5.24 a & d), where the surface shows some evidence of longitudinally aligned substructures, albeit no crimp or distinguishable fibril features. The 2D height images (Figure 5.24 b & e) show some fibril structures which are orientated longitudinally along fascicle length; however, these seem to be covered by a layer, masking the sharper features of the fascicular matrix. The randomly positioned fascicle substructures, likely collagen fibrils, correspond to damaged or ruptured structures, also visible in the 3D topography (f). The topographical representation of native fascicles seems smooth yet containing many peaks and troughs (c). The layer enveloping the native fascicles made it difficult for precise fibril width and collagen D-spacing measurements.

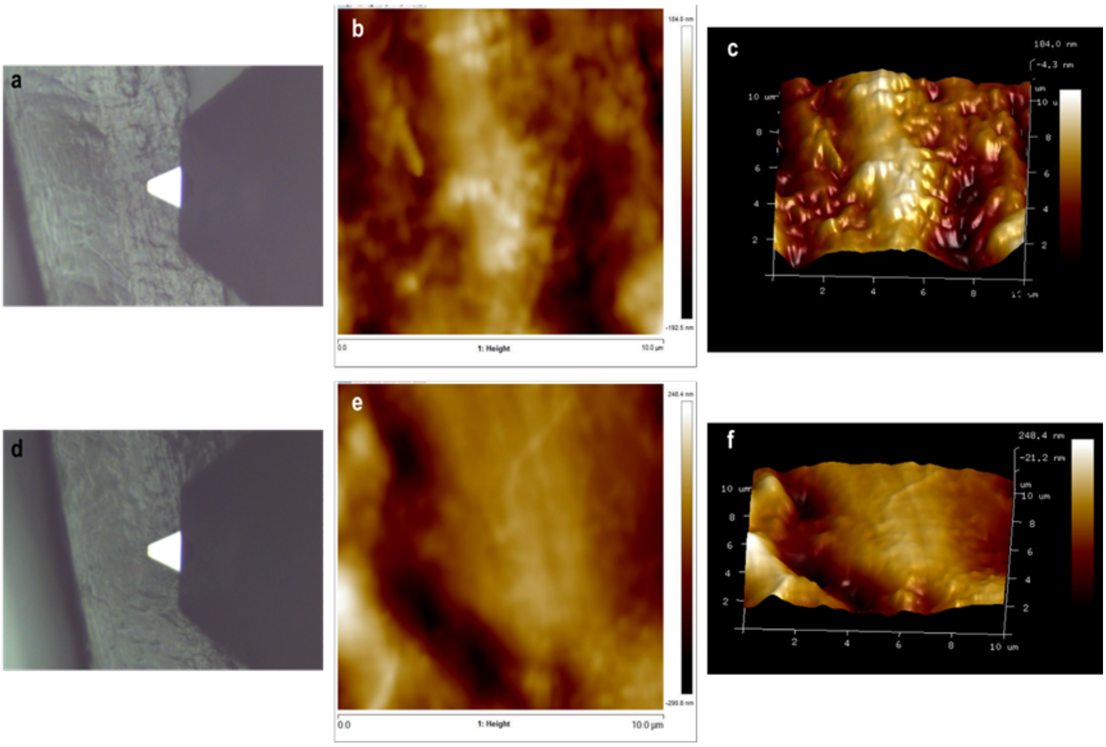

Figure 5.24: Topography of native fascicle surfaces, imaged in air.
Areas of the fascicle where the AFM scanning was conducted as captured by the camera; the AFM probe positioned above the sample can be seen as a bright triangular area connected to a black base (a, d); 2D height images (b, e) and 3D topography (c, f). Evidence of fibril structures aligned longitudinally along fascicle length. Some fibril damage observed with randomly positioned structures (e). Underlying structures appear to be covered by protective sheath, giving rise to a smoother topography observed in (c, f).

The decellularised pSFT fascicles imaged in air are presented in Figure 5.25. The optical images of areas of the different fascicles scanned are shown (Figure 5.25 a & d), where both vertical and horizontally imaged areas (sample was manually rotated to image both directions) showed a primarily longitudinal alignment of fascicle substructures, including visible fibrils. There were some fibril structures with varying angles of inclination, likely due to the evident crimp pattern (a). The fibrils with a more random orientation positioned atop the dense fibril network were likely ruptured or damaged structures (e). The detail in each of the individual fibrils suggests there was a thin or no layer enveloping the decellularised fascicles, allowing the probe to better interact with the fascicular matrix. The characteristic collagen D-spacing was observed in the 2D height images (b & e) as well as the 3D topographical images (c & f). Fibre bundles were observed in Figure 5.25 b & c, with a valley (darker colour) between adjacent fibres. Fibril structure diameters and collagen D-spacing measurements were conducted on decellularised 2D height images (b & e), given there were no distinguishable fibrils in native images (Figure 5.24). The mean fibril width in decellularised pSFT fascicles was 138.08 ± 25.09 nm. The collagen D-spacing was averaged at 68.58 ± 5.46 nm.

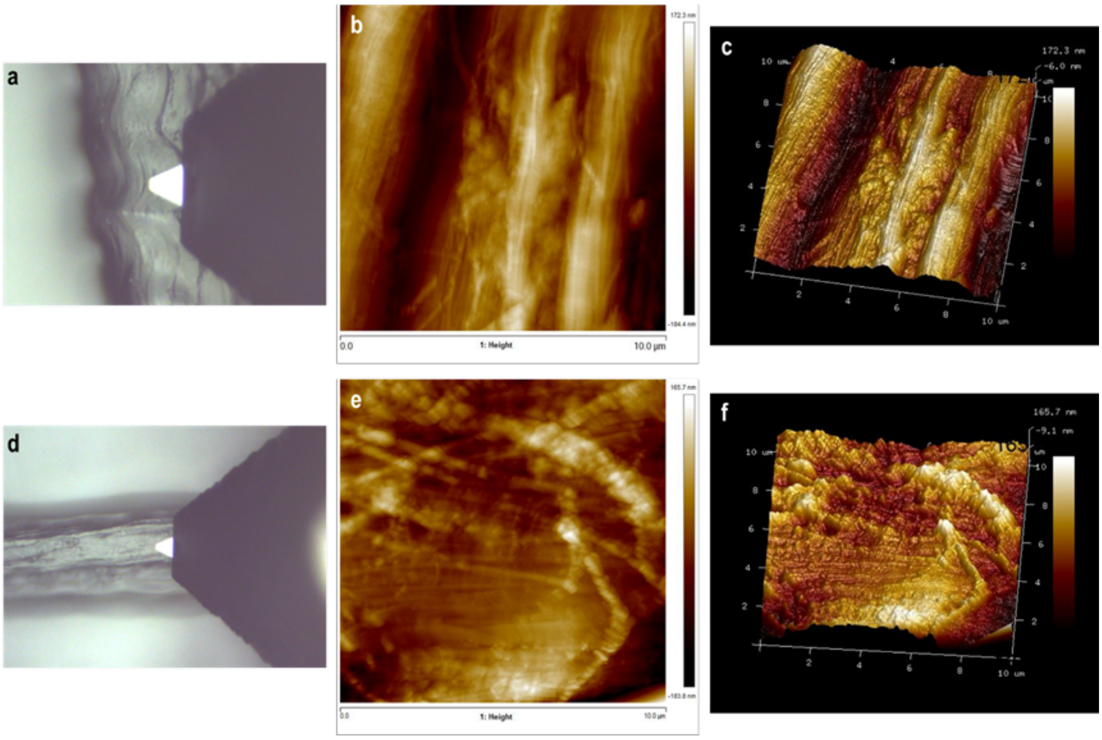

Figure 5.25: Topography of decellularised fascicle surfaces, imaged in air. Optical images of areas of the fascicle scanned by the AFM probe (a, d); 2D height images (b, e) and 3D topography (c, f). Fascicles were imaged vertically (a) and horizontally (d), both showing a mainly longitudinal alignment of fibre and fibril structures with some degrees of inclination, attributed to the characteristic crimp pattern, evident in (a). Evidence of fibril damage with some ruptured structures recoiling atop the otherwise arranged collagen network within the fascicle (b and e). Damaged fibre structures observed in (e), with increased height with respect to the rest of the fascicle surface (f). Collagen D-spacing visible (c, f). Heterogeneous surface, with evidence of valleys in (c).

The roughness, skewness and kurtosis of native and decellularised fascicles imaged in air are presented in Table 5.2. Briefly, skewness values smaller than 1 were indicative of a surface dominated by peaks, smaller than 0 described a surface with pits or valleys, while a skewness value of 0 contained random variations in the surface topography. Kurtosis values greater than 3 contained sharp features, with few high peaks or valleys, lower than 3 described a gradually varying surface with many moderate height features, while a kurtosis value of 3 described a normally distributed surface [401]. There were no significant differences between the roughness, skewness or kurtosis of native and decellularised groups. The skewness of both groups is indicative of a surface mainly comprised of valleys, with kurtosis describing a gradually varying surface.

Table 5.2: Roughness values for native and decellularised fascicles imaged in air,

	Roughness average (Ra)	Skewness	Kurtosis
Native	54.30 ± 15.48 nm	-0.26 ± 0.54	2.81 ± 0.52
Decellularised	42.50 ± 15.68 nm	- 0.21 ± 0.27	2.90 ± 1.23

obtained from a 10 µm 2D height image using NanoScope Analysis software. Data is presented as mean (n = 2) ± 95% CI. Data were compared using an unpaired Student's t-test.

An attempt at obtaining a higher resolution topography of decellularised fascicles led to the images presented in Figure 5.26. The optical images of areas of each fascicle scanned by the AFM probe (a & d) showed clear evidence of collagen substructures and crimp. A mainly longitudinally orientated bundle of fibrils is observed in both specimens. Evidence of fibre organisation is observed (e), with valleys (darker colour) between adjacent fibres. The arrangement of the network of fibrils within the fascicular matrix is clearly visible in (f), where the deeper fibrils appear in a darker colour, yet still with sharp features, particularly of the collagen D-spacing along fibril length. Evidence of a thin enveloping layer on the fascicle surface, where ruptures or damage to the layer revealed gaps where underlying fibril structures (black arrows) were visible. The mean fibril width in decellularised pSFT fascicles was 117.00 ± 29.91 nm. The collagen D-spacing was averaged at 67.17 ± 6.89 nm.

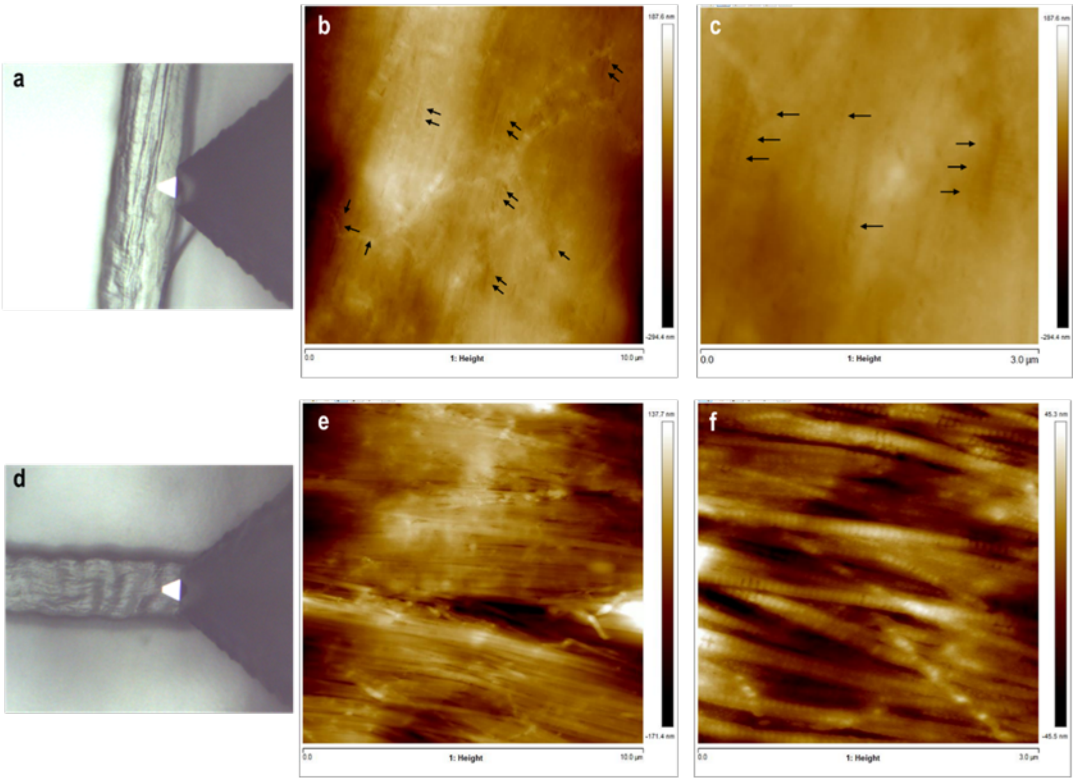

Figure 5.26: High resolution imaging of decellularised fascicle surfaces, imaged in air.
Optical images of areas of the fascicle scanned by the AFM probe (a, d); 2D, 10 µm height images (b, e) and 2D, 3 µm height images (c, f). Collagen fibrils aligning longitudinally along fascicle length with superposing fibrils, creating the organised network within the fascicle unit. Characteristic D-spacing of collagen along fibril length visible, particularly in (f). Evidence of thin, protective sheath enveloping underlying fibrils in (b, c), where damage is observed in areas with clearer fibril structures (black arrows).

5.3.4.2 In liquid

Native (Figure 5.27 a, c, e, g) and decellularised (Figure 5.27 b, d, f, h) fascicles were imaged in PBS. The optical images representing the area which was imaged (a – b, e – f) using the AFM appeared swollen compared to the images in air (see Section 5.3.4.1). The fascicle substructures and collagen crimp were not apparent. Native 2D height images (c, g) showed no apparent similarities between surfaces. An uneven surface was visible in (c), where circular shaped clusters were apparent within a sheath with superficial cracks with some underlying tubular structures. The arrangement of longitudinally aligned fascicle substructures was more evident in (g), where the same outermost layer was visible. Randomly orientated fibrils likely indicative of ruptures or damage observed atop the fascicle surface. Decellularised 2D height images (d, h) showed similar topographies between fascicles. Clearly visible fibril structures, with fibre structures harder to discern. A primarily longitudinally aligned network of fibrils was evident, with some varying degrees of inclination within the fascicular matrix. Collagen D-spacing along fibril length was clearly visible in (d). Ruptured fibrils were observed randomly orientated at the highest point of the fascicle surface (brighter colour), with clear features. Figure 5.27h was not imaged completely due to the interaction between the probe and the specimen being disrupted halfway through the imaging process. Measurements of fibril width and collagen spacing conducted on (d) revealed a mean of 153.56 ± 58.49 nm and 71.82 ± 12.82 nm, respectively.

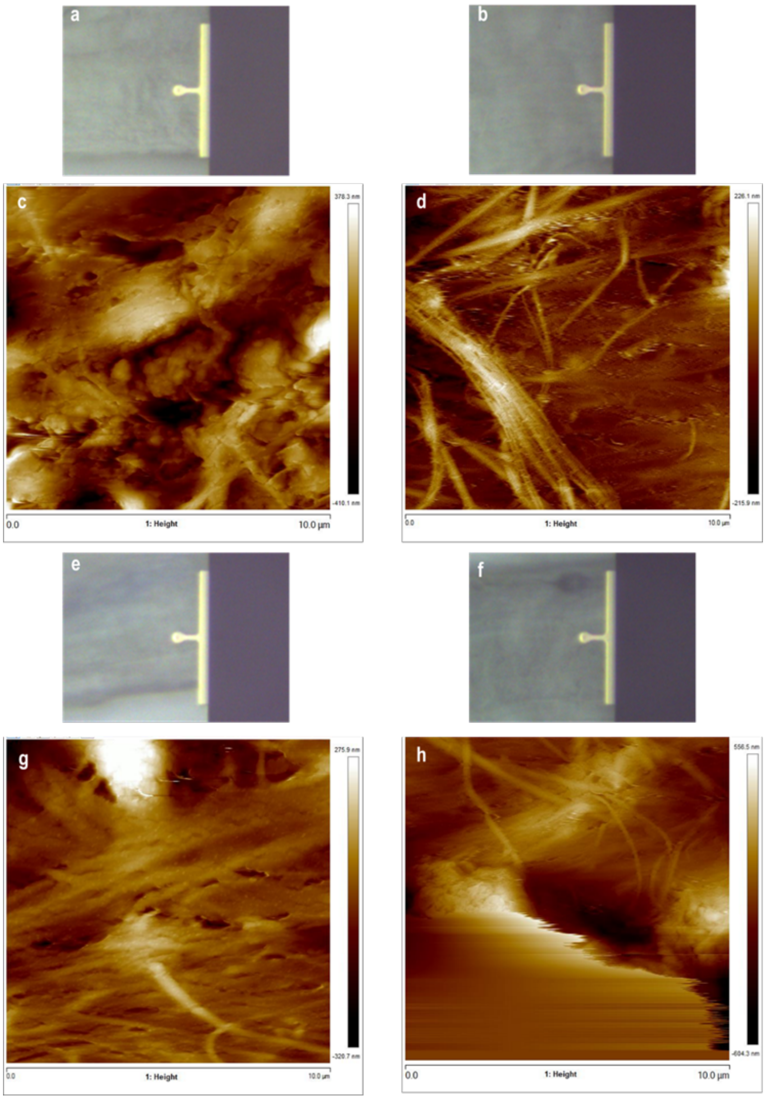

Figure 5.27: Topography of native and decellularised fascicles, imaged hydrated in PBS.
Optical images of areas of the native (a, e) and decellularised (b, f) fascicle areas scanned by the AFM probe. 2D height images of native (c, g) fascicle with varying topography according to the sample and area imaged. Image (c) with a uneven surface, appearing as a protective sheath with underlying structures. In (g), clearer fibre structures aligned mainly longitudinally along fascicle length, with some fibres at different inclinations, creating the arrangement of collagen within fascicle structures. Evidence of damaged fibres superposed with random orientation. 2D height images of decellularised (d, h) fascicle topography showing fibres with similar orientation to native (g), also with some damaged fibres appearing torn and randomly orientated atop the otherwise organised fibre network. Image (h) does not show the complete surface area due to tip-specimen interaction failing; however the observable area is topographically similar to (d).

The roughness, skewness and kurtosis of native and decellularised fascicles imaged in

PBS are presented in Table 5.3. These were obtained from a central 5 µm area of the 2D height images (Figure 5.27 c – d, g – h) due to (h) being incomplete data. There were no significant differences between groups. The skewness of the native group is indicative of a surface rich in valleys, while the decellularised group has random variations in its topography. The kurtosis of the native group speaks of especially sharp valleys, while the decellularised group had more normally distributed features.

Table 5.3: Roughness values for native and decellularised fascicles imaged in PBS,

	Roughness average (Ra)	**Skewness**	**Kurtosis**
Native	71.40 ± 73.69nm	-0.20 ± 0.17	3.16 ± 1.71
Decellularised	61.10 ± 48.22 nm	0.12 ± 0.35	3.02 ± 1.28

obtained from a central 5 µm area of each 2D height image using NanoScope Analysis software. Data is presented as mean (n = 2) ± 95% CI. Data were compared using an unpaired Student's t-test.

Native and decellularised fascicles subjected to ethanol treatment (see Section 5.2.4.1) were hydrated with PBS and imaged in liquid (Figure 5.28). The optical images of the areas scanned by the AFM probe of native (a, e) and decellularised (b, f) showed swelling accompanied by a lesser evident collagen crimp pattern on the fascicular surface. However, the swelling was less visible than in Figure 5.27. Native 2D height images (c, g) showed longitudinal fragmentation of the surface, appearing torn with some small spacing between the cracks. The areas where tears occurred showed fibril-like structures orientated normal to the longitudinal fascicle, where some of these structures appeared torn (g). Decellularised 2D height images (d, h) showed a similar phenomenon, where evident fragmentation of the fascicle surface was observed. The areas where tears occurred revealed wider spacing between adjacent fragments, with many thin fibril-like structures, also orientated normal to the longitudinal fascicle. Evidence of structure rupture was also observed, with a higher amount of damage compared to the native group. Some underlying fascicle substructures were visible in (h).

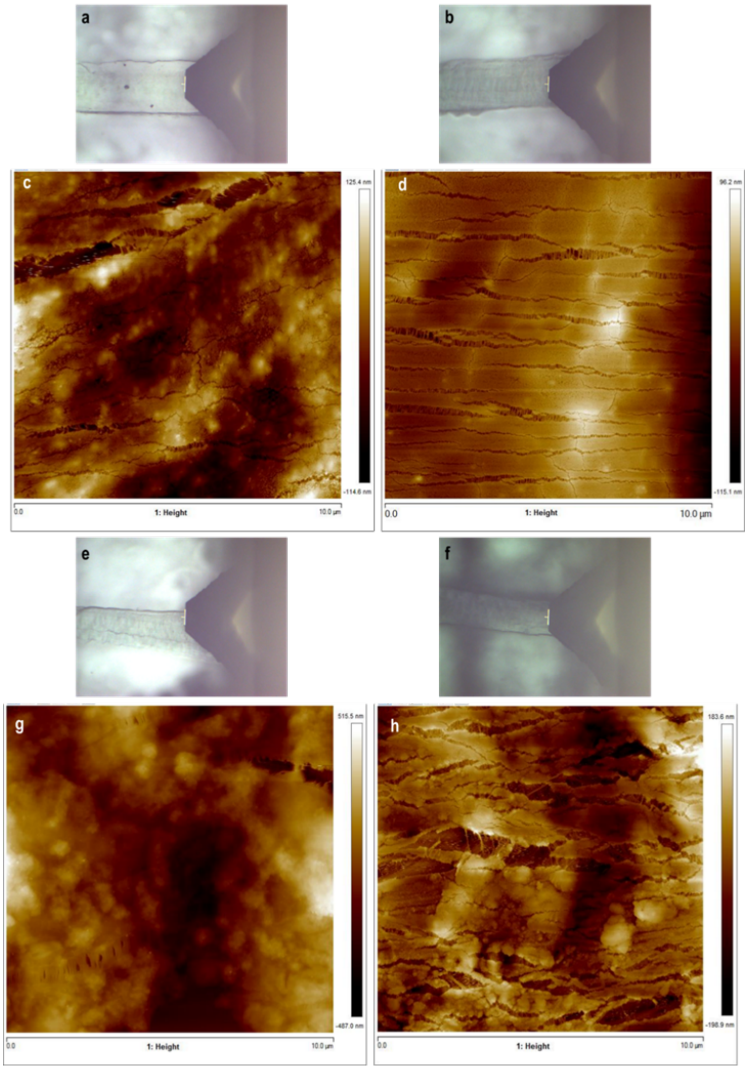

Figure 5.28: Topography of native and decellularised fascicle surfaces dehydrated with ethanol during sample preparation, imaged hydrated in PBS.
Optical images of the areas scanned by the AFM probe of the native (a, e) and decellularised (b, f) fascicles. 2D height images of native (c, g) and decellularised (d, h) fascicle specimens subjected to ethanol dehydration prior to being rehydrated with PBS. Evidence of longitudinal fragmentating damage caused by dehydration revealing fibril substructures beneath most external layer of decellularised fascicle surface (h). Damage is more apparent in decellularised fascicle specimens compared to native specimens, with more visible ruptures, and wider spacing between ruptures in d and h. Tubular/fibril-like structures apparent where ruptures occur, with a more dense arrangement in native specimens (g) compared to the thinner, spaced-out structures in decellularised specimens (d). The tubular/fibril-like structures appear orientated normal to the longitudinal alignment of the fascicle.

The roughness, skewness and kurtosis of ethanol treated native and decellularised fascicles imaged in air are presented in Table 5.4. There were no significant differences between groups. The skewness of the native group indicates random variations in the topography, while the decellularised group had a surface comprised of valleys. The kurtosis of the native group describes a gradually varying surface, while the decellularised group had particularly sharp valleys across its topography.

Table 5.4: Roughness values for ethanol treated native and decellularised fascicles imaged in PBS,

	Roughness average (Ra)	Skewness	Kurtosis
Native	73.85 ± 90.45 nm	0.07 ± 0.17	2.93 ± 0.36
Decellularised	31.95 ± 21.85 nm	0.26 ± 0.23	3.48 ± 0.60

obtained from a 10 µm 2D height image using NanoScope Analysis software. Data is presented as mean (n = 2) ± 95% CI. Data were compared using an unpaired Student's t-test.

The tears observed in both groups (Figure 5.29) show a less damaged topography for the native group (a), with a small space between the visible rupture. The fibril-like structures were abundant, creating a dense network. The tears observed in the decellularised topography (b) were separated by wider spaces, where the fibril-like structures were thin and elongated, some completely ruptured, while not creating as dense a network as seen in the native tears. The mean width of the fibril-like structure of the native fascicle was 34.57 ± 14.04 nm, and the width of the structures of the decellularised fascicle was 26.42 ± 13.90 nm.

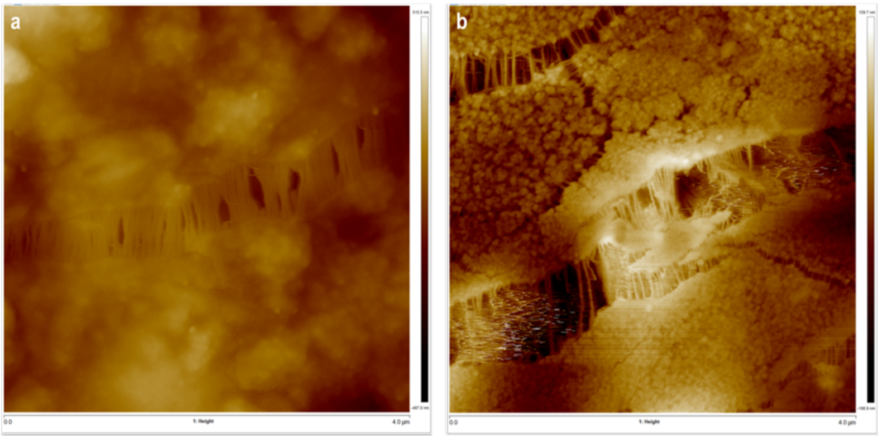

Figure 5.29: Ruptures in native and decellularised fascicle surfaces.
A closer look at the ruptures reveal wider gaps between ruptures in decellularised (b) fascicles compared to the native (a) fascicles. The tubular/fibril-like structures appear thinner, more elongated and some torn in the decellularised specimen. A denser, organised arrangement of the tubular/fibril-like structures is evident in the native specimen.

5.3.5 Nanomechanical characterisation of superflexor tendon fascicles

The topography and modulus of a native pSFT fascicle corresponding to a 3 µm area measured using Peak-Force QNM mode is shown in Figure 5.30. The topographical features of the native fascicle revealed an apparent enveloping layer as observed previously in section 5.3.4. Collagen crimp morphology was visible in the form of the collagen D-spacing in some areas (b). The moduli of the native fascicle appeared not to vary drastically across the surface of the area imaged (c), ranging between 3.98 MPa and 251

MPa. This is observed through an even colour range throughout the log Modulus image (c). The depth analysis histogram revealed a seemingly Gaussian distribution of moduli across the fascicle surface, with a mode of circa 18.62 MPa.

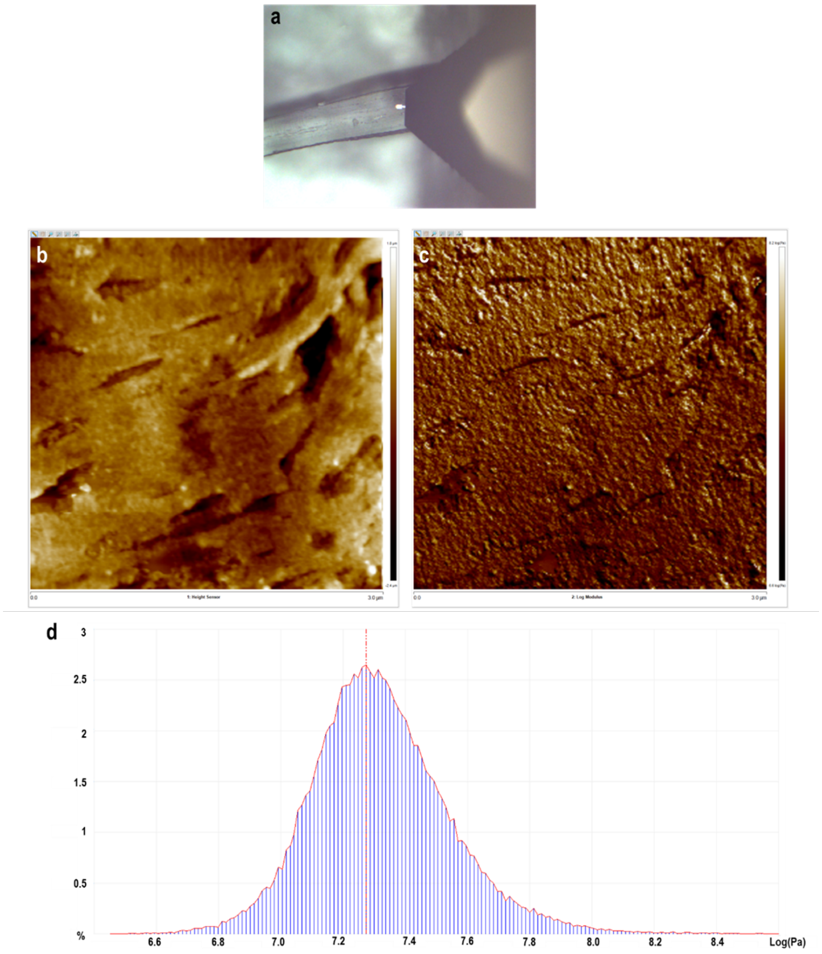

Figure 5.30: Quantitative NanoMechanics (QNM) of a native pSFT fascicle, imaged in air.
Optical image of the area of the fascicle scanned by the AFM probe (a); 2D height image (b), log Modulus image (c) and moduli distribution histogram (d). Evidence of enveloping layer with some apparent crimp pattern in (b). Moduli values appear consistent across the native fascicle surface (c), with an apparent Gaussian distribution between 6.6 and 8.4 log(Pa) in (d).

The topography and modulus of a decellularised pSFT fascicle corresponding to a 5 µm area is shown in Figure 5.31. The topographical features of the decellularised fascicle showed an arrangement of fibril structures with a clearly visible collagen D-spacing along fibril length (b). The orientation of the fibrils was similar to that described in section 5.3.4. The circular features visible across the surface topography were likely adhesive or another contaminant as the specimen was imaged in air. The moduli of the decellularised fascicle showed some lighter areas in (c) through the middle region, flanked at the top and bottom by darker areas, corresponding to lower values of moduli. The depth analysis histogram revealed a range of moduli between 177 MPa and 794 MPa. The mode was found circa 478 MPa.

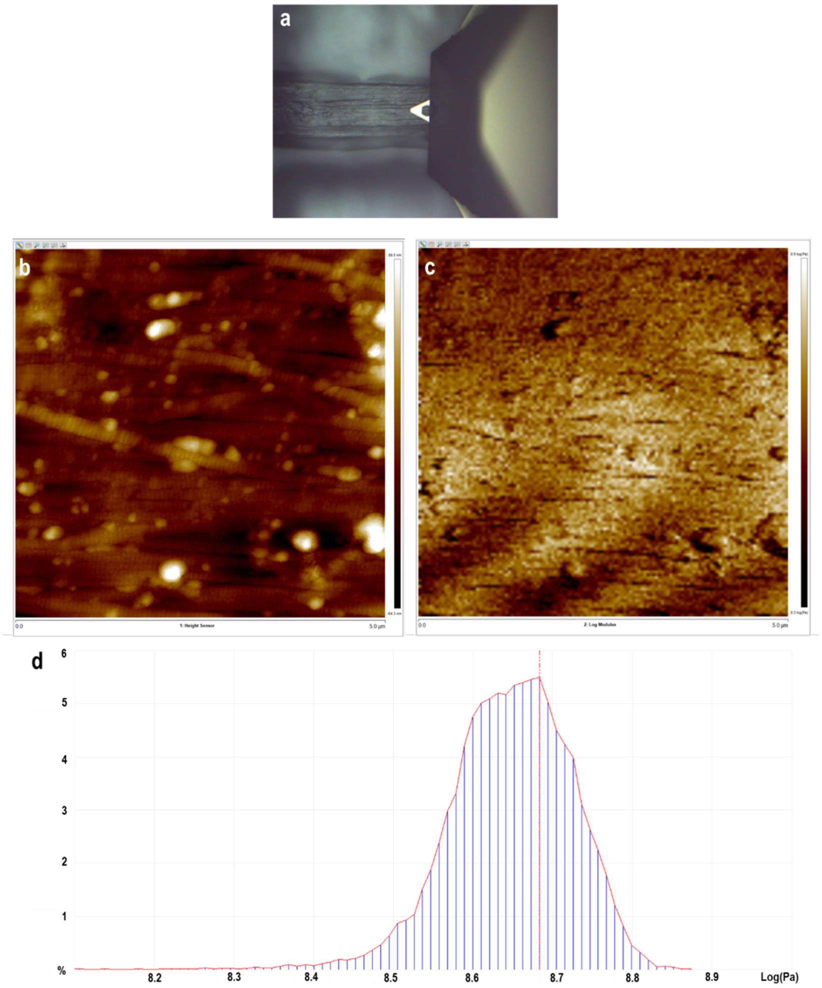

Figure 5.31: QNM of a decellularised pSFT fascicle, imaged in air.
Optical image of the area of the fascicle scanned by the AFM probe (a); 2D height image (b), log Modulus image (c) and moduli distribution histogram (d). Clear evidence of fibril structures with characteristic collagen D-spacing visible. Some bubble-like features across fascicle surface (b). Moduli values appear consistent more consisten in the middle area of the fascicle surface, while lower moduli values exist on the top and bottom areas of (c), corresponding with darker coloured areas. Moduli values ranged between 8.25 and 8.9 log(Pa) in (d).

In order to have a closer look at the decellularised pSFT fascicle surface, a 1 µm area was imaged. The topography and modulus of the sample corresponding to a 1 µm area is shown in Figure 5.32. The topographical features of the fascicle show fibril-like structures with evidence of the characteristic collagen crimp waviness in (b). A predominantly longitudinal orientation was found similar to the observed in Figure 5.31. The moduli varied across the surface of the area images, with some light areas in the bottom of (c), corresponding to higher values (black rectangle), while the darker areas located at the top corresponded to lower moduli values (white rectangle). A depth analysis histogram of the entirety of (c) could not be conducted as not all areas across the surface interacted with the probe (smooth brownish areas and white dots). The histogram corresponding to the lower moduli area (d) ranged between 25.12 MPa and 316 MPa, with a mode at circa 63 MPa. The histogram corresponding to the higher moduli area (e) ranged between 63

MPa and 2.5 GPa. The mode was found circa 316 MPa.

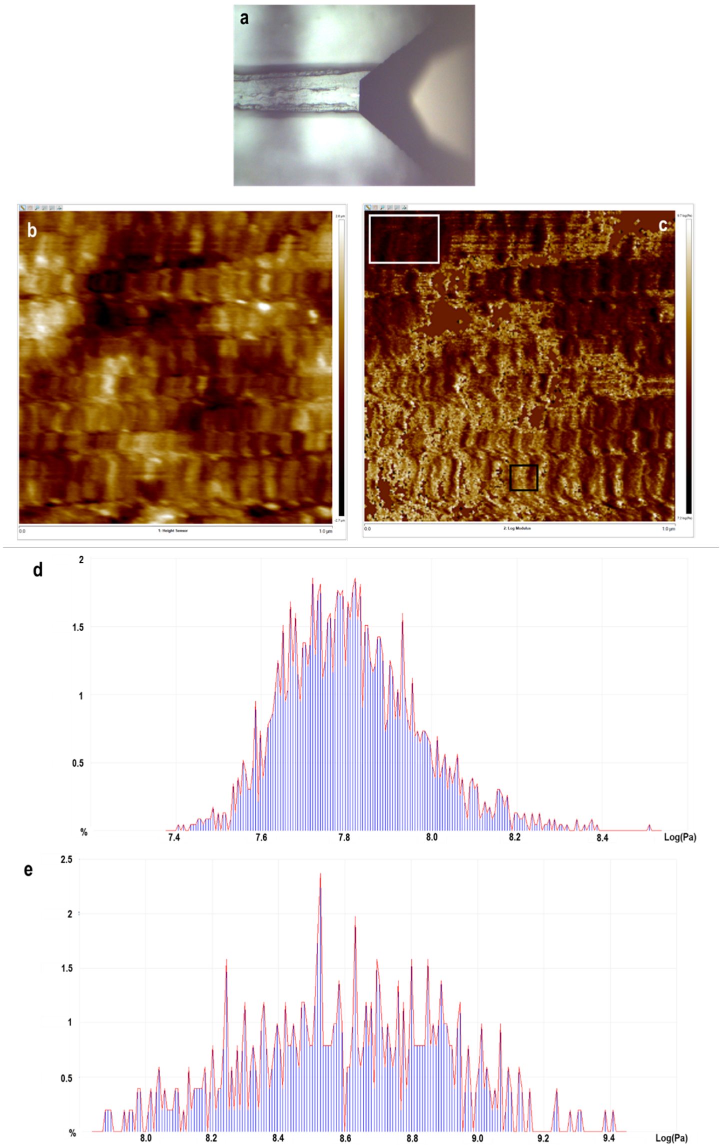

Figure 5.32: QNM of a decellularised pSFT fascicle, imaged in air.
Optical image of the area of the fascicle scanned by the AFM probe (a); 2D height image (b), log Modulus image (c) and moduli distribution histograms (d & e). Apparent fibril structures with crimp pattern visible in (b). Moduli values vary across the fascicle surface, with high moduli in lighter coloured areas and lower moduli in darker coloured areas (c). Moduli values corresponding to a the area within the white rectangle ranged between 7.4 and 8.5 log(Pa) in (d), while the area within the black rectangle reached up to 9.4 log (Pa) in (e).

5.3.6 Preliminary characterisation of the interfascicular matrix of porcine superflexor tendon

Millers elastin staining revealed blue elastic fibres mainly located in the interfascicular spacing of native pSFT sections (Figure 5.33). The gaps between fascicular structures, housing the IFM, contained an organised arrangement of elastic fibres orientated longitudinally along IFM channels, while others forming circular and oval structures. Similarly, some blue stained fibres were located along the periphery of the fascicle structures (A2), while the intrafascicular matrix showed no clear evidence of elastic fibre presence. Cellularity was observed in native sections, with a higher density in IFM channels compared to the fascicular matrix.

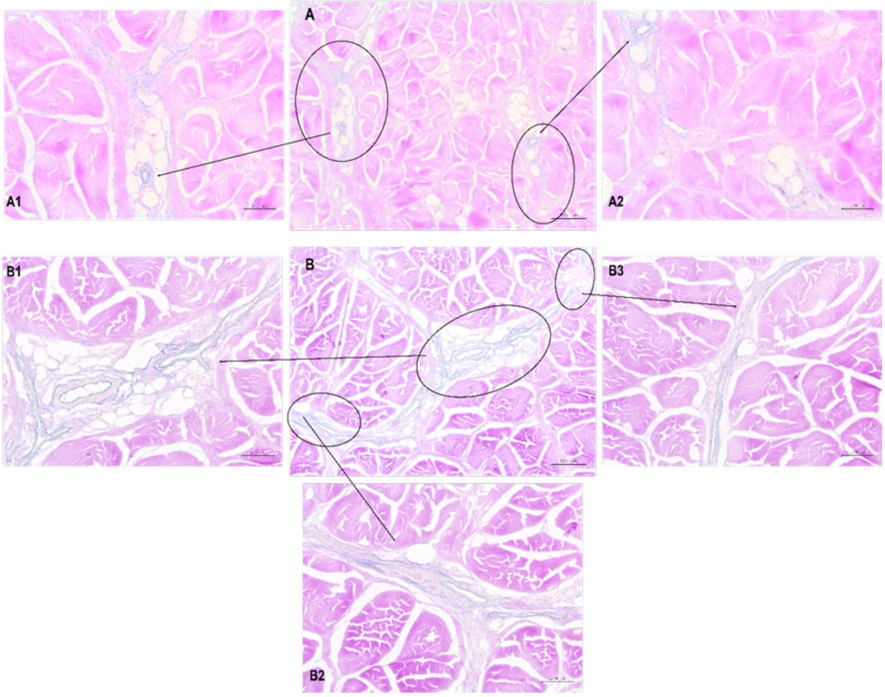

Figure 5.33: Millers elastin staining of transverse sections of native pSFT.
Native sections (A & B) with higher magnification images (A1 – A2, B1 – B3) to represent elastin staining more clearly. The black circles and arrows indicate areas of A and B that are magnified. Blue stained elastic fibres in IFM channels (A, B). Organised, abundant presence of elastic fibres throughout the endotenon, and perifascicular regions (A2). Longitudinal (B2, B3) and circular (A1, A2, B1) arrangement of elastic fibres, with no clear presence of elastin within fascicular matrix. Images (A & B) were taken at 50x magnification (scale bar 200 µm), while images (A1 – A2, B1 – B3) were taken at 100x magnification (scale bar 100 µm).

Decellularised sections showed less presence of elastic fibres throughout pSFT sections (Figure 5.34). Fascicular structures were less noticeable compared to native sections. Interfascicular spacing appeared to have increased post-decellularisation, observed as a higher white background compared to pink stained matrix. In the IFM channels, some blue stained elastic fibres were present, appearing thinner compared to the elastic fibres in native sections (Figure 5.33). The orientation of the elastic fibres was a combination of primarily longitudinal and some circular arrangements. There was evidence of some elastic fibres along the periphery of fascicle structures (B2, B3), albeit thinner and in a lesser amount compared to native sections (Figure 5.33).

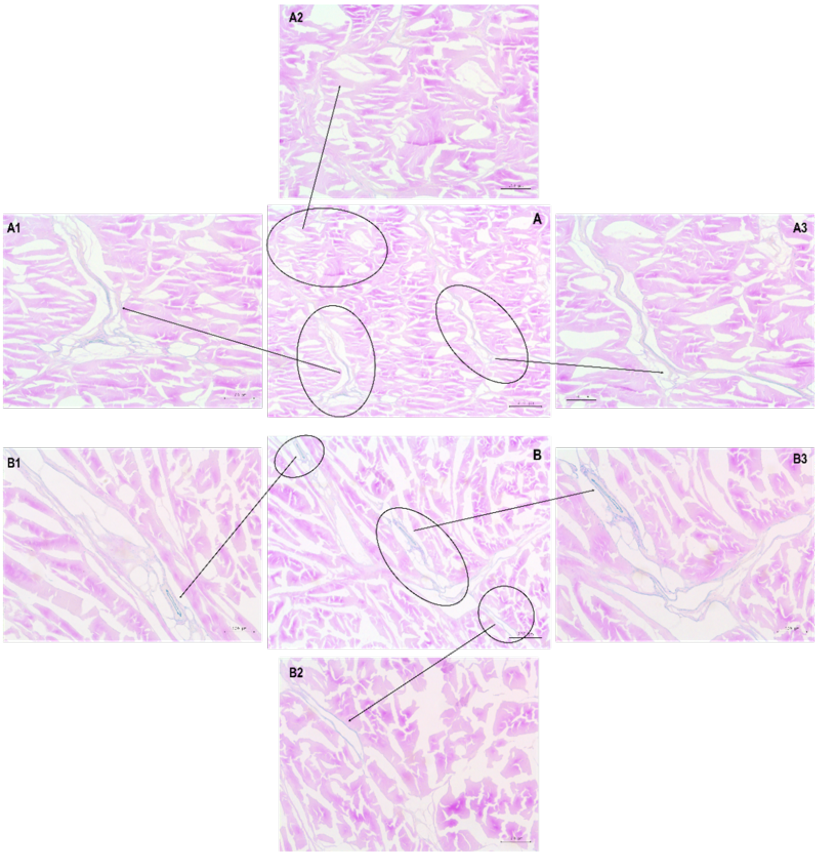

Figure 5.34: Millers elastin staining of transverse sections of decellularised pSFT.

Decellularised sections (A & B) with higher magnification images (A1 – A3, B1 – B3) to represent elastin staining more clearly. The black circles and arrows indicate areas of A and B that are magnified. Blue stained elastic fibres localised in IFM channels (A, B). Thin and scarce staining throughout sections, with some circular (A1, B1, B3) and more longitudinally (A2, A3, B2) arranged elastic fibres. No evidence of elastin in fascicular structures. Images (A & B) were taken at 50x magnification (scale bar 200 µm), while images (A1 – A2, B1 – B3) were taken at 100x magnification (scale bar 100 µm).

Medial regions of native (Figure 5.34 A) and decellularised (Figure 5.35 B) pSFT revealed blue stained elastic fibres mainly located in the interfascicular gaps containing IFM. A clear abundancy was observed in native fascicular matrix (A), with a dark blue staining of seemingly thick fibres, aligned longitudinally along the IFM channels, with some larger fibres, and an array of shorter fibres. A circular arrangement of elastin was also observed in the IFM. Some evidence of thinner fibres along the periphery of fascicle structures was apparent. A clear reduction of elastic fibres was observed in decellularised fascicular matrix (B), with a blue presence of thin elastic fibres in IFM channels, mainly aligned along the interfascicular spacing, with evidence of smaller circular arrangements. Thin elastic fibres observed along the periphery of fascicle structures. Peritenon area of native (C) pSFT show an abundant, randomly aligned collection of short elastic fibres along the peritenon, whereas decellularised (D) sections show a small amount of longer elastic fibres along the peritenon area.

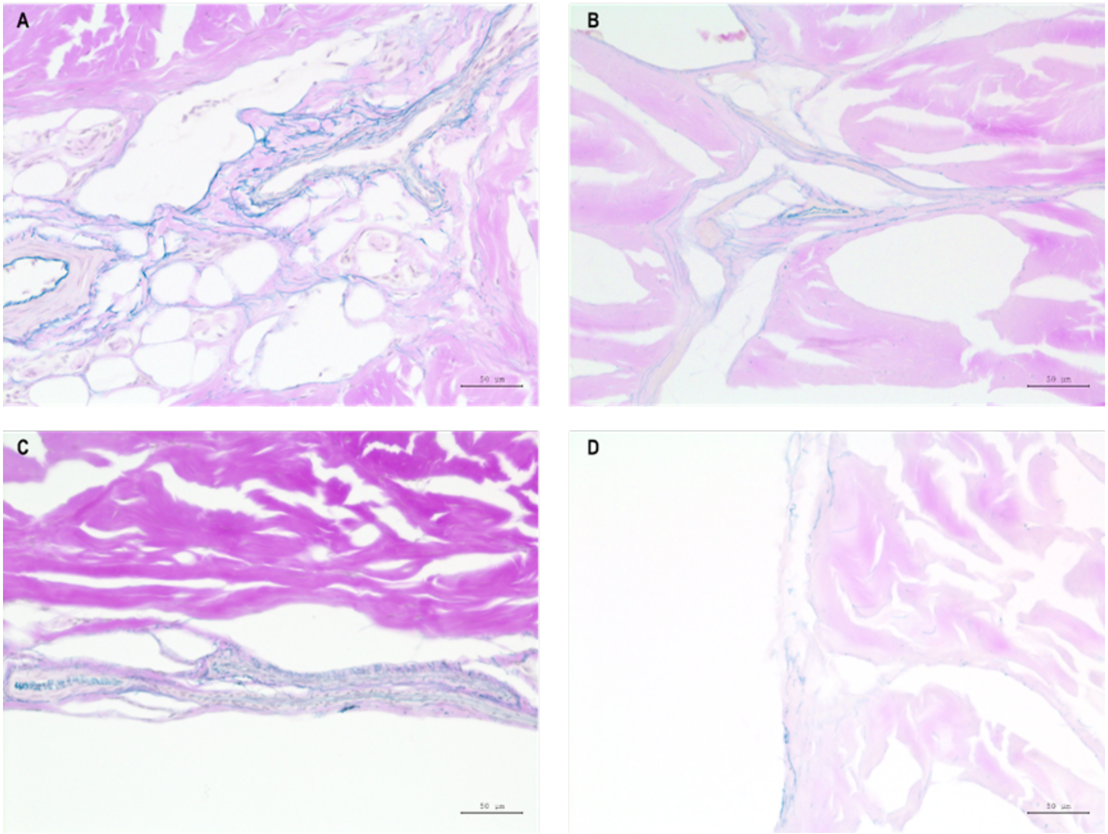

Figure 5.35: Millers elastin staining of native and decellularised fascicular matrix and peritenon region.
Native matrix (A) shows abundant, dense staining of blue stained elastic fibres in IFM channels and perifascicular regions. Decellularised matrix (B) shows a lesser abundance of elastic fibres, similarly localised mainly to the IFM, with some presence along the periphery of fascicle structures. Peritenon regions of native (C) sections show a randomly aligned array of abundant elastic fibres of different lengths, while decellularised (D) peritenon shows a smaller amount of longer elastic fibres. Images were taken at 200x magnification (scale bar 50 µm).

Transverse sections of native and decellularised pSFT for atomic force microscopy imaging are presented in Figure 5.36. When immobilising on adhesive vinyl (A & C), there was no clear evidence of the adhesive interacting with the sample. However, when immobilising on waterproof tape (B & D), there was evidence of the adhesive sticking onto the periphery of the pSFT sections. Native sections (A & B) showed a dense matrix, with little interfascicular spacing. Decellularised sections (C & D) showed more spacing between fascicular matrix, observed as white background between the dark grey/black matrix.

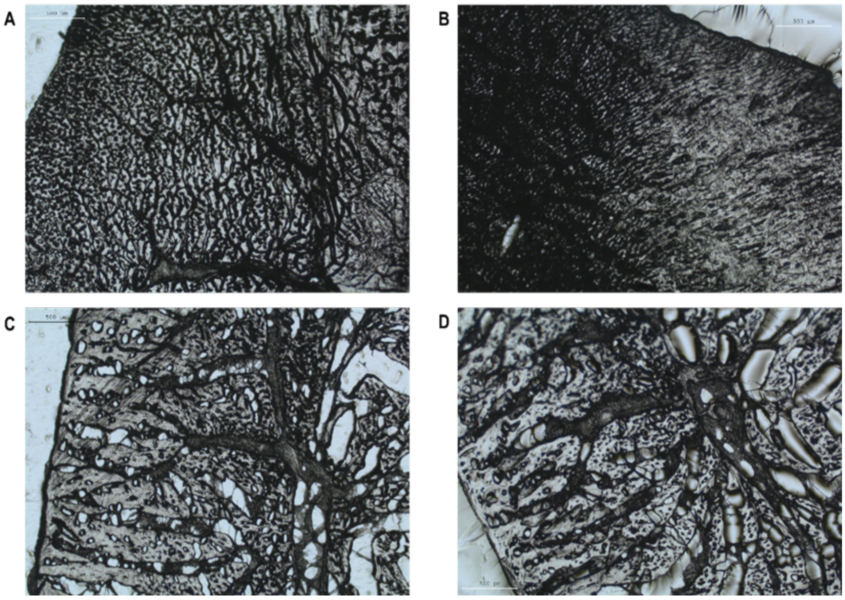

Figure 5.36: Transverse sections of native and decellularised pSFT.
Sections from cryo-embedded tissue immobilised on adhesive vinyl (A, C) and waterproof tape (B, D). Native sections (A, B) show a dense matrix, while more inter- and intrafascicular spacing is evident in decellularised sections (C, D).

Sections immobilised on vinyl adhesive were used for AFM imaging. The areas imaged are shown in Figure 5.37 a and b, where the interfascicular spacing or IFM channels (yellow asterisks) are narrow in native pSFT (a), while considerable larger in decellularised pSFT (b). Similarly, the fascicular matrix of the native area is dense with no apparent intrafascicular spacing, while decellularised matrix has a more open matrix, with some intrafascicular gaps. The 2D height image of native pSFT (c) show a rugged and dense topography, with a seemingly striated pattern across the fascicular matrix. The horizontal lines correspond to a technical issue likely related to the adhesive interacting with the probe. The 2D height image of decellularised pSFT (d) show a less rugged fascicular topography, with an undulation occurring in the central area of the image. The striated topography of native pSFT was not evident in decellularised pSFT.

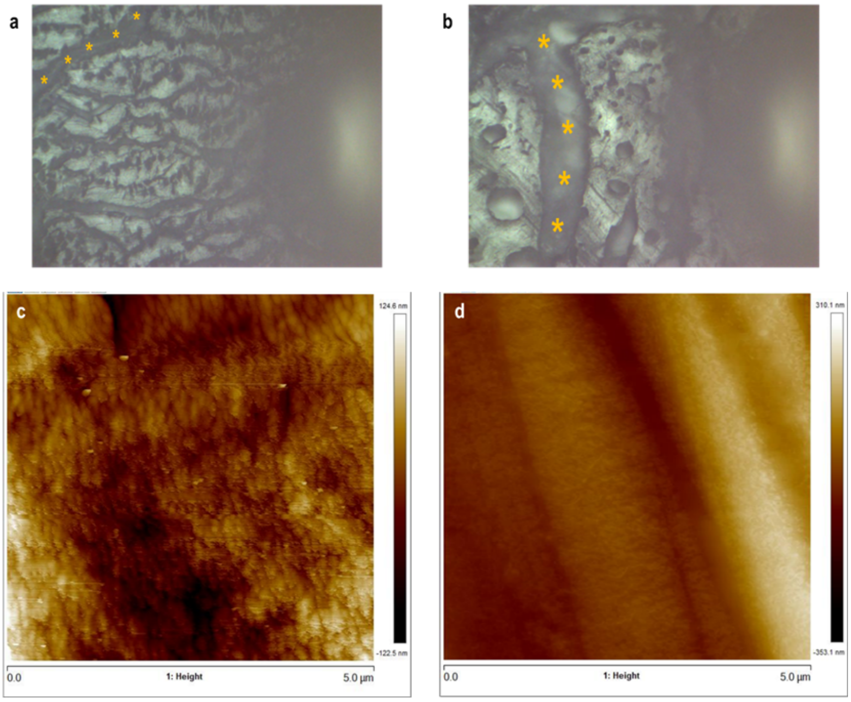

Figure 5.37: Topograhy of transverse sections of native and decellularised pSFT, imaged in air.
Area of the native (a) and decellularised (b) areas imaged, where interfascicular spacing is much larger in the decellularised area (asterisks). 2D height images of native (c) and decellularised (e) fascicular matrix. A rougher, compact topography in native specimens, compared to a smoother topography of decellularised specimens.

The roughness, skewness and kurtosis of native and decellularised AFM images of transverse sections are given in Table 5.5. The skewness of both groups indicate the topography contained mainly valleys. The kurtosis describes the features as sharp.

Table 5.5: Roughness values for native and decellularised transverse sections,

	Roughness average (Ra)	**Skewness**	**Kurtosis**
Native	20.20 nm	-0.08	3.66
Decellularised	34.50 nm	-0.19	3.75

obtained from a 5 µm 2D height image using NanoScope Analysis software.

AFM images of bulk native and decellularised pSFT specimens are presented in Figure 5.38. The areas of the native (a) and decellularised (b) imaged showed interfasicular spacing in both (asterisks). The imaging of native pSFT allowed an area of 10 µm to be imaged (c), presenting a fascicular structure surrounded by interfascicular spacing (white arrows) before continuing to the next fascicle. The spacing likely containing IFM was a deep valley (darker colour), not rendering a discernible topography due to its height difference with respect to the fascicular matrix (lighter colour). When imaging decellularised pSFT, only an area of 5 µm was obtained (d) due to height differences between fascicular and IFM (valleys), which challenged the probe in continuing its tapping across the specimen. A clear dark valley was observed (white arrows), likely corresponding to the interfascicular spacing where IFM is located. The 3D images of native (e) and decellularised (f) pSFT show the topography mainly of fascicular matrix in a yellow, beige colour, while representing IFM in interfascicular spacing as valleys in a darker colour. The circular features observed in 3D and 2D height images (black arrows) of both appear to be fibre structure endings attributed to the transverse orientation of the fresh tendon specimens.

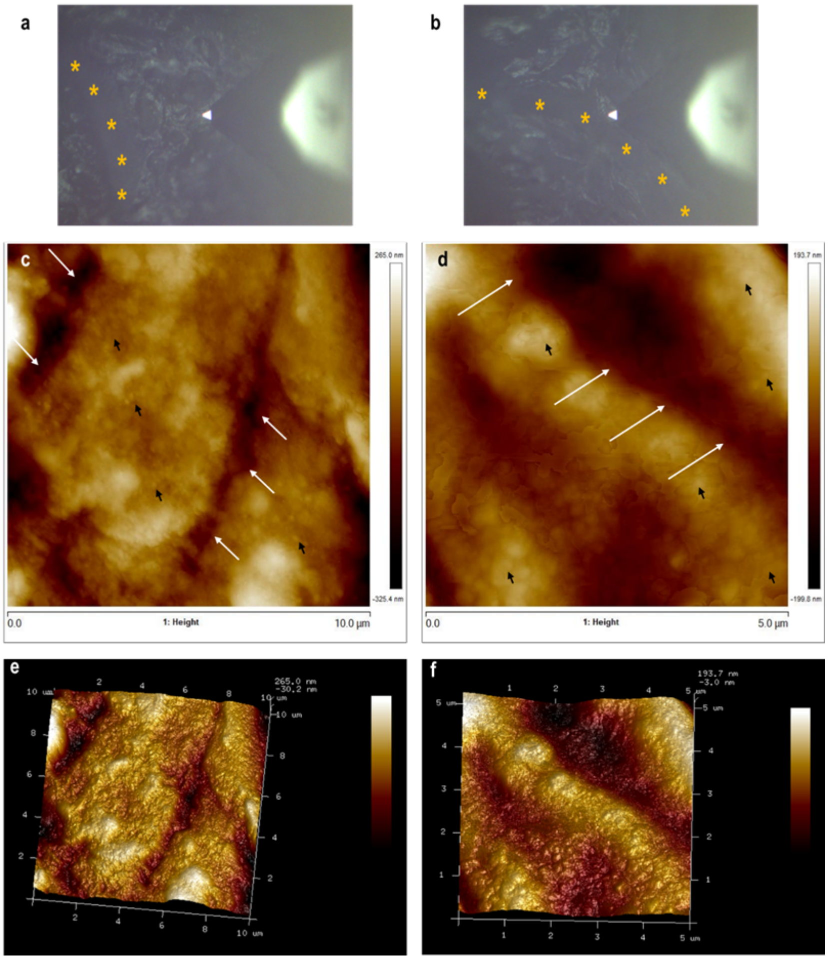

Figure 5.38: Topography of bulk native and decellularised pSFT specimens, imaged in air.
Area of the native (a) and decellularised (b) areas imaged, where interfascicular spacing was evident in both (asterisks). 2D height images of native (c) and decellularised (d) matrix. Native 2D height image with fascicle and inter-fascicular spacing (white arrows), where the differences in height make the topography of the IFM difficult to characterise. Decellularised 2D height image with mainly fascicular topography, while a valley likely IFM (white arrows) is observed. Round areas on surface (black arrows) are fibres visible due to transverse orientation of the bulk specimens. 3D images show the topography of the fascicular matrix, while IFM is shown as a valley due to height differences, evident more in native (e) pSFT. The smaller height differences within the imaged area in decellularised (f) sections show the topography of its fascicular matrix.

The roughness, skewness and kurtosis of native and decellularised AFM images of transversely imaged bulk pSFT are given in Table 5.6. The skewness of both indicate the topograhy contained mainly valleys. The kurtosis of native pSFT, approximating 3 closely may indicate the surface was normally distributed, while decellularised pSFT had a gradually varying surface.

Table 5.6: Roughness values for native and decellularised transverse orientated bulk specimens,

	Roughness average (Ra)	**Skewness**	**Kurtosis**
Native	51.4 nm	-0.38	3.02
Decellularised	44.60 nm	-0.06	2.89

obtained from a 5 µm 2D height image using NanoScope Analysis software.

Due to time and technical limitations, the mechanical properties of the IFM of native and decellularised pSFT could not be investigated (see Section 5.1.1).

5.4 Discussion

5.4.1 Structure and composition of superflexor tendon fascicles

The qualitative study of the structure of native, decellularised and GAG-depleted fascicles using microscopy revealed the presence of fascicle structures of variable diameters (see Table 5.1). However it may be possible that the structures with larger diameter (Figure 5.15d; Figure 5.17b) constitute a bundle of fascicles with a smaller diameter. Dissection techniques and primarily human-related limitations did not allow the strict assessment of fascicle structures presented here to be validated as a single fascicle unit. Nevertheless, the existence of fascicles with distinct diameters coincides with the native anatomy of flexor tendon across species [405].

Fascicles are likely discontinuous within a tendon. They may be continuous in the middle region, but probably not reaching tendon extremities [17]. This would allow a more complex network of structures to conform whole tendon, contributing to the mechanical strength of the tissue. Fascicles have been reported to diverge, converge and split in equine digital flexor tendon [406]. This was also observed during pSFT fascicle dissection, where some parallel structures existed, but many converged with adjacent fascicles, creating a complex network. This also changed according to the region of the pSFT, where a more interwoven and complex arrangement occurred in the ankle and toe region, compared to the middle region. This is likely why the length of the fascicles isolated was always under 20 mm.

There may be a helical component to the fascicle structure of energy storing tendons. This has been reported in equine flexor tendon [13, 17, 406, 407], bovine flexor tendon [408], rat tail tendon [409], canine patellar tendon and anterior cruciate ligament [409] and human Achilles tendon[410]. This arrangement may provide stability [15] and contribute to fascicle ability to resist multidirectional forces [23]. Further, it enables the mechanism for maximising recoil with minimal loss of energy [23]. This was observed to some degree in fascicles from native (Figure 5.15b) and GAG-depleted pSFT (Figure 5.17 a, d). It may be that this arrangement was what produced the well-defined waviness observed in the decellularised fascicle in Figure 5.18b. Similarly, fibre structures within fascicles, though longitudinally aligned, are not parallel to one another, but rather cross, forming spirals or plaits [300]. This was observed in some fascicles substructures across groups (Figure 5.15c, Figure 5.16c, Figure 5.18b, Figure 5.17a). However, these coexisted with longitudinally aligned and parallel fibres and fibril structures. It is noteworthy that transferring the fascicles from the pSFT to the glass slide for visualisation involved an unnatural lengthening of the structure, which may have impacted the native arrangement and morphology of the fascicle.

Fascicles from native and GAG-depleted pSFT shared similar surface features, where substructures within the fascicle were visible, but appeared covered by a layer or sheath, which presumably enveloped the entirety of each structure. Where a denser layer was present, the less distinguishable the features (Figure 5.15a, Figure 5.17d), occurring sometimes in different areas of the same fascicle (Figure 5.15d). This sheath was hypothesised to be made up of the IFM located between fascicles within a tendon. Further, in fascicles obtained from GAG-depleted pSFTs, the structure seemed less firm, with a more compliant surface, which often appeared flattened (Figure 5.17), likely due to the lengthening when placing on the glass slide for observation. GAG removal can cause a reduction in tissue stiffness [411], leading to a more compliant tissue [412], which may affect tendon at different levels of scale. This may explain the less rigid and defined fascicle structures obtained here. The external layer also appeared thinner compared to native fascicles, as substructures were more visible. This is also likely a consequence of GAG removal, given this component is heavily localised to the IFM in tendon [413]. This loss of a specific component inherent to the IFM may have also occurred in decellularised specimens. The enveloping layer appeared thinner, if present, in decellularised fascicles compared to both native and GAG-depleted specimens. Clear underlying structures were visible, including a much sharper collagen crimp pattern along the fascicle length. This is hypothesised to be caused by a partial loss of IFM as a consequence of the decellularisation process. The thinning of this soft, loose matrix may explain why the surface features of decellularised fascicles appear so exposed, having less of the sheath attached during dissection, and therefore, during microscopic observation.

The IFM contains a higher number of cells compared to the fascicular matrix, combining cell populations and morphologies not encountered within fascicle structures [296, 414, 415]. The IFM is rich in proteoglycans and glycoproteins. More specifically, the proteoglycan perlecan, the glycoproteins laminin, transforming growth factor β-indiced protein and adiponectin, collagen type III and cellular proteins including histones, ribosomal and cytoskeletal proteins are also found in large quantities in the IFM [415]. The removal of cellular content and associated proteins during the decellularisation process could be hypothesised to impact the IFM more so than the fascicular matrix, given their cell populations. In doing so, an initial loss of IFM may be evident. The combination of chemical and mechanical methods during decellularisation may have further removed some of the proteoglycans and glycoproteins in IFM, thinning the loose matrix. This could explain the evident differences in the surface features of decellularised fascicles. The changes observed at the sub-tendon scale appear to impact whole tendon, as discussed in Chapters 3 and 4, relating to the changes in the tensile and compressive mechanical properties in pSFT post-decellularisation. This aligns with the fact that the mechanics and the structure-function relationship of tendon are defined by its hierarchically organised arrangement, particularly at the fascicle level [416].

Safranin O and alcian blue staining of fascicles revealed a notable GAG content in tendon fascicles of native and decellularised pSFT. The red-stained GAGs in Figure 5.20, mainly located along the envelope surrounding apparent fascicle structures, may be due to the GAG enriched IFM attached to them, or may partly be unspecific binding of the dye. Given these staining methods are designed for tissue sections, it may be that they are ineffective on denser tissue. However, this staining did not occur in the GAG-depleted fascicles, suggesting the layer surrounding each fascicle in fact contains GAGs. Perlecan is found to associate with heparan sulfate, chondroitin sulfate and/or ketaran sulfate [417]. ChABC removes chondroitin sulfate [369], which may relate to the lack of staining observed in GAG-depleted fascicles. Blue stained GAGS in Figure 5.21 were more longitudinally aligned along fascicle length of both native and decellularised specimens. Densely stained streaks were visible, evenly spaced out and parallel to each other, hypothesised to constitute the matrix between fibre structures within each fascicle. Further, some GAGs may belong to the IFM attached to the surface of the fascicles. The apparent reduction in GAGs observed with this staining in decellularised fascicles compared to native, may relate to the loss of IFM during decellularisation, discussed previously. Finally, sudan black staining (Figure 5.22) revealed some lipid/lipoprotein staining contained mainly in the edges of the fascicle structures, likely the envelope sheath, hypothesised to be primarily IFM. Lipids have been observed in the epitenon and endotenon of tendons and ligaments [418], which may relate to the staining seen, particularly in the sheath surrounding the fascicle structures. Lipids are also the building blocks of cells, constituting around 50% of the mass of cell membranes, while also part of the nuclear membrane, endoplasmic reticulum and Golgi apparatus [419, 420]. This may also relate to the staining obtained, with a more evident presence in native and GAG-depleted fascicles compared to the decellularised specimens. By removing cells, the lipids remaining post-decellularisation may simply be remnants, harder to completely wash out as the fascicles were obtained from a central region of the pSFT, where solution reach may be less effective. The composition of tendons does not include a notable lipid content, rarely mentioned in the literature. Transverse sections of native pSFT stained with sudan black showed small amounts of dark blue staining, mainly in the peritenon, and some in the interfascicular spaces of the matrix (data not shown), aligning with the staining patterns seen at the fascicular level.

A reoccurring limitation in research conducted on the fascicular and IFM lies in the inability to strictly assess the properties of one without the likely influence of the other [414, 421]. This due to their inevitable association within tendon organisation making it unlikely to be completely separated though dissection. This agrees with the observations made here, where native fascicles presented a denser presence of the apparent sheath. This continued to present itself throughout the results presented in this Chapter. The envelope surrounding the fascicle structures isolated for characterisation may be partly or completely comprised of IFM, as hypothesised previously, difficult to detach during dissection. A connective tissue sheath has also been described to connect subfascicle structures [422], which may also form part of the layer described here.

Fascicle diameters have been reported to exist between 50 and 500 µm, and undoubtedly vary according to tendon type, location and species. Within a single pSFT, it was found that fascicle diameters varied considerably, while also varying between pSFT samples within the same sample group (native, decellularised, GAG-depleted), and also between sample groups (see Section 5.3.1). This likely relates to the complexity of the tissue matrix, contributing to its mechanical strength and structural integrity. A range of fascicle diameters from rat tail tendon (80 – 320 µm) have been reported [423], similar to the diameter range reported here. However, the measurements taken along the length of a single fascicle showed some variation. This could be a consequence of irregularities in the structure of the fascicles, positioning of the fascicle prior to being imaged, unsuccessful dissection of a whole fascicle. Further, the measurements were conducted by the author and not validated by an additional researcher. Therefore, a limitation of this study is the repeatability and robustness of the measurements conducted on fascicles, whereby an increase in sample size, and measurements conducted on a more randomly selected group of fascicles by different researchers would lead to more reliable data.

5.4.2 Hydration behaviour of superflexor tendon fascicles

After assessing tissue swelling behaviour at a whole tendon scale in Chapter 3 (see Section 3.3.1 and 3.4.1), it became relevant to study swelling at the sub-tendon scale. Swelling induced by PBS has been reported to occur in whole tendon as well as fascicles [127, 257]. The effect of different solutions on fascicle swelling was therefore investigated. Swelling was taken as the increase in fascicle diameter presented in section 5.3.3. At 3 and 5 min, native fascicles experienced more swelling (larger diameter) when hydrated with PBS, followed by saline and 100% Ringers. The least swelling was observed after hydration in 25% Ringers. This replicates the swelling behaviour of whole native tendon. Decellularised fascicles showed a similar trend to native with the difference of saline causing the most swelling instead of PBS. However, whole decellularised tendon showed the most swelling in PBS, and the least swelling in saline and 25% Ringers, which did not occur in decellularised fascicles. It has been postulated that the quantity and structure of the IFM exercises significant control over fluid flow within tendinous tissue [327], signifying the dehydration and rehydration behaviour at the fascicular level is influenced by the IFM and its interaction with water molecules [424]. When using different solutions, solutes diffuse into specimens in a unique manner, leading to different molecular interactions [261] with the collagenous and non-collagenous components of the fascicle structures. The potential change to the IFM post-decellularisation in combination with the composition of the solutions used may have resulted in the change observed in the swelling behaviour of decellularised pSFT fascicles compared to the whole tendon scale. At 10 min, the trend exits for both groups, whereby fascicle diameters increased similarly in all solutions.

The swelling behaviour of decellularised fascicles was lower (non-statistical comparison) compared to native fascicles over time. This likely relates to the influence of the IFM on fascicle dehydration behaviour mentioned above. It may be that decellularised fascicles undergo a more rapid fluid loss. The changes and potential loss of IFM combined with a more open and porous fascicular matrix occurring as a consequence of the decellularisation process (see Section 3.3.4 and 3.4.4) may contribute to faster dehydration. This was qualitatively observed during the microscopic observation stage of the hydration experiment. The incubation of decellularised fascicles with ethanol over time led to reduced diameters. On the contrary, there was an increase in the diameter of native fascicles incubated in ethanol at each time point. This further indicates that the dehydration of decellularised fascicles occurs at a faster rate than in native specimens, whereby the dehydrating effect of the ethanol was only intensified by naturally occurring fluid loss. However, it may also be possible this trend was a result of chance during the study, and would benefit from a more robust, repeatable methodology.

The GAG-depleted group showed no trends in fascicle swelling over time, with varying increases in fascicle diameters at each time point. This suggests that GAG-depleted fascicles hydrate differently from native and decellularised groups. By removing GAGs, a key component of the IFM was lost, while the water binding function they serve was also impaired. However, swelling was non-statistically higher compared to both native and decellularised groups, suggesting hydration occurred through different mechanisms. This was hypothesised to be a consequence of the loss of tissue rigidity and integral structure observed and discussed in section 5.4.1. Fluid diffusion occurred in all directions in GAG-depleted fascicles, not limited to a confined structure. Similar to the hypothesised effect of ChABC treatment on the peritenon of pSFT (see Section 4.4.4), affecting its collagen and elastic fibres, an analogue effect on the fascicular level of scale may have impacted its structural integrity, leading to the hydration behaviour obtained. Further this swelling behaviour may have been heightened due to the tissue scale, where a more pronounced effect of GAG loss is observable in fascicles than in whole tendon [323]. As stated above, this increase in swelling of GAG-depleted fascicles may not be representative of the group and requires further studies.

The variability observed in diameter measurements, particularly in the GAG-depleted group (see Figure 5.23) may be a result of human error or the inherent variations of fascicle specimens. Nevertheless, the sample size used is likely too small to provide enough data for the method to be robust, possibly leading to the hydration behaviour being non-representative of the sample group. The optimisation of the method occurred by conducting the experiment on a sample size of n = 3 at least twice before the data presented here. However, similarly to the mentioned in Section 5.3.1, the measurements should be conducted by different researchers to overcome robustness and repeatability limitations.

5.4.3 Topographical characterisation of superflexor tendon fascicles

The topographical characterisation of native and decellularised pSFT fascicles revealed the presence of a layer enveloping fascicle structures. It was more apparent in the native specimens, contributing to less distinguishable features of underlying substructures, such as collagen fibres and fibrils. Decellularised specimens also showed presence of the sheath, albeit a more exposed topography of fibril structures suggested it was thinner or at times divided, observed in one area of the fascicle surface, while not apparent in adjacent areas. A study conducted on rat tail tendon sheaths describes a thin, fibrous lamina enveloping fascicle structures, which was named endotendineum [425]. Cells were reported characteristic of the sheath, located throughout its reticular microfibrillar arrangement, also containing elastic fibres. An additional basement membrane-like layer was described to externally surround endotendineum, composed of collagen type IV and laminin [425]. This aligns with the observation presented in AFM data, while also observed in the microscopic characterisation of pSFT fascicles (see Section 5.3.1 and 5.4.1). Further, the enveloping sheath may have IFM attached to it, as it was difficult to remove it entirely during fascicle isolation, also mentioned in past investigations [414, 421].

The decellularisation process has the objective of removing cellular content, and with the enveloping sheath containing a notable amount of cells, this likely affected its composition in decellularised pSFT fascicles. Further the laminin component could have been removed partly or fully during the decellularisation process and may warrant further investigation. Finally, the IFM likely attached to the most external area of the fascicle, having lost its dense cellular content during decellularisation, may have also lost some proteome. This was hypothesised to have occur prior to a topographical assessment, discussed in previous chapters, and aligns with the observations described here. The evident arrangement of subfascicle structures throughout the topography of decellularised fascicles in air and liquid (PBS), suggests the external layer(s) are thinner, perhaps more fragile, and at times disconnected (see Figure 5.26 arrows) as a consequence of the decellularisation process.

Collagen fibrils observed mainly in decellularised specimens revealed a primarily longitudinal alignment. Fibrils from rat tail tendon have shown a relatively straight structure, whereas fibrils from bovine digital tendon show an inhomogeneous population of helical or spiralling fibrils and straight fibrils [426]. Upon closer inspection of Figure 5.25 and 5.26, it became clear that the fibrils observed did not all resemble a flat, straight structure, but rather some were spiralling upon themselves, or on occasion around adjacent fibrils. However, this was a rare observation, attributed to the influence of the forced positioning and immobilisation of the fascicle during sample preparation. It is possible that more fibrils were spiralling, yet lost part of this conformation due to the unnatural lengthening of the fascicle. It is also possible that due to the height differences caused by substructural arrangement within a larger fascicle unit, this characteristic was less visible in the images obtained. An analysis at a lower level of scale, i.e. fibrils may be of interest in future research.

Fibril width was only measurable in decellularised fascicles, taken as a representative value for fibril diameter. The data obtained from imaging in air gave fibril diameters of circa 138 nm, while high resolution data saw diameters of ˜ 117 nm. When imaged in liquid, fibril diameter was approximately 153 nm. No data on porcine flexor tendon fibrils was available to the author's knowledge. However, equine digital flexor tendon fibrils have a diameter ranging between 91 and 130 nm [427], similar to the values obtained in air. GAGs play a role in collagen fibril diameter regulation [428], and it was shown that the decellularisation process did not remove GAGs from pSFT (see Section 3.3.2). This may indicate that fibril diameter was not affected by the decellularisation process, though the fibril diameters from native pSFT require investigating to conduct a more direct comparison.

The collagen fibrillar structure is described as arranged in a staggered parallel alignment, creating a gap and overlap region giving rise to a 67 nm periodicity [429], also called D-periodicity or D-spacing. This is considered a unique nanocharacteristic of fibril-forming collagen [430]. In more recent research, it has been determined that a single spacing value for all collagen fibrils is not accurate [431], but is rather collagen-type and tissue-dependent [430]. The collagen D-spacing of the fibrils observed inside decellularised pSFT fascicles rendered some useful data; however, it was not possible to measure D-spacing in native specimens due to the lack of distinguishable fibril structures. Thus there was no comparison between groups. By assessing the fibrils in decellularised fascicles, it was possible to gain some insight into the preservation of the fibril structures within the fascicle unit following the decellularisation process. The mean collagen D-spacing of fibrils from 2 specimens imaged in air was circa 68 nm, while higher resolution images (2 specimens) resulted in a ˜ 67 nm spacing. This may indicate the decellularisation process does not alter the structural arrangement of collagen fibrils.

Collagen serves as a functional scaffold for cells, influencing cellular morphodynamics, playing a key role in cell adhesion and phenotype [432]. It has been shown that cells interact directionally to the D-spacing in collagen fibrils. This has been hypothesised to relate to a possible integrin-binding site in the D-spacing, or a potential periodicity in the cellular adhesion apparatus [433]. The collagen D-spacing of decellularised pSFT fibrils imaged in air approximated the 67 nm periodicity closely. The D-spacing had higher variability in the decellularised fascicles imaged in PBS, likely due to fascicle swelling caused by the solution itself. However, the value remained similar to both samples imaged in air and also the generally accepted 67 nm spacing. This may present an advantage during recellularisation of decellularised pSFT when used as a biological graft, providing some information regarding the interaction the tendon substructures may have with host cells.

The average roughness is a commonly used parameter which represents the average or absolute deviation of the surface irregularity from the mean [434, 435]. Further, parameters that provide insight into the surface structure including flatness, asymmetry and sharpness of surface features include skewness and kurtosis moments [401]. Skewness is the third moment of profile amplitude probability density function used to measure the symmetry with respect to the mean, while kurtosis moment is the fourth moment of profile amplitude probability function corresponding to a measure of surface sharpness [405]. There was a trend in the skewness of native and decellularised fascicle surfaces imaged in air and liquid, with a topography mainly containing valleys. This may be attributed to the intrinsic arrangement occurring within the fascicle which reflects as some valleys between more densely packed substructures, but may also be influenced by dissection techniques, followed by the unnatural immobilisation of the specimens. The skewness in ethanol treated samples resulted in a more randomly varying topography for the native specimen, speaking to a more symmetrical height distribution. The decellularised specimens treated with ethanol observed a negative moment, with more valleys. This is evident as there was a more fragmented topography in this group, with the gaps described in Figure 5.28 taken as valleys, contributing to this skewness. The kurtosis described a similarly varying topography containing many features of moderate height when imaged in air; however, when imaged in liquid, the increased moment described particularly sharp topographical features. This is hypothesised to occur as a consequence of the swelling effect PBS has on the fascicle level in pSFT, likely enhancing the valleys of the surface with respect to the mean height. Finally, the roughness of native fascicles was always higher than the decellularised specimens (non-statistical comparison), attributed to the pronounced height differences between the surface and the valleys across the surface. The decellularised fascicles, while containing a less apparent cover enveloping the structure, exposed more of the underlying substructures, depicting a less pronounced height loss in the existent valleys throughout the surface.

AFM imaging in liquid of decellularised fascicles showed some similarities to AFM images of chicken tendon imaged in PBS, where randomly orientated substructures were also present [436]. This may indicate that within a predominantly longitudinal arrangement of collagen fibres and fibrils, some fascicle substructures are inherently not parallelly aligned. This was hypothesised to be a consequence of ruptures or damage occurring during fascicle dissection and sample preparation techniques, but may be a combination of both. This complex arrangement also aligns with the previously discussed plaiting and spiralling orientations [300] existing at the sub-tendon scale (see Section 5.4.1). In native fascicles, there was a notable difference between the topography of different specimens. This may be due to variations in the fascicular surface occurring as a consequence of sample preparation, normal variations within fascicle structures, or contamination of the probe with some external element, e.g. tape adhesive or superglue that attached to the tip interacting with the specimen during the tapping process. The swelling behaviour when fascicles were hydrated in PBS was less evident than anticipated. Though there were some apparent differences in fibril width, mainly observable in decellularised height images, compared to those obtained in air, collagen D-spacing was still visible. This agrees with [260], observing the swelling of a single fibril from patellar tendon, also with distinguishable features such as the collagen periodicity when immersed in PBS. When measuring fibril width and D-spacing, both were larger compared to measurements taken from fibrils imaged in air (non-statistical comparison). This difference was attributed to the fascicle swelling; however, the accuracy of fibril width measurements may have been affected by their spatial arrangement which often left little to no space between adjacent fibrils, making it difficult to distinguish the full width of individual structures. This has occurred in previous research [437].

Ethanol is a widely used dehydrant [438, 439], used priorly in the hydration experiment (see Section 5.3.3), where the dehydrating effect of the ethanol made the fascicle surface features more visible. This is likely due to ethanol removing free water from the tissue, often with a shrinking effect [438]. This was hypothesised to be beneficial for the topographical analysis, as the endotendineum and IFM made it difficult to observe underlying substructures, particularly in the native fascicles. Thus an ethanol dehydration step was incorporated during sample preparation (see Section 5.2.4.1), rendering unexpected surface features. The tears in the endotendineum of native and decellularised fascicles were accompanied by fibril-like structures elongating between the gaps in the tears, doing so in the direction of the tear, usually visible as normal to the longitudinal direction of the fascicle itself. These fibril-like structures appeared denser and wider in native specimens, suggesting the endotendineum itself was thicker and less susceptible to fragmentation due to dehydration, aligning with previous observations. The endotendineum of decellularised fascicles contained more tears with wider gaps, where the fibril-like structures were thinner and sparser, possibly indicating a more fragile layer, prone to damage caused by dehydration. It is possible the endotendineum is combined with IFM, sharing collagenous components. Collagen type III has been found in significant quantities in tendon IFM, essential for collagen type I fibrillogenesis [440]. It is hypothesised that a combination of smaller collagen type I and type III constitute the endotendineum and are observed in the tears occurring throughout the surface of native and decellularised fascicles. AFM imaging of type III collagen appear similar to the presented here [441, 442]. Laminin molecules are generally cruciform [443, 444], but may also form part of the structures visible between the torn endotendineum. A proteomic analysis at a sub-tendon scale could provide useful for determining the differences between native and decellularised endotendineum and IFM.

5.4.4 Nanomechanical characterisation of superflexor tendon fascicles

The native fascicle topography once again revealed the endotendineum atop underlying fibril structures (Figure 5.30), with some evidence of collagen D-spacing visible as banding features in some areas of the height image (Figure 5.30b). Though a wide range of moduli existed across the fascicle surface, the mode was found at 18.62 MPa. Native pSFT at the whole-tendon scale has a linear modulus greater than 500 MPa (see Figure 3.25). Literature is in agreement that a higher modulus and overall mechanical properties exist in whole tendon compared to their constituent fascicles. The difference between the modulus at the whole-tendon and sub-tendon scale may depend on various factors, including the influence of the interfascicular matrix, as well as the methods conducted during fascicle isolation [17, 416]. In equine tendon, the modulus of whole tendons was circa 614 MPa, while for fascicles it was ˜ 336 MPa [17]. Here, there were regions of the fascicle surface that reached 251 MPa, approximately half of the linear elastic modulus value of whole pSFT tendon. This difference is somewhat similar to that found in equine tendon. Other studies conducted on rat tail tendon fascicles have reported moduli of 641 MPa, 691 MPa, 1 GPa [445] and 1.5 GPa [55]. However, fascicle modulus values are generally obtained through standard mechanical testing using microtensile rigs. Therefore, the data is not directly comparable to the results presented, yet serves to determine whether the methods conducted here obtained reasonable figures.

The decellularised fascicle in Figure 5.31 showed no clear evidence of endotendineum, with clearly visible fibril structures aligned longitudinally, similarly to previously presented decellularised fascicles (section 5.3.4). There were however, bubble-like features across the specimen surface of increased height, seen as a lighter yellow colour (Figure 5.31b) that were likely adhesive dragged along by the probe while tapping across the fascicle surface, or another contaminant that may have landed or stuck to the specimen surface during mounting. Due to the fascicles being imaged in Peak-Force QNM mode in air, there was a greater risk of contamination, compared to when imaged in liquid. The time invested in sample optimisation limited the opportunity to conduct QNM in PBS. The modulus of the decellularised fascicle surface revealed values greater than those obtained in the native fascicle, starting at 177 MPa, with a mode at circa 478 MPa, reaching 794 MPa. The highest modulus values appeared in the central region of the imaged area. When observing Figure 5.31 b and c, it appears fibril structures are higher (b, lighter yellow colour) in the central region, potentially explaining the higher modulus seen. In the areas where a lower modulus is observed (c, darker colour), the fibrils appear deeper inside the fascicle structure. This may indicate the probe was able to interact with some areas better than others, obtaining a more even modulus along the middle region. The modulus of the decellularised fascicle, evidently greater than the native fascicle could be the result of the influence of the endotendineum. This layer, which likely also contains some IFM is a seemingly loose, soft material that when interacting directly with the probe, results in a low modulus. The decellularisation process, removing or thinning this envelope leads to a higher modulus as the probe interacts with a stiffer material consisting primarily of fibrils. To the author's knowledge, there is no report of IFM modulus, yet is worthy of investigation.

Figure 5.32 showed the variability in moduli within an area of a decellularised fascicle, with the higher moduli region having a mode at circa 316 MPa, while the lower moduli region resulted in a mode of circa 63 MPa. Firstly, the values obtained are not as similar as would be expected when comparing to the other decellularised specimen (Figure 5.31), which may speak to the effect of the decellularisation method on individual fascicles within whole pSFT. This is further discussed in Chapter 6. Nevertheless, a similar phenomenon was observed between both decellularised fascicles, where a higher modulus was obtained in areas where the underlying structures were higher, easily interacting with the probe. On the contrary, regions where there was a loss in height, characterised by a darker colour, corresponded to lower moduli, and absence of data, where the probe could not interact with the specimen surface. This is the result of the unevenness of decellularised fascicle surfaces, which was observed throughout the structural and topographical characterisation in this Chapter. It is possible that further sample optimisation is required to obtain more reliable data. Finally, the wide ranges observed in Figure 5.32 d and e could be attributed the inherent morphology of tendon fibrils. The gap and overlap regions have been reported to differ in modulus values, where a greater modulus exists in the overlap region compared to the gap region [446].

The research conducted on tendon fibril mechanics share similarities with the methods used here, relying on AFM. There are different reports of modulus values for mammalian tendon fibrils ranging between 0.3 – 1.5 GPa [14], human patellar tendon fibrils reaching circa 2.8 GPa [315] and rat tail tendon fibrils ranging between 16 – 33 MPa [446]. This speaks to a biological variability involving species and tendon type/location, among other factors. The results presented in Figure 5.31 could be thought as representative of fibril moduli rather than fascicle modulus; however, the values seem low compared to those reported for larger mammals, i.e. humans. Therefore, it is presented here as the elastic modulus of decellularised fascicles, but requires repeating as data was not obtained on an acceptable sample size.

5.4.5 Preliminary characterisation of the interfascicular matrix of porcine superflexor tendon

The results of Chapters 3 and 4 discussed a hypothesis relating to the consequences of decellularisation on the IFM of pSFT. Tendon fascicles are surrounded by IFM or endotenon, a soft matrix, rich in proteoglycans and elastin [447]. It was suggested that the IFM underwent a considerable change during the decellularisation process, possibly reducing the protein content of this softer matrix. Elastic fibres are constituted by elastin and microfibrils. The microfibrils include fibrillin-1 coupled with microfibril associated protein 4 [448]. These have been reported to localise primarily within the endotenon sheath or IFM [22, 440, 449, 450], possibly enhancing interfascicular sliding and thus contributing to IFM and whole tendon mechanics [449]. Therefore, it seemed an appropriate research route to assess the composition and distribution of elastic fibres in native and decellularised tendon.

Millers elastin staining of transversely sectioned native pSFT revealed a distinct arrangement of elastic fibres localised mainly in the IFM, seen as the channels or spacing between fascicle structures (see Figure 5.33). The blue stained fibres had a combination of alignments creating a dense mesh-like network [451]. The most predominant orientation was parallel to the IFM, with a lesser amount of fibres perpendicularly aligned. This combination of fibre alignments have been proposed to serve as a bridge between adjacent fascicles, permitting interfascicular sliding [22]. Finally, the circular arrangement observed may be the elastic component associated with blood vessels, which when sectioned transversely, give rise to the circular or tubular morphology.

The staining of decellularised pSFT showed an observable reduction in elastic fibres (see Figure 5.34). The network was no longer dense, with a primarily parallel alignment to the IFM as well as circular morphologies. The perpendicularly orientated fibres appeared minimal, and in combination with the increase in interfascicular spacing, this may indicate the bridging of fascicles is affected by the decellularisation process. Over 90% of the elastin found in tendon is found in IFM [22], so the evident reduction in decellularised pSFT may speak to a more general reduction of the IFM itself, coinciding with histological observations in Chapter 3 (see Section 3.3.4.5).

The IFM plays a crucial role in tendon function as it facilitates interfascicular sliding, permitting maximum extension while protecting fascicle structures from excessive strains, thus reducing the risk of damage [17, 452]. The composition of the IFM contributes to its ability in resisting and recovering from cyclic or fatigue loading [396]. The lubricin facilitates the shearing role, while elastin enables its recoiling function [414]. The IFM is capable of resisting significant loads, thus facilitating sliding between likely discontinuous fascicles [415]. The alterations to any of the proteins that make up the IFM and ensuing structural changes would affect the mechanics at the fascicular level, thus impacting whole tendon mechanical behaviour, including a reduced fatigue resistance [421]. This agrees with the hypotheses discussed in Chapter 3 and 4, where the changes in the mechanical properties of decellularised pSFT may well be related to a reduction in the proteome of its IFM.

The turnover of the IFM is greater than that of the fascicular matrix, which suggests this soft, loose matrix may be at higher risk of damage [13], partly attributed to the shear it withstands [415]. Given the likely loss of IFM post-decellularisation, this characteristically faster rate of turnover proves beneficial, as it helps maintain a degree of structural integrity. Despite the obvious effects of IFM loss to tendon structure-function, decellularised pSFT graft once implanted in a host, may recover from this rapidly, with the high rate of repair which is inherent to this component.

The decellularisation process carried out on pSFT specimens utilises SDS (see Section 2.2.2.2), which disrupts protein-protein interactions and solubilises cell membranes effectively [199]. It has been reported that SDS may damage collagen and elastin fibres [33, 199, 453–455]. The use of potassium laurate instead of SDS during the decellularisation of rat lung was reported to retain more elastin [456]. A similar occurrence was reported in porcine lung tissue [457]. However, the decellularisation of porcine muscle using SDS did not adversely affect elastin in the ECM [458]. While controversial, the use of SDS during decellularisation may be one of the factors involved in the removal of elastin observed in decellularised pSFT sections.

AFM imaging on whole tendon and tendon fascicles is limited. A study showing AFM data of bovine deep digital flexor tendon conducted sample preparation with longitudinal slicing of the tissue, showing collagen fibrils with long axes parallel to the image plane [459]. The topography of the native transverse section (Figure 5.37 c) showed similarities with the bovine tendon, possibly due to sample preparation techniques. The transverse sectioning of cryoembedded sections may have occurred at an angle, revealing a glimpse of the alignment of pSFT substructures within the fascicular matrix. The evenness seen in the decellularised section (Figure 5.37 d) may be due to the inter- and intra-fascicular spacing observed (Figure 5.37 b), where the probe may have interacted mainly inside an area where little to no fascicular matrix came in contact. The topography could be a combination of the adhesive vinyl surface used to immobilise the tissue section, after which some adhesive remained on the probe, providing the same topography when in contact with fascicular matrix, distinguished only by a change in height (brighter colour). To the author's knowledge, this is the first time decellularised pSFT has been imaged transversely using a cryoembedded section.

The bulk tendon specimen imaging rendered a distinct visualisation of the fascicle structures within pSFT. This was clearer in the native topography (Figure 5.38 c, e), where the fascicular matrix was surrounded by a darker coloured valley, likely constituting the IFM. Some fibril-like structures were observed between adjacent fascicles, possibly components of the IFM such as elastin and collagen III. The smaller image of the decellularised pSFT showed a similar topography to the native specimen, however, the fascicle structure was more difficult to distinguish, only made evident by the pronounced dark valley (Figure 5.38 d; white arrows). When observing the 3D topography (Figure 5.38 e, f), there was clearly a height difference between the fascicular and interfascicular areas in native pSFT, with an elevated fascicular matrix compared to the interfascicular spaces. However, this does not occur in decellularised pSFT, where even in the likely fascicular area, there were considerable height differences, only more pronounced when reaching the interfascicular space. It was hypothesised that due to the density of the fresh bulk specimen used, the dehydration behaviour influenced these observations. The dehydration of the denser, tightly packed fascicular matrix may not occur with the same speed as the looser, softer IFM. A more rapid loss of fluids in the IFM, compared to fascicles, would partly explain the height differences. Further, the probe interacting (tapping) on the IFM could push the matrix down, rather than providing its topographical features, while encountering more resistance when tapping over fascicular surface, thus providing its topography more effectively. In decellularised pSFT, the dehydration may have occurred faster than in native specimens, given a more open matrix is characteristic of this tissue, contributing to rapid fluid loss (see Section 5.3.3 and 5.4.2). Further, due to a loss of cellular components and possible rearrangement of the fascicular matrix post-decellularisation, the density and transverse strength of fascicle structures may have been affected, being pushed down by the probe during contact, visualised as an uneven surface with more height differences within the fascicle area itself. Accordingly, the decellularised IFM, suffering possible component loss (see above) combined with a more notable loss of fluid appeared as a deep valley. Finally, the circular features observed throughout the apparent fascicular matrix are likely fibril endings (where these were incised). This is similar to the transverse section of rat tail tendon imaged using transmission electron microscopy (TEM), where circular fibrils of varying diameters were observed [127].

5.5 Conclusion

The structure, composition and topographical characterisation of native and decellularised fascicles was investigated for the first time. The method development for the characterisation presented forms a stepping stone for more robust, repeatable and optimal techniques to be developed based on investigative intents. An enveloping layer likely consisting of a combination of endotendineum and IFM was observed in native fascicles, while appearing thinner in decellularised fascicles allowing clearer visibility of underlying structures and their features. Histological techniques revealed a reduction in elastin content of decellularised pSFT, which in addition to the thinning of the enveloping layer and increase in interfascicular spacing seen with AFM imaging, is indicative of IFM loss due to the decellularisation process. This agrees with the conclusions of Chapters 3 and 4. Although some information regarding the nanomechanics of native and decellularised fascicles was obtained, revealing the latter had higher modulus across specimens' surface, these require investigating further. Finally, the proteomics and mechanical properties of decellularised pSFT IFM warrant investigating, as this softer matrix contributes to tendon mechanics and may be key in cell-matrix interaction when implanted in a host.

Chapter 6

Conclusions and future work

6.1 Key findings

Approximately 1 – 10 in every thousand individuals suffer from an ACL rupture each year, affecting over 200 thousand globally [148, 151]. The younger population demographic is increasingly affected by ACL ruptures, with up to 14 thousand ACLR occurring annually in the UK alone [225], requiring a graft to substitute the torn ligament. Autografts remain the current gold standard for ACLR, with significant disadvantages such as donor site morbidity, initial necrosis leading to a failure in maintaining cell viability and ensuing structural degradation [230]. Further, 1 – 11% of patients subjected to ACLR suffer from a second rupture, likely related to graft failure [460], while some patients have limited options with previous surgeries having required autografts. This represents a significant economic burden for healthcare, necessitating an alternative solution.

Decellularised porcine superflexor tendon provides a biocompatible structure [461], with biological and biochemical cues which promote tissue remodelling. The decellularisation process reduces the risk of adverse immune response significantly [196]. The use of decellularised pSFT would eliminate the need for invasive procedures, donor site morbidity and limited availability of currently used grafts. However, the decellularisation process has been shown to produce changes in the structure and mechanical properties of pSFT [220–224]. Therefore, the aim of this work was to investigate the biological and biomechanical consequences of decellularisation on pSFT at different levels of scale to determine its suitability as a potential graft for ACLR. The hierarchical approach included analyses on whole tendon (Chapter 3 & 4) and fascicle units (Chapter 5), revealing the effect of decellularisation on the collagenous and non-collagenous components of pSFT ECM, the compressive and tensile properties of pSFT and the characterisation of the structure, component distribution and topographical features of pSFT fascicles.

The use of alternative solutions (25% Ringers, 100% Ringers, 0.9% saline) to PBS during end-stage washes of the decellularisation process removed cellular content just as effectively (Figure 3.12 & 3.17), while reducing the swelling of pSFT post-decellularisation (Table 3.2). However, only the 25% Ringers groups showed tensile properties similar to native pSFT (Figure 3.25). Similarly, the compressive properties of both 25% Ringers and saline groups were significantly higher than remaining decellularised groups (Figure 4.7 & 4.8). These results promote the use of 25% Ringers during the end-stage washes of the decellularisation process, however further biocompatibility analyses are required. Further, the analysis of the swelling of native and decellularised pSFT showed that decellularised specimens had a different swelling behaviour in the different solutions used, indicating that the decellularisation process influences their hydration. In doing so, it was observed that saline solution did not swell the tissue excessively, compared to PBS for example. Therefore, saline solution, commonly used during ACLR for graft hydration, would not significantly increase tissue dimensions, while also not adversely impacting decellularised pSFT biomechanics, proving useful in a clinical setting.

Biochemical analyses revealed that standard and modified decellularisation methods do not reduce collagen (Figure 3.8) or GAG (Figure 3.7) content in pSFT, contrary to earlier findings in [222]. The mechanical function and contribution of both collagen and GAGs to pSFT mechanics were predominantly unaffected by decellularisation, with comparable compressive properties (Figure 4.14 – 4.16), revealing only a significant reduction in compressive peak stress, and the tensile linear modulus (Table 4.2). This was likely related to tissue swelling. Further, it was hypothesised that other pSFT components could have been affected during the decellularisation process, leading to the biomechanical changes observed. It was discussed throughout Chapter 3, 4 and 5 that the IFM may have undergone compositional changes or loss, translating to structural and functional alterations post-decellularisation. This was also apparent through the histological assessment of pSFT matrix (section 3.3.4) at whole tendon scale, while also speculated to have been shown through the AFM imaging of fascicles at the sub-tendon scale (section 5.3.1, 5.3.2, 5.3.4).

The IFM plays a key role in tendon mechanics, capable of resisting significant loads, facilitating interfascicular sliding through a shearing and recoiling function allowing significant extension while providing protection from excessive strain [17, 414, 415, 452]. Additionally, its interaction with fluids attributed to its porous, highly hydratable structure, contribute to the viscoelastic behaviour of tendons, resisting and recovering from fatigue loading [13, 137, 327]. A change or loss of the IFM post-decellularisation would therefore affect the fluid flow within tendon, as well as its mechanical behaviour, possibly observable at different levels of scale. It is possible that IFM-related changes to pSFT biomechanics were further enhanced by the effect of the solutions used during decellularisation and mechanical testing as it has been shown that higher IFM to fascicle ratio reduces the effect of bath solutions on tendon biomechanics [424]. Consequently, IFM loss post-decellularisation likely influenced the changes in strength, stress relaxation (Table 3.5) and compressive properties significantly. One specific component localised to the IFM was further studied. Elastin, proposed to enhance interfascicular sliding, contributing to IFM and whole tendon mechanics [449] was shown to be reduced post-decellularisation (Figure 5.33 – 5.33). There was also evidence of elastin loss in the peritenon (Figure 5.35), hypothesised to have affected the structural integrity of decellularised pSFT, compromising its ability to resist compressive loads in Chapter 4. This supports the IFM loss hypothesised, speaking to a change in the proteome of pSFT IFM as a consequence of decellularisation, warranting further investigation.

A complete mechanical assessment of decellularised pSFT was obtained for the first time, providing the tensile and compressive properties of native and decellularised pSFT. The results suggest decellularised pSFT is mechanically competent to act as a graft for ACLR, agreeing with previous studies [220–226, 449]. Further, it may be suitable for other tendon or ligament repair applications, given the main ECM components are preserved post-decellularisation, with seemingly unaffected functions, and no major changes to collagen quality (section 3.3.3) or collagen crimp morphology (section 3.3.5), contributing to the retainment of structural and mechanical integrity of the graft post-decellularisation. However, the variance observed in the compression testing results require more extensive experimental studies, possibly accompanied by an optimisation of the loading profile, according to its intended purpose.

In the specific use of decellularised pSFT for ACLR, it is important to note the importance of the fixation method, as this will avoid graft displacement, facilitating integration into the bone tunnel, occurring approximately three months post-surgery [462]. Despite the frequency with which compression methods, such as the interference screw are utilised, there is currently no gold standard for fixation. Alternative methods include suspensory, post and hybrid techniques. In addition to the chosen method for graft fixation, it is imperative that the graft provide the biomechanical strength to enable early rehabilitation after ACLR. There should be mobilisation of the affected knee immediately after surgery as this reduces the risk of adverse effects on surrounding soft tissue [463]. Current guidelines confirm early weight bearing, immediate mobilisation and rapid achievement of full knee extensions are necessary to preserve knee range and function [464]. Therefore, the biomechanical properties of a graft should cater to immediate loading in tension and compression, and the results obtained here suggest decellularised pSFT could function appropriately, but would benefit from studies investigating early implantation.

The structure and topography of sub-tendon units of native and decellularised pSFT were investigated for the first time. Dissection techniques were developed and optimised for this work, lacking an appropriate assessment of the fascicle structures observed to be validated as a single sub-tendon unit. An enveloping layer was observed in fascicles from native, decellularised and GAG-depleted pSFT, hypothesised to consist of endotendineum and some IFM (section 5.3.4). The latter is difficult to separate completely from individual fascicles during dissection and has been reported to have occurred in other studies [414, 421]. However, this layer was observed thinner and at times torn in decellularised fascicles (Figure 5.26 & 5.28), likely related to the loss of IFM discussed earlier. The effect of decellularisation on the loss of IFM was therefore supported by analyses conducted at the fascicle scale. Additionally, the data obtained from transverse sections of whole tendon using AFM techniques further demonstrated a difference between the IFM of native and decellularised pSFT, where an apparent loss of the soft matrix agreed with previous results. Despite these findings, the changes to IFM occurring as a consequence of the decellularisation process were not shown to impact the function or biomechanics of pSFT drastically. The fast turnover rate of IFM could lead to a speedy repair once the graft is implanted into a host, dampening the effects of its loss. The insight into fascicles and sub-fascicular structures presented in Chapter 6 may be useful in understanding, predicting and experimentally analysing cell infiltration, cell-matrix interactions and proliferation during graft recellularisation, speaking to the regenerative capacity of decellularised pSFT as a graft for ACLR.

The differences in the composition, hydration and mechanical behaviour of decellularised fascicles compared to whole tendon may be indicative of a change in its structure-function relationship following decellularisation. The loss of the cellular component in the tissue and ensuing structural changes could lead to a shift in the intrinsic relation that exists between tendon mechanics and function with its hierarchical organisation. The extent to which decellularised fascicles contribute to whole tendon mechanics could be affected compared to native tissue. Fascicles have been described to differ in composition and mechanical behaviour within a given tendon, acting as independent entities [465]. The behaviour of fascicle units may differ from one another, and the decellularisation process could affect some substructures more than others, depending on the penetration of the different solution used and their effects on pSFT matrix. Accordingly, there could be a combination of fascicles with biological and biomechanical properties resembling native fascicles, while others may behave differently, ultimately contributing to the changes in the mechanical properties of decellularised pSFT obtained at the whole tendon scale. However, this requires further investigation, utilising similar techniques to those presented in Chapter 5 using a larger sample size, optimising the nanomechanical analysis, and incorporating additional studies looking into the proteomics of fascicle units.

6.2 Future studies

The research conducted has elicited further investigations worthy of pursuing. A combination of improvements to the methods used and discussed in section 6.1, along with additional areas worth investigating have been identified. The most noteworthy future studies are proposed here.

6.2.1 Biomechanics in compression

To the author's knowledge, this thesis presents the compressive biomechanical properties of decellularised pSFT for the first time. This proves relevant for a biological graft material proposed for ACLR, but also if intended to use in other tendon/ligament repair. As mentioned in Section 1.3.2, decellularised pSFT has the potential to act as a graft for tendon repair, including ruptured tendon and tendinopathies, which so burden the healthcare system (see Section 1.1.3). The structure, function and composition would match that of other energy-storing tendons in the body (see Table 1.7). Having proven the collagenous and non-collagenous components of the ECM are retained post-decellularisation, it can provide a native-like scaffold for common tendon injuries, such as Achilles tendon ruptures and rotator cuff tears. These affect 84 thousand individuals and 85 people per 100 thousand individuals across the globe, per year, respectively [466].

During surgical repair of tendon and ligament, interference screws, and alternative methods of anchor fixation are required, often compressing the graft against bony tissue [338]. Further, tendons and ligaments in different parts of the body may be subject to multiaxial states of stress [329, 330]. Using decellularised pSFT for tendon/ligament repair in areas of the body other than the knee requires a complete mechanical assessment. This would help determine the graft capabilities of resisting tensile and compressive loading in a suitable manner to substitute native tissue efficiently.

Experimental conditions should be tailored to evaluate the compressive mechanical loading of the tendon/ligament which the decellularised pSFT aims to substitute. The experimental methods used in this project provide a starting point for a tendon- or ligament-specific loading profile to be constructed according to the application for which the decellularised pSFT is intended. Further, as discussed in Chapter 3, tendon undergoes lateral compressive loads [328], particularly in distal regions. The distal regions of the decellularised pSFT may become part of the enthesis when implanted into a host. It could prove useful to assess the compressive behaviour of different regions of pSFT, including distal and medial regions. This could provide insight into how the biomechanics change relative to ECM composition and structure within the same tendon. This should be conducted firstly on native pSFT to characterise its biomechanical properties according to the region of the tendon. Next, decellularised, GAG-depleted and potentially elastin-depleted groups could be assessed. This would provide more thorough information of the compressive biomechanics of decellularised pSFT and how it may be affected by decellularisation or specific matrix component depletion.

6.2.2 Biocompatibility

The modification to the end stage washes of the decellularisation process, discussed in Chapter 2, may have affected the otherwise negligible cytotoxicity of decellularised pSFT to mammalian cells. Biocompatibility may be defined as the biological scaffold's ability to carry out the function it was designed for without eliciting adverse local or systemic effects in the host. The biomaterial should create an advantageous cellular and tissue response [335]. The biocompatibility of decellularised pSFT using the standard decellularisation process has been evaluated previously [222, 223, 226], showing the end-stage PBS washes removed most of the reagents used during the process, thus reducing risk of cytotoxicity. However, as end-stage washes of the decellularisation process were altered (Chapter 2), substituting PBS with alternative solutions, biocompatibility should be verified. This should be conducted on pSFTs from each of the modified decellularisation methods, to ensure minimal to no risk of adverse effects on host cells and possibly neighbouring tissues when implanted.

Detergents, particularly SDS, used during decellularisation is cytotoxic, and requires extensive washing processes to remove from tissue ECM [199]. Complete removal of SDS remains an issue in decellularisation methods [467], requiring a minimum of 48 h wash [468]. The end stage washes of the method used in this project include a 48 h wash followed by a circa 60 h wash and finally a 7 day wash. The standard method washes with PBS, commonly used in decellularisation methods to wash out residual chemicals. However, by using alternative solutions, detailed in Chapter 2, the effectiveness of these critical washes may have been reduced.

A commonly used in vitro model for biocompatibility is cell seeding. If cells adhere and proliferate on the scaffold, penetrating the ECM, the decellularised pSFT is not cytotoxic [469]. Cytotoxicity is an important part of biocompatibility assessment, in line with ISO 10993-5:2009 [470]. Contact cytotoxicity observes changes in cell confluency and morphological changes using optical microscopy [471]. Extract cytotoxicity assesses cell viability after these have been cultured in growth medium with digested decellularised tissue [472]. This can be carried out through the measurement of ATP [473], mitochondrial dehydrogenase performance measurement [471], lactate dehydrogenase release [474], calcein AM-Hoechst staining [475].

All biocompatibility should be conducted using samples taken from different regions of the decellularised pSFT. This will ensure peripheral and deep tissue regions are assessed, as reagents may be washed more effectively from peripheral regions during the decellularisation process, while remain in potentially cytotoxic quantities in the deeper regions of the tendon.

Biomaterials should comply with a high degree of resistance to corrosion and wear, as well as chemical stability, particularly when implanted into a patient [476]. This is due to the fact that exposure and contact will occur over an extended period of time. Short-term studies like the aforementioned constitute only the first stage of assessing the material's biocompatibility; however, investigating the effects it may produce after a longer period of time is key. The suitability of a biological graft depends significantly on its longevity relating to unchanging properties after long-term contact with biological surroundings. Implantation tests surgically place the material in a suitable site or tissue representative of its intended application to evaluate the pathological effects on living tissue [477]. This can be carried out as a short-term study using rats or rabbits for up to 12 weeks, or long-term with animal of a longer life expectancy such as sheep or goats. A histopathological analysis is required to determine the response of the surrounding live tissue to the graft in terms of inflammatory cell behaviour, fibrous capsule formation, fatty infiltration, necrosis, granuloma or material debris [476].

6.2.3 Quantitative nanomechanical analysis

Atomic Force Microscopy (AFM) was used in Chapter 5 to analyse fascicles from native and decellularised pSFT, providing a topographical characterisation at the nanoscale. It was also used for investigating nanomechanical properties, i.e. the modulus of pSFT fascicles. However, AFM can also provide adhesion, deformation, stiffness and energy dissipation of materials [478], simultaneous surface morphology mapping [479]. This project attempted to develop a method for optimal analysis of the nanomechanics of fascicle structures, albeit requiring further optimisation to provide more consistent results. In addition, it was only possible to explore the modulus at the sub-tendon scale, while the previously mentioned nanomechanical properties remain to be investigated.

A more thorough nanomechanical characterisation of native and decellularised pSFT fascicles would allow a direct comparison between groups to truly understand the consequences of the decellularisation process at the sub-tendon level and how the tendon's basic functional unit (fascicles) is affected. This would then relate to the changes in whole tendon biomechanics obtained in Chapter 2, providing insight into the mechanisms behind the minor changes in pSFT mechanical properties post-decellularisation. A third group (GAG-depleted fascicles) could be introduced to further understand the consequences of GAG removal on the mechanics and topographical structure of pSFT fascicles. This may explain the compliancy of the tissue discussed in Chapter 3, affecting the compressive mechanical properties of GAG-depleted tendon.

Finally, if the decellularised pSFT is recellularised (see Section 6.2.5), quantitative nanomechanical analysis would prove helpful in studying the effects of cell repopulation on the mechanical properties of the biological scaffold at the fascicle level. It would simultaneously provide the topographical and structural layout after cell colonisation has occurred and possible synthesis of new ECM. This could then be compared to native pSFT fascicle topography, and significant differences may be worthy of further investigation.

6.2.4 Analysis of the interfascicular matrix

Chapter 5 attempted to investigate the interfascicular matrix (IFM) also referred to as endotenon, to determine whether the differences in the mechanical properties of native and decellularised pSFT at the whole tendon scale could be attributed to compositional and structural changes occurring in the softer matrix located between fascicle structures. However, there were limitations in the techniques utilised, rendering some insight into the consequences of decellularisation on pSFT IFM, albeit warranting further examination.

As discussed in previous chapters, IFM is a specialised matrix with proteins unique to it. These include elastic fibres, specific GAGs, decorin, versican, lubricin, small amounts of collagen types III and VI [17], fibronectin and fibrillin [344]. Interest in the proteomic analysis of tendon IFM has increased recently, establishing techniques which could be applied to native and decellularised pSFT. It could also be of interest to examine GAG-depleted pSFT to determine the effect of the enzymatic method on the IFM. Analyses have primarily been conducted on changes to tendon protein profiles with ageing and in disease [440]; however, to the author's knowledge, this has not been investigated in decellularised tendon. Therefore, it would be novel and insightful to understand the effects of the decellularisation methods on pSFT IFM. It may be that analysing IFM and fascicular matrix separately facilitates detecting changes that may not be apparent when the tendon is assessed as a whole.

Proteomics can be defined as a protein-based systematic analysis of the proteome of a tissue but can be conducted at the cellular or organism level [480]. This would allow to characterise the proteome of IFM and would also be useful to conduct on fascicular matrix of native tissue. Once this is obtained, a proteome comparison study could be conducted with decellularised and GAG-depleted groups. Protein immunolocalisation would be assessed using immunohistochemistry techniques for decorin, versican, lubricin. This technique would permit the specific binding between an antibody and antigen to localise specific components in the tissue, further examined with light or fluorescence microscopy [481]. Elastin could be assessed in terms of distribution using Verhoeff-van Gieson's staining as well as quantitatively using the FASTIN Elastin Assay (Biocolor, UK) [22, 413]. Laser capture microdissection would obtain suitable samples for protein extraction, using a laser ablation microscope with laser power and focus optimised for each specimen, to minimise tissue damage [440]. Mass spectrometry analyses, peptide identification and quantification could be conducted following previously established methods [413, 440].

6.2.5 Recellularisation

Recellularisation involves the repopulation of the decellularised scaffold with specific cell types or stem cells [21, 482]. Different cell types can be used for recellularising decellularised scaffolds; however, mesenchymal stem cells (MSCs) are commonly used. This is attributed to their long-term culture, but principally given they can be derived from different sources (adipose, bone marrow) with a quicker proliferation rate [210, 483]. Cell seeding in vitro would provide insight into cell behaviour relating to cell viability and distribution, colonization of the decellularised ECM, and cell proliferation. A suitable endogenous cell repopulation of decellularised graft implanted into a host may provide beneficial effects in terms of reinforcing the regeneration process [484].

Some of the methods for cell seeding include injection [485], spray [486], direct seeding onto the scaffold surface, bioreactors [487]. Cell penetration has proven limited when recellularising decellularised tendon previously, requiring modification of the decellularised scaffold in terms of porosity (ultrasonication) and structure (fascicular scaffolds) [275]. It could prove beneficial to opt for a bioreactor, enabling a more uniform cell distribution. Some of the most commonly used bioreactors include spinning flasks, rotating cylindrical devices, microfluidic systems and perfusion bioreactors [483].

The influence of cell repopulation on the decellularised ECM could be assessed using histological and immunocytochemistry techniques. Cell senescence could be evaluated using beta-galactosidase staining [488]. Cell viability could be measured through different techniques, including fluorescence lifetime imaging, colorimetric/absorbance assays (MTT, trypan blue), histology. A proteomic analysis of the recellularised tissue would provide insight into cellular activity and the regenerative potential of the graft. At a sub-structural level, techniques discussed in Chapter 5 could be useful to investigate cellular phenotype, distribution and proliferation across fascicular and potentially interfascicular matrix, utilising AFM. Finally, it would be important to characterise the biomechanical properties of the recellularised ECM in tension and compression, to determine the effect of cell repopulation on the scaffold.

6.3 Conclusion

The modification of the decellularisation process using alternative solutions to PBS during end-stage washes led to less tissue swelling accompanied by an increase in tensile and compressive mechanical properties with respect to the standard PBS group. In particular, the 25% Ringers solution resulted in the least swelling with native-like mechanical properties in tension. All decellularised groups retained the collagenous and non-collagenous (glycosaminoglycan) components in the fascicular matrix of pSFT, albeit a loss in interfascicular matrix was observed. A complete mechanical profile of native and decellularised pSFT including tensile and compressive mechanical properties revealed decellularisation did not impair the mechanical function or integrity of pSFT, with comparable biomechanics to native tendon. It was also shown that glycosaminoglycans are likely crucial in compressive load bearing while playing a less significant role in withstanding tensile loads. The structural and topographical characterisation of native and decellularised fascicles revealed the endotendineum and IFM enveloping these structures was affected by decellularisation, likely related to the biomechanical changes observed at the whole tendon scale.

This work therefore showed the biological and biomechanical consequences of the decellularisation process on porcine superflexor tendon at whole and sub-tendon scales, proving it has the structural, composition and mechanical capability to act as a biological graft for anterior cruciate ligament reconstruction, while likely optimal for use in tendon repair.

6.4 Final remarks

This thesis investigated the biomechanical and biological consequences of decellularisation on porcine superflexor tendon at different levels of scale. The project reveals decellularised superflexor tendon is a viable biological graft for anterior cruciate ligament reconstruction, with potential for other tendon or ligament repair applications. The methods developed provide the basis upon which more tendon-orientated research could be conducted. I am optimistic the research conducted provides a useful stepping stone for future investigations. Hopefully, this work is as interesting and inspiring to others as it was for me to conduct it.

Bibliography

[1] Margareta Nordin, Tobias Lorenz, and Marco Campello. Biomechanics of tendons and ligaments. In Stephen C Cowin and Stephen B Doty, editors, *Tissue Mechanics*, pages 102–125. Springer New York, New York, NY, 2007. ISBN: 978-0-387-49985-7. DOI: `10.1007/978-0-387-49985-7_16`. URL: `https://doi.org/10.1007/978-0-387-49985-7_16`.

[2] Derya Özer Kaya. Chapter 9 - Architecture of tendon and ligament and their adaptation to pathological conditions. In Salih Angin and Ibrahim Engin ÅimÅek, editors, *Comparative Kinesiology of the Human Body*, pages 115–147. Academic Press, 2020. ISBN: 978-0-12-812162-7. DOI: `https://doi.org/10.1016/B978-0-12-812162-7.00009-6`. URL: `https://www.sciencedirect.com/science/article/pii/B9780128121627000096`.

[3] Payvand Kamrani, Geoffrey Marston, Tafline C. Arbor, and Arif Jan. Connective Tissue, 2023. URL: `https://www.ncbi.nlm.nih.gov/books/NBK538534/`.

[4] M Benjamin, H Toumi, J R Ralphs, G Bydder, T M Best, and S Milz. Where tendons and ligaments meet bone: attachment sites ('entheses') in relation to exercise and/or mechanical load. eng. *Journal of anatomy*, 208(4):471–490, 2006. ISSN: 0021-8782 (Print). DOI: `10.1111/j.1469-7580.2006.00540.x`.

[5] Benjamin Charvet, Florence Ruggiero, and Dominique Le Guellec. The development of the myotendinous junction. A review. eng. *Muscles, ligaments and tendons journal*, 2(2):53–63, 2012. ISSN: 2240-4554 (Print).

[6] Arul Subramanian and Thomas F Schilling. Tendon development and musculoskeletal assembly: emerging roles for the extracellular matrix. eng. *Development (Cambridge, England)*, 142(24):4191–4204, 2015. ISSN: 1477-9129 (Electronic). DOI: `10.1242/dev.114777`.

[7] Frederick H Silver, Joseph W Freeman, and Gino Bradica. Structure and Function of Ligaments, Tendons, and Joint Capsule. In William R Walsh, editor, *Repair and Regeneration of Ligaments, Tendons, and Joint Capsule*, pages 15–47. Humana Press, Totowa, NJ, 2006. ISBN: 978-1-59259-942-4. DOI: `10.1385/1-59259-942-7:015`. URL: `https://doi.org/10.1385/1-59259-942-7:015`.

[8] M. R. Doschak and Ronald F. Zernicke. Structure, function and adaptation of bone-tendon and bone-ligament complexes, 2005.

[9] Nitya Waghray, G Aruna Jyothi, Mariya Imran, Sabah Yaseen, and Upasana Chaudhary. Enthesis: A Brief Review. *Apollo Medicine*, 12(1):32–38, 2015. ISSN: 0976-0016. DOI: `https://doi.org/10.1016/j.apme.2015.01.003`. URL: `https://www.sciencedirect.com/science/article/pii/S0976001615000046`.

[10] John Apostolakos, Thomas Js Durant, Corey R Dwyer, Ryan P Russell, Jeffrey H Weinreb, Farhang Alaee, Knut Beitzel, Mary Beth McCarthy, Mark P Cote, and Augustus D Mazzocca. The enthesis: a review of the tendon-to-bone insertion. eng. *Muscles, ligaments and tendons journal*, 4(3):333–342, 2014. ISSN: 2240-4554 (Print).

[11] Rene B Svensson, Katja Maria Heinemeier, Christian Couppé, Michael Kjaer, and S Peter Magnusson. Effect of aging and exercise on the tendon. *Journal of Applied Physiology*, 121(6):1353–1362, 2016. DOI: `10.1152/japplphysiol.00328.2016`. URL: `https://doi.org/10.1152/japplphysiol.00328.2016`.

[12] Savio L.-Y. Woo, Richard E Debski, Jennifer Zeminski, Steven D Abramowitch, Serena S Chan Saw MS, and James A Fenwick. Injury and Repair of Ligaments and Tendons. *Annual Review of Biomedical Engineering*, 2(1):83–118, 2000. DOI: `10.1146/annurev.bioeng.2.1.83`. URL: `https://doi.org/10.1146/annurev.bioeng.2.1.83`.

[13] C T Thorpe, E M Spiesz, S Chaudhry, H R C Screen, and P D Clegg. Science in brief: recent advances into understanding tendon function and injury risk. eng, 2015. DOI: `10.1111/evj.12346`.

[14] Jared L Zitnay and Jeffrey A Weiss. Load transfer, damage, and failure in ligaments and tendons. *Journal of Orthopaedic Research*, 36(12):3093–3104, 2018. DOI: `https://doi.org/10.1002/jor.24134`. URL: `https://onlinelibrary.wiley.com/doi/abs/10.1002/jor.24134`.

[15] Joseph P R O Orgel, Thomas C Irving, Andrew Miller, and Tim J Wess. Microfibrillar structure of type I collagen in situ. eng. *Proceedings of the National Academy of Sciences of the United States of America*, 103(24):9001–9005, 2006. ISSN: 0027-8424 (Print). DOI: `10.1073/pnas.0502718103`.

[16] Seyed Mohammad Siadat, Alexandra A Silverman, Charles A DiMarzio, and Jeffrey W Ruberti. Measuring collagen fibril diameter with differential interference contrast microscopy. *Journal of Structural Biology*, 213(1):107697, 2021. ISSN: 1047-8477. DOI: `https://doi.org/10.1016/j.jsb.2021.107697`. URL: `https://www.sciencedirect.com/science/article/pii/S1047847721000022`.

[17] Chavaunne T Thorpe, Helen L Birch, Peter D Clegg, and Hazel R C Screen. The role of the non-collagenous matrix in tendon function. eng. *International journal of experimental pathology*, 94(4):248–259, 2013. ISSN: 1365-2613 (Electronic). DOI: `10.1111/iep.12027`.

[18] Hiroshi Asahara, Masafumi Inui, and Martin K Lotz. Tendons and Ligaments: Connecting Developmental Biology to Musculoskeletal Disease Pathogenesis. eng. *Journal of bone and mineral research : the official journal of the American Society for Bone and Mineral Research*, 32(9):1773–1782, 2017. ISSN: 1523-4681 (Electronic). DOI: `10.1002/jbmr.3199`.

[19] Jess G Snedeker and Jasper Foolen. Tendon injury and repair â A perspective on the basic mechanisms of tendon disease and future clinical therapy. *Acta Biomaterialia*, 63:18–36, 2017. ISSN: 1742-7061. DOI: `https://doi.org/10.1016/j.actbio.2017.08.032`. URL: `http://www.sciencedirect.com/science/article/pii/S1742706117305469`.

[20] Mariana L Santos, Márcia T Rodrigues, Rui M A Domingues, Rui Luís Reis, and Manuela E Gomes. *Biomaterials as Tendon and Ligament Substitutes: Current Developments.* In *Regenerative Strategies for the Treatment of Knee Joint Disabilities.* Joaquim Miguel Oliveira and Rui Luís Reis, editors. Springer International Publishing, Cham, 2017, pages 349–371. ISBN: 978-3-319-44785-8. DOI: `10.1007/978-3-319-44785-8_17`. URL: `https://doi.org/10.1007/978-3-319-44785-8_17`.

[21] Xuewei Zhang, Xi Chen, Hua Hong, Rubei Hu, Jiashang Liu, and Changsheng Liu. Decellularized extracellular matrix scaffolds: Recent trends and emerging strategies in tissue engineering. eng. *Bioactive materials*, 10:15–31, 2022. ISSN: 2452-199X (Electronic). DOI: `10.1016/j.bioactmat.2021.09.014`.

[22] Marta S C Godinho, Chavaunne T Thorpe, Steve E Greenwald, and Hazel R C Screen. Elastin is Localised to the Interfascicular Matrix of Energy Storing Tendons and Becomes Increasingly Disorganised With Ageing. *Scientific Reports*, 7(1):9713, 2017. ISSN: 2045-2322. DOI: `10.1038/s41598-017-09995-4`. URL: `https://doi.org/10.1038/s41598-017-09995-4`.

[23] Chavaunne T Thorpe, Christian Klemt, Graham P Riley, Helen L Birch, Peter D Clegg, and Hazel R C Screen. Helical sub-structures in energy-storing tendons provide a possible mechanism for efficient energy storage and return. *Acta Biomaterialia*, 9(8):7948–7956, 2013. ISSN: 1742-7061. DOI: `https://doi.org/10.1016/j.actbio.2013.05.004`. URL: `https://www.sciencedirect.com/science/article/pii/S1742706113002365`.

[24] Andrea Hoffmann and Gerhard Gross. Tendon and ligament engineering in the adult organism: mesenchymal stem cells and gene-therapeutic approaches. eng. *International orthopaedics*, 31(6):791–797, 2007. ISSN: 0341-2695 (Print). DOI: `10.1007/s00264-007-0395-9`.

[25] R C Bray, A W Fisher, and C B Frank. Fine vascular anatomy of adult rabbit knee ligaments. eng. *Journal of anatomy*, 172:69–79, 1990. ISSN: 0021-8782 (Print).

[26] Guang Yang, Benjamin B Rothrauff, and Rocky S Tuan. Tendon and ligament regeneration and repair: clinical relevance and developmental paradigm. eng. *Birth defects research. Part C, Embryo today : reviews*, 99(3):203–222, 2013. ISSN: 1542-9768 (Electronic). DOI: `10.1002/bdrc.21041`.

[27] Chavaunne T Thorpe, Helen L Birch, Peter D Clegg, and Hazel R C Screen. Chapter 1 - Tendon Physiology and Mechanical Behavior: StructureâFunction Relationships. In Manuela E Gomes, Rui L Reis, and Márcia T Rodrigues, editors, *Tendon Regeneration*, pages 3–39. Academic Press, Boston, 2015. ISBN: 978-0-12-801590-2. DOI: `https://doi.org/10.1016/B978-0-12-801590-2.00001-6`. URL: `https://www.sciencedirect.com/science/article/pii/B9780128015902000016`.

[28] Shichen Zhang, Wei Ju, Xiaoyi Chen, Yanyan Zhao, Lingchong Feng, Zi Yin, and Xiao Chen. Hierarchical ultrastructure: An overview of what is known about tendons and future perspective for tendon engineering. eng. *Bioactive materials*, 8:124–139, 2022. ISSN: 2452-199X (Electronic). DOI: `10.1016/j.bioactmat.2021.06.007`.

[29] M Benjamin and D McGonagle. Entheses: tendon and ligament attachment sites. *Scandinavian Journal of Medicine & Science in Sports*, 19(4):520–527, 2009. DOI: `https://doi.org/10.1111/j.1600-0838.2009.00906.x`. URL: `https://onlinelibrary.wiley.com/doi/abs/10.1111/j.1600-0838.2009.00906.x`.

[30] Kalpesh Parmar. Tendon and ligament: basic science, injury and repair. *Orthopaedics and Trauma*, 32(4):241–244, 2018. ISSN: 1877-1327. DOI: `https://doi.org/10.1016/j.mporth.2018.05.008`. URL: `https://www.sciencedirect.com/science/article/pii/S1877132718300733`.

[31] M. Benjamin and J. R. Ralphs. The cell and developmental biology of tendons and ligaments. *International Review of Cytology*, 196:85–130, 2000. ISSN: 00747696. DOI: `10.1016/s0074-7696(00)96003-0`.

[32] Samuel Tozer and Delphine Duprez. Tendon and ligament: development, repair and disease. eng. *Birth defects research. Part C, Embryo today : reviews*, 75(3):226–236, 2005. ISSN: 1542-975X (Print). DOI: `10.1002/bdrc.20049`.

[33] Yunkai Tang, Zhen Wang, Lei Xiang, Zhenyu Zhao, and Wenguo Cui. Functional biomaterials for tendon/ligament repair and regeneration. *Regenerative Biomaterials*, 9, 2022. ISSN: 2056-3418. DOI: `10.1093/rb/rbac062`. URL: `https://doi.org/10.1093/rb/rbac062`.

[34] Steven A Fenwick, Brian L Hazleman, and Graham P Riley. The vasculature and its role in the damaged and healing tendon. eng. *Arthritis research*, 4(4):252–260, 2002. ISSN: 1465-9905 (Print). DOI: `10.1186/ar416`.

[35] Robert C Bray, Paul T Salo, Ian K Lo, Paul Ackermann, J B Rattner, and David A Hart. Normal ligament structure and physiology. *Sports Med Arthrosc Rev*, 13(3):127–135, 2005.

[36] Shan-Ling Hsu, Rui Liang, and Savio L Y Woo. Functional tissue engineering of ligament healing. *BMC Sports Science, Medicine and Rehabilitation*, 2(1):12, 2010. ISSN: 2052-1847. DOI: `10.1186/1758-2555-2-12`. URL: `https://doi.org/10.1186/1758-2555-2-12`.

[37] Nathaniel A Dyment and Jenna L Galloway. Regenerative biology of tendon: mechanisms for renewal and repair. eng. *Current molecular biology reports*, 1(3):124–131, 2015. ISSN: 2198-6428 (Print). DOI: `10.1007/s40610-015-0021-3`.

[38] Francesca Sardone, Spartaco Santi, Francesca Tagliavini, Francesco Traina, Luciano Merlini, Stefano Squarzoni, Matilde Cescon, Raimund Wagener, Nadir Mario Maraldi, Paolo Bonaldo, Cesare Faldini, and Patrizia Sabatelli. Collagen VIâNG2 axis in human tendon fibroblasts under conditions mimicking injury response. *Matrix Biology*, 55:90–105, 2016. ISSN: 0945-053X. DOI: `https://doi.org/10.1016/j.matbio.2016.02.012`. URL: `https://www.sciencedirect.com/science/article/pii/S0945053X16300233`.

[39] Katja Maria Heinemeier, Peter Schjerling, Tommy F Øhlenschlæger, Christian Eismark, Jesper Olsen, and Michael Kjær. Carbon-14 bomb pulse dating shows that tendinopathy is preceded by years of abnormally high collagen turnover. eng. *FASEB journal : official publication of the Federation of American Societies for Experimental Biology*, 32(9):4763–4775, 2018. ISSN: 1530-6860 (Electronic). DOI: `10.1096/fj.201701569R`.

[40] MICHAEL KJ. Role of Extracellular Matrix in Adaptation of Tendon and Skeletal Muscle to Mechanical Loading. *Physiological Reviews*, 84(2):649–698, 2004. DOI: `10.1152/physrev.00031.2003`. URL: `https://doi.org/10.1152/physrev.00031.2003`.

[41] A. A. Biewener. Tendons and ligaments: Structure, mechanical behavior and biological function. In *Collagen: Structure and Mechanics*. 2008. ISBN: 9780387739052. DOI: `10.1007/978-0-387-73906-9_10`.

[42] Cyril B. Frank. Ligament structure, physiology and function, 2004.

[43] Helen L Birch, Chavaunne T Thorpe, and Adam P Rumian. Specialisation of extracellular matrix for function in tendons and ligaments. eng. *Muscles, ligaments and tendons journal*, 3(1):12–22, 2013. ISSN: 2240-4554 (Print). DOI: `10.11138/mltj/2013.3.1.012`.

[44] Aleksandra Bandzerewicz and Agnieszka Gadomska-Gajadhur. Into the Tissues: Extracellular Matrix and Its Artificial Substitutes: Cell Signalling Mechanisms. eng. *Cells*, 11(5), 2022. ISSN: 2073-4409 (Electronic). DOI: `10.3390/cells11050914`.

[45] Yalda A Kharaz, Elizabeth G Canty-Laird, Simon R Tew, and Eithne J Comerford. Variations in internal structure, composition and protein distribution between intra- and extra-articular knee ligaments and tendons. *Journal of Anatomy*, 232(6):943–955, 2018. DOI: `https://doi.org/10.1111/joa.12802`. URL: `https://onlinelibrary.wiley.com/doi/abs/10.1111/joa.12802`.

[46] D. Amiel, C. Frank, F. Harwood, J. Fronek, and W. Akeson. Tendons and ligaments: A morphological and biochemical comparison. *Journal of Orthopaedic Research*, 1(3):257–265, 1983. ISSN: 1554527X. DOI: `10.1002/jor.1100010305`.

[47] Adam P. Rumian, Andrew L. Wallace, and Helen L. Birch. Tendons and ligaments are anatomically distinct but overlap in molecular and morphological features - A comparative study in an ovine model. *Journal of Orthopaedic Research*, 2007. ISSN: 07360266. DOI: `10.1002/jor.20218`.

[48] D T Kirkendall and W E Garrett. Function and biomechanics of tendons. eng. *Scandinavian journal of medicine science in sports*, 7(2):62–66, 1997. ISSN: 0905-7188 (Print). DOI: `10.1111/j.1600-0838.1997.tb00120.x`.

[49] A A Amis. *The Biomechanics of Ligaments*. In *Biomechanics and Biomaterials in Orthopedics*. Dominique G Poitout, editor. Springer London, London, 2004, pages 550–563. ISBN: 978-1-4471-3774-0. DOI: `10.1007/978-1-4471-3774-0_48`. URL: `https://doi.org/10.1007/978-1-4471-3774-0_48`.

[50] S H Liu, R S Yang, R Al-Shaikh, and J M Lane. Collagen in tendon, ligament, and bone healing. A current review. eng. *Clinical orthopaedics and related research*, (318):265–278, 1995. ISSN: 0009-921X (Print).

[51] Sylvie Ricard-Blum. The collagen family. eng. *Cold Spring Harbor perspectives in biology*, 3(1):a004978, 2011. ISSN: 1943-0264 (Electronic). DOI: `10.1101/cshperspect.a004978`.

[52] Matthew D Shoulders and Ronald T Raines. Collagen structure and stability. eng. *Annual review of biochemistry*, 78:929–958, 2009. ISSN: 1545-4509 (Electronic). DOI: `10.1146/annurev.biochem.77.032207.120833`.

[53] Baptiste Depalle, Zhao Qin, Sandra J Shefelbine, and Markus J Buehler. Influence of cross-link structure, density and mechanical properties in the mesoscale deformation mechanisms of collagen fibrils. eng. *Journal of the mechanical behavior of biomedical materials*, 52:1–13, 2015. ISSN: 1878-0180 (Electronic). DOI: `10.1016/j.jmbbm.2014.07.008`.

[54] Rujun Li and Benjamin J McCoy. Inter- and Intramolecular Crosslinking Kinetics: Partitioning According to Number of Crosslinks. *Macromolecular Rapid Communications*, 25(11):1059–1063, 2004. DOI: `https://doi.org/10.1002/marc.200400058`. URL: `https://onlinelibrary.wiley.com/doi/abs/10.1002/marc.200400058`.

[55] Rene B Svensson, Hindrik Mulder, Vuokko Kovanen, and S Peter Magnusson. Fracture mechanics of collagen fibrils: influence of natural cross-links. eng. *Biophysical journal*, 104(11):2476–2484, 2013. ISSN: 1542-0086 (Electronic). DOI: `10.1016/j.bpj.2013.04.033`.

[56] S P Robins. Biochemistry and functional significance of collagen cross-linking. eng. *Biochemical Society transactions*, 35(Pt 5):849–852, 2007. ISSN: 0300-5127 (Print). DOI: `10.1042/BST0350849`.

[57] N R Davis, O M Risen, and G A Pringle. Stable, nonreducible cross-links of mature collagen. eng. *Biochemistry*, 14(9):2031–2036, 1975. ISSN: 0006-2960 (Print). DOI: `10.1021/bi00680a034`.

[58] A. Viidik. Biomechanics and Functional Adaption of Tendons and Joint Ligaments. *Studies on the Anatomy and Function of Bone and Joints*:17–39, 1966. DOI: `10.1007/978-3-642-99909-3_2`.

[59] Murat Kaya, NazÄ±*mKarahan*, and BarÄ±*ÅYÄ* ± *lmaz*. Tendon Structure and Classification. In Hasan Sözen, editor, *Tendons*, chapter 2. IntechOpen, Rijeka, 2019. DOI: `10.5772/intechopen.84622`. URL: `https://doi.org/10.5772/intechopen.84622`.

[60] K. Gelse, E. Pöschl, and T. Aigner. Collagens - Structure, function, and biosynthesis. *Advanced Drug Delivery Reviews*, 55(12):1531–1546, 2003. ISSN: 0169409X. DOI: `10.1016/j.addr.2003.08.002`. arXiv: `/www-sciencedirect-com.cyber.usask.ca/science/article/pii/S0169409X03001820 [https:]`.

[61] Karl E Kadler, Clair Baldock, Jordi Bella, and Raymond P Boot-Handford. Collagens at a glance. *Journal of Cell Science*, 120(12):1955–1958, 2007. ISSN: 0021-9533. DOI: `10.1242/jcs.03453`. URL: `https://jcs.biologists.org/content/120/12/1955`.

[62] K. S. Silvipriya, K. Krishna Kumar, A. R. Bhat, B. Dinesh Kumar, Anish John, and Panayappan Lakshmanan. Collagen: Animal sources and biomedical application. *Journal of Applied Pharmaceutical Science*, 2015. ISSN: 22313354. DOI: `10.7324/JAPS.2015.50322`.

[63] K Henriksen and M A Karsdal. Chapter 1 - Type I Collagen. In Morten A Karsdal, editor, *Biochemistry of Collagens, Laminins and Elastin*, pages 1–11. Academic Press, 2016. ISBN: 978-0-12-809847-9. DOI: `https://doi.org/10.1016/B978-0-12-809847-9.00001-5`. URL: `http://www.sciencedirect.com/science/article/pii/B9780128098479000015`.

[64] M J Nielsen and M A Karsdal. Chapter 3 - Type III Collagen. In Morten A Karsdal, editor, *Biochemistry of Collagens, Laminins and Elastin*, pages 21–30. Academic Press, 2016. ISBN: 978-0-12-809847-9. DOI: `https://doi.org/10.1016/B978-0-12-809847-9.00003-9`. URL: `http://www.sciencedirect.com/science/article/pii/B9780128098479000039`.

[65] Vickie Shim, Justin Fernandez, Thor Besier, and Peter Hunter. Investigation of the role of crimps in collagen fibers in tendon with a microstructually based finite element model. eng. *Conference proceedings : ... Annual International Conference of the IEEE Engineering in Medicine and Biology Society. IEEE Engineering in Medicine and Biology Society. Annual Conference*, 2012:4871–4874, 2012. ISSN: 1557-170X (Print). DOI: `10.1109/EMBC.2012.6347085`.

[66] Andreas Herchenhan, Nicholas S Kalson, David F Holmes, Patrick Hill, Karl E Kadler, and Lee Margetts. Tenocyte contraction induces crimp formation in tendon-like tissue. eng. *Biomechanics and modeling in mechanobiology*, 11(3-4):449–459, 2012. ISSN: 1617-7940 (Electronic). DOI: `10.1007/s10237-011-0324-0`.

[67] Ewa M Spiesz, Chavaunne T Thorpe, Philipp J Thurner, and Hazel R C Screen. Structure and collagen crimp patterns of functionally distinct equine tendons, revealed by quantitative polarised light microscopy (qPLM). *Acta Biomaterialia*, 70:281–292, 2018. ISSN: 1742-7061. DOI: `https://doi.org/10.1016/j.actbio.2018.01.034`. URL: `http://www.sciencedirect.com/science/article/pii/S174270611830045X`.

[68] James H.C. Wang. Mechanobiology of tendon. *Journal of Biomechanics*, 39(9):1563–1582, 2006. ISSN: 00219290. DOI: `10.1016/j.jbiomech.2005.05.011`.

[69] Renato V Iozzo and Liliana Schaefer. Proteoglycan form and function: A comprehensive nomenclature of proteoglycans. eng. *Matrix biology : journal of the International Society for Matrix Biology*, 42:11–55, 2015. ISSN: 1569-1802 (Electronic). DOI: `10.1016/j.matbio.2015.02.003`.

[70] K Prydz and K T Dalen. Synthesis and sorting of proteoglycans. *Journal of Cell Science*, 113(2):193 LP –205, 2000. URL: `http://jcs.biologists.org/content/113/2/193.abstract`.

[71] Roger K W Smith and Allen E Goodship. Chapter 2.3 - Tendon and ligament physiology: responses to exercise and training. In Kenneth W Hinchcliff, Raymond J Geor, and Andris J Kaneps, editors, *Equine Exercise Physiology*, pages 106–131. W.B. Saunders, Edinburgh, 2008. ISBN: 978-0-7020-2857-1. DOI: `https://doi.org/10.1016/B978-070202857-1.50007-X`. URL: `http://www.sciencedirect.com/science/article/pii/B978070202857150007X`.

[72] J. Parkinson, T. Samiric, M. Z. Ilic, J. Cook, and C. J. Handley. Involvement of proteoglycans in tendinopathy, 2011.

[73] Hazel R.C. Screen, David E. Berk, Karl E. Kadler, Francesco Ramirez, and Marian F. Young. Tendon functional extracellular matrix. In *Journal of Orthopaedic Research*, 2015. DOI: `10.1002/jor.22818`.

[74] M Yanagishita. Function of proteoglycans in the extracellular matrix. eng. *Acta pathologica japonica*, 43(6):283–293, 1993. ISSN: 0001-6632 (Print). DOI: `10.1111/j.1440-1827.1993.tb02569.x`.

[75] R V Iozzo and A D Murdoch. Proteoglycans of the extracellular environment: clues from the gene and protein side offer novel perspectives in molecular diversity and function. eng. *FASEB journal : official publication of the Federation of American Societies for Experimental Biology*, 10(5):598–614, 1996. ISSN: 0892-6638 (Print).

[76] Carli Moorehead, Katsiaryna Prudnikova, and Michele Marcolongo. The regulatory effects of proteoglycans on collagen fibrillogenesis and morphology investigated using biomimetic proteoglycans. *Journal of Structural Biology*, 206(2):204–215, 2019. ISSN: 1047-8477. DOI: `https://doi.org/10.1016/j.jsb.2019.03.005`. URL: `http://www.sciencedirect.com/science/article/pii/S1047847719300504`.

[77] Mirna Z Ilic, Phillip Carter, Alicia Tyndall, Jayesh Dudhia, and Christopher J Handley. Proteoglycans and catabolic products of proteoglycans present in ligament. eng. *The Biochemical journal*, 385(Pt 2):381–388, 2005. ISSN: 1470-8728 (Electronic). DOI: `10.1042/BJ20040844`.

[78] J H Yoon and J Halper. Tendon proteoglycans: biochemistry and function. eng. *Journal of musculoskeletal neuronal interactions*, 5(1):22–34, 2005. ISSN: 1108-7161 (Print).

[79] Kristian Prydz. Determinants of Glycosaminoglycan (GAG) Structure. eng. *Biomolecules*, 5(3):2003–2022, 2015. ISSN: 2218-273X (Electronic). DOI: `10.3390/biom5032003`.

[80] Christina N.M. Ryan, Anna Sorushanova, Alex J. Lomas, Anne Maria Mullen, Abhay Pandit, and Dimitrios I. Zeugolis. Glycosaminoglycans in Tendon Physiology, Pathophysiology, and Therapy. *Bioconjugate Chemistry*, 26(7):1237–1251, 2015. ISSN: 15204812. DOI: `10.1021/acs.bioconjchem.5b00091`.

[81] Fuming Zhang, Zhenqing Zhang, and Robert J Linhardt. Chapter 3 - Glycosaminoglycans. In Richard D Cummings and J Michael Pierce, editors, *Handbook of Glycomics*, pages 59–80. Academic Press, San Diego, 2010. ISBN: 978-0-12-373600-0. DOI: `https://doi.org/10.1016/B978-0-12-373600-0.00003-2`. URL: `http://www.sciencedirect.com/science/article/pii/B9780123736000000032`.

[82] Clair R Cole and Christopher A Smith. Glycoprotein biochemistry (structure and function)âa vehicle for teaching many aspects of... *Biochemical Education*, 17(4):180, 1989.

[83] Elizabeth M Culav, C Heather Clark, and Mervyn J Merrilees. Connective Tissues: Matrix Composition and Its Relevance to Physical Therapy. *Physical Therapy*, 79(3):308–319, 1999. ISSN: 0031-9023. DOI: `10.1093/ptj/79.3.308`. URL: `https://doi.org/10.1093/ptj/79.3.308`.

[84] G Muller, A Michel, and E Altenburg. COMP (cartilage oligomeric matrix protein) is synthesized in ligament, tendon, meniscus, and articular cartilage. eng. *Connective tissue research*, 39(4):233–244, 1998. ISSN: 0300-8207 (Print). DOI: `10.3109/03008209809021499`.

[85] R. K. Smith, M. Gerard, B. Dowling, A. J. Dart, H. L. Birch, and A. E. Goodship. Correlation of cartilage oligomeric matrix protein (COMP) levels in equine tendon with mechanical properties: a proposed role for COMP in determining function-specific mechanical characteristics of locomotor tendons. *Equine veterinary journal. Supplement*, 2002. DOI: `10.1111/j.2042-3306.2002.tb05426.x`.

[86] Krisztina Halasz, Anja Kassner, Matthias Morgelin, and Dick Heinegard. COMP acts as a catalyst in collagen fibrillogenesis. eng. *The Journal of biological chemistry*, 282(43):31166–31173, 2007. ISSN: 0021-9258 (Print). DOI: `10.1074/jbc.M705735200`.

[87] Fan Wu, Michael Nerlich, and Denitsa Docheva. Tendon injuries: Basic science and new repair proposals. *EFORT Open Reviews*, 2017. ISSN: 20585241. DOI: `10.1302/2058-5241.2.160075`.

[88] D Mehr, P D Pardubsky, J A Martin, and J A Buckwalter. Tenascin-C in tendon regions subjected to compression. eng. *Journal of orthopaedic research : official publication of the Orthopaedic Research Society*, 18(4):537–545, 2000. ISSN: 0736-0266 (Print). DOI: `10.1002/jor.1100180405`.

[89] J A Martin, D Mehr, P D Pardubsky, and J A Buckwalter. The role of tenascin-C in adaptation of tendons to compressive loading. eng. *Biorheology*, 40(1-3):321–329, 2003. ISSN: 0006-355X (Print).

[90] Tero A H Järvinen, Lászlo Józsa, Pekka Kannus, Teppo L N Järvinen, Timo Hurme, Martti Kvist, Markku Pelto-Huikko, Hannu Kalimo, and Markku Järvinen. Mechanical loading regulates the expression of tenascin-C in the myotendinous junction and tendon but does not induce de novo synthesis in the skeletal muscle. *Journal of Cell Science*, 116(5):857 LP –866, 2003. DOI: `10.1242/jcs.00303`. URL: `http://jcs.biologists.org/content/116/5/857.abstract`.

[91] Kim S Midwood, Matthias Chiquet, Richard P Tucker, and Gertraud Orend. Tenascin-C at a glance. eng. *Journal of cell science*, 129(23):4321–4327, 2016. ISSN: 1477-9137 (Electronic). DOI: `10.1242/jcs.190546`.

[92] Jaspreet K Kular, Shouvik Basu, and Ram I Sharma. The extracellular matrix: Structure, composition, age-related differences, tools for analysis and applications for tissue engineering. *Journal of Tissue Engineering*, 5:2041731414557112, 2014. DOI: `10.1177/2041731414557112`. URL: `https://doi.org/10.1177/2041731414557112`.

[93] Yulong Sun, Evelyn J. Berger, Chunfeng Zhao, Kai Nan An, Peter C. Amadio, and Gregory Jay. Mapping lubricin in canine musculoskeletal tissues. *Connective Tissue Research*, 2006. ISSN: 03008207. DOI: `10.1080/03008200600846754`.

[94] G Musumeci. The role of lubricin in normal and pathological joint tissue: A contemporary review. *OA Anatomy*, 2013. DOI: `10.13172/2052-7829-1-1-329`.

[95] Timothy M Ritty, Konstantinos Ditsios, and Barry C Starcher. Distribution of the elastic fiber and associated proteins in flexor tendon reflects function. eng. *The Anatomical record*, 268(4):430–440, 2002. ISSN: 0003-276X (Print). DOI: `10.1002/ar.10175`.

[96] Cay M Kielty, Michael J Sherratt, and C Adrian Shuttleworth. Elastic fibres. *Journal of Cell Science*, 115(14):2817–2828, 2002. ISSN: 0021-9533. DOI: `10.1242/jcs.115.14.2817`. URL: `https://doi.org/10.1242/jcs.115.14.2817`.

[97] R Strocchi, V de Pasquale, P Gubellini, A Facchini, M Marcacci, R Buda, S Zaffagnini, and A Ruggeri. The human anterior cruciate ligament: histological and ultrastructural observations. *Journal of anatomy*, 1992. ISSN: 0021-8782.

[98] John Gosline, Margo Lillie, Emily Carrington, Paul Guerette, Christine Ortlepp, and Ken Savage. Elastic proteins: biological roles and mechanical properties. eng. *Philosophical transactions of the Royal Society of London. Series B, Biological sciences*, 357(1418):121–132, 2002. ISSN: 0962-8436 (Print). DOI: `10.1098/rstb.2001.1022`.

[99] Cay M Kielty. Elastic fibres in health and disease. eng. *Expert reviews in molecular medicine*, 8(19):1–23, 2006. ISSN: 1462-3994 (Electronic). DOI: `10.1017/S146239940600007X`.

[100] Kim S Midwood and Jean E Schwarzbauer. Elastic Fibers: Building Bridges Between Cells and Their Matrix. *Current Biology*, 12(8):R279–R281, 2002. ISSN: 0960-9822. DOI: `https://doi.org/10.1016/S0960-9822(02)00800-X`. URL: `https://www.sciencedirect.com/science/article/pii/S096098220200800X`.

[101] Jeffrey Ryan Hill, Jeremy D Eekhoff, Robert H Brophy, and Spencer P Lake. Elastic fibers in orthopedics: Form and function in tendons and ligaments, clinical implications, and future directions. eng. *Journal of orthopaedic research : official publication of the Orthopaedic Research Society*, 38(11):2305–2317, 2020. ISSN: 1554-527X (Electronic). DOI: `10.1002/jor.24695`.

[102] Wei Lee Lim, Ling Ling Liau, Min Hwei Ng, Shiplu Roy Chowdhury, and Jia Xian Law. Current Progress in Tendon and Ligament Tissue Engineering. eng. *Tissue engineering and regenerative medicine*, 16(6):549–571, 2019. ISSN: 2212-5469 (Electronic). DOI: `10.1007/s13770-019-00196-w`.

[103] Natalie L Leong, Jamie L Kator, Thomas L Clemens, Aaron James, Motomi Enamoto-Iwamoto, and Jie Jiang. Tendon and Ligament Healing and Current Approaches to Tendon and Ligament Regeneration. eng. *Journal of orthopaedic research : official publication of the Orthopaedic Research Society*, 38(1):7–12, 2020. ISSN: 1554-527X (Electronic). DOI: `10.1002/jor.24475`.

[104] Andrew M Briggs, Anthony D Woolf, Karsten Dreinhöfer, Nicole Homb, Damian G Hoy, Deborah Kopansky-Giles, Kristina Åkesson, and Lyn March. Reducing the global burden of musculoskeletal conditions. eng. *Bulletin of the World Health Organization*, 96(5):366–368, 2018. ISSN: 1564-0604 (Electronic). DOI: `10.2471/BLT.17.204891`.

[105] N Maffulli. Overuse tendon conditions: Time to change a confusing terminology. *Arthroscopy: The Journal of Arthroscopic Related Surgery*, 14(8):840–843, 1998. ISSN: 0749-8063. DOI: `https://doi.org/10.1016/S0749-8063(98)70021-0`. URL: `https://www.sciencedirect.com/science/article/pii/S0749806398700210`.

[106] Ian Burton. Autoregulation in Resistance Training for Lower Limb Tendinopathy: A Potential Method for Addressing Individual Factors, Intervention Issues, and Inadequate Outcomes. *Frontiers in Physiology*, 12, 2021. ISSN: 1664-042X. DOI: `10.3389/fphys.2021.704306`. URL: `https://www.frontiersin.org/articles/10.3389/fphys.2021.704306`.

[107] Lorena Canosa-Carro, María Bravo-Aguilar, Vanesa Abuín-Porras, Jaime Almazán-Polo, Guillermo García-Pérez-de Sevilla, Isabel Rodríguez-Costa, Daniel López-López, Emmanuel Navarro-Flores, and Carlos Romero-Morales. Current understanding of the diagnosis and management of the tendinopathy: An update from the lab to the clinical practice. *Disease-a-Month*, 68(10):101314, 2022. ISSN: 0011-5029. DOI: `https://doi.org/10.1016/j.disamonth.2021.101314`. URL: `https://www.sciencedirect.com/science/article/pii/S0011502921001905`.

[108] William J Ribbans, Alison V September, and Malcolm Collins. Tendon and Ligament Genetics: How Do They Contribute to Disease and Injury? A Narrative Review. *Life*, 12(5), 2022. ISSN: 2075-1729. DOI: `10.3390/life12050663`. URL: `https://www.mdpi.com/2075-1729/12/5/663`.

[109] A. E. Ellison and E. E. Berg. Embryology, anatomy, and function of the anterior cruciate ligament. *Orthopedic Clinics of North America*, 1985. ISSN: 00305898.

[110] Leon Chaitow and Judith DeLany. Chapter 13 - The knee. In Leon Chaitow and Judith DeLany, editors, *Clinical Application of Neuromuscular Techniques, Volume 2 (Second Edition)*, pages 447–501. Churchill Livingstone, Oxford, second edi edition, 2011. ISBN: 978-0-443-06815-7. DOI: `https://doi.org/10.1016/B978-0-443-06815-7.00013-9`. URL: `http://www.sciencedirect.com/science/article/pii/B9780443068157000139`.

[111] M. Marieswaran, Ishita Jain, Bhavuk Garg, Vijay Sharma, and Dinesh Kalyanasundaram. A Review on Biomechanics of Anterior Cruciate Ligament and Materials for Reconstruction. *Applied Bionics and Biomechanics*, 2018. ISSN: 1176-2322. DOI: `10.1155/2018/4657824`.

[112] Marcio Bottene Villa Albers, Daniel Guenther, Carola F. van Eck, and Freddie H. Fu. Individualized Anatomical Anterior Cruciate Ligament Reconstruction. *Operative Techniques in Orthopaedics*, 27(1):20–26, 2017. ISSN: 15583848. DOI: `10.1053/j.oto.2017.01.005`.

[113] Lin Sha, Guoming Xie, Song Zhao, and Jinzhong Zhao. A morphologic and quantitative comparison of mechanoreceptors in the tibial remnants of the ruptured human anterior cruciate ligament. eng. *Medicine*, 96(5):e6081, 2017. ISSN: 1536-5964 (Electronic). DOI: `10.1097/MD.0000000000006081`.

[114] V B Duthon, C Barea, S Abrassart, J H Fasel, D Fritschy, and J Ménétrey. Anatomy of the anterior cruciate ligament. eng. *Knee surgery, sports traumatology, arthroscopy : official journal of the ESSKA*, 14(3):204–213, 2006. ISSN: 0942-2056 (Print). DOI: `10.1007/s00167-005-0679-9`.

[115] Yalda Ashraf Kharaz. *The Molecular and Cellular Differences Between Tendons and Ligaments*. PhD thesis, 2015. URL: `https://livrepository.liverpool.ac.uk/2048079/3/AshrafkharazYal_Mar2015_2048079.pdf`.

[116] S P Arnoczky. Anatomy of the anterior cruciate ligament. eng. *Clinical orthopaedics and related research*, (172):19–25, 1983. ISSN: 0009-921X (Print).

[117] W Petersen and B Tillmann. Structure and vascularization of the cruciate ligaments of the human knee joint. eng. *Anatomy and embryology*, 200(3):325–334, 1999. ISSN: 0340-2061 (Print). DOI: `10.1007/s004290050283`.

[118] Monika Senftl, Daniel Petek, Matthias Jacobi, Alex Schallberger, Jonathan Spycher, Anna Stock, Rolf Hess, and Moritz Tannast. Occurrence of inadequate ACL healing after Dynamic Intraligamentary Stabilization and functional outcome-a multicentre case series. eng. *European journal of orthopaedic surgery traumatology : orthopedie traumatologie*, 32(7):1265–1274, 2022. ISSN: 1432-1068 (Electronic). DOI: `10.1007/s00590-021-03096-9`.

[119] S. Scheffler. The cruciate ligaments: Anatomy, biology, and biomechanics. *The Knee Joint: Surgical Techniques and Strategies*, 9782287993(2):11–21, 2012. DOI: `10.1007/978-2-287-99353-4_2`.

[120] Hideo Matsumoto, Yasunori Suda, Toshiro Otani, Yasuo Niki, Bahaa B Seedhom, and Kyosuke Fujikawa. Roles of the anterior cruciate ligament and the medial collateral ligament in preventing valgus instability. *Journal of Orthopaedic Science*, 6(1):28–32, 2001. ISSN: 1436-2023. DOI: `10.1007/s007760170021`. URL: `https://doi.org/10.1007/s007760170021`.

[121] Frank R Noyes. The function of the human anterior cruciate ligament and analysis of single- and double-bundle graft reconstructions. eng. *Sports health*, 1(1):66–75, 2009. ISSN: 1941-7381 (Print). DOI: `10.1177/1941738108326980`.

[122] J. Zavatsky, A; O'Connor. ACL function in the normal knee. *Biomecânica*, III(5):121–132, 1995.

[123] J. Dargel, M. Gotter, K. Mader, D. Pennig, J. Koebke, and R. Schmidt-Wiethoff. Biomechanics of the anterior cruciate ligament and implications for surgical reconstruction. *Strategies in Trauma and Limb Reconstruction*, 2(1):1–12, 2007. ISSN: 18288936. DOI: `10.1007/s11751-007-0016-6`.

[124] Christoph Domnick, Michael J Raschke, and Mirco Herbort. Biomechanics of the anterior cruciate ligament: Physiology, rupture and reconstruction techniques. eng. *World journal of orthopedics*, 7(2):82–93, 2016. ISSN: 2218-5836 (Print). DOI: `10.5312/wjo.v7.i2.82`.

[125] Carola F. Van Eck and Freddie H. Fu. Anatomic anterior cruciate ligament reconstruction using an individualized approach. *Asia-Pacific Journal of Sports Medicine, Arthroscopy, Rehabilitation and Technology*, 1(1):19–25, 2014. ISSN: 22146873. DOI: `10.1016/j.asmart.2013.12.008`. URL: `http://dx.doi.org/10.1016/j.asmart.2013.12.008`.

[126] Savio L-Y Woo, Changfu Wu, Ozgur Dede, Fabio Vercillo, and Sabrina Noorani. Biomechanics and anterior cruciate ligament reconstruction. *Journal of Orthopaedic Surgery and Research*, 1(1):2, 2006. ISSN: 1749-799X. DOI: `10.1186/1749-799X-1-2`. URL: `https://doi.org/10.1186/1749-799X-1-2`.

[127] Hazel R C Screen, Julia C Shelton, Vivek H Chhaya, Michael V Kayser, Dan L Bader, and David A Lee. The Influence of Noncollagenous Matrix Components on the Micromechanical Environment of Tendon Fascicles. *Annals of Biomedical Engineering*, 33(8):1090–1099, 2005. ISSN: 1573-9686. DOI: `10.1007/s10439-005-5777-9`. URL: `https://doi.org/10.1007/s10439-005-5777-9`.

[128] Savio L-Y. Woo, Eric K Wong, J Mi Lee, Masayoshi Yagi, and Freddie H Fu. Ligaments of the Knee in Sports Injuries and Rehabilitation. In Giancarlo Puddu, Arrigo Giombini, and Alberto Selvanetti, editors, *Rehabilitation of Sports Injuries: Current Concepts*, pages 1–10. Springer Berlin Heidelberg, Berlin, Heidelberg, 2001. ISBN: 978-3-662-04369-1. DOI: `10.1007/978-3-662-04369-1_1`. URL: `https://doi.org/10.1007/978-3-662-04369-1_1`.

[129] Joseph W. Freeman, Mia D. Woods, and Cato T. Laurencin. Tissue engineering of the anterior cruciate ligament using a braid-twist scaffold design. *Journal of Biomechanics*, 40(9):2029–2036, 2007. ISSN: 00219290. DOI: `10.1016/j.jbiomech.2006.09.025`.

[130] Himadri S Gupta and Hazel R C Screen. Structural Building Blocks of Soft Tissues: Tendons and Heart Valves. In Stéphane Avril and Sam Evans, editors, *Material Parameter Identification and Inverse Problems in Soft Tissue Biomechanics*, pages 1–35. Springer International Publishing, Cham, 2017. ISBN: 978-3-319-45071-1. DOI: `10.1007/978-3-319-45071-1_1`.

[131] Mitsuo Ochi, Konsei Shino, Kazunori Yasuda, and Masahiro Kurosaka. *ACL injury and its treatment.* 2016. ISBN: 9784431558583. DOI: `10.1007/978-4-431-55858-3`.

[132] J B Morrison. The mechanics of the knee joint in relation to normal walking. eng. *Journal of biomechanics*, 3(1):51–61, 1970. ISSN: 0021-9290 (Print). DOI: `10.1016/0021-9290(70)90050-3`.

[133] Savio L.Y. Woo, Richard E. Debski, John D. Withrow, and Marsie A. Janaushek. Biomechanics of knee ligaments. *American Journal of Sports Medicine*, 27(4):533–543, 1999. ISSN: 03635465. DOI: `10.1177/03635465990270042301`. arXiv: `99/2727-0533$02.00/0 [0363-5465]`.

[134] F R Noyes and E S Grood. The strength of the anterior cruciate ligament in humans and Rhesus monkeys. eng. *The Journal of bone and joint surgery. American volume*, 58(8):1074–1082, 1976. ISSN: 0021-9355 (Print).

[135] Johanna Buschmann and Gabriella Meier Bürgisser. 2 - Biomechanical properties of tendons and ligaments in humans and animals. In Johanna Buschmann and Gabriella Meier Bürgisser, editors, *Biomechanics of Tendons and Ligaments*, pages 31–61. Woodhead Publishing, 2017. ISBN: 978-0-08-100489-0. DOI: `https://doi.org/10.1016/B978-0-08-100489-0.00002-8`. URL: `http://www.sciencedirect.com/science/article/pii/B9780081004890000028`.

[136] C R Allen, G A Livesay, E K Wong, and S L Woo. Injury and reconstruction of the anterior cruciate ligament and knee osteoarthritis. eng. *Osteoarthritis and cartilage*, 7(1):110–121, 1999. ISSN: 1063-4584 (Print). DOI: `10.1053/joca.1998.0166`.

[137] Hazel R C Screen. Investigating load relaxation mechanics in tendon. *Journal of the Mechanical Behavior of Biomedical Materials*, 1(1):51–58, 2008. ISSN: 1751-6161. DOI: `https://doi.org/10.1016/j.jmbbm.2007.03.002`. URL: `http://www.sciencedirect.com/science/article/pii/S1751616107000033`.

[138] H. R.C. Screen, S. Toorani, and J. C. Shelton. Microstructural stress relaxation mechanics in functionally different tendons. *Medical Engineering and Physics*, 35:96–102, 2013. ISSN: 13504533. DOI: `10.1016/j.medengphy.2012.04.004`.

[139] Alexandre Pedro Nicolini, Rogério Teixeira de Carvalho, Marcelo Mitsuro Matsuda, Jorge Sayum Filho, and Moisés Cohen. Common injuries in athletes' knee: Experience of a specialized center. *Acta Ortopedica Brasileira*, 2014. ISSN: 14137852. DOI: `10.1590/1413-78522014220300475`.

[140] Alicia M Montalvo, Daniel K Schneider, Kate E Webster, Laura Yut, Marc T Galloway, Robert S Jr Heidt, Christopher C Kaeding, Timothy E Kremcheck, Robert A Magnussen, Shital N Parikh, Denver T Stanfield, Eric J Wall, and Gregory D Myer. Anterior Cruciate Ligament Injury Risk in Sport: A Systematic Review and Meta-Analysis of Injury Incidence by Sex and Sport Classification. eng. *Journal of athletic training*, 54(5):472–482, 2019. ISSN: 1938-162X (Electronic). DOI: `10.4085/1062-6050-407-16`.

[141] J Evans and Jl Nielson. Anterior Cruciate Ligament (ACL) Knee Injuries, 2023. URL: `https://www.ncbi.nlm.nih.gov/books/NBK499848/`.

[142] T. Jamil, U. Ansari, M. Najabat Ali, and M. Mir. A Review on Biomechanical and Treatment Aspects Associated with Anterior Cruciate Ligament. *Irbm*, 38(1):13–25, 2017. ISSN: 18760988. DOI: `10.1016/j.irbm.2016.10.002`.

[143] D H O'DONOGHUE. THE UNHAPPY TRIAD: ETIOLOGY, DIAGNOSIS AND TREATMENT. eng. *The American journal of orthopedics*, 6:242–7 PASSIM, 1964. ISSN: 0891-7507 (Print).

[144] K D Shelbourne and P A Nitz. The O'Donoghue triad revisited. Combined knee injuries involving anterior cruciate and medial collateral ligament tears. eng. *The American journal of sports medicine*, 19(5):474–477, 1991. ISSN: 0363-5465 (Print). DOI: `10.1177/036354659101900509`.

[145] Amir Human Hoveidaei, Reza Sattarpour, Haleh Dadgostar, Saeed Razi, and Mohammad Razi. Unhappy triad of the knee: What are the current concepts and opinions? eng. *World journal of orthopedics*, 14(5):268–274, 2023. ISSN: 2218-5836 (Print). DOI: `10.5312/wjo.v14.i5.268`.

[146] Andrea Ferretti, Edoardo Monaco, Antonio Ponzo, Matthew Dagget, Matteo Guzzini, Daniele Mazza, Andrea Redler, and Fabio Conteduca. The unhappy triad of the knee re-revisited. *International Orthopaedics*, 43(1):223–228, 2019. ISSN: 1432-5195. DOI: `10.1007/s00264-018-4181-7`. URL: `https://doi.org/10.1007/s00264-018-4181-7`.

[147] Daniel Niederer, Michael Behringer, and Thomas Stein. Functional outcomes after anterior cruciate ligament reconstruction: unravelling the role of time between injury and surgery, time since reconstruction, age, gender, pain, graft type, and concomitant injuries. *BMC Sports Science, Medicine and Rehabilitation*, 15(1):49, 2023. ISSN: 2052-1847. DOI: `10.1186/s13102-023-00663-x`. URL: `https://doi.org/10.1186/s13102-023-00663-x`.

[148] Patrick Vavken and Martha M. Murray. ACL injury epidemiology. In *The ACL Handbook: Knee Biology, Mechanics, and Treatment.* 2013. ISBN: 9781461407607. DOI: `10.1007/978-1-4614-0760-7_1`.

[149] Seth L Sherman, Jacob Calcei, Taylor Ray, Robert A Magnussen, Volker Musahl, Christopher C Kaeding, Mark Clatworthy, John A Bergfeld, and Marcus P Arnold. ACL Study Group presents the global trends in ACL reconstruction: biennial survey of the ACL Study Group. *Journal of ISAKOS*, 6(6):322–328, 2021. ISSN: 2059-7754. DOI: `https://doi.org/10.1136/jisakos-2020-000567`. URL: `https://www.sciencedirect.com/science/article/pii/S2059775421003102`.

[150] Neeraj Singh. International Epidemiology of Anterior Cruciate Ligament Injuries. *Orthopedic Research Online Journal*, 2018. DOI: `10.31031/oproj.2018.03.000562`.

[151] Simon G.F. Abram, Andrew J. Price, Andrew Judge, and David J. Beard. Anterior cruciate ligament (ACL) reconstruction and meniscal repair rates have both increased in the past 20 years in England: Hospital statistics from 1997 to 2017. *British Journal of Sports Medicine*:1–7, 2019. ISSN: 14730480. DOI: `10.1136/bjsports-2018-100195`.

[152] Nicholas A. Beck, J. Todd R. Lawrence, James D. Nordin, Terese A. DeFor, and Marc Tompkins. ACL Tears in School-Aged Children and Adolescents Over 20 Years. *Pediatrics*, 139(3):e20161877, 2017. ISSN: 0031-4005. DOI: `10.1542/peds.2016-1877`. URL: `http://pediatrics.aappublications.org/lookup/doi/10.1542/peds.2016-1877`.

[153] Maximiliano Barahona and José Tomás Rojas. The evolution of knee anterior cruciate ligament tear incidence in a single ski resort : 23 years overview. 0(3):103–106, 2018. DOI: `10.15406/mojsm2018.02.00055`.

[154] Karen M Sutton and James Montgomery Bullock. Anterior cruciate ligament rupture: differences between males and females. eng. *The Journal of the American Academy of Orthopaedic Surgeons*, 21(1):41–50, 2013. ISSN: 1067-151X (Print). DOI: `10.5435/JAAOS-21-01-41`.

[155] Joanne L Parsons, Stephanie E Coen, and Sheree Bekker. Anterior cruciate ligament injury: towards a gendered environmental approach. *British Journal of Sports Medicine*, 55(17):984–990, 2021. ISSN: 0306-3674. DOI: `10.1136/bjsports-2020-103173`. URL: `https://bjsm.bmj.com/content/55/17/984`.

[156] Helen C Smith, Pamela Vacek, Robert J Johnson, James R Slauterbeck, Javad Hashemi, Sandra Shultz, and Bruce D Beynnon. Risk factors for anterior cruciate ligament injury: a review of the literature - part 1: neuromuscular and anatomic risk. eng. *Sports health*, 4(1):69–78, 2012. ISSN: 1941-0921 (Electronic). DOI: `10.1177/1941738111428281`.

[157] Timothy E. Hewett, Gregory D. Myer, and Kevin R. Ford. Anterior cruciate ligament injuries in female athletes: Part 1, mechanisms and risk factors, 2006. DOI: `10.1177/0363546505284183`.

[158] J.Winslow Alford and Bernard R. Bach Jr. Managing ACL tears: Evaluation and diagnosis. *Journal Of Musculoskeletal Medicine*, 21(July):381–390, 2004. ISSN: 0899-2517. URL: `http://www.westbayortho.com/orthopaedics/docs/alford/ACLpartIevaldx.pdf`.

[159] S H Liu, R A Al-Shaikh, V Panossian, G A Finerman, and J M Lane. Estrogen affects the cellular metabolism of the anterior cruciate ligament. A potential explanation for female athletic injury. eng. *The American journal of sports medicine*, 25(5):704–709, 1997. ISSN: 0363-5465 (Print). DOI: `10.1177/036354659702500521`.

[160] Alexis Lew, Aryan Haratian, Amir Fathi, Michael Kim, Laith Hasan, Ioanna K Bolia, Alexander Weber, and Frank Petrigliano. Gender Differences in Anterior Cruciate Ligament Injury: A Review of Risk Factors, Mechanisms, and Mitigation Strategies in the Female Athlete. *Journal of Orthopaedics and Surgical Sports Medicine*, 4(1), 2021. DOI: `10.31579/2641-0427/022`.

[161] The female ACL: Why is it more prone to injury? eng. *Journal of orthopaedics*, 13(2):A1–4, 2016. ISSN: 0972-978X (Print). DOI: `10.1016/S0972-978X(16)00023-4`.

[162] A. M. Kiapour and M. M. Murray. Basic science of anterior cruciate ligament injury and repair. *Bone Joint Research*, 2014. ISSN: 2046-3758. DOI: `10.1302/2046-3758.32.2000241`.

[163] Carl Imhauser, Craig Mauro, Daniel Choi, Eric Rosenberg, Stephen Mathew, Joseph Nguyen, Yan Ma, and Thomas Wickiewicz. Abnormal Tibiofemoral Contact Stress and Its Association With Altered Kinematics After Center-Center Anterior Cruciate Ligament Reconstruction: An In Vitro Study. *The American Journal of Sports Medicine*, 41(4):815–825, 2013. DOI: `10.1177/0363546512475205`. URL: `https://doi.org/10.1177/0363546512475205`.

[164] David Simon, Randy Mascarenhas, Bryan M. Saltzman, Meaghan Rollins, Bernard R. Bach, and Peter MacDonald. The Relationship between Anterior Cruciate Ligament Injury and Osteoarthritis of the Knee, 2015. DOI: `10.1155/2015/928301`.

[165] Nikolaos K Paschos. Anterior cruciate ligament reconstruction and knee osteoarthritis. eng, 2017. DOI: `10.5312/wjo.v8.i3.212`.

[166] Nicole A Friel and Constance R Chu. The role of ACL injury in the development of posttraumatic knee osteoarthritis. eng. *Clinics in sports medicine*, 32(1):1–12, 2013. ISSN: 1556-228X (Electronic). DOI: `10.1016/j.csm.2012.08.017`.

[167] Edward C Cheung, Marcus DiLallo, Brian T Feeley, and Drew A Lansdown. Osteoarthritis and ACL Reconstruction-Myths and Risks. eng. *Current reviews in musculoskeletal medicine*, 13(1):115–122, 2020. ISSN: 1935-973X (Print). DOI: `10.1007/s12178-019-09596-w`.

[168] H Higuchi, K Shirakura, M Kimura, M Terauchi, T Shinozaki, H Watanabe, and K Takagishi. Changes in biochemical parameters after anterior cruciate ligament injury. eng. *International orthopaedics*, 30(1):43–47, 2006. ISSN: 0341-2695 (Print). DOI: `10.1007/s00264-005-0023-5`.

[169] Vanessa G Cuellar, Jason M Cuellar, S Raymond Golish, David C Yeomans, and Gaetano J Scuderi. Cytokine profiling in acute anterior cruciate ligament injury. eng. *Arthroscopy : the journal of arthroscopic related surgery : official publication of the Arthroscopy Association of North America and the International Arthroscopy Association*, 26(10):1296–1301, 2010. ISSN: 1526-3231 (Electronic). DOI: `10.1016/j.arthro.2010.02.011`.

[170] Hugues Louboutin, R Debarge, J Richou, Tarik Ait Si Selmi, Simon T Donell, Philippe Neyret, and F Dubrana. Osteoarthritis in patients with anterior cruciate ligament rupture: a review of risk factors. eng. *The Knee*, 16(4):239–244, 2009. ISSN: 1873-5800 (Electronic). DOI: `10.1016/j.knee.2008.11.004`.

[171] James Min-Leong Wong, Tanvir Khan, Chethan S Jayadev, Wasim Khan, and David Johnstone. Anterior Cruciate Ligament Rupture and Osteoarthritis Progression. *The Open Orthopaedics Journal*, 6:295–300, 2012. ISSN: 1874-3250. DOI: `10.2174/1874325001206010295`.

[172] Hugh P Jones, Richard C Appleyard, Sanjeev Mahajan, and George A C Murrell. Meniscal and Chondral Loss in the Anterior Cruciate Ligament Injured Knee. *Sports Medicine*, 33(14):1075–1089, 2003. ISSN: 1179-2035. DOI: `10.2165/00007256-200333140-00004`. URL: `https://doi.org/10.2165/00007256-200333140-00004`.

[173] James Philip Bliss. Anterior Cruciate Ligament Injury, Reconstruction, and the Optimization of Outcome. eng. *Indian journal of orthopaedics*, 51(5):606–613, 2017. ISSN: 0019-5413 (Print). DOI: `10.4103/ortho.IJOrtho_237_17`.

[174] Daniel A Shaerf, Philip S Pastides, Khaled M Sarraf, and Charles A Willis-Owen. Anterior cruciate ligament reconstruction best practice: A review of graft choice. eng. *World journal of orthopedics*, 5(1):23–29, 2014. ISSN: 2218-5836 (Print). DOI: `10.5312/wjo.v5.i1.23`.

[175] Eric N Bowman, Orr Limpisvasti, Brian J Cole, and Neal S ElAttrache. Anterior Cruciate Ligament Reconstruction Graft Preference Most Dependent on Patient Age: A Survey of United States Surgeons. *Arthroscopy: The Journal of Arthroscopic Related Surgery*, 37(5):1559–1566, 2021. ISSN: 0749-8063. DOI: `https://doi.org/10.1016/j.arthro.2021.01.042`. URL: `https://www.sciencedirect.com/science/article/pii/S0749806321000591`.

[176] David J Beard, Loretta Davies, Jonathan A Cook, Jamie Stokes, Jose Leal, Heidi Fletcher, Simon Abram, Katie Chegwin, Akiko Greshon, William Jackson, Nicholas Bottomley, Matt Dodd, Henry Bourke, Beverly A Shirkey, Arsenio Paez, Sarah E Lamb, Karen Barker, Michael Phillips, Mark Brown, Vanessa Lythe, Burhan Mirza, Andrew Carr, Paul Monk, Carlos Morgado Areia, Sean O'Leary, Fares Haddad, Chris Wilson, Andrew Price, Richard Emsley, George Peat, Martyn Snow, Marion Campbell, Tessa Howell, Hilary Johnson, Stephen McDonnell, Thomas Pinkney, Mark Williams, Helen Campbell, Jackie Davies, Jiyang Li, Christina Bagg, Laura Haywood, Anne Nicholson, Joanne Riches, Sean Symons, Mark Vertue, Louay Al Mouazzen, Rachel Bray, Damian Clark, James Coulthard, Tim Holland, Nick Howells, Andrew Jones, Richard Kapur, Alastair Kiszely, Harry Krishnan, Karen MacDonald-Taylor, Jon Manara, James Murray, Corina Negrut, Vishai Pai, Andrew Porteous, Sven Putnis, James Robinson, Shav Rupasinghe, Veenesh Selvaratnam, James Smith, Nick Smith, Jarrad Stevens, Clare Taylor, Anthony Theodorides, Niraj Vetharajan, Helen Vint, Lucy Young, Susan Bullock, Rebecca Cook, Alexander Dodds, Amanda Freeman-Hicks, Paula Hillout, Thomas Cornell, Abbie Coutts, Suzy Dean, Nicki Devooght-Johnson, Emma Ferrell, Eve Fletcher, Chrissie Hall, Benjamin Kent, Sandra Kessly, Robin Kincaid, Mohamed Lazizi, Ahmed Mostafa, Toby Nisbett, Tim Powell, Peter Riddlestone, Andrew Roberton, Jessica Summers, Lucy Whitbread, Belinda Wroath, Emma

Fenlon, Andrew Hall, Helen Jeffrey, Raghuram Thonse, Debra Dunne, Andy Metcalfe, Kerri McGowan, Simon Middleton, Feisal Shah, Tim Spalding, Charlie Marie Suddens, Tamar Sweed, Joanna Teuke, Peter Thompson, David Wright, Justine Amero, Emma Brown, Hugh Chissell, Andrea Croucher, Gareth Dickinson, Catherine Hawkes-Blackburn, Alice Peacocke, Graham Smith, Carol Snipe, Kim Dearnley, Reza Mayahi, Barry Andrews, Massimo Barcelona, Hazel Giles, Abdulkerim Gokturk, Paul Harnett, Katie Jeeves, Joyce Kadunyi, Sheena Mendoza, Ines Reichert, Marta Santamaria, Harshinder Virdee, Sanjeev Anand, Nayef Aslam-Pervez, Stephen Draycott, Faye Howarth, Irfan Jina, Niall Maher, Denise Ross, Lindsey Worstenholme, Abdul Baig, Arun Bhaskaran, Daniel Banks, Tracy Brear, Carla Christie, Laura Cowen, Jack Davis, Ross Dixey, Colin Esler, Amirah Essop-Adam, Christina Haines, Linzy Houchen-Wolloff, Husein Varachia, Richard Wood, Glaxy Gray, Jessica Nichols, Alice Panes, Susan Partridge, Lawrie Rogerson, Pankaj Sharma, David Triggs, Ian Venables, Danielle Wilcock, Sarah Buckley, Thelma Darian, Elizabeth Denis, Jo Duncan, Charlotte Hirst, James Newman, Fern Richardson, Jon Smith, Megan Adcode, Megan Cottingham, Eliza Foster, Andrew Kelly, Niamh McKay, Jane Rewbury, Alison Whitcher, James Williams, Esther Zebracki, Llinos Davies, Jayadeep Jayachandran, Alison Tardivel, Victoria Whitehead, Martha Batting, Amy Bond, Marc Deakin, Christopher Dodd, Alison Hudak, Samantha Hynes, Luke Jones, Gail Lang, David McKenna, Susan Morris, Clare Scott-Dempster, Adam Sykes, Iason Vichos, Simon Wood, Rupert Clifton, Stephanie Diaz, Craig Hendy, Nishil Modi, Brendan O'Mahony, Susan O'Sullivan, Nicola Parker, Mira Pecheva, Rowan Rumonovic, Emma McLoughlin, Jeremy Rushbrook, Anna Thornhill, Valerie Parkinson, Rafael Sales, Katja Van De Snepscheut-Jones, David Wilcock, Daniel Wright, Joanna Allison, Simon Baker, Kate Beesley, Gill Ferrari, Benedict Lankester, Alison Lewis, Joanne Lyons, Jamie O'Callaghan, Sarah Sutcliffe, Dianne Wood, Emily Bannister, Chloe Brown, Debbie Burden, Terence Campbell, Emma Craig, Rashmi Easow, Julie Foxton, Alexandra Hazlerigg, Chethan Jayabev, Rosie Murdoch, Georgie Parsons, Harry Brown, Paula Carvelli, Rugaia Montaser, Ali Pepper, Sinduja Sivarajan, Oliver Templeton-Ward, Eva Wilson, Julie Cronin, Sarah Diment, Victoria King, Katharine Shean, Leonidas Vachtsevanos, Katharine Wilcocks, Ben Wilson, Paul McNestry, Joanna Ollerenshaw, James Stoddard, Paul Sutton, Sanjay Anand, Judith Bell, Albert Chikate, Diane Daniel, Timothy Davies, Tom Finnigan, Antonio Frasquet-Garcia, Susan Hopkins, Sharon Kerrison, Angela McGowan, David Sands Johnson, Lara Smith, Philip Turner, Helen Wilkinson, Lynne Allsop, Deborah Anthony, Rebecca Boulton, Sarah Brown, Vikram Desai, Mandy Gill, Cheryl Heeley, Sushrut Kulkarni, Wayne Lovegrove, Dominic Nash, Terri Ann Sewell, Sarah Shelton, Katie Slack, James Cartwright, Lynda Connor, Andrew Davies, Caroline Davies, Glyn Gainard, Dave Graham-Woollard, Carl Murphy, Leanne Quinn, Caradog Thomas, Jenny Travers, Marie Williams, Amanda Bell, Sunny Deo, Katharine Francis, Tracy Jackson, Laura McCafferty, Basalingappa Navadgi, Karan Plank, Venkat Satish, Claire Thelwall, Rachel Knight, Rahul Patel, Bruce Paton, Ashutosh Acharya, Utuman Aland, Miltiades Areirobulos, Pascal de Feyter, Lisa Ditchfield, Hafiz Iqbaz, Daniel Massey, Gareth Stables, Sarah Appleby, Michael Brown, Sarah Cable, Alexander Damen, Joana Da Rocha, Louise Foster, Elizabeth Hamilton, Catriona Hatton, Cassie Honeywell, Kunal Kulkarni, Lucy Markham, Haadiya Mohammed, John O'Grady, Yogesh Joshi, Heather

Mclintock, Tania Morgan, Jane Stockport, Victoria Whitehead, Pranshu Agrawal, Jo Armstrong, Shannon Briggs, Ben Coupe, Anne Evans, Rob Gilbert, Sandra Latham, and Aslam Mohammed. Rehabilitation versus surgical reconstruction for non-acute anterior cruciate ligament injury (ACL SNNAP): a pragmatic randomised controlled trial. *The Lancet*, 400(10352):605–615, 2022. ISSN: 0140-6736. DOI: `10.1016/S0140-6736(22)01424-6`. URL: `https://doi.org/10.1016/S0140-6736(22)01424-6`.

[177] Ish Kumar Dhammi, Rehan-Ul-Haq, and Sudhir Kumar. Graft choices for anterior cruciate ligament reconstruction. eng. *Indian journal of orthopaedics*, 49(2):127–128, 2015. ISSN: 0019-5413 (Print). DOI: `10.4103/0019-5413.152393`.

[178] Chadwick C Prodromos and Brian T Joyce. 13 - Relative Strengths of Anterior Cruciate Ligament Autografts and Allografts. In Chadwick C Prodromos, editor, *The Anterior Cruciate Ligament (Second Edition)*, 71 –73.e1. Elsevier, second edi edition, 2018. ISBN: 978-0-323-38962-4. DOI: `https://doi.org/10.1016/B978-0-323-38962-4.00013-8`. URL: `http://www.sciencedirect.com/science/article/pii/B9780323389624000138`.

[179] G. Vunjak-Novakovic, Gregory Altman, Rebecca Horan, and David L. Kaplan. Tissue Engineering of Ligaments. *Annu. Rev. Biomed. Eng.*, 6:131–56, 2004.

[180] Cédric Laurent, Xing Liu, Natalia De Isla, Xiong Wang, and Rachid Rahouadj. Defining a scaffold for ligament tissue engineering: What has been done, and what still needs to be done. *Journal of Cellular Immunotherapy*, 4(1):4–9, 2018. ISSN: 2352-1775. DOI: `https://doi.org/10.1016/j.jocit.2018.09.002`. URL: `http://www.sciencedirect.com/science/article/pii/S2352177518300074`.

[181] Ojas Pujji, Nikita Keswani, Naomi Collier, Marion Black, and Lucy Doos. Evaluating the Functional Results and Complications of Autograft vs Allograft Use for Reconstruction of the Anterior Cruciate Ligament: A Systematic Review. eng. *Orthopedic reviews*, 9(1):6833, 2017. ISSN: 2035-8237 (Print). DOI: `10.4081/or.2017.6833`.

[182] Zhen-Yu Jia, Chen Zhang, Shi-qi Cao, Chen-chen Xue, Tian-ze Liu, Xuan Huang, and Wei-Dong Xu. Comparison of artificial graft versus autograft in anterior cruciate ligament reconstruction: a meta-analysis. *BMC Musculoskeletal Disorders*, 18(1):309, 2017. ISSN: 1471-2474. DOI: `10.1186/s12891-017-1672-4`.

[183] Robert K Peterson, Walter R Shelton, and Anna Laura Bomboy. Allograft versus autograft patellar tendon anterior cruciate ligament reconstruction: A 5-year follow-up. *Arthroscopy: The Journal of Arthroscopic Related Surgery*, 17(1):9–13, 2001. ISSN: 0749-8063. DOI: `https://doi.org/10.1053/jars.2001.19965`.

[184] Chadwick C. Prodromos and Charles H. Brown. Preparation of 5- and 6-Strand 1 Hamstring Tendon Grafts for Single-Bundle Hamstring Anterior Cruciate Ligament Reconstruction. In *The Anterior Cruciate Ligament: Reconstruction and Basic Science*, chapter 5. Elsevier, Philadelphia, 2nd edition, 2017. ISBN: 9780323497398.

[185] Michael I Iosifidis and Alexandros Tsarouhas. Allografts in Anterior Cruciate Ligament Reconstruction. eng, 2010. DOI: `10.1007/978-3-642-15630-4_58`.

[186] Kaitlyn Sadtler, Anirudha Singh, Matthew T Wolf, Xiaokun Wang, Drew M Pardoll, and Jennifer H Elisseeff. Design, clinical translation and immunological response of biomaterials in regenerative medicine. *Nature Reviews Materials*, 1(7):16040, 2016. ISSN: 2058-8437. DOI: `10.1038/natrevmats.2016.40`.

[187] Dharmesh Vyas, Stephen J Rabuck, and Christopher D Harner. Allograft Anterior Cruciate Ligament Reconstruction: Indications, Techniques, and Outcomes. *Journal of Orthopaedic Sports Physical Therapy*, 42(3):196–207, 2012. DOI: `10.2519/jospt.2012.4083`. URL: `https://doi.org/10.2519/jospt.2012.4083`.

[188] Dharmesh Vyas, Stephen J. Rabuck, and Christopher D. Harner. Allograft anterior cruciate ligament reconstruction: Indications, Techniques, and outcomes, 2012. DOI: `10.2519/jospt.2012.4083`.

[189] Katherine Coyner, Jamie Friedman, and Colin Pavano. Chapter 11 - Biologics in Orthopedic Surgery: Ligament Reconstruction in the Knee. In Augustus D Mazzocca and Adam D Lindsay, editors, *Biologics in Orthopaedic Surgery*, pages 105–122. Content Repository Only!, Philadelphia, 2019. ISBN: 978-0-323-55140-3. DOI: `https://doi.org/10.1016/B978-0-323-55140-3.00011-4`.

[190] E M Corner. Notes of a Case Illustrative of an Artificial Anterior Crucial Ligament, Demonstrating the Action of That Ligament. *Proceedings of the Royal Society of Medicine*, 7(Clin_Sect):120–121, 1914. DOI: `10.1177/003591571400700264`. URL: `https://doi.org/10.1177/003591571400700264`.

[191] A Philpott, D J Epstein, and T Lording. No evidence of reduced autograft ACL rupture rates with synthetic reinforcement: A systematic review. *Journal of ISAKOS*, 7(6):173–180, 2022. ISSN: 2059-7754. DOI: `10.1016/j.jisako.2022.04.005`. URL: `https://doi.org/10.1016/j.jisako.2022.04.005`.

[192] Claudio Legnani and Alberto Ventura. Synthetic grafts for anterior cruciate ligament reconstructive surgery. *Medical Engineering Physics*, 117:103992, 2023. ISSN: 1350-4533. DOI: `https://doi.org/10.1016/j.medengphy.2023.103992`. URL: `https://www.sciencedirect.com/science/article/pii/S1350453323000474`.

[193] Joanna Baawa-Ameyaw, Ricci Plastow, Fahima Aarah Begum, Babar Kayani, Hyder Jeddy, and Fares Haddad. Current concepts in graft selection for anterior cruciate ligament reconstruction. *EFORT Open Reviews*, 6(9):808–815, 2021. DOI: `10.1302/2058-5241.6.210023`. URL: `https://eor.bioscientifica.com/view/journals/eor/6/9/2058-5241.6.210023.xml`.

[194] Elena Garreta, Roger Oria, Carolina Tarantino, Mateu Pla-Roca, Patricia Prado, Francisco Fernández-Avilés, Josep Maria Campistol, Josep Samitier, and Nuria Montserrat. Tissue engineering by decellularization and 3D bioprinting. *Materials Today*, 20(4):166–178, 2017. ISSN: 1369-7021. DOI: `https://doi.org/10.1016/j.mattod.2016.12.005`.

[195] Young Chan Choi, Ji Suk Choi, Beob Soo Kim, Jae Dong Kim, Hwa In Yoon, and Yong Woo Cho. Decellularized extracellular matrix derived from porcine adipose tissue as a xenogeneic biomaterial for tissue engineering. eng. *Tissue engineering. Part C, Methods*, 18(11):866–876, 2012. ISSN: 1937-3392 (Electronic). DOI: `10.1089/ten.TEC.2012.0009`.

[196] Jonathan M Fishman, Mark W Lowdell, Luca Urbani, Tahera Ansari, Alan J Burns, Mark Turmaine, Janet North, Paul Sibbons, Alexander M Seifalian, Kathryn J Wood, Martin A Birchall, and Paolo De Coppi. Immunomodulatory effect of a decellularized skeletal muscle scaffold in a discordant xenotransplantation model. *Proceedings of the National Academy of Sciences*, 110(35):14360–14365, 2013. ISSN: 0027-8424. DOI: `10.1073/pnas.1213228110`. URL: `https://www.pnas.org/content/110/35/14360`.

[197] Thomas W. Gilbert, Tiffany L. Sellaro, and Stephen F. Badylak. Decellularization of tissues and organs. *Biomaterials*, 27(19):3675–3683, 2006. ISSN: 01429612. DOI: `10.1016/j.biomaterials.2006.02.014`.

[198] Thomas W Gilbert. Strategies for tissue and organ decellularization. *Journal of Cellular Biochemistry*, 113(7):2217–2222, 2012. DOI: `10.1002/jcb.24130`. URL: `https://onlinelibrary.wiley.com/doi/abs/10.1002/jcb.24130`.

[199] Anna Gilpin and Yong Yang. Decellularization Strategies for Regenerative Medicine: From Processing Techniques to Applications, 2017. DOI: `10.1155/2017/9831534`.

[200] Sara Dutton Sackett, Daniel M Tremmel, Fengfei Ma, Austin K Feeney, Rachel M Maguire, Matthew E Brown, Ying Zhou, Xiang Li, Cori O'Brien, Lingjun Li, William J Burlingham, and Jon S Odorico. Extracellular matrix scaffold and hydrogel derived from decellularized and delipidized human pancreas. *Scientific Reports*, 8(1):10452, 2018. ISSN: 2045-2322. DOI: `10.1038/s41598-018-28857-1`. URL: `https://doi.org/10.1038/s41598-018-28857-1`.

[201] Ricardo Londono and Stephen F Badylak. Biologic Scaffolds for Regenerative Medicine: Mechanisms of In vivo Remodeling. *Annals of Biomedical Engineering*, 43(3):577–592, 2015. ISSN: 1573-9686. DOI: `10.1007/s10439-014-1103-8`. URL: `https://doi.org/10.1007/s10439-014-1103-8`.

[202] Yi Sheng, Ding Fei, Gong Leiiei, and Gu Xiaosong. Extracellular Matrix Scaffolds for Tissue Engineering and Regenerative Medicine. *Current Stem Cell Research Therapy*, 12(3), 2017. ISSN: 22123946. DOI: `10.2174/1574888X11666160905092`.

[203] Denver M Faulk and Stephen F Badylak. Chapter 8 - Natural Biomaterials for Regenerative Medicine Applications. In Giuseppe Orlando, Jan Lerut, Shay Soker, and Robert J Stratta, editors, *Regenerative Medicine Applications in Organ Transplantation*, pages 101–112. Academic Press, Boston, 2014. ISBN: 978-0-12-398523-1. DOI: `https://doi.org/10.1016/B978-0-12-398523-1.00008-2`. URL: `https://www.sciencedirect.com/science/article/pii/B9780123985231000082`.

[204] Peter M. Crapo, Thomas W. Gilbert, and Stephen F. Badylak. An overview of tissue and whole organ decellularization processes. *Biomaterials*, 32(12):3233–3243, 2011. ISSN: 01429612. DOI: `10.1016/j.biomaterials.2011.01.057`. arXiv: `NIHMS150003`. URL: `http://dx.doi.org/10.1016/j.biomaterials.2011.01.057`.

[205] Kamal Hany Hussein, Tarek Saleh, Ebtehal Ahmed, Ho-Hyun Kwak, Kyung-Mee Park, Se-Ran Yang, Byung-Jae Kang, Ki-Young Choi, Kyung-Sun Kang, and Heung-Myong Woo. Biocompatibility and hemocompatibility of efficiently decellularized whole porcine kidney for tissue engineering. *Journal of Biomedical Materials Research Part A*, 106(7):2034–2047, 2018. DOI: `https://doi.org/10.1002/jbm.a.36407`. URL: `https://onlinelibrary.wiley.com/doi/abs/10.1002/jbm.a.36407`.

[206] Stephen F Badylak, Donald O Freytes, and Thomas W Gilbert. Extracellular matrix as a biological scaffold material: Structure and function. *Acta Biomaterialia*, 5(1):1–13, 2009. ISSN: 1742-7061. DOI: `https://doi.org/10.1016/j.actbio.2008.09.013`. URL: `https://www.sciencedirect.com/science/article/pii/S1742706108002821`.

[207] F Blaudez, S Ivanovski, S Hamlet, and C Vaquette. An overview of decellularisation techniques of native tissues and tissue engineered products for bone, ligament and tendon regeneration. *Methods*, 171:28–40, 2020. ISSN: 1046-2023. DOI: `https://doi.org/10.1016/j.ymeth.2019.08.002`. URL: `https://www.sciencedirect.com/science/article/pii/S1046202318304328`.

[208] Yong-Guang Yang and Megan Sykes. Xenotransplantation: current status and a perspective on the future. eng. *Nature reviews. Immunology*, 7(7):519–531, 2007. ISSN: 1474-1733 (Print). DOI: `10.1038/nri2099`.

[209] Christina W Cheng, Loran D Solorio, and Eben Alsberg. Decellularized tissue and cell-derived extracellular matrices as scaffolds for orthopaedic tissue engineering. eng. *Biotechnology advances*, 32(2):462–484, 2014. ISSN: 1873-1899 (Electronic). DOI: `10.1016/j.biotechadv.2013.12.012`.

[210] Arianna B Lovati, Marta Bottagisio, and Matteo Moretti. Decellularized and Engineered Tendons as Biological Substitutes: A Critical Review. eng. *Stem cells international*, 2016:7276150, 2016. ISSN: 1687-966X (Print). DOI: `10.1155/2016/7276150`.

[211] Timothy J Keane, Christine-Maria Horejs, and Molly M Stevens. Scarring vs. functional healing: Matrix-based strategies to regulate tissue repair. eng. *Advanced drug delivery reviews*, 129:407–419, 2018. ISSN: 1872-8294 (Electronic). DOI: `10.1016/j.addr.2018.02.002`.

[212] C. R. Deeken, A. K. White, S. L. Bachman, B. J. Ramshaw, D. S. Cleveland, T. S. Loy, and S. A. Grant. Method of preparing a decellularized porcine tendon using tributyl phosphate. *Journal of Biomedical Materials Research - Part B Applied Biomaterials*, 96 B(2):199–206, 2011. ISSN: 15524973. DOI: `10.1002/jbm.b.31753`.

[213] Thorsten M. Seyler, Daniel N. Bracey, Johannes F. Plate, Mark O. Lively, Sandeep Mannava, Thomas L. Smith, Justin M. Saul, Gary G. Poehling, Mark E. Van Dyke, Patrick W. Whitlock, Seyler T.M., Bracey D.N., Plate J.F., Lively M.O., Mannava S., Smith T.L., Saul J.M., Poehling G.G., Van Dyke M.E., Thorsten M. Seyler, Daniel N. Bracey, Johannes F. Plate, Mark O. Lively, Sandeep Mannava, Thomas L. Smith, Justin M. Saul, Gary G. Poehling, Mark E. Van Dyke, and Patrick W. Whitlock. The Development of a Xenograft-Derived Scaffold for Tendon and Ligament Reconstruction Using a Decellularization and Oxidation Protocol. English. *Arthroscopy - Journal of Arthroscopic and Related Surgery*, 33(2):374–386, 2017. ISSN: 0749-8063. DOI: `10.1016/j.arthro.2016.07.016`. URL: `http://www.elsevier.com/inca/publications/store/6/2/3/1/2/4/index.hthttp://ovidsp.ovid.com/ovidweb.cgi?T=JS&PAGE=reference&D=emed18&NEWS=N&AN=613488546`.

[214] Aysegul Dede Eren, Ravi Sinha, Egemen Deniz Eren, Yuan Huipin, Sultan Gulce-Iz, Henriette Valster, Lorenzo Moroni, Jasper Foolen, and Jan de Boer. Decellularized Porcine Achilles Tendon Induces Anti-inflammatory Macrophage Phenotype In Vitro and Tendon Repair In Vivo. *Journal of Immunology and Regenerative Medicine*, 8:100027, 2020. ISSN: 2468-4988. DOI: `https://doi.org/10.1016/j.regen.2020.100027`. URL: `https://www.sciencedirect.com/science/article/pii/S2468498820300019`.

[215] Gordon Blunn and Karin Hing. ACL replacement using a decellularised xenograft tendon. *Frontiers in Bioengineering and Biotechnology*, 2016. ISSN: 2296-4185. DOI: `10.3389/conf.FBIOE.2016.01.02088`.

[216] W F Mao, Y F Wu, Youlang Zhou, and J B Tang. A study of the anatomy and repair strengths of porcine flexor and extensor tendons: Are they appropriate experimental models? *The Journal of hand surgery, European volume*, 36:663–669, 2011. DOI: `10.1177/1753193411414117`.

[217] Mohamed Omar, Antonios Dratzidis, Michael Klintschar, Sebastian Kwisda, Christian Krettek, and Max Ettinger. Are porcine flexor digitorum profundus tendons suitable graft substitutes for human hamstring tendons in biomechanical in vitro-studies? *Archives of Orthopaedic and Trauma Surgery*, 136(5):681–686, 2016. ISSN: 1434-3916. DOI: `10.1007/s00402-016-2425-9`.

[218] K Miyata, K Yasuda, E Kondo, H Nakano, S Kimura, and N Hara. Biomechanical comparisons of anterior cruciate ligament: reconstruction procedures with flexor tendon graft. eng. *Journal of orthopaedic science : official journal of the Japanese Orthopaedic Association*, 5(6):585–592, 2000. ISSN: 0949-2658 (Print).

[219] Patrick W Whitlock, Thomas L Smith, Gary G Poehling, Jeffrey S Shilt, and Mark Van Dyke. A naturally derived, cytocompatible, and architecturally optimized scaffold for tendon and ligament regeneration. *Biomaterials*, 28(29):4321–4329, 2007. ISSN: 0142-9612. DOI: `https://doi.org/10.1016/j.biomaterials.2007.05.029`.

[220] Anthony Herbert, Gemma L. Jones, Eileen Ingham, and John Fisher. A biomechanical characterisation of acellular porcine super flexor tendons for use in anterior cruciate ligament replacement: Investigation into the effects of fat reduction and bioburden reduction bioprocesses. *Journal of Biomechanics*, 48(1):22–29, 2015. ISSN: 18732380. DOI: `10.1016/j.jbiomech.2014.11.013`.

[221] Anthony Herbert, Jennifer H. Edwards, Gemma L Jones, Eileen Ingham, and John Fisher. Preclinical assessment of acellular porcine super flexor tendon using an ovine model of anterior cruciate ligament repair. English. *Journal of Orthopaedic Research*. 2017 Annual Meeting of the Orthopaedic Research Society. United States. 35(Supplement 1), 2017. ISSN: 1554-527X. URL: `http://ovidsp.ovid.com/ovidweb.cgi?T=JS&PAGE=reference&D=emed18&NEWS=N&AN=616815318https://www.imbe.leeds.ac.uk/wp-content/uploads/sites/54/2018/01/Poster_289_AH_ORS2017.pdf`.

[222] Gemma L Jones, Anthony Herbert, Helen Berry, Jennifer Helen Edwards, John Fisher, and Eileen Ingham. Decellularization and Characterization of Porcine Superflexor Tendon: A Potential Anterior Cruciate Ligament Replacement. *Tissue Engineering Part A*, 23(3-4):124–134, 2017. ISSN: 1937-3341. DOI: `10.1089/ten.`

tea.2016.0114. URL: http://online.liebertpub.com/doi/10.1089/ten.tea.2016.0114.

[223] Jennifer H. Edwards, Anthony Herbert, Gemma L. Jones, Iain W. Manfield, John Fisher, and Eileen Ingham. The effects of irradiation on the biological and biomechanical properties of an acellular porcine superflexor tendon graft for cruciate ligament repair. English. *Journal of Biomedical Materials Research - Part B Applied Biomaterials*, 105(8):2477–2486, 2017. ISSN: 1552-4973. DOI: http://dx.doi.org/10.1002/jbm.b.33786. URL: http://onlinelibrary.wiley.com/journal/10.1002/(ISSN)1552-4981http://ovidsp.ovid.com/ovidweb.cgi?T=JS&PAGE=reference&D=emed18&NEWS=N&AN=612380336.

[224] Jennifer Helen Edwards, Eileen Ingham, and Anthony Herbert. Decellularisation affects the strain rate dependent and dynamic mechanical properties of a xenogeneic tendon intended for anterior cruciate ligament replacement. *Journal of the Mechanical Behavior of Biomedical Materials*, 91:18–23, 2019.

[225] Samuel Whitaker, Jennifer H. Edwards, Stephen Guy, Eileen Ingham, and Anthony Herbert. Stratifying the mechanical performance of a decellularized xenogeneic tendon graft for anterior cruciate ligament reconstruction as a function of graft diameter. English. *Bone joint research*, 8(11):518–525, 2019. ISSN: 2046-3758 (electronic). DOI: http://dx.doi.org/10.1302/2046-3758.811.BJR-2019-0065.R1. URL: http://www.ncbi.nlm.nih.gov/pubmed/31832171http://www.pubmedcentral.nih.gov/articlerender.fcgi?artid=PMC6888738https://online.boneandjoint.org.uk/doi/10.1302/2046-3758.811.BJR-2019-0065.R1http://ovidsp.ovid.com/ovidweb.cgi?T=JS&PAGE=reference&D=emexa&N.

[226] Jennifer Helen Edwards, Gemma Louise Jones, Anthony Herbert, John Fisher, and Eileen Ingham. Integration and functional performance of a decellularised porcine superflexor tendon graft in an ovine model of anterior cruciate ligament reconstruction. *Biomaterials*, 279:121204, 2021. ISSN: 0142-9612. DOI: https://doi.org/10.1016/j.biomaterials.2021.121204. URL: https://www.sciencedirect.com/science/article/pii/S0142961221005615.

[227] Tissue Regenix Ltd (TRX Orthopedics). NCT03562299. OrthoPure XT Pilot Clinical Study, United States, 2018. DOI: NCT03562299.

[228] Masafumi Itoh, Junya Itou, Shinya Imai, Ken Okazaki, and Kiyotaka Iwasaki. A survey on the usage of decellularized tissues in orthopaedic clinical trials. eng. *Bone joint research*, 12(3):179–188, 2023. ISSN: 2046-3758 (Print). DOI: 10.1302/2046-3758.123.BJR-2022-0383.R1.

[229] Neil Hunt. 8 Month Follow-upFirst in human clinical data from a novel xenograft biologic scaffold used to treat primary acl reconstruction. 24 48 Month Follow-up4. In *20th ESSKA Congress*, Paris, 2022.

[230] Rob P A Janssen and Sven U Scheffler. Intra-articular remodelling of hamstring tendon grafts after anterior cruciate ligament reconstruction. eng. *Knee surgery, sports traumatology, arthroscopy : official journal of the ESSKA*, 22(9):2102–2108, 2014. ISSN: 1433-7347 (Electronic). DOI: 10.1007/s00167-013-2634-5.

[231] Thomas W Stapleton, Joanne Ingram, Jaynath Katta, Richard Knight, Sotirios Korossis, John Fisher, and Eileen Ingham. Development and characterization of an acellular porcine medial meniscus for use in tissue engineering. eng. *Tissue engineering. Part A*, 14(4):505–518, 2008. ISSN: 1937-3341 (Print). DOI: `10.1089/tea.2007.0233`.

[232] Anthony Herbert, Christopher Brown, Paul Rooney, John Kearney, Eileen Ingham, and John Fisher. Bi-linear mechanical property determination of acellular human patellar tendon grafts for use in anterior cruciate ligament replacement. *Journal of Biomechanics*, 2016. ISSN: 18732380. DOI: `10.1016/j.jbiomech.2016.03.041`.

[233] Richard W Farndale, Christine A Sayers, and Alan J Barrett. A Direct Spectrophotometric Microassay for Sulfated Glycosaminoglycans in Cartilage Cultures. *Connective Tissue Research*, 9(4):247–248, 1982. DOI: `10.3109/03008208209160269`. URL: `https://doi.org/10.3109/03008208209160269`.

[234] D M Templeton. The basis and applicability of the dimethylmethylene blue binding assay for sulfated glycosaminoglycans. eng. *Connective tissue research*, 17(1):23–32, 1988. ISSN: 0300-8207 (Print). DOI: `10.3109/03008208808992791`.

[235] R E NEUMAN and M A LOGAN. The determination of hydroxyproline. eng. *The Journal of biological chemistry*, 184(1):299–306, 1950. ISSN: 0021-9258 (Print).

[236] Kathleen Hofman, Bronwyn Hall, Helen Cleaver, and Susan Marshall. High-throughput quantification of hydroxyproline for determination of collagen. *Analytical Biochemistry*, 417(2):289–291, 2011. ISSN: 0003-2697. DOI: `https://doi.org/10.1016/j.ab.2011.06.019`. URL: `https://www.sciencedirect.com/science/article/pii/S0003269711004039`.

[237] Derek D Cissell, Jarrett M Link, Jerry C Hu, and Kyriacos A Athanasiou. A Modified Hydroxyproline Assay Based on Hydrochloric Acid in Ehrlich's Solution Accurately Measures Tissue Collagen Content. eng. *Tissue engineering. Part C, Methods*, 23(4):243–250, 2017. ISSN: 1937-3392 (Electronic). DOI: `10.1089/ten.tec.2017.0018`.

[238] Ruud A Bank, Marianne Krikken, Bob Beekman, Reinout Stoop, Alice Maroudas, Floris P J G Lafebers, and Johan M Te Koppele. A simplified measurement of degraded collagen in tissues: Application in healthy, fibrillated and osteoarthritic cartilage. *Matrix Biology*, 16(5):233–243, 1997. ISSN: 0945-053X. DOI: `https://doi.org/10.1016/S0945-053X(97)90012-3`. URL: `https://www.sciencedirect.com/science/article/pii/S0945053X97900123`.

[239] Honey Goel, Komal Saini, Karan Razdan, Rajneet Kaur Khurana, Amal Ali Elkordy, and Kamalinder K Singh. Chapter 3 - In vitro physicochemical characterization of nanocarriers: a road to optimization. In Prashant Kesharwani and Kamalinder K Singh, editors, *Nanoparticle Therapeutics*, pages 133–179. Academic Press, 2022. ISBN: 978-0-12-820757-4. DOI: `https://doi.org/10.1016/B978-0-12-820757-4.00018-1`. URL: `https://www.sciencedirect.com/science/article/pii/B9780128207574000181`.

[240] Pooria Gill, Tahereh Tohidi Moghadam, and Bijan Ranjbar. Differential scanning calorimetry techniques: applications in biology and nanoscience. eng. *Journal of biomolecular techniques : JBT*, 21(4):167–193, 2010. ISSN: 1943-4731 (Electronic).

[241] Deepakkumar Mishra, Katie Glover, Shilpa Gade, Rahul Sonawane, and Thakur Raghu Raj Singh. 10 - Safety, biodegradability, and biocompatibility considerations of long-acting drug delivery systems. In Eneko Larrañeta, Thakur Raghu Raj Singh, and Ryan F Donnelly, editors, *Long-Acting Drug Delivery Systems*, Woodhead Publishing Series in Biomaterials, pages 289–317. Woodhead Publishing, 2022. ISBN: 978-0-12-821749-8. DOI: `https://doi.org/10.1016/B978-0-12-821749-8.00008-2`. URL: `https://www.sciencedirect.com/science/article/pii/B9780128217498000082`.

[242] A Cooper, M A Nutley, and A Wadood. Differential scanning microcalorimetry in SE Harding and BZ Chowdhry (Eds.), Protein-Ligand Interactions: hydrodynamics and calorimetry, 2000.

[243] Bruno Thorihara Tomoda, Patrícia Hissae Yassue-Cordeiro, Júlia Vaz Ernesto, Patricia Santos Lopes, Laura Oliveira Péres, Classius Ferreira da Silva, and Mariana Agostini de Moraes. Chapter 3 - Characterization of biopolymer membranes and films: Physicochemical, mechanical, barrier, and biological properties. In Mariana Agostini de Moraes, Classius Ferreira da Silva, and Rodrigo Silveira Vieira, editors, *Biopolymer Membranes and Films*, pages 67–95. Elsevier, 2020. ISBN: 978-0-12-818134-8. DOI: `https://doi.org/10.1016/B978-0-12-818134-8.00003-1`. URL: `https://www.sciencedirect.com/science/article/pii/B9780128181348000031`.

[244] W E Grizzle. Special symposium: fixation and tissue processing models. eng. *Biotechnic histochemistry : official publication of the Biological Stain Commission*, 84(5):185–193, 2009. ISSN: 1473-7760 (Electronic). DOI: `10.3109/10520290903039052`.

[245] James S Lowe and Peter G Anderson. Chapter 1 - Histology. In James S Lowe and Peter G Anderson, editors, *Stevens Lowe's Human Histology (Fourth Edition) (Fourth Edition)*, pages 1–10. Mosby, Philadelphia, fourth edi edition, 2015. ISBN: 978-0-7234-3502-0. DOI: `https://doi.org/10.1016/B978-0-7234-3502-0.00001-2`. URL: `http://www.sciencedirect.com/science/article/pii/B9780723435020000012`.

[246] Brad Chazotte. Labeling nuclear DNA using DAPI. *Cold Spring Harbor Protocols*, 2011. ISSN: 15596095. DOI: `10.1101/pdb.prot5556`.

[247] N Schmitz, S Laverty, V B Kraus, and T Aigner. Basic methods in histopathology of joint tissues. *Osteoarthritis and Cartilage*, 18:S113 –S116, 2010. ISSN: 1063-4584. DOI: `https://doi.org/10.1016/j.joca.2010.05.026`. URL: `http://www.sciencedirect.com/science/article/pii/S1063458410002402`.

[248] Alexandra N Kalof, Mark F Evans, and Kumarasen Cooper. 1 - Special Diagnostic Techniques in Surgical Pathology. In Paolo Gattuso, Vijaya B Reddy, Odile David, Daniel J Spitz, and Meryl H Haber, editors, *Differential Diagnosis in Surgical Pathology (Second Edition)*, pages 1–38. W.B. Saunders, Philadelphia, second edi edition, 2010. ISBN: 978-1-4160-4580-9. DOI: `https://doi.org/10.1016/B978-1-4160-4580-9.00001-0`. URL: `http://www.sciencedirect.com/science/article/pii/B9781416045809000010`.

[249] Raed Lattouf, Ronald Younes, Didier Lutomski, Nada Naaman, Gaston Godeau, Karim Senni, and Sylvie Changotade. Picrosirius red staining: a useful tool to appraise collagen networks in normal and pathological tissues. eng. *The journal of histochemistry and cytochemistry : official journal of the Histochemistry Society*, 62(10):751–758, 2014. ISSN: 1551-5044 (Electronic). DOI: `10.1369/0022155414545787`.

[250] François Gagné. Tissue Preparation and Subcellular Fractionation Techniques. In François Gagné, editor, *Biochemical Ecotoxicology*, pages 21–31. Academic Press, Oxford, 2014. ISBN: 978-0-12-411604-7. DOI: `https://doi.org/10.1016/B978-0-12-411604-7.00002-7`. URL: `http://www.sciencedirect.com/science/article/pii/B9780124116047000027`.

[251] D Chimich, N Shrive, C Frank, L Marchuk, and R Bray. Water content alters viscoelastic behaviour of the normal adolescent rabbit medial collateral ligament. *Journal of Biomechanics*, 25(8):831–837, 1992. ISSN: 0021-9290. DOI: `https://doi.org/10.1016/0021-9290(92)90223-N`. URL: `http://www.sciencedirect.com/science/article/pii/002192909290223N`.

[252] Tammy L Haut and Roger C Haut. The state of tissue hydration determines the strain-rate-sensitive stiffness of human patellar tendon. *Journal of Biomechanics*, 30(1):79–81, 1997. ISSN: 0021-9290. DOI: `https://doi.org/10.1016/S0021-9290(96)00108-X`. URL: `https://www.sciencedirect.com/science/article/pii/S002192909600108X`.

[253] Theresa S Atkinson, Benjamin J Ewers, and Roger C Haut. The tensile and stress relaxation responses of human patellar tendon varies with specimen cross-sectional area. *Journal of Biomechanics*, 32(9):907–914, 1999. ISSN: 0021-9290. DOI: `https://doi.org/10.1016/S0021-9290(99)00089-5`. URL: `https://www.sciencedirect.com/science/article/pii/S0021929099000895`.

[254] G M Thornton, N G Shrive, and C B Frank. Altering ligament water content affects ligament pre-stress and creep behaviour. *Journal of Orthopaedic Research*, 19(5):845–851, 2001. ISSN: 0736-0266. DOI: `https://doi.org/10.1016/S0736-0266(01)00005-5`. URL: `https://www.sciencedirect.com/science/article/pii/S0736026601000055`.

[255] Allen H Hoffman, Daniel R Robichaud, Jeffrey J Duquette, and Peter Grigg. Determining the effect of hydration upon the properties of ligaments using pseudo Gaussian stress stimuli. *Journal of Biomechanics*, 38(8):1636–1642, 2005. ISSN: 0021-9290. DOI: `https://doi.org/10.1016/j.jbiomech.2004.07.032`. URL: `https://www.sciencedirect.com/science/article/pii/S0021929004003811`.

[256] Ellen T Bloom, Andrea H Lee, and Dawn M Elliott. Tendon Multiscale Structure, Mechanics, and Damage Are Affected by Osmolarity of Bath Solution. eng. *Annals of biomedical engineering*, 49(3):1058–1068, 2021. ISSN: 1573-9686 (Electronic). DOI: `10.1007/s10439-020-02649-z`.

[257] Hazel R C Screen, Vivek H Chhaya, Steve E Greenwald, Dan L Bader, David A Lee, and Julia C Shelton. The influence of swelling and matrix degradation on the microstructural integrity of tendon. *Acta Biomaterialia*, 2(5):505–513, 2006. ISSN: 1742-7061. DOI: `https://doi.org/10.1016/j.actbio.2006.05.008`. URL: `http://www.sciencedirect.com/science/article/pii/S1742706106000638`.

[258] Colin A Grant, David J Brockwell, Sheena E Radford, and Neil H Thomson. Tuning the Elastic Modulus of Hydrated Collagen Fibrils. *Biophysical Journal*, 97(11):2985–2992, 2009. ISSN: 0006-3495. DOI: `https://doi.org/10.1016/j.bpj.2009.09.010`. URL: `https://www.sciencedirect.com/science/article/pii/S0006349509014544`.

[259] Colin A Grant, David J Brockwell, Sheena E Radford, and Neil H Thomson. Effects of hydration on the mechanical response of individual collagen fibrils. *Applied Physics Letters*, 92(23):233902, 2008. DOI: `10.1063/1.2937001`. URL: `https://doi.org/10.1063/1.2937001`.

[260] René B Svensson, Tue Hassenkam, Colin A Grant, and S Peter Magnusson. Tensile Properties of Human Collagen Fibrils and Fascicles Are Insensitive to Environmental Salts. *Biophysical Journal*, 99(12):4020–4027, 2010. ISSN: 0006-3495. DOI: `https://doi.org/10.1016/j.bpj.2010.11.018`. URL: `http://www.sciencedirect.com/science/article/pii/S0006349510014153`.

[261] Babak N Safa, Kyle D Meadows, Spencer E Szczesny, and Dawn M Elliott. Exposure to buffer solution alters tendon hydration and mechanics. eng. *Journal of biomechanics*, 61:18–25, 2017. ISSN: 1873-2380 (Electronic). DOI: `10.1016/j.jbiomech.2017.06.045`.

[262] Pasquale Strazzullo and Catherine Leclercq. Sodium. eng. *Advances in nutrition (Bethesda, Md.)*, 5(2):188–190, 2014. ISSN: 2156-5376 (Electronic). DOI: `10.3945/an.113.005215`.

[263] H Schechtman and D L Bader. In vitro fatigue of human tendons. *Journal of Biomechanics*, 30(8):829–835, 1997. ISSN: 0021-9290. DOI: `https://doi.org/10.1016/S0021-9290(97)00033-X`. URL: `http://www.sciencedirect.com/science/article/pii/S002192909700033X`.

[264] Ning-Jiun Jan, Bryn L Brazile, Danielle Hu, Garrett Grube, Jacob Wallace, Alexandra Gogola, and Ian A Sigal. Crimp around the globe; patterns of collagen crimp across the corneoscleral shell. eng. *Experimental eye research*, 172:159–170, 2018. ISSN: 1096-0007 (Electronic). DOI: `10.1016/j.exer.2018.04.003`.

[265] John H Highberger. The Isoelectric Point of Collagen. *Journal of the American Chemical Society*, 61(9):2302–2303, 1939. ISSN: 0002-7863. DOI: `10.1021/ja01878a010`. URL: `https://doi.org/10.1021/ja01878a010`.

[266] Svetlana Morozova and Murugappan Muthukumar. Electrostatic effects in collagen fibril formation. *The Journal of Chemical Physics*, 149(16):163333, 2018. DOI: `10.1063/1.5036526`. URL: `https://doi.org/10.1063/1.5036526`.

[267] Rami K Korhonen and Jukka S Jurvelin. Compressive and tensile properties of articular cartilage in axial loading are modulated differently by osmotic environment. *Medical Engineering Physics*, 32(2):155–160, 2010. ISSN: 1350-4533. DOI: `https://doi.org/10.1016/j.medengphy.2009.11.004`. URL: `https://www.sciencedirect.com/science/article/pii/S1350453309002367`.

[268] ShaoKuan Zheng and Yang Xia. Effect of phosphate electrolyte buffer on the dynamics of water in tendon and cartilage. eng. *NMR in biomedicine*, 22(2):158–164, 2009. ISSN: 0952-3480 (Print). DOI: `10.1002/nbm.1294`.

[269] Qiqing Zhang, Lingrong Liu, Haiying Zhou, Xiaoyu Wu, and K D Yao. Ph-Responsive Swelling Behavior of Collagen Complex Materials. *Artificial Cells, Blood Substitutes, and Biotechnology*, 28(3):255–262, 2000. ISSN: 1073-1199. DOI: `10.3109/10731190009119356`. URL: `https://doi.org/10.3109/10731190009119356`.

[270] Michael Meyer. Processing of collagen based biomaterials and the resulting materials properties. *BioMedical Engineering OnLine*, 18(1):24, 2019. ISSN: 1475-925X. DOI: `10.1186/s12938-019-0647-0`. URL: `https://doi.org/10.1186/s12938-019-0647-0`.

[271] R Usha and T Ramasami. Effect of pH on dimensional stability of rat tail tendon collagen fiber. *Journal of Applied Polymer Science*, 75(13):1577–1584, 2000. ISSN: 0021-8995. DOI: `https://doi.org/10.1002/(SICI)1097-4628(20000328)75:13<1577::AID-APP3>3.0.CO;2-O`. URL: `https://doi.org/10.1002/(SICI)1097-4628(20000328)75:13%3C1577::AID-APP3%3E3.0.COhttp://2-o`.

[272] Hazel L Fermor, Serena L Russell, Sophie Williams, John Fisher, and Eileen Ingham. Development and characterisation of a decellularised bovine osteochondral biomaterial for cartilage repair. *Journal of Materials Science: Materials in Medicine*, 26(5):186, 2015. ISSN: 1573-4838. DOI: `10.1007/s10856-015-5517-0`. URL: `https://doi.org/10.1007/s10856-015-5517-0`.

[273] Yu Seon Kim, Marjan Majid, Anthony J. Melchiorri, and Antonios G. Mikos. Applications of decellularized extracellular matrix in bone and cartilage tissue engineering. *Bioengineering Translational Medicine*, 4:83–95, 2019. ISSN: 2380-6761. DOI: `10.1002/btm2.10110`.

[274] Jeffrey S Cartmell and Michael G Dunn. Development of cell-seeded patellar tendon allografts for anterior cruciate ligament reconstruction. eng. *Tissue engineering*, 10(7-8):1065–1075, 2004. ISSN: 1076-3279 (Print). DOI: `10.1089/ten.2004.10.1065`.

[275] Joanne Helen Ingram, Sotirios Korossis, Graeme Howling, John Fisher, Eileen Ingham, Ingram J.H., Korossis S., Howling G., Fisher J., Joanne Helen Ingram, Sotirios Korossis, Graeme Howling, John Fisher, Eileen Ingham, Ingram J.H., Korossis S., Howling G., and Fisher J. The use of ultrasonication to aid recellularization of acellular natural tissue scaffolds for use in anterior cruciate ligament reconstruction. English. *Tissue Engineering*, 13(7):1561–1572, 2007. ISSN: 1076-3279. DOI: `http://dx.doi.org/10.1089/ten.2006.0362`. URL: `http://ovidsp.ovid.com/ovidweb.cgi?T=JS&PAGE=reference&D=emed10&NEWS=N&AN=47105763`.

[276] Thomas Tischer, Stephan Vogt, Sebastian Aryee, Erwin Steinhauser, Christopher Adamczyk, Stefan Milz, Vladimir Martinek, and Andreas B Imhoff. Tissue engineering of the anterior cruciate ligament: a new method using acellularized tendon allografts and autologous fibroblasts. eng. *Archives of orthopaedic and trauma surgery*, 127(9):735–741, 2007. ISSN: 0936-8051 (Print). DOI: `10.1007/s00402-007-0320-0`.

[277] Lijie Zhang, Jerry Hu, and Kyriacos A. Athanasiou. The role of tissue engineering in articular cartilage repair and regeneration. *Critical Reviews in Biomedical Engineering*, 37(1-2):1–57, 2009. ISSN: 0278940X. DOI: `10.1615/CritRevBiomedEng.v37.i1-2.10`.

[278] Liang Ju Ning, Yi Zhang, Xiao He Chen, Jing Cong Luo, Xiu Qun Li, Zhi Ming Yang, and Ting Wu Qin. Preparation and characterization of decellularized tendon slices for tendon tissue engineering. *Journal of Biomedical Materials Research - Part A*, 100 A(6):1448–1456, 2012. ISSN: 15493296. DOI: `10.1002/jbm.a.34083`.

[279] Daniel W. Youngstrom, Jennifer G. Barrett, Rod R. Jose, David L. Kaplan, Youngstrom D.W., Barrett J.G., Jose R.R., Daniel W. Youngstrom, Jennifer G. Barrett, Rod R. Jose, and David L. Kaplan. Functional Characterization of Detergent-Decellularized Equine Tendon Extracellular Matrix for Tissue Engineering Applications. English. *PLoS ONE*, 8(5):e64151, 2013. ISSN: 1932-6203 (electronic). DOI: `10.1371/journal.pone.0064151`. URL: `http://www.plosone.org/article/fetchObject.action?uri=info%3Adoi%2F10.1371%2Fjournal.pone.0064151&representation=PDFhttp://ovidsp.ovid.com/ovidweb.cgi?T=JS&PAGE=reference&D=emed14&NEWS=N&AN=369013308`.

[280] Janina Burk, Ina Erbe, Dagmar Berner, Johannes Kacza, Cornelia Kasper, Bastian Pfeiffer, Karsten Winter, and Walter Brehm. Freeze-thaw cycles enhance decellularization of large tendons. eng. *Tissue engineering. Part C, Methods*, 20(4):276–284, 2014. ISSN: 1937-3392 (Electronic). DOI: `10.1089/ten.TEC.2012.0760`.

[281] Shuxing Xing, Cong Liu, Bing Xu, Jianchang Chen, Dongfeng Yin, and Chunhao Zhang. Effects of various decellularization methods on histological and biomechanical properties of rabbit tendons. eng. *Experimental and therapeutic medicine*, 8(2):628–634, 2014. ISSN: 1792-0981 (Print). DOI: `10.3892/etm.2014.1742`.

[282] Eren A.D., Sinha R., Eren E.D., Huipin Y., Gulce-Iz S., Valster H., Moroni L., Foolen J., and Aysegul Dede; ORCID: http://orcid.org/0000-0001-8170-6133 A O Eren de Boer J. AO - Eren Egemen Deniz; ORCID: http://orcid.org/0000-0002-5614-6784 AO - Gulce-Iz, Sultan; ORCID: http://orcid.org/0000-0002-9275-6272 AO - Sinha, Ravi; ORCID: http://orcid.org/0000-0003-4185-5198 AO - Huipin, Yuan; ORCID: http://orcid.or. Decellularized Porcine Achilles tendon induces anti-inflammatory macrophage phenotype in Vitro and tendon repair in vivo. English. *Journal of Immunology and Regenerative Medicine*, 8:100027, 2020. ISSN: 2468-4988 (electronic). DOI: `http://dx.doi.org/10.1016/j.regen.2020.100027`. URL: `https://www.journals.elsevier.com/journal-of-immunology-and-regenerative-medicinehttp://ovidsp.ovid.com/ovidweb.cgi?T=JS&PAGE=reference&D=emexa&NEWS=N&AN=2004800512`.

[283] Samuel P Veres and J Michael Lee. Designed to Fail: A Novel Mode of Collagen Fibril Disruption and Its Relevance to Tissue Toughness. *Biophysical Journal*, 102(12):2876–2884, 2012. ISSN: 0006-3495. DOI: `https://doi.org/10.1016/j.bpj.2012.05.022`. URL: `https://www.sciencedirect.com/science/article/pii/S0006349512005759`.

[284] Frederick H Silver, Joseph W Freeman, and Gurinder P Seehra. Collagen self-assembly and the development of tendon mechanical properties. *Journal of Biomechanics*, 36(10):1529–1553, 2003. ISSN: 0021-9290. DOI: `https://doi.org/10.1016/S0021-9290(03)00135-0`. URL: `https://www.sciencedirect.com/science/article/pii/S0021929003001350`.

[285] Christopher A Miles, Thengiz V Burjanadze, and Allen J Bailey. The Kinetics of the Thermal Denaturation of Collagen in Unrestrained Rat Tail Tendon Determined by Differential Scanning Calorimetry. *Journal of Molecular Biology*, 245(4):437–446, 1995. ISSN: 0022-2836. DOI: `https://doi.org/10.1006/jmbi.1994.0035`. URL: `https://www.sciencedirect.com/science/article/pii/S0022283684700350`.

[286] Thomas L Willett, Rosalind S Labow, and J Michael Lee. Mechanical Overload Decreases the Thermal Stability of Collagen in an In Vitro Tensile Overload Tendon Model. *Journal of Orthopaedic Research*, 26(12):1605–1610, 2008. DOI: `10.1002/jor.20672`.

[287] Hanna Trębacz, Agnieszka Szczęsna, and Marta Arczewska. Thermal stability of collagen in naturally ageing and in vitro glycated rabbit tissues. *Journal of Thermal Analysis and Calorimetry*, 134(3):1903–1911, 2018. ISSN: 1588-2926. DOI: `10.1007/s10973-018-7375-8`. URL: `https://doi.org/10.1007/s10973-018-7375-8`.

[288] J Kopp, Madeleine Bonnet, and J P Renou. Effect of Collagen Crosslinking on Collagen-Water Interactions (A DSC Investigation). *Matrix*, 9(6):443–450, 1990. ISSN: 0934-8832. DOI: `https://doi.org/10.1016/S0934-8832(11)80013-2`. URL: `https://www.sciencedirect.com/science/article/pii/S0934883211800132`.

[289] Hanna Trebacz and Krzysztof Wójtowicz. Thermal stabilization of collagen molecules in bone tissue. eng. *International journal of biological macromolecules*, 37(5):257–262, 2005. ISSN: 0141-8130 (Print). DOI: `10.1016/j.ijbiomac.2005.04.007`.

[290] Christopher A Miles and Nicholas C Avery. Thermal stabilization of collagen in skin and decalcified bone. *Physical Biology*, 8(2):26002, 2011. DOI: `10.1088/1478-3975/8/2/026002`. URL: `https://dx.doi.org/10.1088/1478-3975/8/2/026002`.

[291] Michael Titford. Progress in the Development of Microscopical Techniques for Diagnostic Pathology. *Journal of Histotechnology*, 32(1):9–19, 2009. ISSN: 0147-8885. DOI: `10.1179/his.2009.32.1.9`. URL: `https://doi.org/10.1179/his.2009.32.1.9`.

[292] Hani A Alturkistani, Faris M Tashkandi, and Zuhair M Mohammedsaleh. Histological Stains: A Literature Review and Case Study. eng. *Global journal of health science*, 8(3):72–79, 2015. ISSN: 1916-9736 (Print). DOI: `10.5539/gjhs.v8n3p72`.

[293] Douglas L Rosene and Kenneth J Rhodes. [21] - Cryoprotection and Freezing Methods to Control Ice Crystal Artifact in Frozen Sections of Fixed and Unfixed Brain Tissue. In P Michael Conn, editor, *Quantitative and Qualitative Microscopy*. Volume 3, Methods in Neurosciences, pages 360–385. Academic Press, 1990. DOI: `https://doi.org/10.1016/B978-0-12-185255-9.50026-2`. URL: `https://www.sciencedirect.com/science/article/pii/B9780121852559500262`.

[294] K Tashiro and M Tsuru. [The rapid microscopical diagnosis of brain and spinal cord tumors by cryostat-cut frozen section (author's transl)]. jpn. *No shinkei geka. Neurological surgery*, 3(4):323–327, 1975. ISSN: 0301-2603 (Print).

[295] Min-Ah Koo, HaKyeong Jeong, Seung Hee Hong, Gyeung Mi Seon, Mi Hee Lee, and Jong-Chul Park. Preconditioning process for dermal tissue decellularization using electroporation with sonication. *Regenerative Biomaterials*, 9, 2021. ISSN: 2056-3418. DOI: `10.1093/rb/rbab071`. URL: `https://doi.org/10.1093/rb/rbab071`.

[296] Neil Marr, Danae E Zamboulis, Dirk Werling, Alessandro A Felder, Jayesh Dudhia, Andrew A Pitsillides, and Chavaunne T Thorpe. The tendon interfascicular basement membrane provides a vascular niche for CD146+ cell subpopulations. eng. *Frontiers in cell and developmental biology*, 10:1094124, 2022. ISSN: 2296-634X (Print). DOI: `10.3389/fcell.2022.1094124`.

[297] Paul S. Robinson, Tung Fu Huang, Elan Kazam, Renato V. Iozzo, David E. Birk, and Louis J. Soslowsky. Influence of decorin and biglycan on mechanical properties of multiple tendons in knockout mice. *Journal of Biomechanical Engineering*, 127(1):181–185, 2005. ISSN: 01480731. DOI: `10.1115/1.1835363`.

[298] Spencer P Lake, Kristin S Miller, Dawn M Elliott, and Louis J Soslowsky. Effect of fiber distribution and realignment on the nonlinear and inhomogeneous mechanical properties of human supraspinatus tendon under longitudinal tensile loading. eng. *Journal of orthopaedic research : official publication of the Orthopaedic Research Society*, 27(12):1596–1602, 2009. ISSN: 1554-527X (Electronic). DOI: `10.1002/jor.20938`.

[299] J. E. Scott and C. R. Orford. Dermatan sulphate-rich proteoglycan associates with rat tail-tendon collagen at the d band in the gap region. *Biochemical Journal*, 197:231–6, 1981. ISSN: 02646021. DOI: `10.1042/bj1970213`.

[300] P Kannus. Structure of the tendon connective tissue. eng. *Scandinavian journal of medicine science in sports*, 10(6):312–320, 2000. ISSN: 0905-7188 (Print). DOI: `10.1034/j.1600-0838.2000.010006312.x`.

[301] Hazel R.C. Screen. Hierarchical Approaches to Understanding Tendon Mechanics. *Journal of Biomechanical Science and Engineering*, 4(4):481–499, 2009. DOI: `10.1299/jbse.4.481`.

[302] Consuelo M López De Padilla, Michael J Coenen, Alejandro Tovar, Rodolfo E De la Vega, Christopher H Evans, and Sebastian A Müller. Picrosirius Red Staining: Revisiting Its Application to the Qualitative and Quantitative Assessment of Collagen Type I and Type III in Tendon. *Journal of Histochemistry & Cytochemistry*, 69(10):633–643, 2021. DOI: `10.1369/00221554211046777`. URL: `https://doi.org/10.1369/00221554211046777`.

[303] J C Danz, M Habegger, D D Bosshardt, C Katsaros, and A Stavropoulos. Virtual tissue alignment and cutting plane definition â a new method to obtain optimal longitudinal histological sections. *Journal of Anatomy*, 224(2):85–94, 2014. DOI: `https://doi.org/10.1111/joa.12140`. URL: `https://onlinelibrary.wiley.com/doi/abs/10.1111/joa.12140`.

[304] J Diamant, A Keller, E Baer, M Litt, and R G C Arridge. Collagen; Ultrastructure and Its Relation to Mechanical Properties as a Function of Ageing. *Proceedings of the Royal Society of London. Series B, Biological Sciences*, 180(1060):293–315, 1972. ISSN: 00804649. URL: `http://www.jstor.org/stable/76283`.

[305] Kristi A Hansen, Jeffrey A Weiss, and Jennifer K Barton. Recruitment of tendon crimp with applied tensile strain. eng. *Journal of biomechanical engineering*, 124(1):72–77, 2002. ISSN: 0148-0731 (Print). DOI: `10.1115/1.1427698`.

[306] Marco Franchi, Alessandra Trirè, Marilisa Quaranta, Ester Orsini, and Victoria Ottani. Collagen structure of tendon relates to function. eng. *TheScientificWorldJournal*, 7:404–420, 2007. ISSN: 1537-744X (Electronic). DOI: `10.1100/tsw.2007.92`.

[307] H R C Screen, D A Lee, D L Bader, and J C Shelton. An investigation into the effects of the hierarchical structure of tendon fascicles on micromechanical properties. *Proceedings of the Institution of Mechanical Engineers, Part H: Journal of Engineering in Medicine*, 218(2):109–119, 2004. DOI: `10.1243/095441104322984004`. URL: `https://doi.org/10.1243/095441104322984004`.

[308] C N Maganaris and J P Paul. In vivo human tendon mechanical properties. eng. *The Journal of physiology*, 521 Pt 1(Pt 1):307–313, 1999. ISSN: 0022-3751 (Print). DOI: `10.1111/j.1469-7793.1999.00307.x`.

[309] Yuping Li and Elliot P Douglas. Effects of various salts on structural polymorphism of reconstituted type I collagen fibrils. eng. *Colloids and surfaces. B, Biointerfaces*, 112:42–50, 2013. ISSN: 1873-4367 (Electronic). DOI: `10.1016/j.colsurfb.2013.07.037`.

[310] Kristin S Miller, Brianne K Connizzo, Elizabeth Feeney, Jennica J Tucker, and Louis J Soslowsky. Examining differences in local collagen fiber crimp frequency throughout mechanical testing in a developmental mouse supraspinatus tendon model. eng. *Journal of biomechanical engineering*, 134(4):41004, 2012. ISSN: 1528-8951 (Electronic). DOI: `10.1115/1.4006538`.

[311] Manuela Lopera Higuita and Leigh G Griffiths. Antigen removal process preserves function of small diameter venous valved conduits, whereas SDS-decellularization results in significant valvular insufficiency. *Acta Biomaterialia*, 107:115–128, 2020. ISSN: 1742-7061. DOI: `https://doi.org/10.1016/j.actbio.2020.03.003`. URL: `https://www.sciencedirect.com/science/article/pii/S1742706120301355`.

[312] Jun Liao, Erinn M Joyce, and Michael S Sacks. Effects of decellularization on the mechanical and structural properties of the porcine aortic valve leaflet. eng. *Biomaterials*, 29(8):1065–1074, 2008. ISSN: 0142-9612 (Print). DOI: `10.1016/j.biomaterials.2007.11.007`.

[313] Field T Blevins, Mladen Djurasovic, Evan L Flatow, and Kathryn G Vogel. Biology of the rotator cuff tendon. *Orthopedic Clinics*, 28(1):1–16, 1997. ISSN: 0030-5898. DOI: `10.1016/S0030-5898(05)70260-1`. URL: `https://doi.org/10.1016/S0030-5898(05)70260-1`.

[314] Pamela F. Lozano, Mario Scholze, Carsten Babian, Holger Scheidt, Franziska Vielmuth, Jens Waschke, Benjamin Ondruschka, and Niels Hammer. Water-content related alterations in macro and micro scale tendon biomechanics. *Scientific Reports*, 9(7887), 2019. ISSN: 20452322. DOI: `10.1038/s41598-019-44306-z`.

[315] René B Svensson, Philip Hansen, Tue Hassenkam, Bjarki T Haraldsson, Per Aagaard, Vuokko Kovanen, Michael Krogsgaard, Michael Kjaer, and S Peter Magnusson. Mechanical properties of human patellar tendon at the hierarchical levels of tendon and fibril. eng. *Journal of applied physiology (Bethesda, Md. : 1985)*, 112(3):419–426, 2012. ISSN: 1522-1601 (Electronic). DOI: `10.1152/japplphysiol.01172.2011`.

[316] Joost A J van der Rijt, Kees O van der Werf, Martin L Bennink, Pieter J Dijkstra, and Jan Feijen. Micromechanical Testing of Individual Collagen Fibrils. *Macromolecular Bioscience*, 6(9):697–702, 2006. DOI: `https://doi.org/10.1002/mabi.200600063`. URL: `https://onlinelibrary.wiley.com/doi/abs/10.1002/mabi.200600063`.

[317] D L Butler, Y Guan, M D Kay, J F Cummings, S M Feder, and M S Levy. Location-dependent variations in the material properties of the anterior cruciate ligament. eng. *Journal of biomechanics*, 25(5):511–518, 1992. ISSN: 0021-9290 (Print). DOI: `10.1016/0021-9290(92)90091-e`.

[318] Andrew Johnston and Anthony Callanan. Recent Methods for Modifying Mechanical Properties of Tissue-Engineered Scaffolds for Clinical Applications. eng. *Biomimetics (Basel, Switzerland)*, 8(2), 2023. ISSN: 2313-7673 (Electronic). DOI: `10.3390/biomimetics8020205`.

[319] Prasad Sawadkar, Paul Sibbons, Tarek Ahmed, Laurent Bozec, and Vivek Mudera. Engineering of a Functional Tendon Using Collagen As a Natural Polymer. *ACS Biomaterials Science Engineering*, 5(10):5218–5228, 2019. DOI: `10.1021/acsbiomaterials.8b01544`. URL: `https://doi.org/10.1021/acsbiomaterials.8b01544`.

[320] D L Butler, M D Kay, and D C Stouffer. Comparison of material properties in fascicle-bone units from human patellar tendon and knee ligaments. eng. *Journal of biomechanics*, 19(6):425–432, 1986. ISSN: 0021-9290 (Print). DOI: `10.1016/0021-9290(86)90019-9`.

[321] Ben Ventura, Dylan M Ashton, Elizabeth C Clarke, Nicholas Hartnell, Patrick Haubruck, Samantha A Hefferan, Christopher B Little, and Carina L Blaker. In Vitro Collagenase Degradation of Grafts Used Clinically for Anterior Cruciate Ligament Reconstruction: Human Tendon Data. *Biomedical Materials Devices*, 1(2):751–759, 2023. ISSN: 2731-4820. DOI: `10.1007/s44174-022-00046-9`. URL: `https://doi.org/10.1007/s44174-022-00046-9`.

[322] H S Gupta, J Seto, S Krauss, P Boesecke, and H R C Screen. In situ multi-level analysis of viscoelastic deformation mechanisms in tendon collagen. *Journal of Structural Biology*, 169(2):183–191, 2010. ISSN: 1047-8477. DOI: `https://doi.org/10.1016/j.jsb.2009.10.002`. URL: `http://www.sciencedirect.com/science/article/pii/S1047847709002718`.

[323] Kirsten Legerlotz, Graham P Riley, and Hazel R C Screen. GAG depletion increases the stress-relaxation response of tendon fascicles, but does not influence recovery. *Acta Biomaterialia*, 9(6):6860–6866, 2013. ISSN: 1742-7061. DOI: `https://doi.org/10.1016/j.actbio.2013.02.028`. URL: `http://www.sciencedirect.com/science/article/pii/S1742706113000925`.

[324] Dawn M Elliott, Paul S Robinson, Jonathan A Gimbel, Joseph J Sarver, Joseph A Abboud, Renato V Iozzo, and Louis J Soslowsky. Effect of altered matrix proteins on quasilinear viscoelastic properties in transgenic mouse tail tendons. eng. *Annals of biomedical engineering*, 31(5):599–605, 2003. ISSN: 0090-6964 (Print). DOI: `10.1114/1.1567282`.

[325] Gion Fessel and Jess G Snedeker. Evidence against proteoglycan mediated collagen fibril load transmission and dynamic viscoelasticity in tendon. *Matrix Biology*, 28(8):503–510, 2009. ISSN: 0945-053X. DOI: `https://doi.org/10.1016/j.matbio.2009.08.002`. URL: `https://www.sciencedirect.com/science/article/pii/S0945053X09001061`.

[326] Trevor J Lujan, Clayton J Underwood, Nathan T Jacobs, and Jeffrey A Weiss. Contribution of glycosaminoglycans to viscoelastic tensile behavior of human ligament. eng. *Journal of applied physiology (Bethesda, Md. : 1985)*, 106(2):423–431, 2009. ISSN: 8750-7587 (Print). DOI: `10.1152/japplphysiol.90748.2008`.

[327] Andrzej Mlyniec, Sylwia Dabrowska, Marcin Heljak, Wladyslaw P Weglarz, Kaja Wojcik, Martyna Ekiert-Radecka, Rafal Obuchowicz, and Wojciech Swieszkowski. The dispersion of viscoelastic properties of fascicle bundles within the tendon results from the presence of interfascicular matrix and flow of body fluids. *Materials Science and Engineering: C*, 130:112435, 2021. ISSN: 0928-4931. DOI: `https://doi.org/10.1016/j.msec.2021.112435`. URL: `https://www.sciencedirect.com/science/article/pii/S0928493121005750`.

[328] Kathryn G Vogel and Thomas J Koob. Structural Specialization in Tendons under Compression. In K W Jeon and M Friedlander, editors. Volume 115, International Review of Cytology, pages 267–293. Academic Press, 1989. DOI: `https://doi.org/10.1016/S0074-7696(08)60632-4`. URL: `https://www.sciencedirect.com/science/article/pii/S0074769608606324`.

[329] Fei Fang, Amrita S Sawhney, and Spencer P Lake. Different regions of bovine deep digital flexor tendon exhibit distinct elastic, but not viscous, mechanical properties under both compression and shear loading. *Journal of Biomechanics*, 47(12):2869–2877, 2014. ISSN: 0021-9290. DOI: `https://doi.org/10.1016/j.jbiomech.2014.07.026`. URL: `https://www.sciencedirect.com/science/article/pii/S0021929014004072`.

[330] Sean Docking, Tom Samiric, Ebonie Scase, Craig Purdam, and Jill Cook. Relationship between compressive loading and ECM changes in tendons. eng. *Muscles, ligaments and tendons journal*, 3(1):7–11, 2013. ISSN: 2240-4554 (Print). DOI: `10.11138/mltj/2013.3.1.007`.

[331] M Benjamin and J R Ralphs. Fibrocartilage in tendons and ligaments–an adaptation to compressive load. eng. *Journal of anatomy*, 193 (Pt 4(Pt 4):481–494, 1998. ISSN: 0021-8782 (Print). DOI: `10.1046/j.1469-7580.1998.19340481.x`.

[332] S T Samuel Salisbury, C Paul Buckley, and Amy B Zavatsky. Transverse Compression of Tendons. eng. *Journal of biomechanical engineering*, 138(4):41002, 2016. ISSN: 1528-8951 (Electronic). DOI: `10.1115/1.4032627`.

[333] Thomas J Koob, Paul E Clark, Daniel J Hernandez, Frederick A Thurmond, and Kathryn G Vogel. Compression loading in vitro regulates proteoglycan synthesis by tendon fibrocartilage. *Archives of Biochemistry and Biophysics*, 298(1):303–312, 1992. ISSN: 0003-9861. DOI: `https://doi.org/10.1016/0003-9861(92)90127-I`. URL: `https://www.sciencedirect.com/science/article/pii/000398619290127I`.

[334] Seok-Beom Lee, Tomotaka Nakajima, Zong-Ping Luo, Mark E Zobitz, Yi-Wen Chang, and Kai-Nan An. The bursal and articular sides of the supraspinatus tendon have a different compressive stiffness. *Clinical Biomechanics*, 15(4):241–247, 2000. ISSN: 0268-0033. DOI: `https://doi.org/10.1016/S0268-0033(99)00086-8`. URL: `https://www.sciencedirect.com/science/article/pii/S0268003399000868`.

[335] Lakiesha N Williams, Steven H Elder, J L Bouvard, and M F Horstemeyer. The anisotropic compressive mechanical properties of the rabbit patellar tendon. eng. *Biorheology*, 45(5):577–586, 2008. ISSN: 0006-355X (Print).

[336] Markus Böl, Alexander E Ehret, Kay Leichsenring, and Michael Ernst. Tissue-scale anisotropy and compressibility of tendon in semi-confined compression tests. *Journal of Biomechanics*, 48(6):1092–1098, 2015. ISSN: 0021-9290. DOI: `https://doi.org/10.1016/j.jbiomech.2015.01.024`. URL: `http://www.sciencedirect.com/science/article/pii/S0021929015000408`.

[337] Andrea Speziali, Marco Delcogliano, Matteo Tei, Giacomo Placella, Matteo Bartoli, Amerigo Menghi, and Giuliano Cerulli. Fixation techniques for the anterior cruciate ligament reconstruction: early follow-up. A systematic review of level I and II therapeutic studies. *MUSCULOSKELETAL SURGERY*, 98(3):179–187, 2014. ISSN: 2035-5114. DOI: `10.1007/s12306-014-0338-8`. URL: `https://doi.org/10.1007/s12306-014-0338-8`.

[338] A Harvey, N P Thomas, and A A Amis. Fixation of the graft in reconstruction of the anterior cruciate ligament. *The Journal of Bone and Joint Surgery. British volume*, 87-B(5):593–603, 2005. DOI: `10.1302/0301-620X.87B5.15803`. URL: `https://doi.org/10.1302/0301-620X.87B5.15803`.

[339] Giuseppe Milano, Pier Damiano Mulas, Fabio Ziranu, Stefano Piras, Andrea Manunta, and Carlo Fabbriciani. Comparison Between Different Femoral Fixation Devices for ACL Reconstruction With Doubled Hamstring Tendon Graft: A Biomechanical Analysis. *Arthroscopy: The Journal of Arthroscopic Related Surgery*, 22(6):660–668, 2006. ISSN: 0749-8063. DOI: `https://doi.org/10.1016/j.arthro.2006.04.082`. URL: `https://www.sciencedirect.com/science/article/pii/S0749806306005652`.

[340] An M Nguyen and Marc E Levenston. Comparison of osmotic swelling influences on meniscal fibrocartilage and articular cartilage tissue mechanics in compression and shear. *Journal of Orthopaedic Research*, 30(1):95–102, 2012. DOI: `https://doi.org/10.1002/jor.21493`. URL: `https://onlinelibrary.wiley.com/doi/abs/10.1002/jor.21493`.

[341] G Riley. The pathogenesis of tendinopathy. A molecular perspective. eng. *Rheumatology (Oxford, England)*, 43(2):131–142, 2004. ISSN: 1462-0324 (Print). DOI: `10.1093/rheumatology/keg448`.

[342] Charles C Banos, Amelia H Thomas, and Catherine K Kuo. Collagen fibrillogenesis in tendon development: current models and regulation of fibril assembly. eng. *Birth defects research. Part C, Embryo today : reviews*, 84(3):228–244, 2008. ISSN: 1542-9768 (Electronic). DOI: `10.1002/bdrc.20130`.

[343] Mark R Buckley, Elisabeth B Evans, Paul E Matuszewski, Yi-Ling Chen, Lauren N Satchel, Dawn M Elliott, Louis J Soslowsky, and George R Dodge. Distributions of types I, II and III collagen by region in the human supraspinatus tendon. eng. *Connective tissue research*, 54(6):374–379, 2013. ISSN: 1607-8438 (Electronic). DOI: `10.3109/03008207.2013.847096`.

[344] Nandaraj Taye, Stylianos Z Karoulias, and Dirk Hubmacher. The âotherâ 15â40%: The Role of Non-Collagenous Extracellular Matrix Proteins and Minor Collagens in Tendon. *Journal of Orthopaedic Research*, 38(1):23–35, 2020. DOI: `https://doi.org/10.1002/jor.24440`. URL: `https://onlinelibrary.wiley.com/doi/abs/10.1002/jor.24440`.

[345] S Ernst, R Langer, C L Cooney, and R Sasisekharan. Enzymatic degradation of glycosaminoglycans. eng. *Critical reviews in biochemistry and molecular biology*, 30(5):387–444, 1995. ISSN: 1040-9238 (Print). DOI: `10.3109/10409239509083490`.

[346] R V Iozzo. Matrix proteoglycans: from molecular design to cellular function. eng. *Annual review of biochemistry*, 67:609–652, 1998. ISSN: 0066-4154 (Print). DOI: `10.1146/annurev.biochem.67.1.609`.

[347] J E Scott. Structure and function in extracellular matrices depend on interactions between anionic glycosaminoglycans. eng, 2001. DOI: `10.1016/s0369-8114(01)00152-3`.

[348] René B Svensson, Tue Hassenkam, Philip Hansen, Michael Kjaer, and Stig P Magnusson. Tensile Force Transmission in Human Patellar Tendon Fascicles Is Not Mediated by Glycosaminoglycans. *Connective Tissue Research*, 52(5):415–421, 2011. DOI: `10.3109/03008207.2010.551569`. URL: `https://doi.org/10.3109/03008207.2010.551569`.

[349] S Rigozzi, R Müller, A Stemmer, and J G Snedeker. Tendon glycosaminoglycan proteoglycan sidechains promote collagen fibril slidingâAFM observations at the nanoscale. *Journal of Biomechanics*, 46(4):813–818, 2013. ISSN: 0021-9290. DOI: `https://doi.org/10.1016/j.jbiomech.2012.11.017`. URL: `https://www.sciencedirect.com/science/article/pii/S0021929012006690`.

[350] Heath B. Henninger, Clayton J. Underwood, Gerard A. Ateshian, and Jeffrey A. Weiss. Effect of sulfated glycosaminoglycan digestion on the transverse permeability of medial collateral ligament. *Journal of Biomechanics*, 43(13):2567–2573, 2010. ISSN: 00219290. DOI: `10.1016/j.jbiomech.2010.05.012`. URL: `http://dx.doi.org/10.1016/j.jbiomech.2010.05.012`.

[351] Hossein Ahmadzadeh, Brianne K Connizzo, Benjamin R Freedman, Louis J Soslowsky, and Vivek B Shenoy. Determining the contribution of glycosaminoglycans to tendon mechanical properties with a modified shear-lag model. eng. *Journal of biomechanics*, 46(14):2497–2503, 2013. ISSN: 1873-2380 (Electronic). DOI: `10.1016/j.jbiomech.2013.07.008`.

[352] Urmila Nischal, Nischal Kc, and Uday Khopkar. Techniques of skin biopsy and practical considerations. eng. *Journal of cutaneous and aesthetic surgery*, 1(2):107–111, 2008. ISSN: 0974-5157 (Electronic). DOI: `10.4103/0974-2077.44174`.

[353] Deva D Chan, Luyao Cai, Kent D Butz, Stephen B Trippel, Eric A Nauman, and Corey P Neu. In vivo articular cartilage deformation: noninvasive quantification of intratissue strain during joint contact in the human knee. eng. *Scientific reports*, 6:19220, 2016. ISSN: 2045-2322 (Electronic). DOI: `10.1038/srep19220`.

[354] Teralyn E Carter, Kevin A Taylor, Charles E Spritzer, Gangadhar M Utturkar, Dean C Taylor, Claude T 3rd Moorman, William E Garrett, Farshid Guilak, Amy L McNulty, and Louis E DeFrate. In vivo cartilage strain increases following medial meniscal tear and correlates with synovial fluid matrix metalloproteinase activity. eng. *Journal of biomechanics*, 48(8):1461–1468, 2015. ISSN: 1873-2380 (Electronic). DOI: `10.1016/j.jbiomech.2015.02.030`.

[355] Jay M Patel, Brian C Wise, Edward D Bonnevie, and Robert L Mauck. A Systematic Review and Guide to Mechanical Testing for Articular Cartilage Tissue Engineering. eng. *Tissue engineering. Part C, Methods*, 25(10):593–608, 2019. ISSN: 1937-3392 (Electronic). DOI: `10.1089/ten.TEC.2019.0116`.

[356] Grahame A Busby, M Helen Grant, Simon P Mackay, and Philip E Riches. Confined compression of collagen hydrogels. eng. *Journal of biomechanics*, 46(4):837–840, 2013. ISSN: 1873-2380 (Electronic). DOI: `10.1016/j.jbiomech.2012.11.048`.

[357] S A Maas, B J Ellis, G A Ateshian, and J A Weiss. FEBio: finite elements for biomechanics. *Journal of biomechanical Engineering*, 134:011005, 2012.

[358] Fahd Mahmood, Jon Clarke, and Philip Riches. The ionic contribution of proteoglycans to mechanical stiffness of the meniscus. eng. *Medical engineering physics*, 64:23–27, 2019. ISSN: 1873-4030 (Electronic). DOI: `10.1016/j.medengphy.2018.12.010`.

[359] M H Holmes and V C Mow. The nonlinear characteristics of soft gels and hydrated connective tissues in ultrafiltration. *Journal of Biomechanics*, 23(11):1145–1156, 1990. ISSN: 0021-9290. DOI: `https://doi.org/10.1016/0021-9290(90)90007-P`. URL: `https://www.sciencedirect.com/science/article/pii/002192909090007P`.

[360] Philip E Riches. Sensitivity analysis of permeability parameters of bovine nucleus pulposus obtained through inverse fitting of the nonlinear biphasic equation: effect of sampling strategy. *Computer Methods in Biomechanics and Biomedical Engineering*, 15(1):29–36, 2012. DOI: `10.1080/10255842.2010.544301`. URL: `https://doi.org/10.1080/10255842.2010.544301`.

[361] Y S Pek, M Spector, I V Yannas, and L J Gibson. Degradation of a collagenâchondroitin-6-sulfate matrix by collagenase and by chondroitinase. *Biomaterials*, 25(3):473–482, 2004. ISSN: 0142-9612. DOI: `https://doi.org/10.1016/S0142-9612(03)00541-6`. URL: `https://www.sciencedirect.com/science/article/pii/S0142961203005416`.

[362] Moira O'Brien. Anatomy of tendons. *Tendon Injuries: Basic Science and Clinical Medicine*:3–13, 2005. ISSN: 00960667. DOI: `10.1007/1-84628-050-8_1`.

[363] Solomon R Eisenberg and Alan J Grodzinsky. Swelling of articular cartilage and other connective tissues: Electromechanochemical forces. *Journal of Orthopaedic Research*, 3(2):148–159, 1985. DOI: `https://doi.org/10.1002/jor.1100030204`. URL: `https://onlinelibrary.wiley.com/doi/abs/10.1002/jor.1100030204`.

[364] W M Lai, J S Hou, and V C Mow. A triphasic theory for the swelling and deformation behaviors of articular cartilage. eng. *Journal of biomechanical engineering*, 113(3):245–258, 1991. ISSN: 0148-0731 (Print). DOI: `10.1115/1.2894880`.

[365] Eva G Baylon and Marc E Levenston. Osmotic Swelling Responses Are Conserved Across Cartilaginous Tissues With Varied Sulfated-Glycosaminoglycan Contents. *Journal of Orthopaedic Research*, 38(4):785–792, 2020. DOI: `https://doi.org/10.1002/jor.24521`. URL: `https://onlinelibrary.wiley.com/doi/abs/10.1002/jor.24521`.

[366] Evren U Azeloglu, Michael B Albro, Vikrum A Thimmappa, Gerard A Ateshian, and Kevin D Costa. Heterogeneous transmural proteoglycan distribution provides a mechanism for regulating residual stresses in the aorta. *American Journal of Physiology-Heart and Circulatory Physiology*, 294(3):H1197–H1205, 2008. DOI: `10.1152/ajpheart.01027.2007`. URL: `https://doi.org/10.1152/ajpheart.01027.2007`.

[367] Juan Pan, Guo-Ming Liu, Liang-Ju Ning, Yi Zhang, Jing-Cong Luo, Fu-Guo Huang, Ting-Wu Qin, Pan J., Liu G.-M., Ning L.-J., Zhang Y., Luo J.-C., and Huang F.-G. Rotator cuff repair using a decellularized tendon slices graft: an in vivo study in a rabbit model. English. *Knee surgery, sports traumatology, arthroscopy : official journal of the ESSKA*, 23(5):1524–1535, 2015. ISSN: 1433-7347 (electronic). DOI: `http://dx.doi.org/10.1007/s00167-014-2923-7`. URL: `http://ovidsp.ovid.com/ovidweb.cgi?T=JS&PAGE=reference&D=emed16&NEWS=N&AN=613067793http://ovidsp.ovid.com/ovidweb.cgi?T=JS&PAGE=reference&D=med12&NEWS=N&AN=24623185`.

[368] Necmi Dusunceli. An observation of the evolution of equilibrium stress on poly(lactic acid) and poly(lactic acid)/hydroxyapatite nanocomposites. *Proceedings of the Institution of Mechanical Engineers, Part C: Journal of Mechanical Engineering Science*, 235(6):1026–1044, 2021. DOI: `10.1177/0954406220939598`. URL: `https://doi.org/10.1177/0954406220939598`.

[369] Thomas J Koob. Effects of chondroitinase-ABC on proteoglycans and swelling properties of fibrocartilage in bovine flexor tendon. *Journal of Orthopaedic Research*, 7(2):219–227, 1989. DOI: `https://doi.org/10.1002/jor.1100070209`. URL: `https://onlinelibrary.wiley.com/doi/abs/10.1002/jor.1100070209`.

[370] Tom Samiric, Mirna Z Ilic, and Christopher J Handley. Characterisation of proteoglycans and their catabolic products in tendon and explant cultures of tendon. *Matrix Biology*, 23(2):127–140, 2004. ISSN: 0945-053X. DOI: `https://doi.org/10.1016/j.matbio.2004.03.004`. URL: `https://www.sciencedirect.com/science/article/pii/S0945053X04000332`.

[371] J E Scott. Proteoglycan-fibrillar collagen interactions. eng. *The Biochemical journal*, 252(2):313–323, 1988. ISSN: 0264-6021 (Print). DOI: `10.1042/bj2520313`.

[372] T N Wight, M G Kinsella, and E E Qwarnström. The role of proteoglycans in cell adhesion, migration and proliferation. eng. *Current opinion in cell biology*, 4(5):793–801, 1992. ISSN: 0955-0674 (Print). DOI: `10.1016/0955-0674(92)90102-i`.

[373] Deling Shi, Anran Sheng, and Lianli Chi. Glycosaminoglycan-Protein Interactions and Their Roles in Human Disease. eng. *Frontiers in molecular biosciences*, 8:639666, 2021. ISSN: 2296-889X (Print). DOI: `10.3389/fmolb.2021.639666`.

[374] Jarret Casale and Jonathan S. Crane. Biochemistry, Glycosaminoglycans, 2022. URL: `https://www.ncbi.nlm.nih.gov/books/NBK544295/#:$\sim$:text=Inconclusion%2Cglycosaminoglycans(GAGs),%2Canticoagulation%2Candwoundrepair.`.

[375] S Skrzyński, A Sionkowska, and A Marciniak. DSC Study of Collagen in Disc Disease. eng. *Journal of biophysics (Hindawi Publishing Corporation : Online)*, 2009:819635, 2009. ISSN: 1687-8019 (Electronic). DOI: `10.1155/2009/819635`.

[376] G Bruylants, J Wouters, and C Michaux. Differential scanning calorimetry in life science: thermodynamics, stability, molecular recognition and application in drug design. eng. *Current medicinal chemistry*, 12(17):2011–2020, 2005. ISSN: 0929-8673 (Print). DOI: `10.2174/0929867054546564`.

[377] Samuel P Veres, Julia M Harrison, and J Michael Lee. Mechanically overloading collagen fibrils uncoils collagen molecules, placing them in a stable, denatured state. *Matrix Biology*, 33:54–59, 2014. ISSN: 0945-053X. DOI: `https://doi.org/10.1016/j.matbio.2013.07.003`. URL: `https://www.sciencedirect.com/science/article/pii/S0945053X13000966`.

[378] L P Li, W Herzog, R K Korhonen, and J S Jurvelin. The role of viscoelasticity of collagen fibers in articular cartilage: axial tension versus compression. *Medical Engineering Physics*, 27(1):51–57, 2005. ISSN: 1350-4533. DOI: `https://doi.org/10.1016/j.medengphy.2004.08.009`. URL: `https://www.sciencedirect.com/science/article/pii/S135045330400147X`.

[379] K M Khan, J L Cook, F Bonar, P Harcourt, and M Astrom. Histopathology of common tendinopathies. Update and implications for clinical management. eng. *Sports medicine (Auckland, N.Z.)*, 27(6):393–408, 1999. ISSN: 0112-1642 (Print). DOI: `10.2165/00007256-199927060-00004`.

[380] Joseph M. Mansour. Biomechanics of Cartilage. In *Kinesiology: The Mechanics and Pathomechanics of Human Movement*, chapter 5, pages 69–83. 2nd edition, 2003.

[381] S A Baeurle, M G Kiselev, E S Makarova, and E A Nogovitsin. Effect of the counterion behavior on the frictionalâcompressive properties of chondroitin sulfate solutions. *Polymer*, 50(7):1805–1813, 2009. ISSN: 0032-3861. DOI: `https://doi.org/10.1016/j.polymer.2009.01.066`. URL: `https://www.sciencedirect.com/science/article/pii/S0032386109001153`.

[382] Dennis E Discher, Paul Janmey, and Yu-li Wang. Tissue Cells Feel and Respond to the Stiffness of Their Substrate. *Science*, 310(5751):1139–1143, 2005. DOI: `10.1126/science.1116995`. URL: `https://www.science.org/doi/abs/10.1126/science.1116995`.

[383] Robert J Pelham and Yu-li Wang. Cell locomotion and focal adhesions are regulated by substrate flexibility. *Proceedings of the National Academy of Sciences*, 94(25):13661–13665, 1997. DOI: `10.1073/pnas.94.25.13661`. URL: `https://www.pnas.org/doi/abs/10.1073/pnas.94.25.13661`.

[384] R J Pelham and Y L Wang. Cell Locomotion and Focal Adhesions Are Regulated by the Mechanical Properties of the Substrate. *The Biological Bulletin*, 194(3):348–350, 1998. DOI: `10.2307/1543109`. URL: `https://doi.org/10.2307/1543109`.

[385] A R Gannon, T Nagel, A P Bell, N C Avery, and D J Kelly. The changing role of the superficial region in determining the dynamic compressive properties of articular cartilage during postnatal development. *Osteoarthritis and Cartilage*, 23(6):975–984, 2015. ISSN: 1063-4584. DOI: `https://doi.org/10.1016/j.joca.2015.02.003`. URL: `https://www.sciencedirect.com/science/article/pii/S1063458415000448`.

[386] R Obuchowicz, M Ekiert, P Kohut, K Holak, L Ambrozinski, K A Tomaszewski, T Uhl, and A Mlyniec. Interfascicular matrix-mediated transverse deformation and sliding of discontinuous tendon subcomponents control the viscoelasticity and failure of tendons. *Journal of the Mechanical Behavior of Biomedical Materials*, 97:238–246, 2019. ISSN: 1751-6161. DOI: `https://doi.org/10.1016/j.jmbbm.2019.05.027`. URL: `https://www.sciencedirect.com/science/article/pii/S1751616119300943`.

[387] Marco Franchi, Viviana De Pasquale, Désirée Martini, Marilisa Quaranta, Maria Macciocca, Alessio Dionisi, and Vittoria Ottani. Contribution of glycosaminoglycans to the microstructural integrity of fibrillar and fiber crimps in tendons and ligaments. eng. *TheScientificWorldJournal*, 10:1932–1940, 2010. ISSN: 1537-744X (Electronic). DOI: `10.1100/tsw.2010.192`.

[388] Heath B Henninger, Steve A Maas, Clayton J Underwood, Ross T Whitaker, and Jeffrey A Weiss. Spatial distribution and orientation of dermatan sulfate in human medial collateral ligament. *Journal of Structural Biology*, 158(1):33–45, 2007. ISSN: 1047-8477. DOI: `https://doi.org/10.1016/j.jsb.2006.10.008`. URL: `https://www.sciencedirect.com/science/article/pii/S1047847706003157`.

[389] Trevor J Lujan, Clayton J Underwood, Heath B Henninger, Brent M Thompson, and Jeffrey A Weiss. Effect of dermatan sulfate glycosaminoglycans on the quasi-static material properties of the human medial collateral ligament. *Journal of Orthopaedic Research*, 25(7):894–903, 2007. DOI: `https://doi.org/10.1002/jor.20351`. URL: `https://onlinelibrary.wiley.com/doi/abs/10.1002/jor.20351`.

[390] Gion Fessel and Jess G Snedeker. Equivalent stiffness after glycosaminoglycan depletion in tendon â an ultra-structural finite element model and corresponding experiments. *Journal of Theoretical Biology*, 268(1):77–83, 2011. ISSN: 0022-5193. DOI: `https://doi.org/10.1016/j.jtbi.2010.10.007`. URL: `https://www.sciencedirect.com/science/article/pii/S0022519310005357`.

[391] N. L. Nerurkar, W. Han, R. L. Mauck, and D. M. Elliot. Selective removal of extracellular matrix components reveals homologous structure-function relationships between engineered and native fibrocartilage. In *Transactions of the 56rd Annual Meeting of the Orthopaedic Research Society*, 2010.

[392] Jess Gerrit Snedeker, S Rigozzi, and Ralph Müller. Glycosaminoglycan depleted tendon shows increased mechanical stiffness. Rethinking the tendon structure-function paradigm of proteoglycan mediated load sharing, Boston, MA, 2006.

[393] M Benjamin, E Kaiser, and S Milz. Structure-function relationships in tendons: a review. eng. *Journal of anatomy*, 212(3):211–228, 2008. ISSN: 1469-7580 (Electronic). DOI: `10.1111/j.1469-7580.2008.00864.x`.

[394] Jianying Zhang, Feng Li, Kelly M Williamson, Susheng Tan, Devon Scott, Kentaro Onishi, MaCalus V Hogan, and James H-C Wang. Characterization of the structure, vascularity, and stem/progenitor cell populations in porcine Achilles tendon (PAT). eng. *Cell and tissue research*, 384(2):367–387, 2021. ISSN: 1432-0878 (Electronic). DOI: `10.1007/s00441-020-03379-3`.

[395] Danae E Zamboulis, Chavaunne T Thorpe, Yalda Ashraf Kharaz, Helen L Birch, Hazel R C Screen, and Peter D Clegg. Postnatal mechanical loading drives adaptation of tissues primarily through modulation of the non-collagenous matrix. *eLife*, 9:e58075, 2020. Subburaman Mohan, Clifford J Rosen, and Subburaman Mohan, editors. ISSN: 2050-084X. DOI: `10.7554/eLife.58075`. URL: `https://doi.org/10.7554/eLife.58075`.

[396] Chavaunne T Thorpe, Marta S C Godinho, Graham P Riley, Helen L Birch, Peter D Clegg, and Hazel R C Screen. The interfascicular matrix enables fascicle sliding and recovery in tendon, and behaves more elastically in energy storing tendons. *Journal of the Mechanical Behavior of Biomedical Materials*, 52:85–94, 2015. ISSN: 1751-6161. DOI: `https://doi.org/10.1016/j.jmbbm.2015.04.009`. URL: `https://www.sciencedirect.com/science/article/pii/S1751616115001290`.

[397] Konstantinos Evangelou and Vassilis G Gorgoulis. *Sudan Black B, The Specific Histochemical Stain for Lipofuscin: A Novel Method to Detect Senescent Cells.* In *Oncogene-Induced Senescence: Methods and Protocols.* Mikhail A Nikiforov, editor. Springer New York, New York, NY, 2017, pages 111–119. ISBN: 978-1-4939-6670-7. DOI: `10.1007/978-1-4939-6670-7_10`. URL: `https://doi.org/10.1007/978-1-4939-6670-7_10`.

[398] G Binnig, C F Quate, and Ch. Gerber. Atomic Force Microscope. *Phys. Rev. Lett.*, 56(9):930–933, 1986. DOI: `10.1103/PhysRevLett.56.930`. URL: `https://link.aps.org/doi/10.1103/PhysRevLett.56.930`.

[399] Marinella Farré and Damià Barceló. Chapter 1 - Introduction to the Analysis and Risk of Nanomaterials in Environmental and Food Samples. In Marinella Farré and Damià Barceló, editors, *Analysis and Risk of Nanomaterials in Environmental and Food Samples.* Volume 59, Comprehensive Analytical Chemistry, pages 1–32. Elsevier, 2012. DOI: `https://doi.org/10.1016/B978-0-444-56328-6.00001-3`. URL: `https://www.sciencedirect.com/science/article/pii/B9780444563286000013`.

[400] Suprakas Sinha Ray. 4 - Techniques for characterizing the structure and properties of polymer nanocomposites. In Suprakas Sinha Ray, editor, *Environmentally Friendly Polymer Nanocomposites*, Woodhead Publishing Series in Composites Science and Engineering, pages 74–88. Woodhead Publishing, 2013. ISBN: 978-0-85709-777-4. DOI: `https://doi.org/10.1533/9780857097828.1.74`. URL: `https://www.sciencedirect.com/science/article/pii/B9780857097774500048`.

[401] Paul J D Whiteside, Jeffrey A Chininis, and Heather K Hunt. Techniques and Challenges for Characterizing Metal Thin Films with Applications in Photonics. *Coatings*, 6(3), 2016. ISSN: 2079-6412. DOI: `10.3390/coatings6030035`. URL: `https://www.mdpi.com/2079-6412/6/3/35`.

[402] B V Derjaguin, V M Muller, and Yu.P Toporov. Effect of contact deformations on the adhesion of particles. *Journal of Colloid and Interface Science*, 53(2):314–326, 1975. ISSN: 0021-9797. DOI: `https://doi.org/10.1016/0021-9797(75)90018-1`. URL: `https://www.sciencedirect.com/science/article/pii/0021979775900181`.

[403] P J Miller. An elastin stain. eng. *Medical laboratory technology*, 28(2):148–149, 1971. ISSN: 0022-2607 (Print).

[404] Marlene D Castro. The Application of Miller's Elastic Stain to Glycol Methacrylate Tissue Sections. *Stain Technology*, 64(5):233–238, 1989. ISSN: 0038-9153. DOI: `10.3109/10520298909107007`. URL: `https://doi.org/10.3109/10520298909107007`.

[405] Anil Kumar Bajpai, Rinkesh Bhatt, and Ravi Katare. Atomic force microscopy enabled roughness analysis of nanostructured poly (diaminonaphthalene) doped poly (vinyl alcohol) conducting polymer thin films. *Micron*, 90:12–17, 2016. ISSN: 0968-4328. DOI: `https://doi.org/10.1016/j.micron.2016.07.012`. URL: `https://www.sciencedirect.com/science/article/pii/S0968432816301512`.

[406] O J Ali, E J Comerford, P D Clegg, and E G Canty-Laird. Variations during ageing in the three-dimensional anatomical arrangement of fascicles within the equine superficial digital flexor tendon. eng. *European cells materials*, 35:87–102, 2018. ISSN: 1473-2262 (Electronic). DOI: `10.22203/eCM.v035a07`.

[407] Chavaunne T Thorpe, Graham P Riley, Helen L Birch, Peter D Clegg, and Hazel R C Screen. Fascicles from energy-storing tendons show an age-specific response to cyclic fatigue loading. eng. *Journal of the Royal Society, Interface*, 11(92):20131058, 2014. ISSN: 1742-5662 (Electronic). DOI: `10.1098/rsif.2013.1058`.

[408] Benedicto de Campos Vidal. Image analysis of tendon helical superstructure using interference and polarized light microscopy. eng. *Micron (Oxford, England : 1993)*, 34(8):423–432, 2003. ISSN: 0968-4328 (Print). DOI: `10.1016/S0968-4328(03)00039-8`.

[409] Shawn P Reese and Jeffrey A Weiss. Tendon fascicles exhibit a linear correlation between Poisson's ratio and force during uniaxial stress relaxation. eng. *Journal of biomechanical engineering*, 135(3):34501, 2013. ISSN: 1528-8951 (Electronic). DOI: `10.1115/1.4023134`.

[410] Paweł Szaro, Grzegorz Witkowski, Robert Smigielski, Paweł Krajewski, and Bogdan Ciszek. Fascicles of the adult human Achilles tendon - an anatomical study. eng. *Annals of anatomy = Anatomischer Anzeiger : official organ of the Anatomische Gesellschaft*, 191(6):586–593, 2009. ISSN: 1618-0402 (Electronic). DOI: `10.1016/j.aanat.2009.07.006`.

[411] S Rigozzi, R Müller, and J G Snedeker. Local strain measurement reveals a varied regional dependence of tensile tendon mechanics on glycosaminoglycan content. *Journal of Biomechanics*, 42(10):1547–1552, 2009. ISSN: 0021-9290. DOI: `https://doi.org/10.1016/j.jbiomech.2009.03.031`. URL: `https://www.sciencedirect.com/science/article/pii/S0021929009001584`.

[412] Jacqueline Solis-Cordova, Jennifer H Edwards, Hazel L Fermor, Philip Riches, Claire L Brockett, and Anthony Herbert. Characterisation of native and decellularised porcine tendon under tension and compression: A closer look at glycosaminoglycan contribution to tendon mechanics. eng. *Journal of the mechanical behavior of biomedical materials*, 139:105671, 2023. ISSN: 1878-0180 (Electronic). DOI: `10.1016/j.jmbbm.2023.105671`.

[413] Dharmesh Patel, Danae E Zamboulis, Ewa M Spiesz, Helen L Birch, Peter D Clegg, Chavaunne T Thorpe, and Hazel R C Screen. Structure-function specialisation of the interfascicular matrix in the human achilles tendon. *Acta Biomaterialia*, 131:381–390, 2021. ISSN: 1742-7061. DOI: `https://doi.org/10.1016/j.actbio.2021.07.019`. URL: `https://www.sciencedirect.com/science/article/pii/S1742706121004505`.

[414] Chavaunne T Thorpe, Kabelan J Karunaseelan, Jade Ng Chieng Hin, Graham P Riley, Helen L Birch, Peter D Clegg, and Hazel R C Screen. Distribution of proteins within different compartments of tendon varies according to tendon type. eng. *Journal of anatomy*, 229(3):450–458, 2016. ISSN: 1469-7580 (Electronic). DOI: `10.1111/joa.12485`.

[415] Chavaunne T Thorpe, Graham P Riley, Helen L Birch, Peter D Clegg, and Hazel R C Screen. Fascicles and the interfascicular matrix show adaptation for fatigue resistance in energy storing tendons. *Acta Biomaterialia*, 42:308–315, 2016. ISSN: 1742-7061. DOI: `https://doi.org/10.1016/j.actbio.2016.06.012`. URL: `https://www.sciencedirect.com/science/article/pii/S1742706116302896`.

[416] J H Shepherd, S Ghose, S J Kew, A Moavenian, S M Best, and R E Cameron. Effect of fiber crosslinking on collagen-fiber reinforced collagen-chondroitin-6-sulfate materials for regenerating load-bearing soft tissues. *JOURNAL OF BIOMEDICAL MATERIALS RESEARCH PART A*, 101(1):176–184, 2013. ISSN: 1549-3296. DOI: `10.1002/jbm.a.34317`.

[417] Anthony J Hayes, Brooke L Farrugia, Ifechukwude J Biose, Gregory J Bix, and James Melrose. Perlecan, A Multi-Functional, Cell-Instructive, Matrix-Stabilizing Proteoglycan With Roles in Tissue Development Has Relevance to Connective Tissue Repair and Regeneration. eng. *Frontiers in cell and developmental biology*, 10:856261, 2022. ISSN: 2296-634X (Print). DOI: `10.3389/fcell.2022.856261`.

[418] M Benjamin and J R Ralphs. Biology of Fibrocartilage Cells. In volume 233, International Review of Cytology, pages 1–45. Academic Press, 2004. DOI: `https://doi.org/10.1016/S0074-7696(04)33001-9`. URL: `http://www.sciencedirect.com/science/article/pii/S0074769604330019`.

[419] B Alberts, A Johnson, and J Lewis. The Lipid Bilayer, 2002. URL: `https://www.ncbi.nlm.nih.gov/books/NBK26871/`.

[420] Eleonora Muro, G Ekin Atilla-Gokcumen, and Ulrike S Eggert. Lipids in cell biology: how can we understand them better? eng. *Molecular biology of the cell*, 25(12):1819–1823, 2014. ISSN: 1939-4586 (Electronic). DOI: `10.1091/mbc.E13-09-0516`.

[421] Chavaunne T Thorpe, Graham P Riley, Helen L Birch, Peter D Clegg, and Hazel R C Screen. Fascicles and the interfascicular matrix show decreased fatigue life with ageing in energy storing tendons. *Acta Biomaterialia*, 56:58–64, 2017. ISSN: 1742-7061. DOI: `https://doi.org/10.1016/j.actbio.2017.03.024`. URL: `https://www.sciencedirect.com/science/article/pii/S174270611730185X`.

[422] Kirsten Legerlotz, Graham P Riley, and Hazel R C Screen. Specimen dimensions influence the measurement of material properties in tendon fascicles. *Journal of Biomechanics*, 43(12):2274–2280, 2010. ISSN: 0021-9290. DOI: `https://doi.org/10.1016/j.jbiomech.2010.04.040`. URL: `https://www.sciencedirect.com/science/article/pii/S0021929010002678`.

[423] A Galeski J. Kastelic and E Baer. The Multicomposite Structure of Tendon. *Connective Tissue Research*, 6(1):11–23, 1978. DOI: `10.3109/03008207809152283`. URL: `https://doi.org/10.3109/03008207809152283`.

[424] Sylwia Dabrowska, Krzysztof Grabowski, and Andrzej Mlyniec. Rehydration of the Tendon Fascicle Bundles Using Simulated Body Fluid Ensures Stable Mechanical Properties of the Samples. eng. *Materials (Basel, Switzerland)*, 15(9), 2022. ISSN: 1996-1944 (Print). DOI: `10.3390/ma15093033`.

[425] R Strocchi, L Leonardi, S Guizzardi, M Marchini, and A Ruggeri. Ultrastructural aspects of rat tail tendon sheaths. eng. *Journal of anatomy*, 140 (Pt 1(Pt 1):57–67, 1985. ISSN: 0021-8782 (Print).

[426] Laurent Bozec, Gert van der Heijden, and Michael Horton. Collagen Fibrils: Nanoscale Ropes. *Biophysical Journal*, 92(1):70–75, 2007. ISSN: 0006-3495. DOI: `10.1529/biophysj.106.085704`. URL: `https://doi.org/10.1529/biophysj.106.085704`.

[427] Iris Ribitsch, Sinan Gueltekin, Marlies Franziska Keith, Kristina Minichmair, Christian Peham, Florien Jenner, and Monika Egerbacher. Age-related changes of tendon fibril micro-morphology and gene expression. eng. *Journal of anatomy*, 236(4):688–700, 2020. ISSN: 1469-7580 (Electronic). DOI: `10.1111/joa.13125`.

[428] Arjen B. Blom and Wim B. van den Berg. The Synovium and Its Role in Osteoarthritis. In *Bone and Osteoarthritis*. Volume 1, number 10, pages 65–79. 2007. DOI: `10.1007/978-1-84628-701-5_4`.

[429] A J Hodge and J A Petruska. Recent studies with the electron microscope on ordered aggregates of the tropocollagen macromolecule, 1963. URL: `https://eurekamag.com/research/025/350/025350991.php`.

[430] Andreas Stylianou. Assessing Collagen D-Band Periodicity with Atomic Force Microscopy. eng. *Materials (Basel, Switzerland)*, 15(4), 2022. ISSN: 1996-1944 (Print). DOI: `10.3390/ma15041608`.

[431] Blake Erickson, Ming Fang, Joseph M Wallace, Bradford G Orr, Clifford M Les, and Mark M Banaszak Holl. Nanoscale structure of type I collagen fibrils: quantitative measurement of D-spacing. eng. *Biotechnology journal*, 8(1):117–126, 2013. ISSN: 1860-7314 (Electronic). DOI: `10.1002/biot.201200174`.

[432] Anne E Hafner, Noemi G Gyori, Ciaran A Bench, Luke K Davis, and AnÄela Šarić. Modeling Fibrillogenesis of Collagen-Mimetic Molecules. eng. *Biophysical journal*, 119(9):1791–1799, 2020. ISSN: 1542-0086 (Electronic). DOI: `10.1016/j.bpj.2020.09.013`.

[433] Kate Poole, Khaled Khairy, Jens Friedrichs, Clemens Franz, David A Cisneros, Jonathon Howard, and Daniel Mueller. Molecular-scale topographic cues induce the orientation and directional movement of fibroblasts on two-dimensional collagen surfaces. eng. *Journal of molecular biology*, 349(2):380–386, 2005. ISSN: 0022-2836 (Print). DOI: `10.1016/j.jmb.2005.03.064`.

[434] Alisher Maksumov, Ruxandra Vidu, Ahmet Palazoglu, and Pieter Stroeve. Enhanced feature analysis using wavelets for scanning probe microscopy images of surfaces. *Journal of Colloid and Interface Science*, 272(2):365–377, 2004. ISSN: 0021-9797. DOI: `https://doi.org/10.1016/j.jcis.2003.09.047`. URL: `https://www.sciencedirect.com/science/article/pii/S0021979703009470`.

[435] Kateryna Bazaka, Mohan V Jacob, Vi Khanh Truong, Russell J Crawford, and Elena P Ivanova. The Effect of Polyterpenol Thin Film Surfaces on Bacterial Viability and Adhesion. *Polymers*, 3(1):388–404, 2011. ISSN: 2073-4360. DOI: `10.3390/polym3010388`. URL: `https://www.mdpi.com/2073-4360/3/1/388`.

[436] Recep Avci, Mary Schweitzer, Robert D Boyd, Jennifer Wittmeyer, Andrew Steele, Jan Toporski, Iwona Beech, Fernando Teran Arce, Brenda Spangler, Kelly M Cole, and David S McKay. Comparison of AntibodyâAntigen Interactions on Collagen Measured by Conventional Immunological Techniques and Atomic Force Microscopy. *Langmuir*, 20(25):11053–11063, 2004. ISSN: 0743-7463. DOI: `10.1021/la036376i`. URL: `https://doi.org/10.1021/la036376i`.

[437] Arika D Kemp, Chad C Harding, Wayne A Cabral, Joan C Marini, and Joseph M Wallace. Effects of tissue hydration on nanoscale structural morphology and mechanics of individual Type I collagen fibrils in the Brtl mouse model of Osteogenesis Imperfecta. *Journal of Structural Biology*, 180(3):428–438, 2012. ISSN: 1047-8477. DOI: `https://doi.org/10.1016/j.jsb.2012.09.012`. URL: `https://www.sciencedirect.com/science/article/pii/S1047847712002687`.

[438] Nancy W Troiano, Wendy A Ciovacco, and Melissa A Kacena. The Effects of Fixation and Dehydration on the Histological Quality of Undecalcified Murine Bone Specimens Embedded in Methylmethacrylate. eng. *Journal of histotechnology*, 32(1):27–31, 2009. ISSN: 0147-8885 (Print). DOI: `10.1179/his.2009.32.1.27`.

[439] Melissa L Lerch, Daniel R Bauer, Abbey Theiss, David Chafin, Michael Otter, and Geoffrey S Baird. Monitoring Dehydration and Clearing in Tissue Processing for High-Quality Clinical Pathology. eng. *Biopreservation and biobanking*, 17(4):303–311, 2019. ISSN: 1947-5543 (Electronic). DOI: `10.1089/bio.2018.0122`.

[440] Chavaunne T Thorpe, Mandy J Peffers, Deborah Simpson, Elizabeth Halliwell, Hazel R C Screen, and Peter D Clegg. Anatomical heterogeneity of tendon: Fascicular and interfascicular tendon compartments have distinct proteomic composition. *Scientific Reports*, 6(1):20455, 2016. ISSN: 2045-2322. DOI: `10.1038/srep20455`. URL: `https://doi.org/10.1038/srep20455`.

[441] Susumu Yamamoto, Fumio Nakamura, Jiro Hitomi, Masatsugu Shigeno, Shoichi Sawaguchi, Haruki Abe, and Tatsuo Ushiki. Atomic force microscopy of intact and digested collagen molecules. *Journal of Electron Microscopy*, 49(3):423–427, 2000. ISSN: 0022-0744. DOI: `10.1093/oxfordjournals.jmicro.a023824`. URL: `https://doi.org/10.1093/oxfordjournals.jmicro.a023824`.

[442] Joanna Witos, Julien Saint-Guirons, Kristoffer Meinander, Lucia D'Ulivo, and Marja-Liisa Riekkola. Collagen I and III and their decorin modified surfaces studied by atomic force microscopy and the elucidation of their affinity toward positive apolipoprotein B-100 residue by quartz crystal microbalance. *Analyst*, 136(18):3777–3782, 2011. DOI: `10.1039/C1AN15156H`. URL: `http://dx.doi.org/10.1039/C1AN15156H`.

[443] C H Chen, D O Clegg, and H G Hansma. Structures and dynamic motion of laminin-1 as observed by atomic force microscopy. eng. *Biochemistry*, 37(22):8262–8267, 1998. ISSN: 0006-2960 (Print). DOI: `10.1021/bi973097j`.

[444] C H Chen and H G Hansma. Basement membrane macromolecules: insights from atomic force microscopy. eng. *Journal of structural biology*, 131(1):44–55, 2000. ISSN: 1047-8477 (Print). DOI: `10.1006/jsbi.2000.4252`.

[445] Michael V Rosario and Thomas J Roberts. Loading Rate Has Little Influence on Tendon Fascicle Mechanics. *Frontiers in Physiology*, 11, 2020. ISSN: 1664-042X. DOI: `10.3389/fphys.2020.00255`. URL: `https://www.frontiersin.org/articles/10.3389/fphys.2020.00255`.

[446] Samuel J Baldwin, Andrew S Quigley, Charlotte Clegg, and Laurent Kreplak. Nanomechanical mapping of hydrated rat tail tendon collagen I fibrils. eng. *Biophysical journal*, 107(8):1794–1801, 2014. ISSN: 1542-0086 (Electronic). DOI: `10.1016/j.bpj.2014.09.003`.

[447] Marta S Godinho, Chavaunne T Thorpe, Steve E Greenwald, and Hazel R C Screen. Elastase treatment of tendon specifically impacts the mechanical properties of the interfascicular matrix. eng. *Acta biomaterialia*, 123:187–196, 2021. ISSN: 1878-7568 (Electronic). DOI: `10.1016/j.actbio.2021.01.030`.

[448] Shinya Kasamatsu, Akira Hachiya, Tsutomu Fujimura, Penkanok Sriwiriyanont, Keiichi Haketa, Marty O Visscher, William J Kitzmiller, Alexander Bello, Takashi Kitahara, Gary P Kobinger, and Yoshinori Takema. Essential role of microfibrillar-associated protein 4 in human cutaneous homeostasis and in its photoprotection. *Scientific Reports*, 1(1):164, 2011. ISSN: 2045-2322. DOI: `10.1038/srep00164`. URL: `https://doi.org/10.1038/srep00164`.

[449] Tyler M Grant, Mark S Thompson, Jill Urban, and Jing Yu. Elastic fibres are broadly distributed in tendon and highly localized around tenocytes. *Journal of Anatomy*, 222(6):573–579, 2013. DOI: `https://doi.org/10.1111/joa.12048`. URL: `https://onlinelibrary.wiley.com/doi/abs/10.1111/joa.12048`.

[450] Anna Svärd, Malin Hammerman, and Pernilla Eliasson. Elastin levels are higher in healing tendons than in intact tendons and influence tissue compliance. *The FASEB Journal*, 34(10):13409–13418, 2020. DOI: `https://doi.org/10.1096/fj.202001255R`. URL: `https://faseb.onlinelibrary.wiley.com/doi/abs/10.1096/fj.202001255R`.

[451] Jeremy D Eekhoff, James A Abraham, Hayden R Schott, Lorenzo F Solon, Gabriella E Ulloa, Jennifer A Zellers, Paul C Cannon, and Spencer P Lake. Fascicular elastin within tendon contributes to the magnitude and modulus gradient of the elastic stress response across tendon type and species. *Acta Biomaterialia*, 163:91–105, 2023. ISSN: 1742-7061. DOI: `https://doi.org/10.1016/j.actbio.2022.03.025`. URL: `https://www.sciencedirect.com/science/article/pii/S1742706122001568`.

[452] Danae E Zamboulis, Neil Marr, Luca Lenzi, Helen L Birch, Hazel R C Screen, Peter D Clegg, and Chavaunne T Thorpe. The interfascicular matrix of energy storing tendons houses heterogenous cell populations disproportionately affected by ageing. *bioRxiv*, 2023. DOI: `10.1101/2023.01.04.522701`. URL: `https://www.biorxiv.org/content/early/2023/02/01/2023.01.04.522701`.

[453] Nick Merna, Claire Robertson, Anh La, and Steven C George. Optical imaging predicts mechanical properties during decellularization of cardiac tissue. eng. *Tissue engineering. Part C, Methods*, 19(10):802–809, 2013. ISSN: 1937-3392 (Electronic). DOI: `10.1089/ten.TEC.2012.0720`.

[454] Po-Feng Lee, Eric Chau, Rafael Cabello, Alvin T Yeh, Luiz C Sampaio, Andrea S Gobin, and Doris A Taylor. Inverted orientation improves decellularization of whole porcine hearts. eng. *Acta biomaterialia*, 49:181–191, 2017. ISSN: 1878-7568 (Electronic). DOI: `10.1016/j.actbio.2016.11.047`.

[455] Ryan A Behmer Hansen, Xinming Wang, Gitanjali Kaw, Valinteshley Pierre, and Samuel E Senyo. Accounting for Material Changes in Decellularized Tissue with Underutilized Methodologies. eng. *BioMed research international*, 2021:6696295, 2021. ISSN: 2314-6141 (Electronic). DOI: `10.1155/2021/6696295`.

[456] Tomohiro Obata, Tomoshi Tsuchiya, Sadanori Akita, Takayoshi Kawahara, Keitaro Matsumoto, Takuro Miyazaki, Hiroshi Masumoto, Eiji Kobayashi, Laura E Niklason, and Takeshi Nagayasu. Utilization of Natural Detergent Potassium Laurate for Decellularization in Lung Bioengineering. eng. *Tissue engineering. Part C, Methods*, 25(8):459–471, 2019. ISSN: 1937-3392 (Electronic). DOI: `10.1089/ten.TEC.2019.0016`.

[457] John D O'Neill, Rachel Anfang, Annabelle Anandappa, Joseph Costa, Jeffrey Javidfar, Holly M Wobma, Gopal Singh, Donald O Freytes, Matthew D Bacchetta, Joshua R Sonett, and Gordana Vunjak-Novakovic. Decellularization of Human and Porcine Lung Tissues for Pulmonary Tissue Engineering. *The Annals of Thoracic Surgery*, 96(3):1046–1056, 2013. ISSN: 0003-4975. DOI: `https://doi.org/10.1016/j.athoracsur.2013.04.022`. URL: `https://www.sciencedirect.com/science/article/pii/S000349751300828X`.

[458] Jian Zhang, Zhi Qian Hu, Neill J Turner, Shi Feng Teng, Wen Yue Cheng, Hai Yang Zhou, Li Zhang, Hong Wei Hu, Qiang Wang, and Stephen F Badylak. Perfusion-decellularized skeletal muscle as a three-dimensional scaffold with a vascular network template. eng. *Biomaterials*, 89:114–126, 2016. ISSN: 1878-5905 (Electronic). DOI: `10.1016/j.biomaterials.2016.02.040`.

[459] J M R Tilley, A J Carr, and J T Czernuszka. Atomic Force Microscopy of bulk tendon samples: Affect of location and fixation on tissue ultrastructure. *Micron*, 42(5):531–535, 2011. ISSN: 0968-4328. DOI: `https://doi.org/10.1016/j.micron.2011.01.001`. URL: `https://www.sciencedirect.com/science/article/pii/S0968432811000023`.

[460] Itai Gans, Julia S Retzky, Lynne C Jones, and Miho J Tanaka. Epidemiology of Recurrent Anterior Cruciate Ligament Injuries in National Collegiate Athletic Association Sports: The Injury Surveillance Program, 2004-2014. eng. *Orthopaedic journal of sports medicine*, 6(6):2325967118777823, 2018. ISSN: 2325-9671 (Print). DOI: `10.1177/2325967118777823`.

[461] Jennifer H. Edwards, Anthony Herbert, H L Fermor, J. N Kearney, Paul Rooney, John Fisher, and Eileen Ingham. Regenerative capacity and functional performance of an acellular human bone-patellar tendon-bone graft in an ovine model of anterior cruciate ligament repair. *J. Orthop. Res.*, 35(S1), 2017. ISSN: 1554-527X. URL: `https://www.embase.com/search/results?subaction=viewrecord&id=L616814490&from=exportU2-L616814490`.

[462] Emily McDermott, Mikalyn T DeFoor, Olivia K Blaber, Zachary S Aman, Nicholas N DePhillipo, and Travis J Dekker. Biomechanical comparison of anterior cruciate ligament reconstruction fixation methods and implications on clinical outcomes. *Annals of Joint; Vol 8 (April 30, 2023): Annals of Joint*, 2023. URL: `https://aoj.amegroups.org/article/view/7980`.

[463] Sarah M Jenkins, Alvarho Guzman, Brandon B Gardner, Stewart A Bryant, Shane Rayos Del Sol, Patrick McGahan, and James Chen. Rehabilitation After Anterior Cruciate Ligament Injury: Review of Current Literature and Recommendations. eng. *Current reviews in musculoskeletal medicine*, 15(3):170–179, 2022. ISSN: 1935-973X (Print). DOI: `10.1007/s12178-022-09752-9`.

[464] Douglas Adams, David S Logerstedt, Airelle Hunter-Giordano, Michael J Axe, and Lynn Snyder-Mackler. Current concepts for anterior cruciate ligament reconstruction: a criterion-based rehabilitation progression. eng. *The Journal of orthopaedic and sports physical therapy*, 42(7):601–614, 2012. ISSN: 1938-1344 (Electronic). DOI: `10.2519/jospt.2012.3871`.

[465] Jens Bojsen and S Peter Magnusson. Mechanical properties, physiological behavior, and function of aponeurosis and tendon. *Journal of Applied Physiology*, 126(6):1800–1807, 2019. ISSN: 8750-7587. DOI: `10.1152/japplphysiol.00671.2018`. URL: `https://doi.org/10.1152/japplphysiol.00671.2018`.

[466] Sara Steinmann, Christian G Pfeifer, Christoph Brochhausen, and Denitsa Docheva. Spectrum of Tendon Pathologies: Triggers, Trails and End-State. eng. *International journal of molecular sciences*, 21(3), 2020. ISSN: 1422-0067 (Electronic). DOI: `10.3390/ijms21030844`.

[467] Serghei Cebotari, Igor Tudorache, Thomas Jaekel, Andres Hilfiker, Suzanne Dorfman, Waldemar Ternes, Axel Haverich, and Artur Lichtenberg. Detergent decellularization of heart valves for tissue engineering: toxicological effects of residual detergents on human endothelial cells. eng. *Artificial organs*, 34(3):206–210, 2010. ISSN: 1525-1594 (Electronic). DOI: `10.1111/j.1525-1594.2009.00796.x`.

[468] Morteza Alizadeh, Leila Rezakhani, Mostafa Soleimannejad, Esmaeel Sharifi, Maryam Anjomshoa, and Akram Alizadeh. Evaluation of vacuum washing in the removal of SDS from decellularized bovine pericardium: method and device description. eng. *Heliyon*, 5(8):e02253, 2019. ISSN: 2405-8440 (Print). DOI: `10.1016/j.heliyon.2019.e02253`.

[469] Maria Stefania Massaro, Richard Pálek, Jáchym Rosendorf, Lenka Červenková, Václav Liška, and Vladimíra Moulisová. Decellularized xenogeneic scaffolds in transplantation and tissue engineering: Immunogenicity versus positive cell stimulation. *Materials Science and Engineering: C*, 127:112203, 2021. ISSN: 0928-4931. DOI: `https://doi.org/10.1016/j.msec.2021.112203`. URL: `https://www.sciencedirect.com/science/article/pii/S092849312100343X`.

[470] Eva Jablonská, JiÅí Kubásek, Dalibor Vojtěch, Tomáš Ruml, and Jan Lipov. Test conditions can significantly affect the results of in vitro cytotoxicity testing of degradable metallic biomaterials. eng. *Scientific reports*, 11(1):6628, 2021. ISSN: 2045-2322 (Electronic). DOI: `10.1038/s41598-021-85019-6`.

[471] Weijia Li, Jing Zhou, and Yuyin Xu. Study of the in vitro cytotoxicity testing of medical devices. eng. *Biomedical reports*, 3(5):617–620, 2015. ISSN: 2049-9434 (Print). DOI: `10.3892/br.2015.481`.

[472] Joanna Gola. Chapter 10 - Quality Control of BiomaterialsâOverview of the Relevant Technologies. In Marek J Łos, Andrzej Hudecki, and Emilia Wiecheć, editors, *Stem Cells and Biomaterials for Regenerative Medicine*, pages 143–161. Academic Press, 2019. ISBN: 978-0-12-812258-7. DOI: `https://doi.org/10.1016/B978-0-12-812258-7.00010-1`. URL: `https://www.sciencedirect.com/science/article/pii/B9780128122587000101`.

[473] C Wiegand and U.-C. Hipler. Evaluation of Biocompatibility and Cytotoxicity Using Keratinocyte and Fibroblast Cultures. *Skin Pharmacology and Physiology*, 22(2):74–82, 2009. ISSN: 1660-5527. DOI: `10.1159/000178866`. URL: `https://doi.org/10.1159/000178866`.

[474] Weidong Weng, Filippo Zanetti, David Bovard, Bianca Braun, Sabrina Ehnert, Tatiana Uynuk-Ool, Tina Histing, Julia Hoeng, Andreas K Nussler, and Romina H Aspera-Werz. A simple method for decellularizing a cell-derived matrix for bone cell cultivation and differentiation. eng. *Journal of materials science. Materials in medicine*, 32(9):124, 2021. ISSN: 1573-4838 (Electronic). DOI: `10.1007/s10856-021-06601-y`.

[475] Roberto Gaetani, Soraya Aude, Lea Lara DeMaddalena, Heinz Strassle, Monika Dzieciatkowska, Matthew Wortham, R Hugh F Bender, Kim-Vy Nguyen-Ngoc, Geert W Schmid-Schöenbein, Steven C George, Christopher C W Hughes, Maike Sander, Kirk C Hansen, and Karen L Christman. Evaluation of Different Decellularization Protocols on the Generation of Pancreas-Derived Hydrogels. eng. *Tissue engineering. Part C, Methods*, 24(12):697–708, 2018. ISSN: 1937-3392 (Electronic). DOI: `10.1089/ten.TEC.2018.0180`.

[476] Bogdan Huzum, Bogdan Puha, Riana Maria Necoara, Stefan Gheorghevici, Gabriela Puha, Alexandru Filip, Paul Dan Sirbu, and Ovidiu Alexa. Biocompatibility assessment of biomaterials used in orthopedic devices: An overview (Review). eng. *Experimental and therapeutic medicine*, 22(5):1315, 2021. ISSN: 1792-1015 (Electronic). DOI: `10.3892/etm.2021.10750`.

[477] Walid Al-Zyoud, Dana Haddadin, Sameer Ahmad Hasan, Hussamaldeen Jaradat, and Olfa Kanoun. Biocompatibility Testing for Implants: A Novel Tool for Selection and Characterization. *Materials*, 16(21), 2023. ISSN: 1996-1944. DOI: `10.3390/ma16216881`. URL: `https://www.mdpi.com/1996-1944/16/21/6881`.

[478] Seongoh Kim, Yunkyung Lee, Manhee Lee, Sangmin An, and Sang-Joon Cho. Quantitative Visualization of the Nanomechanical Young's Modulus of Soft Materials by Atomic Force Microscopy. eng. *Nanomaterials (Basel, Switzerland)*, 11(6), 2021. ISSN: 2079-4991 (Print). DOI: `10.3390/nano11061593`.

[479] Anita Kwaśniewska, Michał Świetlicki, Adam Prószyński, and Grzegorz Gładyszewski. The Quantitative Nanomechanical Mapping of Starch/Kaolin Film Surfaces by Peak Force AFM. eng. *Polymers*, 13(2), 2021. ISSN: 2073-4360 (Electronic). DOI: `10.3390/polym13020244`.

[480] Nadeem Ali-Khan, Xun Zuo, and David W Speicher. Overview of proteome analysis. eng. *Current protocols in protein science*, Chapter 22:22.1.1–22.1.19, 2003. ISSN: 1934-3663 (Electronic). DOI: `10.1002/0471140864.ps2201s30`.

[481] Shino Magaki, Seyed A Hojat, Bowen Wei, Alexandra So, and William H Yong. An Introduction to the Performance of Immunohistochemistry. eng. *Methods in molecular biology (Clifton, N.J.)*, 1897:289–298, 2019. ISSN: 1940-6029 (Electronic). DOI: `10.1007/978-1-4939-8935-5_25`.

[482] Karl H Hillebrandt, Hannah Everwien, Nils Haep, Eriselda Keshi, Johann Pratschke, and Igor M Sauer. Strategies based on organ decellularization and recellularization. *Transplant International*, 32(6):571–585, 2019. DOI: `https://doi.org/10.1111/tri.13462`. URL: `https://onlinelibrary.wiley.com/doi/abs/10.1111/tri.13462`.

[483] Shehnaz Ahmed, Veeren M Chauhan, Amir M Ghaemmaghami, and Jonathan W Aylott. New generation of bioreactors that advance extracellular matrix modelling and tissue engineering. eng. *Biotechnology letters*, 41(1):1–25, 2019. ISSN: 1573-6776 (Electronic). DOI: `10.1007/s10529-018-2611-7`.

[484] Heejo Yang, Anthony Atala, and James J Yoo. Kidney regeneration approaches for translation. eng. *World journal of urology*, 38(9):2075–2079, 2020. ISSN: 1433-8726 (Electronic). DOI: `10.1007/s00345-019-02999-x`.

[485] Tiziana Martinello, Ilaria Bronzini, Andrea Volpin, Vincenzo Vindigni, Lisa Maccatrozzo, Giovanni Caporale, Franco Bassetto, and Marco Patruno. Successful recellularization of human tendon scaffolds using adipose-derived mesenchymal stem cells and collagen gel. *Journal of Tissue Engineering and Regenerative Medicine*, 8(8):612–619, 2014. DOI: `https://doi.org/10.1002/term.1557`. URL: `https://onlinelibrary.wiley.com/doi/abs/10.1002/term.1557`.

[486] Dana M Schwartz, Meryem O Pehlivaner Kara, Allan M Goldstein, Harald C Ott, and Adam K Ekenseair. Spray Delivery of Intestinal Organoids to Reconstitute Epithelium on Decellularized Native Extracellular Matrix. eng. *Tissue engineering. Part C, Methods*, 23(9):565–573, 2017. ISSN: 1937-3392 (Electronic). DOI: `10.1089/ten.TEC.2017.0269`.

[487] Ru-Huei Fu, Yu-Chi Wang, Shih-Ping Liu, Ton-Ru Shih, Hsin-Lien Lin, Yue-Mi Chen, Jiun-Huei Sung, Chia-Hui Lu, Jing-Rong Wei, Zih-Wan Wang, Shyh-Jer Huang, Chang-Hai Tsai, Woei-Cherng Shyu, and Shinn-Zong Lin. Decellularization and Recellularization Technologies in Tissue Engineering. *Cell Transplantation*, 23(4-5):621–630, 2014. ISSN: 0963-6897. DOI: `10.3727/096368914X678382`. URL: `https://doi.org/10.3727/096368914X678382`.

[488] Aida Shakouri-Motlagh, Andrea J O'Connor, Shaun P Brennecke, Bill Kalionis, and Daniel E Heath. Native and solubilized decellularized extracellular matrix: A critical assessment of their potential for improving the expansion of mesenchymal stem cells. *Acta Biomaterialia*, 55:1–12, 2017. ISSN: 1742-7061. DOI: `https://doi.org/10.1016/j.actbio.2017.04.014`. URL: `https://www.sciencedirect.com/science/article/pii/S1742706117302398`.

Appendix A

Materials

Table A.1: Equipment and consumables used throughout the project.

Equipment/consumable	Model/Part number	Supplier/Manufacturer
AFM probes	-	Bruker
Atomic Force Microscope	FastScan	Bruker
Biobath	2752-005	Instron
Biological safety cabinet (class II)	Biological safety cabinet (class II)	Thermo Scientific
Biopunch (6 mm diameter)	WHAWB100082	Sigma-Aldrich
Block heater	AccuBlockTM digital dry bath	Labnet International Inc.
Centrifuge	Harrier 15/80	SANYO Biomedical Europe BV
Class II safety cabinet	Herasafe	Hereaus
Coplin jar	900470	Wheaton Scientific
Cryostat	CM1850	Leica Biosystems
Digital balance	GX-2000	A&D
Digital microbalance	ABJ220-4NM	KERN
Dissection scissors	E101/03	S Murray
Embedding station & cryo plate	EG1150C	Leica Biosystems
Filter paper	-	SLS
Fine tip stainless steel forceps	E12	Raymond A Lamb
Forceps	E003-E004	Samco
Freeze dryer	ModulyoD-230	ThermoSavant
Histology cassettes	720-0887	VWR International
Hotplate	E18.1	Raymond Lamb
Incubator	Heraeus	Jencons PLC
Incubator	MIR-262	Sanyo

Large histology cover slips	3800198G	Leica Biosystems
Long hair brush No. 6	E6	Raymond A Lamb
Magnetic stirrer	CB161	Stuart Scientific
Magnifying lamp (1.75X)	D20251	The Daylight Company
Materials testing Machine	3365	Instron
Microplate 96 well flat	439454	Thermo Scientific
Microplate spectrophotometer	Multiskan spectrum	Thermo Scientific
Microtome	RM2255	Leica Biosystems
Microtome blades	3808311E	Leica Biosystems
Orbital shaker	POS 300/ PSU-10i	Grant
Para-film	SEL-400-030P	Thermo Scientific
Pasteur pipette	pmk-500-070w	Fisher Scientific
pH meter	3510	Jenway
Polypropylene universal (30 mL)	SLS7516	Scientific Laboratory Supplies
Scalpel blades	12398009	Fisher Scientific
Scalpel handle No. 3	12464070	Fisher Scientific
Scalpel handle No. 4	12348019	Fisher Scientific
Serological pipette (various volumes)	CLS4251-200EA	Sigma-Aldrich
Staining rack	12676756	Fisher Scientific
Standard histology cover slips	MIC3228	Scientific Laboratory Supplies
Standard histology moulds	E10.8/4161	Raymond A Lamb
Sterile bijou tube	SLS7522	Scientific Laboratory Supplies
Sterile pots (150 mL)	Con7580S	SLS
Sterilisation oven	-	GenLab
Superfrost plus microscope slides	MIC3022	SLS
Syringe (various volumes)	GS57X	Terumo
Syringe filter 0.22 µm	SLGP033RS	Merck Millipore Ltd
Tissue processor	TP1020	Leica
Universal tube (30 mL polypropylene)	SLS7516	Scientific Laboratory Supplies
Water Bath	MH8515	Barnstead Electrothermal
Wax dispenser	E66	R.A.LAMB

Table A.3: Chemicals and reagents used throughout the project.

Reagent/Chemical	Catalogue number	Supplier
0.9% Sodium chloride	UKF7124	Baxter
1,9 dimethylmethylene blue	341,088	Sigma-Aldrich
Absolute ethanol	E/0650DF	Fisher Scientific
Acetone	20065.362	VWR International
Alcian Blue (pH 2.5)/PAS stain kit	RRSK6-500	Atom Scientific
alpha chymotrypsin	C4129-10	Sigma
Amphotericin B	A2942-100ML	Sigma
Aprotonin (10000 KIU.mL^{-1})	AP-R	Nordic Pharma
Aqueous mountant	S3023	Dako
Benzonase ® Nuclease HC, Purity >90%	71205-3	Merck Chemicals
Bovine serum albumin	A7030-100G	Sigma-Aldrich
Calcium chloride	ALFA12316.A1	VWR International
Calcium chloride (dihydrate)	C7902	Sigma-Aldrich
Chlormine T hydrate	857319	VWR International
Chondroitin sulphate B	C3788	Sigma-Aldrich
Chondroitinase ABC	C2905-10UN	Sigma
Citric acid (monohydrate)	20276.292	VWR International
DAPI stain	D9564	Sigma-Aldrich
Disodium ethylenediaminetetraacetic acid (EDTA)	F/P140/65	Thermo Fisher Scientific Ltd.
Disodium hydrogen orthophosphate (anhydrous)	1.06586.0500	Merck Millipore
DPX mountant	RRSP29	Atom Scientific
Dulbecco's PBS tablets	BR0014	Oxoid
Eosin Y	1.09844.1000	Merck Millipore
Ethylenediaminetetraacetic acid	E/P140/65	Thermo Fisher Scientific Ltd.
Fast green	F7258	Sigma-Aldrich
Formaldehyde (formalin)	F-8775	Sigma
Formic acid	10,652-6	Sigma-Aldrich
Glacial acetic acid	10001	VWR International
Hydrochloric acid	2611.5	VWR International
Industrial Grade superglue (various viscosities)	-	Everbuild
L-cysteine hydrochloride anhydrous	C1276	Sigma-Aldrich

Leica Cryofact Disinfectant	LCR4 P301213	Ecolab
Liquid Nitrogen	-	BOC
Magnesium chloride hexahydrate	25108.26	VWR International
Mayer's haematoxylin	RRSP60	Atom Scientific
Millers stain	LAMB/080-D	Raymond A Lamb
Neutral buffered formalin	RRFF4000-G	Atom Scientific
OCT embedding matrix	LAMB/OCT	Raymond A Lamb
Oxalic acid	1017440	VWR International
Papain	AC416761000	Acros Organics
Paraffin wax	W2	Raymond A Lamb
p-dimethylaminobenzaldehyde	D2004	Sigma-Aldrich
Peracetic acid (38-40%)	107222	Merck
Perchloric acid (60%)	20583.26	VWR International
Picric acid	36011	Sigma-Aldrich
Potassium permanganate	P/6520/53	Fisher Scientific
Propan-1-ol	20861.363	VWR International
Ringer's tablets	BR0052G	Oxoid
Ringer's tablets	96724-100TAB	Sigma-Aldrich
Safranin O	41921-0250	Acros Organics
Scott's tap water	RRSP190	Atom Scientific
Sirius red	F3B	VWR International
Sodium acetate (trihydrate)	S/2040/53	Thermo Fisher Scientific Ltd.
Sodium chloride	42429-5000	Thermo Fisher Scientific Ltd.
Sodium dihydrogen orthophosphate	102454R	VWR International
Sodium dodecyl sulphate (SDS)	71727	Sigma-Aldrich
Sodium formate	A178813	Alfa Aesar
sodium hdi-hydrogen orthophosphate monohydrate	102454R	VWR International
Sodium hydroxide pellets	S/4920/60	Thermo Fisher Scientific Ltd.
Sudan Black staining kit	YS-RRSK17-2011	Atom Scientific
Superglue	-	Henkel
Trans-4-hydrozy-L-proline	A11851	Alfa Aesar
Trizma base	T-1503	Sigma-Aldrich
Weigert's haematoxylin A/B	RRSP7X-D	Atom Scientific
Xylene	GPS1001-G	Atom Scientific